

TECHNISCHE  
UNIVERSITÄT  
MÜNCHEN



WALTHER - MEISSNER -  
INSTITUT FÜR TIEF -  
TEMPERATURFORSCHUNG



BAYERISCHE  
AKADEMIE DER  
WISSENSCHAFTEN

# Magnetization control in multiferroic heterostructures

Diploma thesis  
Mathias Weiler

Advisor: Prof. Dr. Rudolf Gross

Munich, December 2007



# Contents

<b>1</b>	<b>Introduction</b>	<b>1</b>
<b>2</b>	<b>Ferroics and multiferroics</b>	<b>5</b>
2.1	Ferroics . . . . .	6
2.1.1	Ferromagnets . . . . .	9
2.1.2	Ferroelectrics . . . . .	11
2.1.3	Ferroelastics . . . . .	12
2.2	Multiferroics . . . . .	13
2.3	The magnetic free energy density . . . . .	14
2.3.1	Contributions to the magnetic free energy density . . . . .	16
2.3.2	Magnetoelastic effect . . . . .	17
2.3.3	Magnetoelectric effect . . . . .	17
2.4	Conclusion . . . . .	18
<b>3</b>	<b>Materials</b>	<b>21</b>
3.1	Ferromagnetic materials . . . . .	21
3.1.1	Nickel . . . . .	22
3.1.2	Cobalt . . . . .	22
3.1.3	Magnetite . . . . .	23
3.2	Barium titanate . . . . .	24
3.3	Lead zirconate titanate . . . . .	27
3.4	Magnesium oxide . . . . .	27
<b>4</b>	<b>Experimental techniques</b>	<b>29</b>
4.1	SQUID magnetometry . . . . .	29
4.2	Ferromagnetic resonance spectroscopy . . . . .	30
4.2.1	Theoretical background . . . . .	30
4.2.2	Experimental setup for FMR measurements . . . . .	33

---

4.2.3	Modulation and lock-in detection . . . . .	33
4.3	High resolution X-ray diffraction . . . . .	36
4.3.1	Experimental setup . . . . .	36
4.3.2	Scattering theory . . . . .	36
4.3.3	Reflections in reciprocal space . . . . .	37
4.3.4	Determination of lattice constants . . . . .	39
4.3.5	Precise lattice parameter determination . . . . .	40
<b>5</b>	<b>Measuring strain in MgO single crystals</b>	<b>43</b>
5.1	Introduction . . . . .	43
5.2	Elastic theory . . . . .	44
5.3	Measurement results . . . . .	46
5.3.1	Strain effect on the out-of-plane lattice constant . . . . .	46
5.3.2	Estimation of the measurement uncertainty . . . . .	48
5.3.3	Strain effect on the in-plane lattice constants . . . . .	48
5.4	Discussion . . . . .	54
<b>6</b>	<b>Strain-induced magnetization switching in ferromagnetic thin films</b>	<b>57</b>
6.1	Motivation . . . . .	57
6.2	Sample preparation . . . . .	58
6.3	Cobalt thin films . . . . .	60
6.3.1	In-plane FMR measurements . . . . .	61
6.3.2	Discussion . . . . .	61
6.4	Nickel thin films . . . . .	63
6.4.1	In-plane FMR measurements . . . . .	63
6.4.2	Out-of-plane FMR measurements . . . . .	65
6.4.3	Linearity and reversibility of voltage dependence . . . . .	65
6.4.4	Discussion . . . . .	67
6.4.5	Numerical simulations . . . . .	67
6.5	Theoretical description . . . . .	69
6.6	Manipulating the magnetization switching behavior with external mag- netic fields . . . . .	75
6.7	Application: Piezomodulated ferromagnetic resonance . . . . .	80
6.7.1	Modulation parameters . . . . .	80
6.7.2	PMFMR experiments . . . . .	81

---

6.7.3	In-plane anisotropy . . . . .	83
6.7.4	Influence of modulation amplitude and frequency . . . . .	84
6.7.5	Comparison to conventional FMR measurements . . . . .	86
<b>7</b>	<b>Converse magnetoelectric effect in <math>\text{Fe}_3\text{O}_4/\text{BaTiO}_3</math> heterostructures</b>	<b>89</b>
7.1	Introduction . . . . .	89
7.1.1	The converse magnetoelectric effect in multiferroic heterostructures . . . . .	90
7.1.2	Sample . . . . .	90
7.2	Polarization in the ferroelectric $\text{BaTiO}_3$ phase . . . . .	91
7.3	HRXRD measurements . . . . .	92
7.3.1	Measurement results . . . . .	93
7.3.2	Discussion . . . . .	93
7.4	Magnetization in the ferromagnetic $\text{Fe}_3\text{O}_4$ phase . . . . .	95
7.5	SQUID measurements . . . . .	95
7.5.1	Measurement results . . . . .	96
7.5.2	Discussion . . . . .	100
7.6	FMR measurements . . . . .	101
7.6.1	Measurement results . . . . .	102
7.6.2	Discussion . . . . .	106
7.7	Theoretical description . . . . .	107
7.7.1	Linear piezoelectric effect . . . . .	108
7.7.2	Domain effects . . . . .	110
7.7.3	Possible antisymmetric effects . . . . .	114
<b>8</b>	<b>Temperature dependent magnetic resonance in <math>\text{Fe}_3\text{O}_4/\text{BaTiO}_3</math> heterostructures</b>	<b>117</b>
8.1	Introduction . . . . .	117
8.2	Measurement results . . . . .	119
8.2.1	ESR spectra of barium titanate . . . . .	119
8.2.2	Temperature dependence of FMR . . . . .	120
8.2.3	Magnetic anisotropy of the $\text{Fe}_3\text{O}_4$ film as a function of the $\text{BaTiO}_3$ crystalline phase . . . . .	123
8.3	Numerical simulations . . . . .	126
8.4	Theoretical description . . . . .	127

---

<b>9</b>	<b>Summary and Outlook</b>	<b>133</b>
9.1	Summary . . . . .	133
9.1.1	Strain-induced magnetization switching in ferromagnetic thin films . . . . .	134
9.1.2	Converse magnetoelectric effect in $\text{Fe}_3\text{O}_4/\text{BaTiO}_3$ heterostructures . . . . .	136
9.1.3	Temperature dependent magnetic resonance in $\text{Fe}_3\text{O}_4/\text{BaTiO}_3$ heterostructures . . . . .	138
9.2	Outlook . . . . .	139
	<b>Bibliography</b>	<b>143</b>

# List of Figures

2.1	Free energy and hysteresis loops . . . . .	8
2.2	Phase control in multiferroics . . . . .	13
2.3	Coordinate system . . . . .	15
3.1	Temperature dependence of BaTiO <sub>3</sub> lattice parameters . . . . .	25
3.2	BaTiO <sub>3</sub> unit cell and spontaneous polarization . . . . .	25
3.3	BaTiO <sub>3</sub> unit cell surfaces . . . . .	26
4.1	SQUID magnetometer . . . . .	30
4.2	FMR setup . . . . .	34
4.3	Example FMR spectrum . . . . .	35
4.4	HRXRD setup and Bragg's law . . . . .	37
4.5	Reciprocal space . . . . .	38
4.6	Example $2\theta$ - $\theta$ -scan and RSM . . . . .	39
4.7	Dependence of systematic error on diffraction angle . . . . .	40
5.1	Sample and schematic view of lattice strain . . . . .	44
5.2	$2\theta$ - $\theta$ -scans of the MgO (002) and (004) reflections . . . . .	47
5.3	Out-of-plane lattice constant as a function of actuator voltage . . . . .	47
5.4	Nelson Riley correction of $c^{\text{MgO}}$ . . . . .	49
5.5	RSM: MgO (204) . . . . .	51
5.6	RSM: MgO (024) . . . . .	52
5.7	RSM: MgO (224) . . . . .	53
6.1	Magnetoelastic effect in Fe <sub>3</sub> O <sub>4</sub> . . . . .	58
6.2	Sample on actuator . . . . .	59
6.3	Sample mounting for FMR measurements . . . . .	61
6.4	Strain dependent in-plane anisotropy for CP1 . . . . .	62
6.5	Strain dependent in-plane anisotropy for NP2 . . . . .	64

6.6	Strain dependent in-plane anisotropy for NP3 . . . . .	64
6.7	Strain dependent out-of-plane anisotropy for NP2 . . . . .	65
6.8	Strain dependent out-of-plane anisotropy for NP3 . . . . .	66
6.9	Linear effect of strain on NP3 resonance field . . . . .	66
6.10	NP3 $\mu_0 H_{\text{res}}$ ip: Numerical simulation and experimental data . . . . .	69
6.11	NP3 $\mu_0 H_{\text{res}}$ oop: Numerical simulation and experimental data . . . . .	70
6.12	NP3 FMR resonance fields, theory and experiment . . . . .	74
6.13	Strain dependence of the NP3 free energy surface . . . . .	75
6.14	Irreversible demagnetization due to degenerate free energy minima . . . . .	76
6.15	Magnetization switching with applied magnetic field . . . . .	78
6.16	Calculated free energy surfaces for NP3 with applied magnetic field . . . . .	79
6.17	Schematic principle of anisotropic signal modulation . . . . .	82
6.18	CP1 in-plane anisotropy by PMFMR . . . . .	83
6.19	Influence of modulation frequency on PMFMR signal . . . . .	84
6.20	Influence of modulation amplitude on PMFMR signal . . . . .	85
6.21	Comparison to conventional FMR . . . . .	86
7.1	Schematic view of sample and BaTiO <sub>3</sub> domains . . . . .	91
7.2	RSMs showing domains in BaTiO <sub>3</sub> . . . . .	93
7.3	BaTiO <sub>3</sub> domain fractions at different electric fields . . . . .	94
7.4	$M(H)$ -loops of Fe <sub>3</sub> O <sub>4</sub> /BaTiO <sub>3</sub> as a function of $V_{\text{BTO}}$ . . . . .	96
7.5	$M(E)$ -loops of Fe <sub>3</sub> O <sub>4</sub> /BaTiO <sub>3</sub> for $\mathbf{H} \parallel [100]$ . . . . .	97
7.6	Symmetric and antisymmetric contribution to $M(E)$ -loop . . . . .	98
7.7	Maximum relative change in $m$ as a function of $\mu_0 H$ . . . . .	98
7.8	$M(H)$ - and $M(E)$ -loop of Fe <sub>3</sub> O <sub>4</sub> /BaTiO <sub>3</sub> for $\mathbf{H} \parallel [001]$ . . . . .	100
7.9	In-plane FMR spectra of Fe <sub>3</sub> O <sub>4</sub> /BaTiO <sub>3</sub> . . . . .	103
7.10	In-plane FMR resonance fields of Fe <sub>3</sub> O <sub>4</sub> /BaTiO <sub>3</sub> . . . . .	104
7.11	Symmetric and antisymmetric contributions to $\mu_0 H_{\text{res}}$ . . . . .	105
7.12	Out-of-plane FMR spectra of Fe <sub>3</sub> O <sub>4</sub> /BaTiO <sub>3</sub> . . . . .	105
7.13	In-plane and out-of-plane anisotropy of unpoled Fe <sub>3</sub> O <sub>4</sub> /BaTiO <sub>3</sub> . . . . .	106
7.14	Top and side view of our heterostructure . . . . .	108
7.15	$d_{31}$ -effect in BaTiO <sub>3</sub> . . . . .	109
7.16	Ferroelectric BaTiO <sub>3</sub> domains as elastic domains . . . . .	112
8.1	Sample and temperature dependence of BaTiO <sub>3</sub> lattice parameters . . . . .	118

---

8.2	ESR spectra of BaTiO <sub>3</sub> in different BaTiO <sub>3</sub> phases . . . . .	120
8.3	Temperature dependence of ESR spectra in Fe <sub>3</sub> O <sub>4</sub> / BaTiO <sub>3</sub> . . . . .	121
8.4	$\mu_0 H_{\text{res}}(T)$ for $\mathbf{H}_0 \parallel [100]$ and $\mathbf{H}_0 \parallel [010]$ . . . . .	122
8.5	In-plane ESR spectra of Fe <sub>3</sub> O <sub>4</sub> /BaTiO <sub>3</sub> as a function of $T$ . . . . .	124
8.6	In-plane anisotropy of $\mu_0 H_{\text{res}}(T)$ . . . . .	125
8.7	Temperature dependence of anisotropy fields . . . . .	126
8.8	Free energy obtained from magnetoelastic theory and simulation . . . . .	129
8.9	Temperature dependent strains in Fe <sub>3</sub> O <sub>4</sub> / BaTiO <sub>3</sub> . . . . .	130
9.1	Strain control of magnetic anisotropy in nickel thin films . . . . .	134
9.2	Electric field control of magnetization in Fe <sub>3</sub> O <sub>4</sub> / BaTiO <sub>3</sub> . . . . .	136
9.3	Temperature control of magnetization in Fe <sub>3</sub> O <sub>4</sub> / BaTiO <sub>3</sub> . . . . .	138
9.4	Multiferroic multilayer . . . . .	141

# List of Tables

2.1	Analogies between different ferroic materials. . . . .	6
3.1	Nickel – material constants . . . . .	22
3.2	Cobalt – material constants 1 . . . . .	23
3.3	Cobalt – material constants 2 . . . . .	23
3.4	$\text{Fe}_3\text{O}_4$ – material constants . . . . .	24
3.5	$\text{BaTiO}_3$ – material constants . . . . .	27
3.6	PZT – material constants . . . . .	27
3.7	MgO – material constants . . . . .	28
6.1	NP3 anisotropy constants . . . . .	68
7.1	$\text{Fe}_3\text{O}_4/\text{BaTiO}_3$ – anisotropy constants at $V_{\text{BTO}}=0\text{V}$ . . . . .	106
7.2	$\text{Fe}_3\text{O}_4/\text{BaTiO}_3$ – local strains and anisotropy constants . . . . .	111

# Chapter 1

## Introduction

In contrast to conventional electronic devices which utilize only the charge degree of freedom, spintronic devices take advantage of the electron spin degree of freedom and thus unite magnetic and electric properties. Due to their application relevance and their outstanding fundamental physical principles, they are a vigorously investigated topic. Concerning their technological applications, spintronic devices are nowadays most prominently used as hard disk drive reading heads. By awarding this year's Nobel prize in physics to Albert Fert and Peter Grünberg for the discovery of the giant magnetoresistance [1, 2], the importance of this field of research is unambiguously emphasized.

Controlling the magnetization is a very important aspect for the realization of spintronic devices. Naturally, magnetization can be controlled by external magnetic fields. However, the implementation of magnetic fields of sufficient strength to switch the magnetization is technologically difficult on sufficiently small length scales and power consuming. Hence, other approaches to control the magnetization are needed. From a technological point of view, electric fields are easy to implement on even very small length scales, power efficient and fully switchable. The ability to reversibly switch the magnetization orientation by an electric field is thus considered a milestone on the way to new functional spintronic devices.

The necessary physical properties for such an electric field control of magnetization are given in materials that exhibit ferromagnetic and ferroelectric properties at the same time. These so-called multiferroic materials are an important topic of current research as multiferroic devices may be employed in future random access memories that combine the advantages of magnetic and ferroelectric random access memories [3, 4].

In this thesis, we investigate the properties of multiferroic heterostructures rather than that of materials which unite ferromagnetic and ferroelectric properties in one phase, as only heterostructures show robust multiferroic properties at room temperature [5].

A brief overview of the general concept of ferroic materials and their description by a free energy is given in Chapter 2, along with the introduction to the properties of multiferroic materials and the expected interactions between ferromagnetic and ferroelectric phases. The material parameters of the ferroic materials used in this thesis are summarized in Chapter 3. In addition to the elemental ferromagnetic materials cobalt and nickel, the iron oxide magnetite ( $\text{Fe}_3\text{O}_4$ ) is investigated. Thin films of these ferromagnetic materials are deposited on ferroelectric substrates. With barium titanate ( $\text{BaTiO}_3$ ) and PZT-based piezoelectric actuators, two ferroelectric substrates that will show vastly different influences on the ferromagnetic thin films are presented.

This thesis makes use of high resolution X-ray diffraction (HRXRD), ferromagnetic resonance (FMR) and superconducting quantum interference device (SQUID) magnetometry, which represent a powerful set of techniques to determine structural as well as magnetic properties. The most relevant aspects of these techniques for the measurements performed during this thesis are summarized in Chapter 4.

The first half of the experimental part of this thesis is concerned with the magnetoelastic effect that describes the influence of strain on magnetic anisotropy. To this end, a magnetostrictive and a piezoelectric phase are coupled in heterostructures of ferromagnetic thin films on voltage controlled ferroelectric actuators.

The strains involved in this coupling can directly be observed by HRXRD as shown exemplarily for single crystals of MgO that are glued onto actuators in Chapter 5. In Chapter 6, polycrystalline thin films of cobalt and nickel that are evaporated onto piezoelectric actuators are investigated. The magnetic anisotropy of these heterostructures is determined at room temperature by FMR as a function of the voltage applied to the actuator. Numerical simulations of the free energy surfaces yield the voltage dependent equilibrium orientation of the magnetization. These results are compared to those expected from magnetoelastic theory and the effect of external magnetic fields on the magnetization is considered. A technological application for this voltage-strain-control of magnetization orientation, that replaces the magnetic field modulation of conventional FMR, is introduced.

In the second half of this thesis, the multiferroic material system consisting of  $\text{Fe}_3\text{O}_4$  thin films that are deposited onto  $\text{BaTiO}_3$  substrates by pulsed laser deposition is presented. The dependence of the magnetization on the electric polarization of the  $\text{BaTiO}_3$  substrate at room temperature is investigated in Chapter 7. To this end, the polarization of the  $\text{BaTiO}_3$  substrate is studied by HRXRD measurements and its influence on the magnetization is probed by SQUID and FMR measurements.

Finally, in Chapter 8, we investigate the FMR of a  $\text{Fe}_3\text{O}_4/\text{BaTiO}_3$  heterostructure as a function of temperature.  $\text{BaTiO}_3$  exhibits several structural phase transitions at characteristic phase transition temperatures that influence the magnetization of the  $\text{Fe}_3\text{O}_4$  thin film by interface strain coupling. Hence, in addition to electric fields, temperature is a second means of controlling the magnetization in this heterostructure.



# Chapter 2

## Ferroics and multiferroics

Materials that exhibit spontaneous electric polarization, magnetization or strain are called ferroics. They are of the utmost technological importance, as the natural remanence of these materials opens the possibility to use them e.g. for information storage devices. Hard disk drives that rely on platters with ferromagnetic surfaces for non-volatile data storage are indispensable to cope with today's data volume in information technology. Ferroelectric random access memory is commercially available and widely used in smartcards [6]. Ferroelastic materials are used amongst others in medical applications such as minimally invasive stents that widen narrowed blood vessels.

The already extremely high technological importance of ferroic materials could be further increased if two or more ferroic properties are united in the same phase. Such materials are called multiferroics. For example, many materials combine ferroelectric and ferroelastic properties. Unfortunately, materials combining ferromagnetic and ferroelectric properties – such as  $\text{HoMnO}_3$  – are very rare and do not show robust multiferroic properties at room temperature [5]. However, materials showing magnetoelectric coupling are of great interest, as they would allow for an electric field control of magnetization that may be used in magnetoresistive random access memory or other devices utilizing magnetoresistive effects.

Robust room temperature multiferroic properties are found in heterostructures consisting of separate ferromagnetic and ferroelectric phases, which allows for an electric field control of magnetization. In this thesis, multiferroic heterostructures consisting of a ferromagnetic thin film and a ferroelectric substrate are investigated. This allows us to determine the interaction between the different ferroic properties.

	Ferromagnetic	Ferroelectric	Ferroelastic
$\eta$	Magnetization $M$	Polarization $P$	Strain $\varepsilon$
$\xi$	Magnetic field $H$	Electric field $E$	Stress $\sigma$
$T \geq T_c$	Paramagnetic phase	Paraelectric phase	Austenite phase
$T < T_c$	Ferromagnetic phase	Ferroelectric phase	Martensite phase
Domain walls	Bloch or Neel walls	Ferroelectric domain walls	Boundaries between variants

**Table 2.1:** Analogies between different ferroic materials.

## 2.1 Ferroics

Several crystals undergo phase transitions if external parameters such as pressure or temperature are changed. If, in a certain crystal, at least one of these phase transitions is accompanied by a spontaneous change of directional symmetry, one speaks of a ferroic crystal. Landau and Lifshitz [7] pointed out that crystal symmetry may spontaneously be broken even if the atoms in the crystal itself are rearranged continuously, which is obvious if one for example imagines a cubic crystal becoming distorted to tetragonal shape by an arbitrary small displacement of lattice atoms. A phase transition involving a spontaneous break of symmetry caused by a continuously evolving order parameter  $\eta$  is called a second-order phase transition. In our case, the order parameter is the magnetization  $M$ , polarization  $P$  or strain  $\varepsilon$  and the phase transition to the ferroic state occurs if the order parameter becomes different from zero. It is important to note that this ordering needs to be *spontaneous*, thus must occur even in the absence of an external field. The analogies between the different ferroic materials are shown in Tab. 2.1. In the absence of applied fields, thermodynamic equilibrium is determined by minimizing the Helmholtz free energy  $F(\eta, T)$  with respect to the order parameter  $\eta$ . Thus the necessary condition for equilibrium is given by [8]:

$$\frac{\partial F}{\partial \eta} \stackrel{!}{=} 0. \quad (2.1)$$

If an external field  $\xi$  is applied, which in our case is given by a magnetic field  $H$ , electric field  $E$  or a mechanical stress  $\sigma$ , the total free energy is quantified by the

Gibbs relation:

$$G(\eta, \xi, T) = F(\eta, T) - \xi\eta, \quad (2.2)$$

and thermodynamic equilibrium is reached if

$$\begin{aligned} \frac{\partial G}{\partial \eta} = 0 \quad , \quad \frac{\partial^2 G}{\partial^2 \eta} > 0 \\ \Leftrightarrow \frac{\partial F}{\partial \eta} = \xi \quad , \quad \frac{\partial^2 F}{\partial^2 \eta} > 0 \end{aligned} \quad (2.3)$$

is fulfilled. Therefore Eq. (2.3) describes the adjustment of the order parameter to balance the internal energy with the work caused by the external field. The spontaneous ordering in the absence of an external field is described by  $\eta(T) = 0$  for  $T \geq T_c$  and  $\eta(T) \neq 0$  for  $T < T_c$ .  $T_c$  is the Curie temperature at which the crystal undergoes the phase transition to the ferroic state (often referred to as disorder-order or soft-mode transition). If  $T \geq T_c$ , the ferroic material is in a non-ordered state which is called paramagnetic, paraelectric or austenite, respectively (cf. Tab 2.1). In this state, the order parameter  $\eta \in \{M, P, \varepsilon\}$  is a linear function of the field  $\xi \in \{H, E, \sigma\}$  for sufficiently small fields. For paramagnetic materials it is given by  $M = C \cdot H/T$  with the Curie-constant  $C$  and for paraelectric materials by  $P = \varepsilon_0 \chi E$  with the permittivity of free space  $\varepsilon_0$  and the electric susceptibility  $\chi$ . Finally, for austenite materials, the order parameter is given by  $\varepsilon = s^E \sigma$  with Young's modulus  $s^E$ .

If we now assume  $T < T_c$ , the breaking of symmetry leads to a spontaneous ordering of magnetization, polarization or strain in the crystal even without an external field, and the material is now in its ferromagnetic, ferroelectric or martensite phase. If no external field is applied, all orientations of the order parameter are equally favorable and therefore domains enclosing regions of equally oriented order parameter emerge in such a way that the macroscopic ordering may remain zero.

The dependence of the order parameter on an external field can be described by an appropriately chosen Helmholtz free energy  $F$ , which for ferromagnetic and ferroelectric materials can be derived from the Taylor expansion of the Helmholtz free energy shown in [9] as:

$$F(\eta) = \begin{cases} \frac{1}{2}\kappa(\eta + \eta_R)^2 & , \eta \leq -\eta_I \\ \frac{1}{2}\kappa(\eta - \eta_R)^2 & , \eta \geq \eta_I \\ \frac{1}{2}\kappa(\eta_I - \eta_R) \left( \frac{\eta^2}{\eta_I} - \eta_R \right) & , |\eta| < \eta_I \end{cases} \quad (2.4)$$

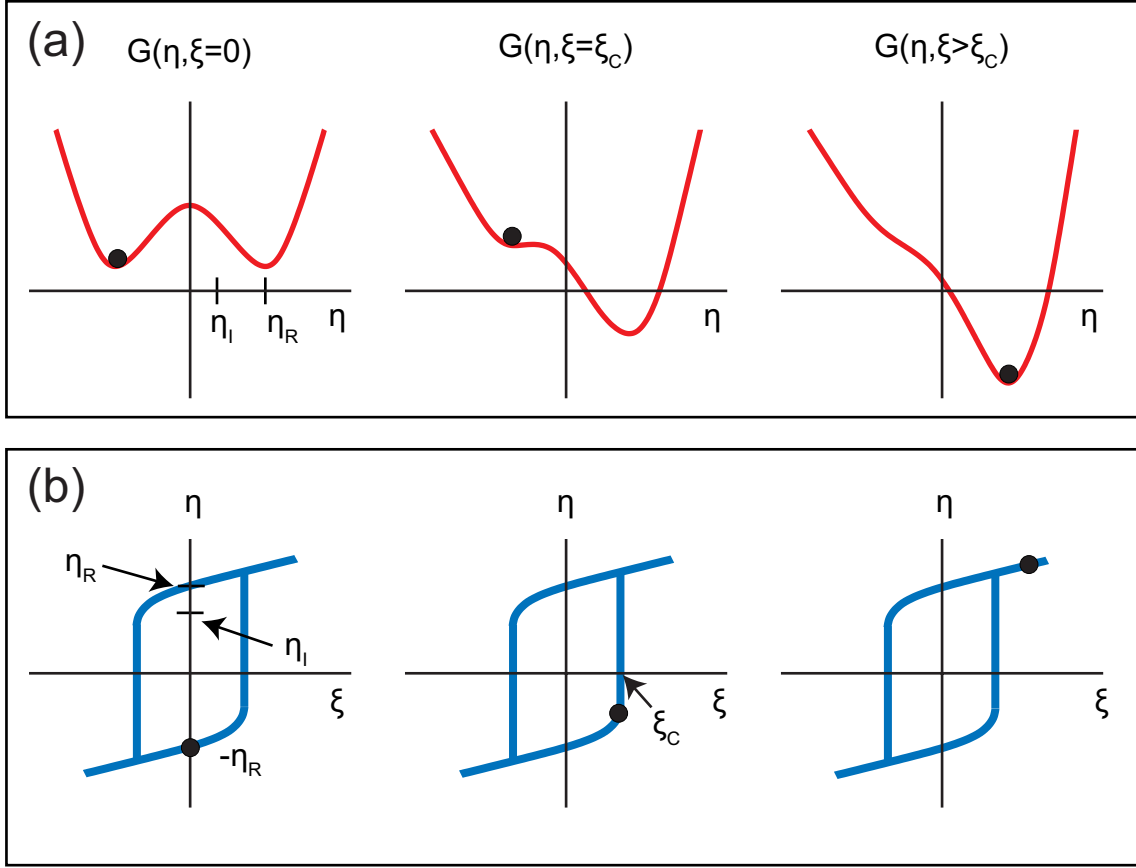


**Figure 2.1:** (a) Gibbs free energy and (b) resulting hysteresis of the order parameter  $\eta \in \{M, P, \varepsilon\}$  depending on the external field  $\xi \in \{H, E, \sigma\}$ .

The resulting Gibbs free energy  $G(\eta, \xi) = F(\eta) - \xi\eta$  is plotted in Fig. 2.1(a) for  $T < T_c$ . Here,  $\pm\eta_R$  denote the minima of  $G(\eta, \xi)$ ,  $\eta_I$  one inflection point of  $G(\eta, \xi)$  and  $\kappa$  the reciprocal slope of the curve depicted in Fig. 2.1(b) for  $|\xi| > \xi_C$ , with the coercive field

$$\xi_C = \kappa(\eta_R - \eta_I). \quad (2.5)$$

For  $T < T_c$ ,  $G(\eta, \xi)$  has the shape of a double well potential, unlike for  $T \geq T_c$  where it shows a single well potential [9]. The order parameter can now be imagined as a ball resting in the potential in Fig. 2.1(a) – it will stay in a local minimum unless the applied field is large enough to let it overcome the potential barrier to the global minimum of the potential. Hence hysteresis can only occur if the potential shows more than one well, thus only in ferroic materials.

For ferroelastic materials, the Helmholtz free energy can be derived in a similar

way [10], but as the microscopic physical ordering is quite different for ferroelastic materials if compared to ferromagnetic and ferroelectric materials, other parameters need to be involved, although  $G(\eta, \xi)$  qualitatively shows the same evolution as depicted in Fig. 2.1(a).

It is important for the understanding of the free energy concept, that the expression for the free energy shown above is just one possible description of the free energy in ferroic materials. Depending on which physical properties of the system one wants to describe, appropriate expressions for the free energy need to be derived. The free energy shown above was used because it unifies the macroscopic properties common to all ferroic materials. There exist several other approaches to free energy descriptions of ferroic materials that are no longer applicable for the entire class of materials, but concentrate on a more precise description of one ferroic material. For example, a commonly used theory to provide the relation between order parameter and field in ferroelectric materials is the Devonshire-Slater [11, 12] free energy. In ferromagnetic materials the mean field (Weiss) theory [13, 14, 15] is applied and for ferroelastic materials Landau and Lifshitz [16] established the Landau theory of elasticity.

We have shown three features common to all ferroic materials: The existence of a Curie temperature  $T_c$  as well as the existence of hysteresis and domains. This was done by the introduction of the general concept of free energy, which resulted in an order parameter that will always reside in such a state that the free energy is in a local minimum.

In the following sections, a microscopic description of the respective order parameter for all three investigated ferroic materials will be given.

### 2.1.1 Ferromagnets

In ferromagnets, the order parameter is the magnetization  $\mathbf{M}$ , which is defined as the magnetic moment  $\boldsymbol{\mu}$  per unit volume  $V$ .

$$\mathbf{M} = \frac{d\boldsymbol{\mu}}{dV} \quad (2.6)$$

The magnetic moment  $\boldsymbol{\mu}$  is microscopically caused by the classical orbital angular momentum  $\mathbf{L}$  of an electron in the atomic shell as well as its spin  $\mathbf{S}$ , resulting in

$$\boldsymbol{\mu} = \mu_B (\mathbf{L} + g_e \mathbf{S}) \quad (2.7)$$

with the Bohr magneton  $\mu_B$  and the Landé factor  $g_e$  of the electron. Quantum mechanical exchange interaction results in the parallel orientation of magnetic moments in ferromagnets, thus ferromagnetism is a quantum mechanical phenomenon.

In this work, magnetic fields will be described by the magnetic induction  $\mathbf{B} = \mu_0 \mathbf{H}$ .  $\mathbf{M}$  is related to  $\mathbf{B}$  by

$$\mathbf{B} = \mu_0 (\mathbf{H} + \mathbf{M}) . \quad (2.8)$$

In ferromagnetic materials, the relation between the magnetic field intensity  $\mathbf{H}$  and the magnetization  $\mathbf{M}$  is non-linear because of hysteresis as shown in Fig. 2.1(b). In Eq. (2.3) this relation was shown to be

$$\frac{\partial F}{\partial M} = B = \mu_0 H , \quad (2.9)$$

which is obviously only valid if the vector properties of  $\mathbf{M}$  and  $\mathbf{H}$  are disregarded, which can only be done if  $\mathbf{M}$  and  $\mathbf{H}$  are parallel.

The magnetic field dependence of the magnetization is referred to as the magnetic susceptibility  $\chi_M$ :

$$\chi_M = \frac{\partial M}{\partial H} . \quad (2.10)$$

If one now is interested in the equilibrium orientation of  $\mathbf{M}$  rather than just its magnitude and wants to consider the more general case of  $\mathbf{M}$  and  $\mathbf{H}$  not being necessarily parallel,  $\mathbf{M}$  as well as  $\mathbf{H}$  need to be parameterized in a suitable way by choosing an appropriate coordinate system and representation of  $\mathbf{M}$  and  $\mathbf{H}$  as a function of the chosen parameters. Due to the importance of this step, which will involve the introduction of the so called magnetic anisotropy, it will be carried out in a separate Section later in this Chapter.

Another important ferromagnetic property is the formation of ferromagnetic domains that enclose regions of identical magnetic moment orientation. If the macroscopic magnetization is saturated at high external magnetic fields ( $H > H_c = \xi_c$  in Fig. 2.1(b)) the ferromagnet is in a single domain state. Upon removal of the external magnetic field ( $H = 0$ ) some domains will form to minimize the free energy of the crystal and the macroscopic magnetization is reduced to the so called remanent magnetization  $M_R$ . If the external magnetic field is now reversed to  $H = -H_c$  the macroscopic magnetization diminishes to zero. However, as the crystal is still in a ferromagnetic state there is spontaneous magnetization and the vanishing macroscopic

magnetization is caused by the decay into domains that each still show a magnetization. The domains are separated by domain walls in which the magnetization orientation continuously adjusts from the orientation in one domain to the orientation in the adjacent domain. If the magnetization vector rotates in the domain wall plane (in a plane perpendicular to the domain wall) one speaks of a Neel (Bloch) domain wall. Furthermore, adjacent domains with antiparallel magnetization are called 180° domains and adjacent domains with orthogonal magnetization are called 90° domains.

### 2.1.2 Ferroelectrics

The ferroelectric order parameter  $\mathbf{P}$  is defined as the dipole moment  $\mathbf{p}$  per unit volume  $V$ :

$$\mathbf{P} = \frac{d\mathbf{p}}{dV} , \quad (2.11)$$

which is related non-linearly to the electric field  $\mathbf{E}$  as depicted in Fig. 2.1(b) by:

$$\frac{\partial F}{\partial P} = E . \quad (2.12)$$

This again will only hold true for  $\mathbf{P}$  parallel to  $\mathbf{E}$ . In general, the electric field dependence of the polarization is defined as the electric susceptibility  $\chi_E$ : [17]

$$\chi_E = \frac{\partial P}{\partial E} . \quad (2.13)$$

Microscopically, the ferroelectric polarization in the materials investigated in this thesis (lead zirconium titanate and barium titanate) is caused by the displacement  $\mathbf{x}_i$  of lattice ions bearing the electric charge  $q_i$ . The total dipole moment for  $N$  displaced ions thus is given by

$$\mathbf{p} = \sum_{i=1}^N \mathbf{x}_i q_i , \quad (2.14)$$

and one speaks of displacement polarization. In ferroelectric materials, polarization thus will always be accompanied by a deformation of the unit cells, which immediately leads to the conclusion that for a ferroelectric material the unit cell has a higher symmetry in its paraelectric state than in its ferroelectric state.

The induction of a polarization to the sample by an applied mechanical stress is called the piezoelectric effect, and the strain resulting from an electric field is

called the inverse piezoelectric effect. Note that while all ferroelectric materials show piezoelectricity, there are piezoelectric materials that are not ferroelectric such as quartz. Two basic equations correlate the electric polarization  $P$ , the electric field  $E$ , the elastic strain  $\varepsilon$  and the mechanical stress  $\sigma$  [18]:

$$\begin{aligned} P &= -d_{\text{Piezo}}\sigma + \chi E \\ \varepsilon &= -s^{\text{E}}\sigma + d_{\text{Piezo}}E, \end{aligned} \quad (2.15)$$

with the dielectric susceptibility  $\chi$ , the elastic compliance  $s^{\text{E}}$  and the piezoelectric strain coefficient  $d_{\text{Piezo}}$ . For applications in actuators, the most relevant case of Eq. (2.15) is the so called  $d_{33}$ -effect which describes the elongation (or contraction) of the ferroelectric material parallel to the applied electric field:

$$\varepsilon_3 = s_{33}^{\text{E}}\sigma_3 + d_{33}E_3, \quad (2.16)$$

with  $\varepsilon_3$  usually being in the range of 0.1%.

The concept of ferroelectric domains is similar to that for ferromagnetic domains. Just as in ferromagnetic materials, one distinguishes between  $90^\circ$  domain walls separating domains with perpendicular polarization and  $180^\circ$  domain walls separating domains with antiparallel polarization. A detailed introduction to ferroelectric domain walls can be found in the textbook by Jona and Shirane [19].

### 2.1.3 Ferroelastics

In ferroelastics, the order parameter is the strain  $\varepsilon$  which is linked to the stress  $\sigma$  by

$$\frac{\partial F}{\partial \varepsilon} = \sigma, \quad (2.17)$$

for parallel stress  $\sigma$  and strain  $\varepsilon$ .

It was already mentioned above that microscopically ferroelasticity differs from ferromagnetism and ferroelectricity in such a way that the free energy shown in Eq. (2.4) is only a coarse approximation. This is due to the phase mixture present in pure ferroelastics even below  $T_c$  [9]. While ferromagnetic and ferroelectric materials show domains enclosing regions with identical order parameter, in ferroelastic materials domains separate martensite and austenite regions. Hence a change of the order parameter in ferroelastic materials is linked to phase transitions rather than just domain

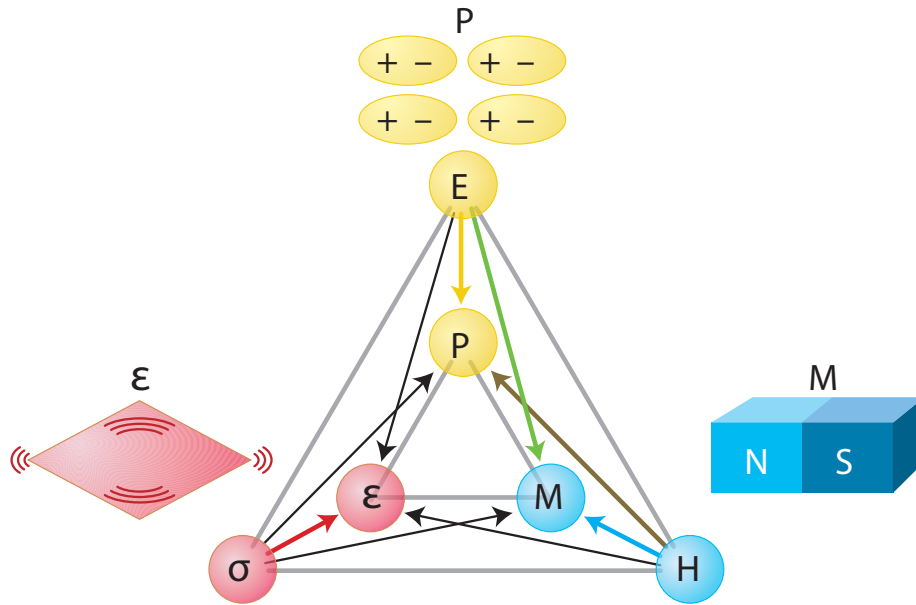


**Figure 2.2:** Phase control in multiferroics [5].

reformation.

Ferroelectric materials showing a displacement polarization are commonly referred to as being ferroelastic as well. This is due to the piezoelectric effect that results in a coupling of strain and polarization. Hence the strain in these ferroelectric materials is hysteretic as well as the polarization and ferroelectric domains show elastic behavior [20]. As this denomination of ferroelectric piezoelectric materials as ferroelastics is ambiguous, we will always refer to them just as ferroelectrics.

## 2.2 Multiferroics

Figure 2.2 [5] shows the relation between the different ferroic order parameters magnetization  $M$ , polarization  $P$  and strain  $\varepsilon$  that are responses to magnetic field  $H$ , electric field  $E$  and stress  $\sigma$ , respectively. In multiferroic materials, all three order parameters may be influenced by all three fields. Thus, in addition to the direct effects of the fields on their respective order parameter (depicted by the blue, yellow and red arrows in Fig. 2.2), the following six effects may be observed:

- $H \rightarrow P$  magnetoelectric effect

- $E \rightarrow M$  converse magnetoelectric effect
- $H \rightarrow \varepsilon$  magnetostrictive effect
- $\sigma \rightarrow M$  magnetoelastic effect
- $E \rightarrow \varepsilon$  inverse piezoelectric effect
- $\sigma \rightarrow P$  piezoelectric effect.

In intrinsic multiferroic materials there now exists a single phase where at least two ferroic order parameters show spontaneous ordering. Unfortunately, materials uniting ferroelectric and ferromagnetic properties have proven to be rare, though to the present date it is not understood in detail why there are so few magnetic ferroelectrics. However, as the ferromagnetic exchange is mediated by itinerant 3d-electrons that result in lattice conductivity and thus reduce the tendency for displacement polarization [21, 22], ferromagnetic and ferroelectric properties seem to be mutually exclusive. This constraint can be circumvented by the use of multiferroic heterostructures that show all the desirable multiferroic properties and can straightforwardly be fabricated by depositing a ferromagnetic film on a ferroelectric substrate. Multiferroic heterostructures of this kind will be the focus of this work and have been vigorously investigated for the last years [5, 23, 24, 25, 26], driven by technological aspirations.

For example, an approach to MRAM that utilizes the GMR effect [27] may be found by utilizing the converse magnetoelectric effect (marked by the green arrow in Fig. 2.2) which allows for the manipulation of magnetization by electric fields instead of magnetic fields. As all ferroelectric materials exhibit piezoelectricity, strain will always be involved in (converse) magnetoelectric effects in multiferroic heterostructures. This allows for the use of electric field induced magnetoelastic effects in heterostructures of ferromagnets and ferroelectrics to control the equilibrium orientation of magnetization.

## 2.3 The magnetic free energy density

As already mentioned above, we are interested in the vector properties of the magnetization of ferromagnetic materials, where the magnetization  $\mathbf{M}$  and magnetic field  $\mathbf{H}$  are no longer necessarily parallel. Furthermore, even for  $H = 0$ ,  $\mathbf{M}$  may have preferential directions, which is not covered by the free energy description used so far.

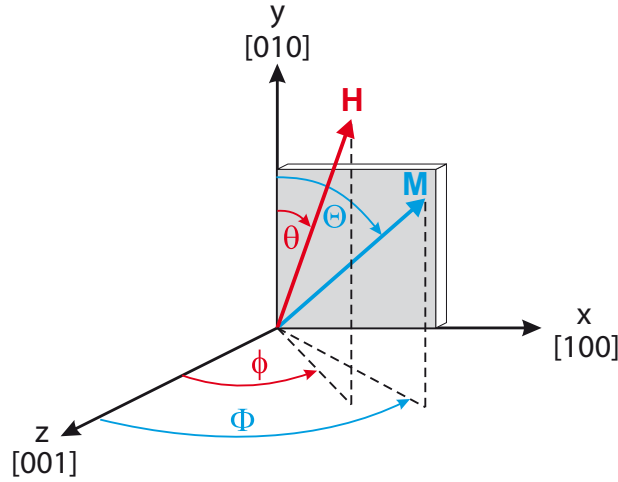


**Figure 2.3:** Coordinate system relative to sample [28].

Hence, we need to introduce a more detailed free energy model which takes into account microscopic effects on the magnetization orientation. Since free energy is always additive [7], we can include any desired effect just by finding an appropriate free energy description and adding it to the total free energy density of the system, which will be denoted by  $F_{\text{tot}}$ . Before doing so, we introduce the coordinate system shown in Fig. 2.3 [28] used to describe the orientation of both  $\mathbf{M}$  and  $\mathbf{H}$  relative to a sample. Capital greek letters describe the equilibrium orientation of magnetization and lower case letters the orientation of the external magnetic field. Thus we achieve the parametrization:

$$\mathbf{M} = (M, \Theta, \Phi) \quad (2.18)$$

$$\mathbf{H} = (H, \theta, \phi), \quad (2.19)$$

which will allow us to incorporate the vector properties of  $\mathbf{M}$  and  $\mathbf{H}$  in the mathematical description of the free energy density  $F_{\text{tot}} = F_{\text{tot}}(M, \Theta, \Phi, H, \theta, \phi)$ . Magnetization directions coinciding with a maximum of  $F_{\text{tot}}$  are called "magnetically hard" and those coinciding with a minimum of  $F_{\text{tot}}$  are called "magnetically easy", hence the total magnetic free energy density  $F_{\text{tot}}$  is a measure for the angular-dependent magnetic hardness. As shown in Eq. (2.3), in equilibrium  $\mathbf{M}$  points towards a minimum of  $F_{\text{tot}}$ , thus along a magnetically easy axis.

### 2.3.1 Contributions to the magnetic free energy density

We will now briefly introduce contributions to the total free magnetic energy density. We start with the only term dependent on the external magnetic field, generally introduced in Eq. (2.2) as  $F = -\xi\eta$ :

$$F_{\text{stat}} = -\mu_0 \mathbf{H} \cdot \mathbf{M} , \quad (2.20)$$

which is called Zeemann or magnetostatic term [29]. If expressed with the parametrization introduced above, it becomes

$$F_{\text{stat}} = -\mu_0 M H (\sin \Theta \sin \Phi \sin \theta \sin \phi + \cos \Theta \cos \theta + \sin \Theta \cos \Phi \sin \theta \cos \phi) . \quad (2.21)$$

If we only regard the above term, the magnetization will always be parallel to the external magnetic field as this minimizes  $F_{\text{stat}}$ . Thus to account for magnetic anisotropy further terms need to be introduced.

Due to the sample's geometry and the discontinuity of the magnetization at the sample surfaces, the magnetic free energy density generally is anisotropic. For a thin film, which is appropriate to describe all ferromagnetic samples used in this work, this anisotropy is given by [30]:

$$F_{\text{demag}} = \frac{\mu_0}{2} M^2 \sin^2 \Theta \cos^2 \Phi \quad (2.22)$$

and is referred to as shape anisotropy or demagnetization term for thin films. It describes an uniaxial anisotropy with a hard axis perpendicular to the sample plane.

Further contributions to the total free magnetic energy density arise from the crystalline structure of the sample, which for a cubic crystal may be approximated by

$$F_c = \frac{1}{4} K_{c1} (\sin^2 (2\Theta) + \sin^4 \Theta \sin^2 (2\Phi)) . \quad (2.23)$$

This expression disregards higher order cubic contributions discussed e.g. in the textbook by Chikazumi [29] and is therefore referred to as the first order cubic anisotropy term and  $K_{c1}$  is called first order cubic anisotropy constant<sup>1</sup>.

So far we have derived a total magnetic free energy density  $F_{\text{tot}} = F_{\text{stat}} + F_{\text{demag}} + F_c$  that may be used to describe the magnetization orientation in cubic single crystal

<sup>1</sup>As all free energy densities used in this work will only include first order anisotropy terms,  $K_{c1}$  is here simply called cubic anisotropy constant.

ferromagnetic thin films. We will now consider the additional effects on magnetization that are expected in multiferroic heterostructures.

### 2.3.2 Magnetoelastic effect

The magnetostrictive effect describes the elongation (or contraction) of a ferromagnet if it is exposed to a magnetic field and is responsible for the familiar hum of transformers. The magnetoelastic (converse magnetostrictive) effect thus describes the effect of stress – that results in strains in the ferromagnet – on magnetization. If only strains parallel to the orthogonal [100], [010] and [001] directions are regarded, shear strains can be neglected and we obtain pure uniaxial strains. Hence, the effect on the magnetic free energy density will be uniaxial as well and can generally be described by three orthogonal uniaxial contributions parallel to the directions of the strains:

$$F_{\text{strain}} = K_{u,[100]} \sin^2 \Theta \sin^2 \Phi + K_{u,[010]} \cos^2 \Theta + K_{u,[001]} \sin^2 \Theta \cos^2 \Phi . \quad (2.24)$$

Magnetoelastic theory may be used to calculate the anisotropy constants in the above equation for any given strain. This will be done in Chapter 6. We further note that the term in  $F_{\text{strain}}$  proportional to  $K_{u,[001]}$  and the demagnetization term  $F_{\text{demag}}$  possess a two-fold symmetry with identical angular dependence in thin films. It is hence common practice to unite both terms in the effective uniaxial anisotropy term  $F_{u,\text{eff},[001]} = K_{u,\text{eff},[001]} \sin^2 \Theta \cos^2 \Phi$ .

For ferromagnetic films deposited onto a substrate, there usually are epitaxial strains that arise from a small lattice mismatch between the film and the substrate. These uniaxial strains are present even if no external stress is applied to the sample and thus  $F_{\text{strain}}$  most often needs to be included in free energy descriptions of ferromagnetic thin films.

We finally would like to emphasize that, if the strain in the ferromagnetic film can be tuned continuously and reversibly, this will allow for a control of its magnetic anisotropy.

### 2.3.3 Magnetoelectric effect

We have so far described the effects of intrinsic magnetic anisotropy on magnetization as well as the effects of strains by appropriate terms in the total free energy density. To complete the effects proposed in Fig. 2.2, we now have to regard the

magnetolectric effect that describes the influence of magnetic fields on polarization and the converse magnetolectric effect that describes the influence of electric fields on magnetization [31]:

$$\begin{aligned}\mathbf{P} &\propto \hat{\alpha}\mathbf{H} \\ \mathbf{M} &\propto \hat{\alpha}\mathbf{E}.\end{aligned}\tag{2.25}$$

The magnitude of these effects is given by the second rank magnetolectric tensor  $\hat{\alpha}$ . The magnetolectric (ME) effect can be described by an additional term  $F_{\text{ME}}$  in the free energy [31]:

$$F_{\text{ME}} = \hat{\alpha}\mathbf{E} \cdot \mathbf{H}.\tag{2.26}$$

So far, no description of the physical origin of the magnetolectric effect was given in this thesis. This is due to the vast difference of this effect in single phase multiferroic materials and multiferroic heterostructures. In the former, microscopic interactions of the lattice atoms and the electric field, such as the displacement of ions, occur [32, 33]. In the latter, the magnetolectric effect is primarily caused by strain coupling at the interface of the ferromagnetic and the ferroelectric phase. Whereas the microscopic effect in intrinsic multiferroic materials is usually small, much larger magnetolectric coupling is observed in heterostructures.

## 2.4 Conclusion

The most important physical principles of ferroic and multiferroic materials as far as this thesis is concerned were introduced. We gave a brief description of the free energy concept in ferroic materials and the possible interactions in multiferroic structures. The multiferroics contributions to the magnetic free energy density were introduced and the complete multiferroic magnetic free energy density is given by:

$$F_{\text{tot}} = F_{\text{stat}} + F_{\text{u,eff,[001]}} + F_{\text{c}} + F_{\text{u,[100]}} + F_{\text{u,[010]}} + F_{\text{ME}}.\tag{2.27}$$

The magnetolectric effect led to the proposal of a new class of ferroic materials with the order parameter  $\mathbf{T}$  being the antisymmetric component of the magnetolectric tensor  $\hat{\alpha}$  [34].  $\mathbf{T}$  is called toroidal moment and describes local vortices of the magnetic moment. The materials showing a spontaneous toroidal moment are referred to as

ferrotoroidic materials. The renewed interest in the magnetoelectric effect that arose in the past years [32] led to the very recent finding of ferrotoroidic domains [35], which are an indispensable property of any ferroic material. Hence ferroic materials still pose a viable field of fundamental research, whereas multiferroic materials are investigated vigorously mainly due to their application potential.



# Chapter 3

## Materials

In the previous Chapter, we introduced the physical principles of ferroic and multi-ferroic materials. The most relevant material properties of the ferroic materials used in this thesis will be discussed here. Unless stated otherwise, the properties in this Chapter apply to bulk materials at a temperature of 300 K and a pressure of 1 kPa. In thin films, that will be used throughout this thesis, material constants may differ from bulk values. These deviations will be discussed in the respective Sections.

### 3.1 Ferromagnetic materials

As we strive to control the magnetization in multiferroic heterostructures, ferromagnetic materials will be present throughout all aspects of this work. Among the elemental ferromagnetic materials, only cobalt (Co), nickel (Ni) and iron (Fe) have Curie temperatures well above room temperature and are therefore relevant for applications. We investigate the classic ferromagnetic transition metals nickel and cobalt, as well as magnetite ( $\text{Fe}_3\text{O}_4$ ) as a prototype for a more complex magnetic material. This Section briefly outlines the material properties relevant to this thesis, a detailed introduction to ferromagnetic materials can be found in the textbooks by Chikazumi [29] and Morrish [30].

As magnetoelastic effects are a main focus of this thesis, the material parameters relevant to this effect will be presented for the investigated materials in addition to the basic magnetic properties given by the saturation magnetization  $M_s$ <sup>1</sup> and the  $g$ -factor. The elastic moduli  $c_{ij}$  describe the stress per strain ratio of the material  $c_{ij} = \sigma_i / \epsilon_j$  in

---

<sup>1</sup>In literature, the saturation magnetization  $M_s$  is often quoted in cgs units as emu / g. Conversion to SI units is calculated with the density  $\rho$  by  $1 \frac{\text{kA}}{\text{m}} = \frac{10}{4\pi} \frac{\text{emu}}{\text{g}} \frac{\text{g}}{\text{cm}^3}$ .

$M_s$ (kA/m)	$g$ -factor	$\lambda_{100} \times 10^6$	$\lambda_{111} \times 10^6$	$c_{11}$ ( $10^{11}$ N/m <sup>2</sup> )	$c_{12}$ ( $10^{11}$ N/m <sup>2</sup> )
411 [39]	2.185 [40]	-45.9 [41]	-24.3 [41]	2.5 [41]	1.6 [41]

**Table 3.1:** Magnetic, magnetostrictive and elastic moduli of bulk nickel at room temperature.

Voigt notation [36] in the linear regime (Hook’s law). For cubic materials, the magnetostrictive constants  $\lambda_{ijk}$  describe the maximal elongation or contraction  $\lambda = \frac{2}{3}\delta l/l$  of the ferromagnet in the direction  $[ijk]$  of the external magnetic field upon magnetization from the demagnetized state to saturation [29]. Symmetry considerations yield two independent magnetostrictive constants for cubic materials and four independent constants for hexagonal materials.

### 3.1.1 Nickel

Nickel has a curie temperature  $T_c = 627$  K [37] well above room temperature and is a very common element found in every-day items such as coins. Nickel crystallizes stable in the face centered cubic (fcc) structure, though hexagonal closed package (hcp) and body centered cubic (bcc) Ni has been prepared [38]. At room temperature and atmospheric pressure, the crystalline lattice constants are  $a^{\text{Ni}} = b^{\text{Ni}} = c^{\text{Ni}} = 0.35241(7)$  nm [38]. As we will investigate magnetoelastic effects in Ni in Chapter 6, the magnetostrictive constants and elastic moduli are of interest and thus presented in Tab. 3.1. As will be shown in Chapter 6, due to the negative magnetostrictive constant  $\lambda_{100}$  of Ni, a compressive strain along a cubic axis will result in a reduction of the magnetic free energy density in the direction of the strain.

### 3.1.2 Cobalt

Cobalt’s very high Curie temperature  $T_c = 1388$  K [37] and high saturation magnetization  $M_s = 1167$  kA/m [42] make it an ideal model ferromagnet. Cobalt is found in hcp and fcc crystalline structure depending on temperature. For low temperatures it crystallizes in hcp and above the transition temperature  $T_t = 690$  K [43] in fcc structure. Cobalt may be engineered to crystallize in body-centered-cubic (bcc) structure as well [44], but bcc-Co is not found naturally. Hence for our work, only the hcp phase is relevant. At room temperature, the lattice constants of hcp-Co are:

$M_s$ (kA/m)	$g$ -factor	$c_{11}$ ( $10^{11}$ N/m <sup>2</sup> )	$c_{12}$ ( $10^{11}$ N/m <sup>2</sup> )
1167 [42]	2.15 [46]	3.07 [47]	1.65 [47]

**Table 3.2:** Magnetic and elastic constants of hcp cobalt at room temperature.

$\lambda_A \times 10^6$	$\lambda_B \times 10^6$	$\lambda_C \times 10^6$	$\lambda_D \times 10^6$
-45	-95	110	-100

**Table 3.3:** Magnetostrictive constants of hcp cobalt at room temperature [48].

$a^{\text{Co}} = b^{\text{Co}} = 0.251$  nm and  $c^{\text{Co}} = 0.407$  nm [45]. Magnetic and elastic constants are displayed in Tabs. 3.2 and 3.3.

### 3.1.3 Magnetite

Magnetite ( $\text{Fe}_3\text{O}_4$ ) is the oldest known magnetic material and is predicted to be totally spin polarized at the Fermi level, while experimental evidence of  $|P| = 80\%$  in thin films exists [49]. Magnetite is a decent conductor with a conductivity of  $250 \Omega^{-1}\text{cm}^{-1}$  at room temperature [50]. At a temperature of  $T_V = 122$  K, magnetite exhibits a structural Verwey transition [51], discontinuously lowering its electrical conductivity by two orders of magnitude. Its high Curie temperature  $T_c = 858$  K [52] and well studied magnetic anisotropy properties [53, 54, 55, 56] make it an ideal choice for our investigations. In contrast to cobalt and nickel, magnetite is not an elemental ferromagnet but each magnetite unit cell consists of 24 iron and 32 oxygen atoms. At room temperature,  $\text{Fe}_3\text{O}_4$  crystallizes in the inverse cubic spinell structure [57] with lattice constants  $a^{\text{Fe}_3\text{O}_4} = b^{\text{Fe}_3\text{O}_4} = c^{\text{Fe}_3\text{O}_4} = 0.8396$  nm [53]. Microscopically, magnetite shows ferrimagnetic properties, that result in a macroscopic behavior which is equivalent to that of a ferromagnet and thus we will refer to magnetite as being ferromagnetic. Magnetite has been reported to show ferroelectric properties at temperatures below approximately 10 K [58, 59, 60, 61]. Thus, in addition to its ferromagnetic properties, magnetite is an intrinsic multiferroic material. However, no reports of the exact ferroelectric transition temperature or magnitude of the electric polarization exist. Due to the low transition temperature and difficult to prove ferroelectric properties,  $\text{Fe}_3\text{O}_4$  is not suitable for everyday use as an intrinsic multiferroic material. As we

$M_s$ (kA/m)	$g$ -factor	$\lambda_{100} \times 10^6$	$\lambda_{111} \times 10^6$	$c_{11}$ ( $10^{11}$ N/m <sup>2</sup> )	$c_{12}$ ( $10^{11}$ N/m <sup>2</sup> )
381 [62]	2.12 [63]	-20 [64]	80 [64]	2.73 [65]	1.06 [65]

**Table 3.4:** Magnetic, magnetostrictive and elastic constants of Fe<sub>3</sub>O<sub>4</sub> at room temperature.

will investigate magnetite only at temperatures well above the ferroelectric transition temperature, only its ferromagnetic properties are relevant to this thesis.

## 3.2 Barium titanate

Barium titanate (BaTiO<sub>3</sub>) is a very widespread room temperature ferroelectric material often used as a dielectric in capacitors due to its low cost and high dielectric constant  $\epsilon = 4100$  [66]. Its ferroelectric properties have been investigated already several decades ago [67, 68, 69, 70] and it is today commonly used as the ferroelectric phase in multiferroic heterostructures.

Barium titanate exhibits three crystalline phase transitions at distinct temperatures, one from the paraelectric to the ferroelectric state at the Curie temperature  $T_c = 393$  K [19] and two in between ferroelectric phases at lower temperatures  $T_1$  and  $T_2$ . Upon cooling down the crystal from a temperature above  $T_c$ , the crystalline structure changes from the paraelectric cubic phase to the ferroelectric tetragonal, orthorhombic and finally rhombohedral phase. The phase transitions are caused by changes in the spontaneous polarization which result in a deformation of the lattice as explained in the previous Chapter. In Fig. 3.1, the lattice parameters are displayed as a function of temperature in the approximation of a pseudocubic unit cell with the lattice constants  $a, b$  and  $c$  orthogonal to each other in real space [71]. This simplification results in the rhombohedral state being approximated by a cubic unit cell, although there still is a spontaneous polarization along any of the crystalline  $\langle 111 \rangle$  directions.

As can be seen from Fig. 3.1, at room temperature the unit cell is tetragonal. The unit cell crystallizes in the perovskite structure and is shown in Fig. 3.2 for the cubic and for the tetragonal phase. Microscopically, the spontaneous polarization is caused by a displacement of the Ti<sup>4+</sup> ion from its central position which it takes above  $T_c$  [67]. This is schematically shown in Fig. 3.2 for the tetragonal phase. One can see that upon the phase transition to the ferroelectric state, the Ti<sup>4+</sup> ion has six

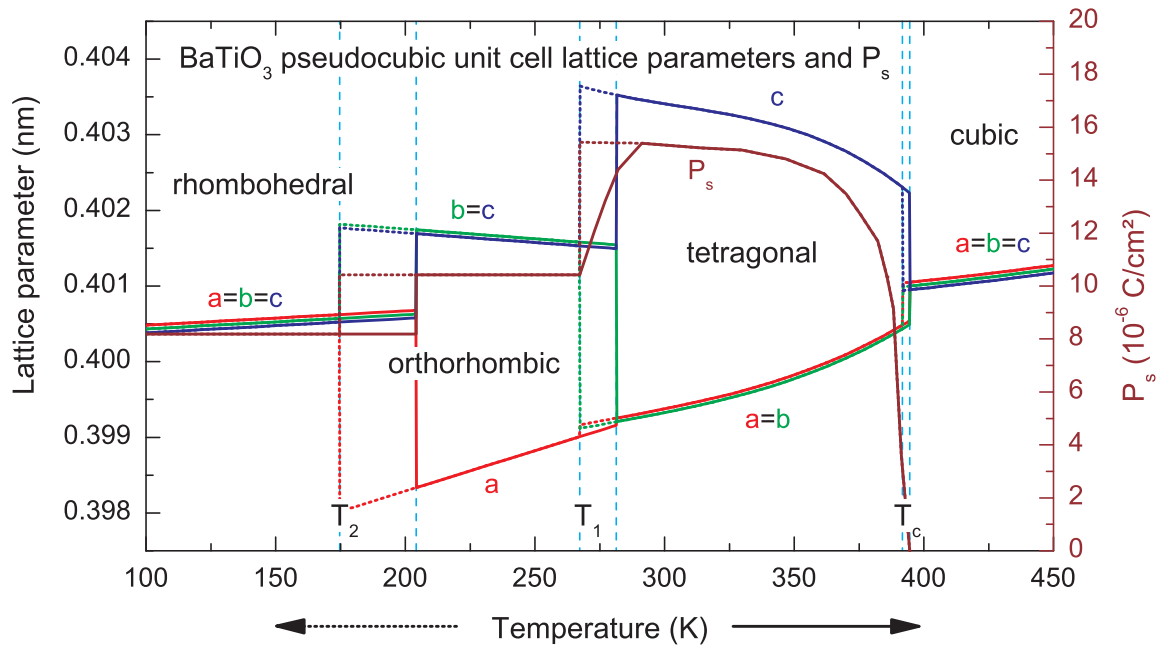


**Figure 3.1:** Barium titanate lattice parameters [71] and spontaneous polarization along [100] [67] as a function of temperature (solid lines correspond to increasing temperature and dotted lines to decreasing temperature).

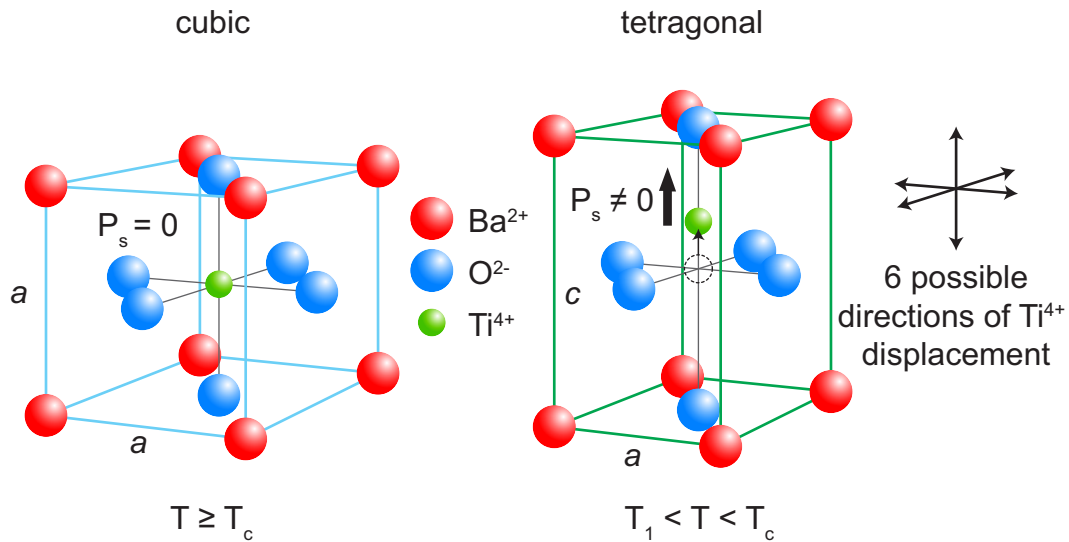


**Figure 3.2:** The barium titanate unit cell and spontaneous polarization caused by a displacement of the Ti<sup>4+</sup> ion.

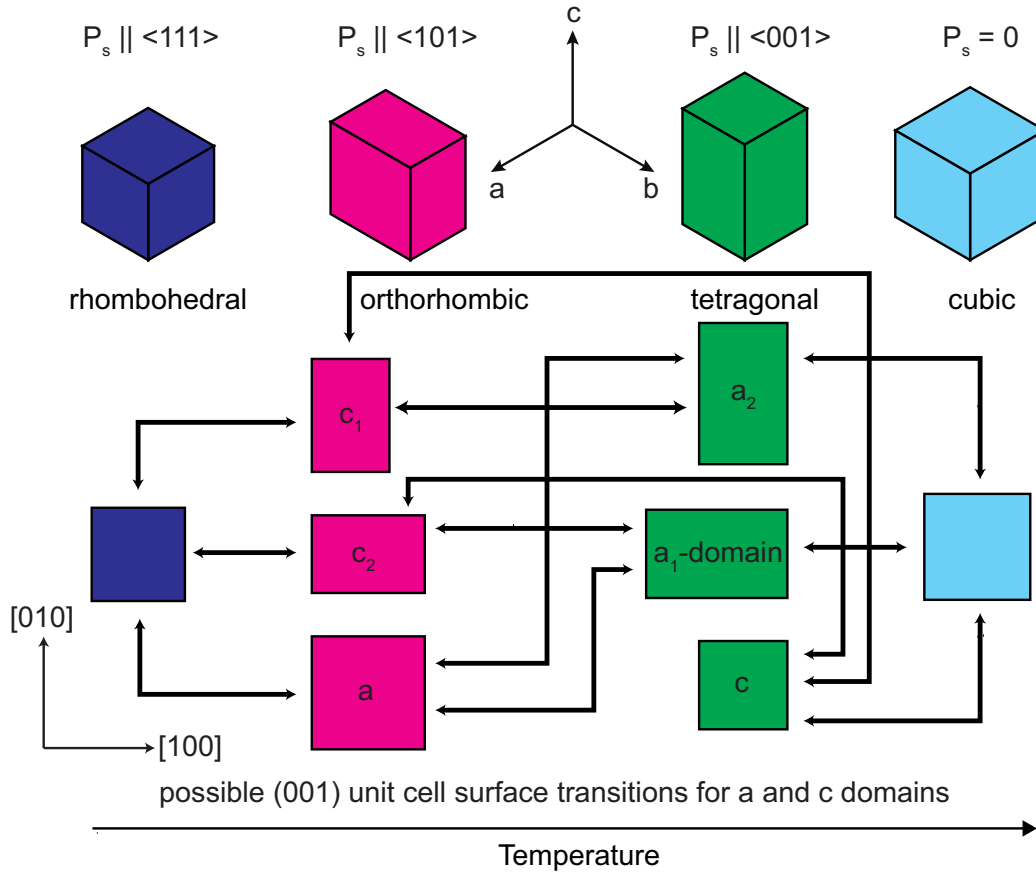


**Figure 3.3:** Surfaces of the  $\text{BaTiO}_3$  unit cells in the four different crystalline phases and possible transitions.

possible displacement directions that may be reduced to a basis of three orthogonal possible displacement vectors. In a crystal consisting of several unit cells, we expect all orientations to be equally favorable if no external electric field is applied. This gives rise to domain formation in the crystal. In the tetragonal phase, we distinguish between  $a$ -domains with  $a \parallel [001]$  and  $c$ -domains with  $c \parallel [001]$ . The  $a$ -domains are further divided into  $a_1$ -domains with  $c \parallel [100]$  and  $a_2$  domains with  $c \parallel [010]$ . Domains in the orthorhombic phase are depicted according to the same scheme. Fig. 3.3 shows the resulting (001) unit cell surfaces for all phases as well as the possible transitions with temperature that can be derived from the lattice parameter evolution shown in Fig. 3.1.

At room temperature,  $\text{BaTiO}_3$  is ferroelectric and thus shows a piezoelectric effect as described in Eq. 2.15. The piezoelectric coefficients and elastic moduli are given in

$d_{31}$ ( $10^{-12}$ C/N)	$d_{33}$ ( $10^{-12}$ C/N)	$c_{11}$ ( $10^{11}$ N/m <sup>2</sup> )	$c_{12}$ ( $10^{11}$ N/m <sup>2</sup> )
-33.4 [72]	90 [72]	2.75 [73]	1.79 [73]

**Table 3.5:** Piezoelectric and elastic constants of BaTiO<sub>3</sub> at room temperature.

$d_{31}$ ( $10^{-12}$ C/N)	$d_{33}$ ( $10^{-12}$ C/N)
-290	640

**Table 3.6:** Piezoelectric coefficients of PZT ceramics at room temperature [76].

Tab. 3.5.

### 3.3 Lead zirconate titanate

Lead [Plumbum] Zirconate Titanate (PZT) is a room temperature ferroelectric nowadays widely used in piezoelectric devices, which utilize the  $d_{33}$ -effect introduced in the previous Chapter. Additionally, PZT has found applications in ferroelectric random access memories [74]. Its chemical structure is  $\text{Pb}[\text{Zr}_{1-x}\text{Ti}_x]\text{O}_3$  ( $0 < x < 1$ ), most commonly  $x \approx 0.5$ . For  $x \geq 0.5$  the ferroelectric phase is tetragonal and for smaller portions of titanium the ferroelectric phase is rhombohedral with an antiferroelectric phase below  $x = 0.1$  [75]. The Curie temperature is dependent on  $x$  as well and increases with increasing  $x$  from  $T_c(x = 0) = 250$  K to  $T_c(x = 1) = 500$  K [75]. For  $x \geq 0.5$ , PZT shows properties similar to BaTiO<sub>3</sub> with a perovskite crystalline structure which is tetragonally distorted below the Curie temperature  $T_c = 350$  K. Piezoelectric actuators built from stacks of PZT may be used to apply stress to a sample attached to the actuator as shown in Chapters 5 and 6. We use Piezomechanik PSt 150/2x3/5 actuators [76] built from stacks of PZT ceramics. The piezoelectric coefficients of the PZT used in these actuators are given in Tab. 3.6.

### 3.4 Magnesium oxide

Magnesium oxide (MgO) crystallizes in the cubic fcc structure with an unstrained lattice constant  $a^{\text{MgO}} = b^{\text{MgO}} = c^{\text{MgO}} = 0.4212$  nm [77]. It is a non-ferroic insulator

---

$c_{11}$ ( $10^{11}$ N/m <sup>2</sup> )	$c_{12}$ ( $10^{11}$ N/m <sup>2</sup> )
2.97	0.965

---

**Table 3.7:** Elastic moduli of MgO at room temperature [77].

and commonly used as a substrate for functional thin films. Due to its simple crystal structure and very high achievable purity it is an ideal candidate to demonstrate the effect of stress on lattice structure as will be done in Chapter 5. The elastic moduli of MgO are displayed in Tab. 3.7.

# Chapter 4

## Experimental techniques

In this Chapter, the experimental techniques used in this thesis are described. Magnetization is the most relevant physical property for ferromagnetic materials. SQUID (superconductive quantum interference device) magnetometry determines the static response of a magnetic system. Thus SQUID magnetometry is suitable to detect static properties such as the saturation magnetization. FMR (ferromagnetic resonance) is sensitive to the dynamic magnetic response and is one of the most precise measurement techniques to determine magnetic anisotropy.

In ferroelectric materials, we observe two effects relevant to this work: Polarization and the corresponding strains. A reversal of polarization is accompanied by displacement currents which may directly be recorded as a function of electric field using standard laboratory equipment. HRXRD (high resolution X-ray diffraction) can be used to precisely determine lattice constants and thus strains in crystals.

### 4.1 SQUID magnetometry

SQUID magnetometry can be used to determine the magnetization  $M$  of a sample with high precision as a function of parameters such as external magnetic field  $H$  or temperature  $T$ . The SQUID magnetometer MPMS XL-7 manufactured by Quantum Design provides a magnetic field of  $-7\text{ T} \leq \mu_0 H \leq +7\text{ T}$  and a temperature range of  $1.8\text{ K} \leq T \leq 400\text{ K}$  in the sample space. As can be seen in Fig. 4.1, a second order gradiometer [78] suppresses the pickup of all static magnetic fields and all signals homogeneous over the gradiometer length – including the sample holder. Apart from the shielding currents in the superconducting loop, only currents induced by the movement of the magnetic sample inside the gradiometer pickup coils are flux-coupled

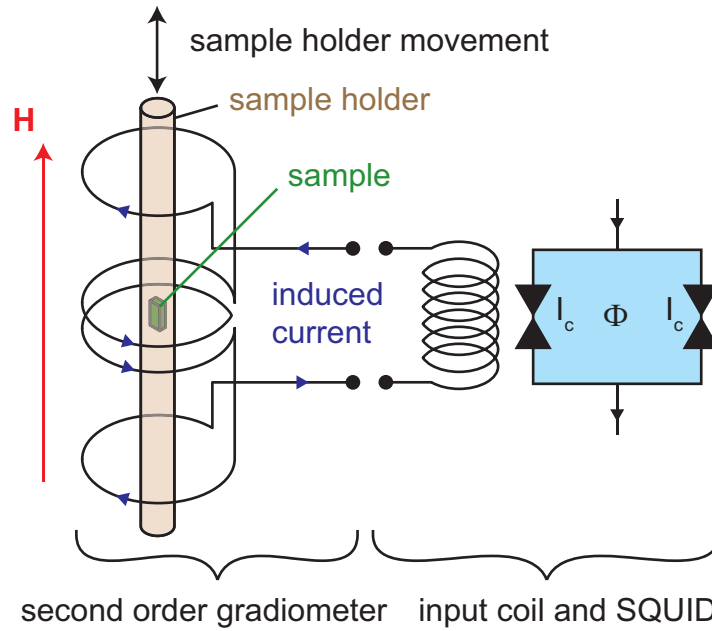


**Figure 4.1:** Schematic illustration of a SQUID magnetometer.

into the SQUID loop. Thereby, a resolution of  $10^{-8}$  emu =  $10^{-11}$  Am<sup>2</sup> is achieved. It is important to note that only the component of  $\mathbf{M}$  parallel to the gradiometer axis and hence parallel to the external magnetic field is detected.

## 4.2 Ferromagnetic resonance spectroscopy

The standard measurement technique to determine the magnetic anisotropy and thereby the equilibrium orientation of magnetization in ferromagnetic thin films is ferromagnetic resonance spectroscopy (FMR). As the theory of FMR is covered in detail in several textbooks [79, 80, 29], only a brief introduction to the relevant aspects to this thesis will be given here.

### 4.2.1 Theoretical background

The resonant absorption of an electromagnetic field in a system of magnetic moments coupled by exchange interaction is referred to as ferromagnetic resonance. Experimentally, the electromagnetic field is realized by the superposition of a static magnetic field  $\mu_0 \mathbf{H}_0$  and an alternating microwave field  $\mu_0 \mathbf{H}_1(\omega t) = \mu_0 \mathbf{H}_1 \sin(\omega t)$ . The microwave

field is of much smaller magnitude and perpendicular to the static field.

The resonance condition is met if the frequency of the external electromagnetic microwave  $\mu_0 \mathbf{H}_1 \sin(\omega t)$  field matches the precession frequency of the magnetization  $\mathbf{M}$  about  $\mathbf{H}_0$ . The most general form of the resonance condition in paramagnets is given by

$$\omega = \gamma \mu_0 H_0, \quad (4.1)$$

with  $\omega$  being the resonance frequency and  $\gamma$  the gyromagnetic ratio

$$\gamma = \frac{g\mu_B}{\hbar}. \quad (4.2)$$

This resonant absorption of electromagnetic waves in a system of uncoupled magnetic moments is called electron spin resonance (ESR).

In ferromagnetic materials, the magnetic moments have a long range order mediated by exchange interaction. Due to the exchange interaction of the magnetic moments, the effective magnetic field  $\mu_0 \mathbf{H}_{\text{eff}}$  – about which  $\mathbf{M}$  precesses – is a non linear function of the external magnetic field  $\mu_0 \mathbf{H}_0$  [81]. Hence, in ferromagnetic materials, the resonance condition is

$$\omega = \gamma \mu_0 H_{\text{eff}}. \quad (4.3)$$

The equation of motion of the magnetization vector around the effective magnetic field is classically given by

$$\partial_t \mathbf{M} = -\mu_0 \gamma \mathbf{M} \times \mathbf{H}_{\text{eff}}. \quad (4.4)$$

The effective magnetic field  $\mu_0 \mathbf{H}_{\text{eff}}$  though is unknown and hence the simple equation of motion (4.4) for the precession of the magnetization around the effective magnetic field is not easily solved in exchange-coupled materials. Furthermore, we have to take into consideration the magnetic anisotropy that causes a finite angle between  $\mathbf{M}$  and  $\mathbf{H}_0$ . Deriving the equation of motion by introducing the magnetic free energy density  $F_{\text{tot}}$  includes the effects of magnetic anisotropy [28] and yields the ferromagnetic resonance equation of motion

$$\left(\frac{\omega}{\gamma}\right)^2 = \frac{1}{M_s^2 \sin^2 \Theta} \left( (\partial_\Phi^2 F_{\text{tot}}) (\partial_\Theta^2 F_{\text{tot}}) - (\partial_\Phi \partial_\Theta F_{\text{tot}})^2 \right). \quad (4.5)$$

This expression usually includes a damping parameter  $\alpha$ , that is neglected in this

thesis. This is a simplification done here as the damping does not influence the FMR resonance position but only the FMR line shape, that is not systematically investigated here. Eq. (4.5) has to be fulfilled simultaneously with the necessary condition for the minimization of the free energy density  $F_{\text{tot}}$  with respect to the orientation of the magnetization given by  $\Theta$  and  $\Phi$  (cf. Fig. 2.3):

$$\partial_{\Phi} F_{\text{tot}} \Big|_{\Phi=\Phi_0} = \partial_{\Theta} F_{\text{tot}} \Big|_{\Theta=\Theta_0} = 0 . \quad (4.6)$$

Equations (4.5) and (4.6) provide the link between the measured resonance fields and the magnetic free energy density  $F_{\text{tot}}$ . An analytic evaluation of these equations is only possible for certain orientations of the external magnetic field  $\mu_0 \mathbf{H}_0$  with respect to the sample. Using the coordinate system shown in Fig. 2.3, this was done in [56] for the total magnetic free energy density

$$\begin{aligned} F_{\text{tot}} &= F_{\text{stat}} + F_{\text{u,eff,[001]}} + F_{\text{u,[010]}} + F_{\text{c}} \quad (4.7) \\ &= -\mu_0 M H_0 (\sin \Theta \sin \Phi \sin \theta \sin \phi + \cos \Theta \cos \theta + \sin \Theta \cos \Phi \sin \theta \cos \phi) + \\ &\quad K_{\text{u,eff,[001]}} \sin^2 \Theta \cos^2 \Phi + \\ &\quad K_{\text{u,[010]}} \cos^2 \Theta + \\ &\quad \frac{1}{4} K_{\text{c1}} (\sin^2 (2\Theta) + \sin^4 \Theta \sin^2 (2\Phi)) , \end{aligned}$$

which will later be shown to be sufficient to describe the magnetic anisotropy of our samples. The contributions to  $F_{\text{tot}}$  in Eq. (4.7) were introduced in Chapter 2.

Solving Eq. (4.5) and (4.6) with  $F_{\text{tot}}$  from (4.7) for  $\mathbf{H}_0$  along the cartesian axes [100], [010] and [001] yields the following analytic expressions:

- $\mathbf{H}_0 \parallel [100]$  ( $\phi = 90^\circ$ ,  $\theta = 90^\circ$ ):

$$\begin{aligned} \left( \frac{\omega}{\gamma} \right)^2 &= \left( \mu_0 H_{\text{res,[100]}} + 2 \frac{K_{\text{u,[010]}}}{M} + 2 \frac{K_{\text{c1}}}{M} \right) \times \quad (4.8) \\ &\quad \left( \mu_0 H_{\text{res,[100]}} + 2 \frac{K_{\text{u,eff,[001]}}}{M} + 2 \frac{K_{\text{c1}}}{M} \right) \end{aligned}$$

- $\mathbf{H}_0 \parallel [010]$  ( $\phi = 90^\circ$ ,  $\theta = 0^\circ$ ):

$$\left(\frac{\omega}{\gamma}\right)^2 = \left( \mu_0 H_{\text{res},[010]} - 2\frac{K_{\text{u},[010]}}{M} + 2\frac{K_{\text{u,eff},[001]}}{M} + 2\frac{K_{\text{c1}}}{M} \right) \times \quad (4.9)$$

$$\left( \mu_0 H_{\text{res},[010]} - 2\frac{K_{\text{u},[010]}}{M} + 2\frac{K_{\text{c1}}}{M} \right)$$

- $\mathbf{H}_0 \parallel [001]$  ( $\phi = 0^\circ$ ):

$$\left(\frac{\omega}{\gamma}\right)^2 = \left( \mu_0 H_{\text{res},[001]} + 2\frac{K_{\text{u},[010]}}{M} - 2\frac{K_{\text{u,eff},[001]}}{M} + 2\frac{K_{\text{c1}}}{M} \right) \times \quad (4.10)$$

$$\left( \mu_0 H_{\text{res},[001]} - 2\frac{K_{\text{u,eff},[001]}}{M} + 2\frac{K_{\text{c1}}}{M} \right)$$

## 4.2.2 Experimental setup for FMR measurements

All FMR measurements described in this work were carried out using a Bruker ESP 300 spin resonance spectrometer featuring a static magnetic field  $5 \text{ mT} \leq \mu_0 H_0 \leq 1 \text{ T}$  and operated at a microwave frequency of approximately 9.3 GHz. A schematic view of the setup – which was kindly granted access to by M. S. Brandt, C. Bihler and H. Hübl at the Walter Schottky Institute – is shown in Fig. 4.2(a). Experimentally, the sample is rotated in the static external magnetic field, though theoretically one describes the rotation of the magnetic field in a coordinate system attached to the sample.

A FMR spectrum from one of the actual samples (CP1) used in this work is shown in Fig. 4.3 and introduces the notation used.

Characteristic features of the spectrum are the extrema  $\mu_0 H_{\text{max}}$  and  $\mu_0 H_{\text{min}}$ , the peak to peak linewidth  $\mu_0 \Delta H_{\text{pp}} = |\mu_0 H_{\text{max}} - \mu_0 H_{\text{min}}|$ , and the resonance position taken throughout to be at  $\mu_0 H_{\text{res}} = \frac{1}{2}(\mu_0 H_{\text{max}} + \mu_0 H_{\text{min}})$ . The shape of the resonance line resembles the derivative of a Lorentzian. This is caused by the magnetic field modulation detection that will be explained in the following.

## 4.2.3 Modulation and lock-in detection

To achieve optimal sensitivity, signal modulation and lock-in amplifier detection is used to extract the resonance signal from the background noise. The lock-in incorporates a phase sensitive detector (PSD) which multiplies the sinusoidally modulated

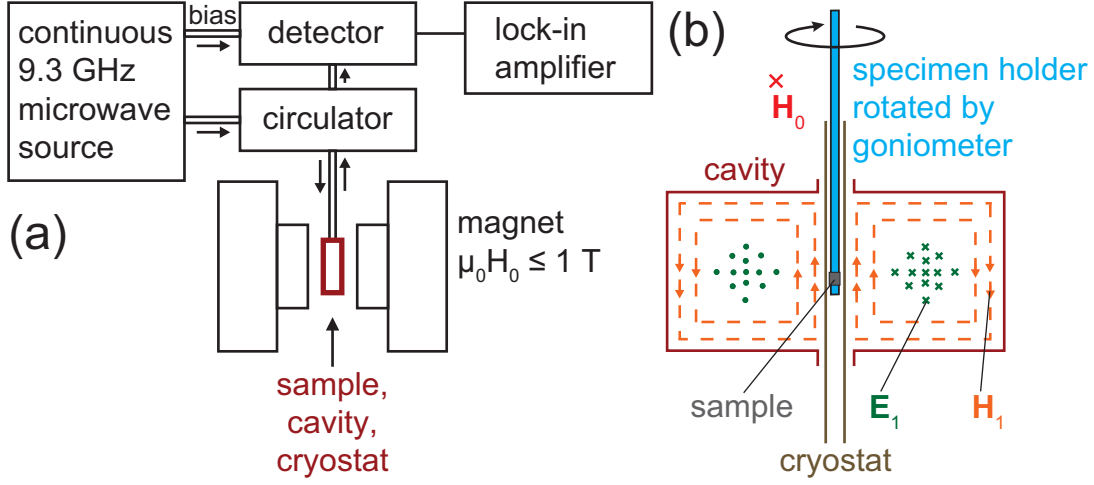


**Figure 4.2:** (a) Schematic view of the FMR setup [82] and (b) of the TE<sub>102</sub> cavity [28], showing the microwave magnetic ( $\mathbf{H}_1$ ) and electric ( $\mathbf{E}_1$ ) fields.  $\mathbf{H}_1$  is orthogonal to the static magnetic field  $\mathbf{H}_0$ .

input signal  $V_{\text{sig}}(t) \sin(\omega_{\text{mod}}t + \phi_{\text{sig}})$  with a pure sine function  $V_{\text{LI}} \sin(\omega_{\text{ref}}t + \phi_{\text{ref}})$ , which yields:

$$\begin{aligned}
 V_{\text{PSD}}(t) &= V_{\text{sig}}(t)V_{\text{LI}} \sin(\omega_{\text{mod}}t + \phi_{\text{sig}}) \sin(\omega_{\text{ref}}t + \phi_{\text{ref}}) \\
 &= \frac{1}{2}V_{\text{sig}}(t)V_{\text{LI}} \cos([\omega_{\text{mod}} - \omega_{\text{ref}}]t + \phi_{\text{sig}} - \phi_{\text{ref}}) - \\
 &\quad \frac{1}{2}V_{\text{sig}}(t)V_{\text{LI}} \cos([\omega_{\text{mod}} + \omega_{\text{ref}}]t + \phi_{\text{sig}} + \phi_{\text{ref}}).
 \end{aligned} \tag{4.11}$$

Thus, the PSD outputs two AC signals, one at the sum frequency ( $\omega_{\text{mod}} + \omega_{\text{ref}}$ ) and one at the difference frequency ( $\omega_{\text{mod}} - \omega_{\text{ref}}$ ).  $V_{\text{PSD}}(t)$  is now passed through a low pass filter which removes the AC signal, leaving only the DC signal component present at  $\omega_{\text{mod}} = \omega_{\text{ref}}$ :

$$V_{\text{out}}(t) = \frac{1}{2}V_{\text{sig}}(t)V_{\text{LI}} \cos(\phi_{\text{sig}} - \phi_{\text{ref}}). \tag{4.12}$$

Hence, if the lock-in's reference frequency  $\omega_{\text{ref}}$  is set to the modulation frequency  $\omega_{\text{mod}}$ , all input signals at other frequencies are suppressed in the lock-in output  $V_{\text{out}}$ . Furthermore, the phase difference  $\phi_{\text{sig}} - \phi_{\text{ref}}$  must not be time dependent. As a last step, the output signal defined in (4.12) is averaged over a certain time, called the

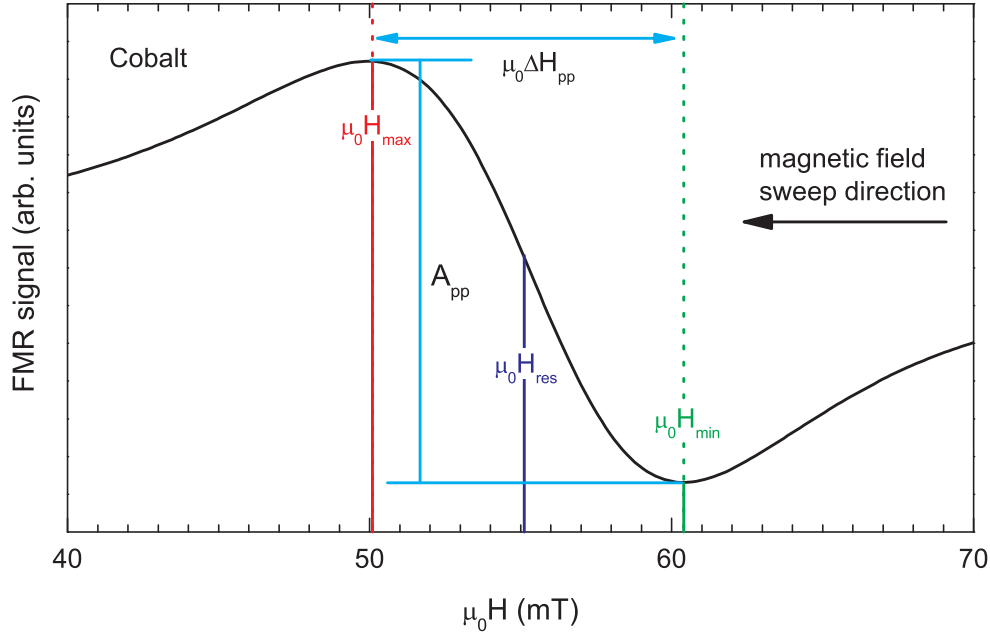


**Figure 4.3:** Example spectrum of a Cobalt thin film with the magnetic field in the film plane.

lock-in time constant  $t_{LI}$ :

$$V_{\text{out,avg}}(t) = \frac{1}{t_{LI}} \int_{t-t_{LI}}^t V_{\text{out}}(\tau) d\tau , \quad (4.13)$$

which for all measurements discussed in this thesis is set to  $t_{LI} = 0.1$  s. This value is chosen because a magnetic field sweep during one single FMR measurement takes 200 s and comprises 1024 data points, which results in a step time of approximately 0.2 s. Therefore, with a larger time constant, resolution would be lost and with a smaller time constant, the signal to noise ratio would be decreased unnecessarily.

The resonant microwave absorption in the cavity is detected by a detector diode, that outputs a voltage  $V_{\text{sig}}$  proportional to the microwave absorption. Modulation is achieved by periodically modulating the external field  $\mu_0 \mathbf{H}_0$  by a parallel AC magnetic field  $\mu_0 \mathbf{H}_{\text{mod}}$  at a frequency  $\omega_{\text{mod}}$ . This results in a sinusoidal FMR signal that is amplitude-modulated with the frequency  $\omega_{\text{mod}}$ . The amplitude of the signal is given by

$$V_{\text{sig,mod}}(\mu_0 H_0) = V_{\text{sig}} \left( \mu_0 H_0 + \frac{1}{2} \mu_0 H_{\text{mod}} \right) - V_{\text{sig}} \left( \mu_0 H_0 - \frac{1}{2} \mu_0 H_{\text{mod}} \right) , \quad (4.14)$$

which, for modulation amplitudes  $H_{\text{mod}} \ll \Delta H_{\text{pp}}$  is equivalent to the first derivative of the pure resonance signal, which explains the lineshape seen in Fig. 4.3. If the modulation amplitude is chosen to be close to or even larger than the linewidth, the signal no longer represents the first derivative of a Lorentzian but becomes distorted, one technically speaks of an overmodulated signal. The influence of modulation amplitude and frequency on the lineshape and noise is covered in detail in the textbook by Poole [80].

## 4.3 High resolution X-ray diffraction

HRXRD is a standard measurement technique to determine lattice constants and crystal structure. Furthermore, conclusions on the crystalline quality and phase purity can be made. In this thesis, HRXRD is utilized for precise lattice parameter determination of crystals with orthorhombic structure, therefore the discussion will be limited to this application. An in-depth description of the HRXRD technique can be found in the textbook by Cullity and Stock [83].

### 4.3.1 Experimental setup

The setup used for all diffraction measurements in this thesis is a Bruker AXS D8-Discover four-circle high resolution X-ray diffractometer. A  $\text{Cu}_{\text{K}\alpha}$  X-ray source and a monochromator provide parallel X-ray beams with a wavelength  $\lambda = 0.154056 \text{ nm}$ . Fig. 4.4(a) shows a schematic view of the setup displaying the eponymous four circles  $\omega$ ,  $\phi$ ,  $\chi$  and  $2\theta$ .

### 4.3.2 Scattering theory

X-ray beams are generally diffracted arbitrarily by the electron sheath of lattice atoms. If parallel and monochromatic X-ray beams with the wavelength  $\lambda$  and wave vector  $\mathbf{k}_i$  are diffracted on lattice atoms arranged in lattice planes with distance  $d$ , the diffracted beams with wave vector  $\mathbf{k}_f$  interfere with each other constructively or destructively. According to Bragg's law, constructive interference occurs if the retardation  $\Delta s$  of the diffracted beams is an integer multiple of  $\lambda$ :

$$\Delta s = 2d_{\text{hkl}} \sin \theta = n\lambda \quad n \in \mathbb{N}, \quad (4.15)$$

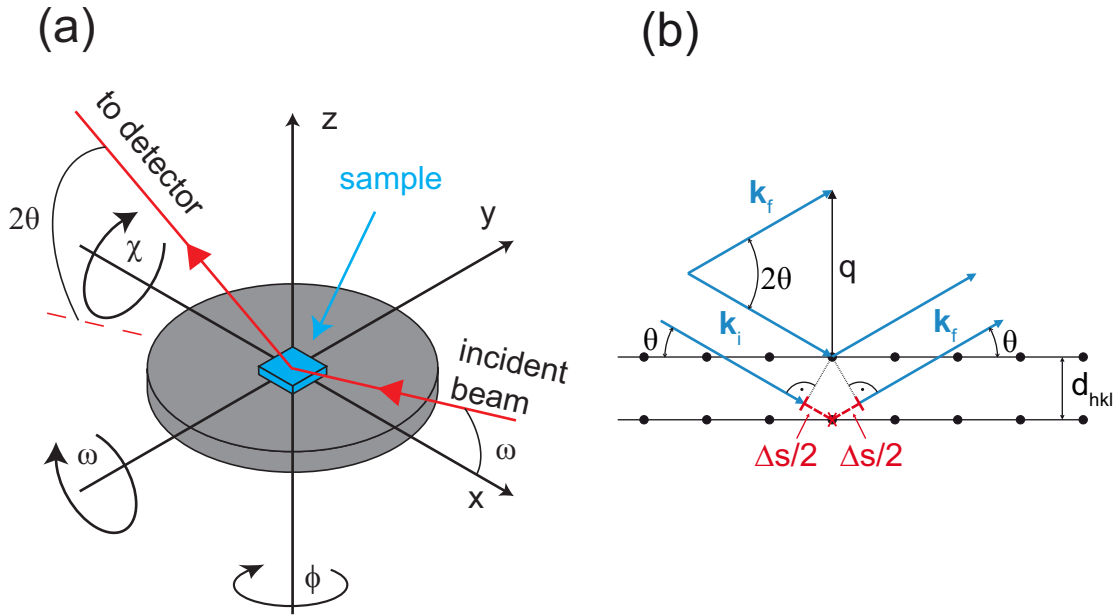


**Figure 4.4:** (a) Schematic view of the 4-circle diffractometer. (b) Diffraction of X-ray beams on lattice planes.

where  $hkl$  are the Miller indices of the atomic plane and  $n$  designates the  $n$ -th order of diffraction. The correlation of  $\Delta s$  and  $\theta$  can easily be seen in Fig. 4.4(b). Equivalently, the constructive interference can be described vectorial by the Laue condition:

$$\mathbf{K}_{hkl} = \mathbf{k}_f - \mathbf{k}_i = \mathbf{q}, \quad (4.16)$$

with  $\mathbf{q}$  denoting the scattering vector and  $\mathbf{K}_{hkl}$  designating a reciprocal lattice vector.

### 4.3.3 Reflections in reciprocal space

The available reflections are dependent on the geometry of the investigated material and may be described by a set of Miller indices ( $hkl$ ), corresponding to a set of parallel atomic layers. According to the Laue condition, constructive interference of the incident beams is achieved if  $\mathbf{q} = \mathbf{K}_{hkl}$ . Fig. 4.5 shows a two-dimensional section of reciprocal space, containing the reflections ( $0kl$ ) of MgO. If a certain reflection is to be measured, one has to choose the appropriate angles  $\omega$ ,  $2\theta$ ,  $\chi$  and  $\phi$ . Due to geometrical restrictions, not all reflections are available. As  $k_i = k_f = 2\pi/\lambda$ , the

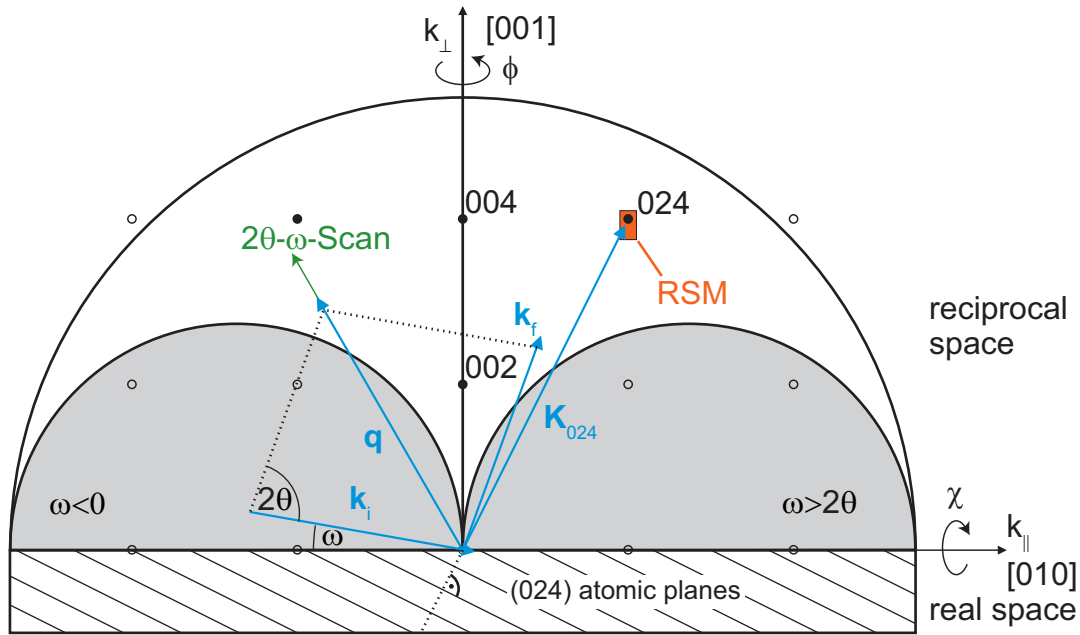


**Figure 4.5:** Two dimensional reciprocal space showing the MgO reflections available for diffraction.

available reflections are encompassed by a half circle with radius  $q_{\max} = k_i + k_f = 2 \cdot 2\pi/\lambda = 4\pi/\lambda$ . Both, the incident and the diffracted beam can not pass the sample plate, this results in the conditions  $\omega > 0$  and  $\omega < 2\theta$  (grey half circles in Fig. 4.5). Two measurement modes relevant for this work are introduced:

### **2 $\theta$ - $\omega$ -scan**

If  $2\theta$  is varied at double angular velocity with respect to  $\omega$ , the scattering vector  $\mathbf{q}$  changes only in magnitude but retains its direction in reciprocal space. This scan is marked by a green arrow in Fig. 4.5. If one chooses  $\omega = \theta$ ,  $\mathbf{q}$  advances in  $[001]$  direction and reaches the  $(00l)$  symmetric reflections. The results of  $2\theta$ - $\omega$ -scans are displayed as the reflection intensity  $I(2\theta)$ . An exemplarily  $2\theta$ - $\theta$ -scan of a magnetite ( $\text{Fe}_3\text{O}_4$ ) thin film on a magnesium oxide (MgO) substrate (scan of the sample that will be investigated in the next Chapter) is displayed in Fig. 4.6(a).

### **Reciprocal Space Map (RSM)**

A RSM provides a rectangular scan of reciprocal space as indicated by the orange box in Fig. 4.5. The rectangular mapping is achieved by varying both  $\omega$  and  $2\theta$

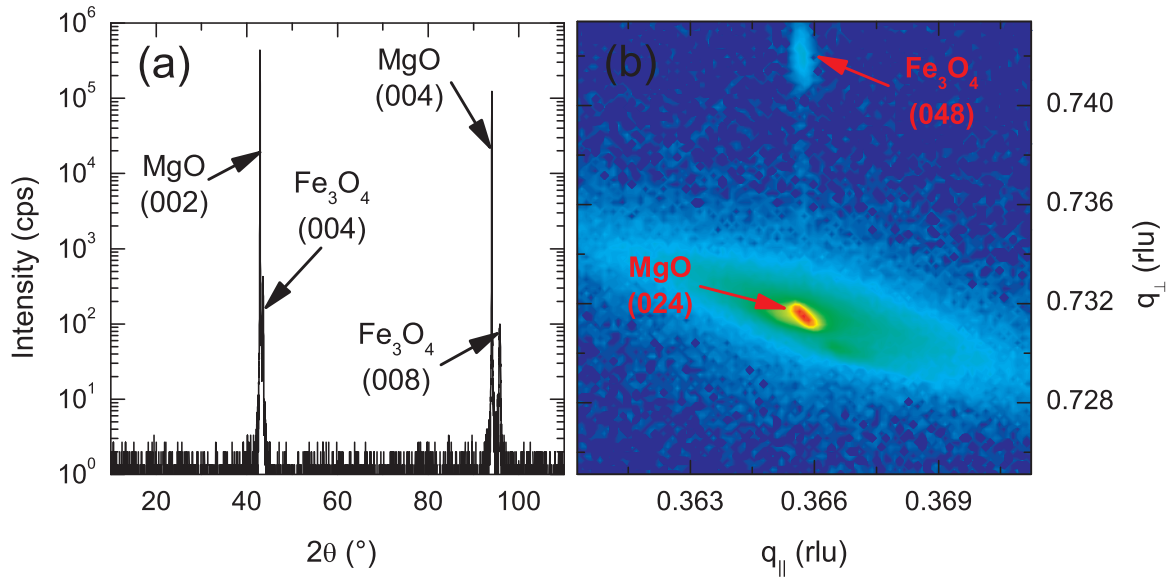


**Figure 4.6:** (a)  $2\theta$ - $\theta$ -scan and (b) reciprocal space map of a  $\text{Fe}_3\text{O}_4$  thin film on MgO substrate with color coded logarithmic intensity (red depicting high intensity and blue depicting zero intensity).

accordingly. In contrast to  $2\theta$ - $\omega$  scans, where the intensity is a function of a single variable, the intensity  $I(q_{\parallel}, q_{\perp})$  obtained from RSMs is a function of two variables.  $q_{\parallel}$  and  $q_{\perp}$  denote the components of  $\mathbf{q}$  perpendicular to [001] and parallel to [001], respectively. An example reciprocal space map of the MgO (024) and  $\text{Fe}_3\text{O}_4$  (048) reflections of the  $\text{Fe}_3\text{O}_4$  thin film on the MgO substrate is displayed in Fig. 4.6(b).

#### 4.3.4 Determination of lattice constants

For an orthorhombic unit cell with lattice constants  $a$ ,  $b$  and  $c$ , the distance  $d$  between lattice planes is given by:

$$\frac{1}{d^2} = \frac{h^2}{a^2} + \frac{k^2}{b^2} + \frac{l^2}{c^2}, \quad (4.17)$$

which in combination with Bragg's equation (4.15) enables us to determine out-of-plane lattice constants from the data achieved by a  $2\theta$ - $\theta$ -scan ( $h = k = 0$ ):

$$c = \frac{\lambda l}{2 \sin \theta}. \quad (4.18)$$

RSMs are conventionally represented not by  $q_{\parallel}$  and  $q_{\perp}$  which are both dependent on the wavelength  $\lambda$ , but in so called reciprocal lattice units (rlu) which are independent

of  $\lambda$ . This is done by normalizing  $4\pi/\lambda = 1$ , which is equivalent to the normalization of the radius of the encompassing half circle in Fig. 4.5 to 1. This results in the renormalization of  $q_{\parallel}(\text{rlu}) = q_{\parallel}/\frac{4\pi}{\lambda}$  and  $q_{\perp}(\text{rlu}) = q_{\perp}/\frac{4\pi}{\lambda}$ . From a RSM represented by these reciprocal lattice vectors, the lattice constants can be calculated by [82]:

$$a = \frac{1}{q_{\parallel a}(\text{rlu})} \frac{\lambda}{2} h \quad (4.19)$$

$$b = \frac{1}{q_{\parallel b}(\text{rlu})} \frac{\lambda}{2} k \quad (4.20)$$

$$c = \frac{1}{q_{\perp c}(\text{rlu})} \frac{\lambda}{2} l. \quad (4.21)$$

### 4.3.5 Precise lattice parameter determination

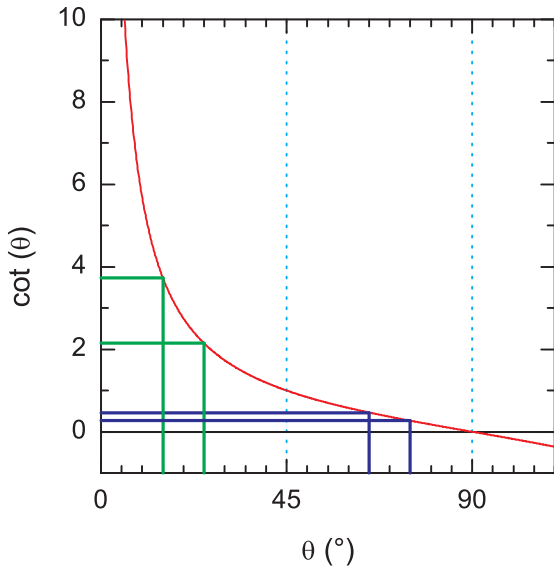


**Figure 4.7:** The systematic error  $\delta c/c$  is proportional to  $\cot \theta$ .

The true value of a lattice constant can therefore be calculated by extrapolating the measured values to  $2\theta = 180^\circ$ . This is done by using an extrapolation function  $f(\theta)$  that accounts for the errors present in the experimental setup. To

As we strive for the determination of small lattice parameter changes, it is indispensable to minimize experimental errors. As evident from Eq. (4.18), HRXRD is an indirect measurement technique, as  $c$  is not a linear function of the measurand  $\theta$ , but of  $\sin \theta$ . We now calculate the deviation  $\delta c/c$  of Eq. (4.18):

$$\frac{\delta c}{c} = \left| \frac{\partial c}{\partial \theta} \cdot \frac{\delta \theta}{c} \right| = |-\cot \theta \delta \theta|. \quad (4.22)$$

Assuming some error  $\delta \theta$ , one can see from Fig. 4.7 that it is desirable to measure reflections coinciding with values of  $2\theta$  as close to  $180^\circ$  as possible. This minimizes the error in the determined lattice constant which is proportional to  $\cot \theta$ .

this end we use the Nelson-Riley extrapolation function [83]:

$$f(\theta) = \frac{\cos^2 \theta}{\sin \theta} + \frac{\cos^2 \theta}{\theta} . \quad (4.23)$$

The Nelson-Riley function accounts for the systematic error introduced by the offset of the sample with respect to the diffractometer axis, as well as beam divergence and the specimen's shape and absorption. Practically, one determines the lattice constants for different reflections by determining  $2\theta$  and calculating  $c$  with Eq. (4.18). If these  $c$  are plotted versus  $f(\theta)$ , the corrected value for  $c$  is found by linear extrapolation to  $f(\theta) = 0$ . Assuming no error at all, it is apparent that the slope of the linear fit is 0. The slope of the linear fit therefore is a measure of the systematic error. In order to achieve a reliable linear fit, one at best measures a high number of reflections at angles close to  $2\theta = 180^\circ$ . Unfortunately, often only a few reflections are available (for MgO, only two reflections – (002) and (004) – are available), thus the reliability of the results can only be checked by statistics, requiring a large number of measurements.



# Chapter 5

## Measuring strain in MgO single crystals

We investigate a magnetite ( $\text{Fe}_3\text{O}_4$ ) thin film which was deposited onto a single crystal magnesium oxide (MgO) substrate by pulsed laser deposition by Andreas Brandlmaier during his Diploma thesis [56]. The  $\text{Fe}_3\text{O}_4$  film is coherently strained, so that any change in substrate lattice constant is transmitted into the film. We now use piezo-electric actuators to induce a stress into the MgO substrate, which in turn results in voltage-controllable strains in the film. These strains can be directly quantified by measuring the lattice constants of either the substrate or the film. We thus use high resolution X-ray diffraction (HRXRD) to determine the lattice constants as a function of actuator voltage, focussing on the MgO substrate with its more intensive XRD reflections. The precise determination of strains is an important procedure, as it allows the application of magnetoelastic theory to calculate the strain-controlled magnetic anisotropy of the ferromagnetic film.

### 5.1 Introduction

In his thesis, Andreas Brandlmaier prepared samples of 30 nm thick magnetite ( $\text{Fe}_3\text{O}_4$ ) thin films on approximately 50  $\mu\text{m}$  thick magnesium oxide (MgO) single crystals that were glued onto voltage driven piezoelectric actuators [56]. The samples were glued face down (actuator–glue– $\text{Fe}_3\text{O}_4$ –MgO) onto Piezomechanik PSt 150/2x3/5 actuators [76] using two component epoxy<sup>1</sup>. The actuator has a nominal expansion of 0.13% along the main axis of elongation within the semi-bipolar voltage range

---

<sup>1</sup>UHU plus endfest 300

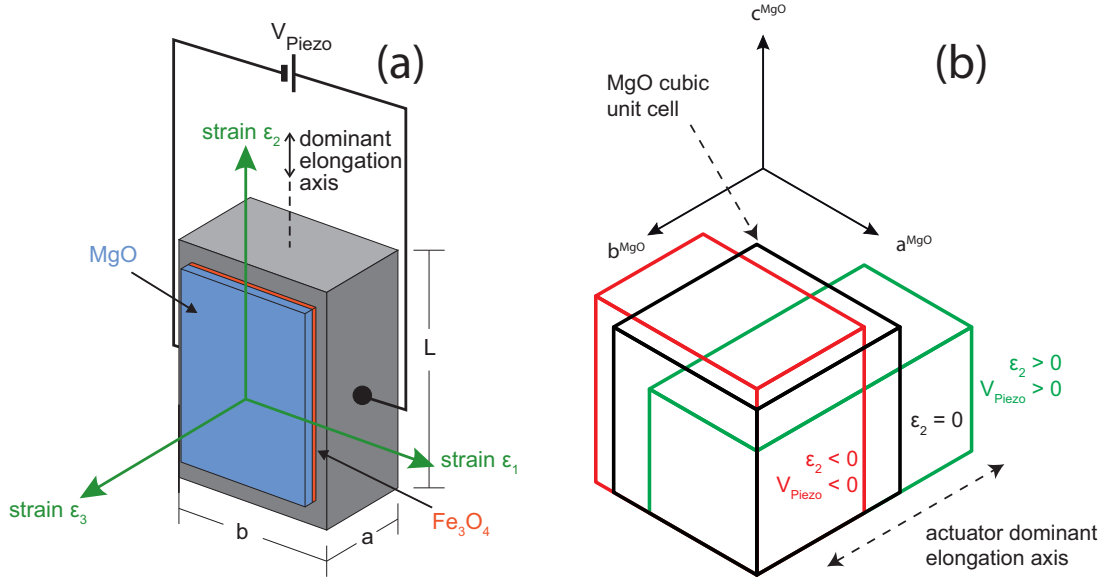


**Figure 5.1:** (a) Schematic view of the sample on actuator. (b) Orthorhombic distortion of MgO unit cell caused by the actuator.

$-30 \text{ V} \leq V_{Piezo} \leq +150 \text{ V}$  and dimensions  $a \times b \times L = 2 \times 3 \times 5 \text{ mm}^3$ . We use one of these samples which is schematically shown in Fig. 5.1(a) and was glued onto the actuator in such a way, that the strain axes coincide with crystalline axes of MgO. We thus expect an orthorhombic deformation of the MgO unit cell as a function of actuator voltage as schematically shown in Fig. 5.1(b). We use a Bruker AXS D8-Discover four circle diffractometer for all HRXRD measurements. An introduction to this setup is given in Chapter 4 and the basic properties of Fe<sub>3</sub>O<sub>4</sub> and MgO are discussed in Chapter 3.

## 5.2 Elastic theory

Due to the elastic properties of crystals, an applied uniaxial stress results in a parallel and two orthogonal pure lattice strains. To calculate the full set of pure in-plane and out-of-plane strains, it is thus sufficient to determine a single strain. The relation of the strains are then given by the crystal's elastic moduli and can be calculated using elastic theory. This will be done for MgO single crystals in the following.

A stress acting on a crystal results in strain which in three dimensional space is described by the  $3 \times 3$  strain matrix  $\epsilon_{ij}$  [45]. We use the contracted Voigt notation [84],

so that in particular  $\varepsilon_i = \varepsilon_{ii}$  ( $i = 1, 2, 3$ ). For a cubic crystal, continuum elastic theory [29] relates the strain to the elastic free energy density  $F_{\text{el}}$ :

$$F_{\text{el}} = \frac{1}{2}c_{11}(\varepsilon_1^2 + \varepsilon_2^2 + \varepsilon_3^2) + c_{12}(\varepsilon_1\varepsilon_2 + \varepsilon_2\varepsilon_3 + \varepsilon_1\varepsilon_3), \quad (5.1)$$

where  $c_{11}$  and  $c_{22}$  are the elastic moduli of MgO (cf. Tab. 3.7). This expression neglects the effects of shear strain ( $\varepsilon_4 = \varepsilon_5 = \varepsilon_6 = 0$ ). This can be done here as the sample – and thus the sides of the crystalline unit cell – is aligned along the actuator's orthogonal axes of elongation or contraction and thus only pure strains  $\varepsilon_i$  ( $i \leq 3$ ) are present. Stresses in the crystal are given by the partial derivatives of the elastic free energy as shown in (2.17). Assuming that the stress and strain are parallel, we obtain:

$$\sigma_i = \frac{\partial F_{\text{el}}}{\partial \varepsilon_i} \quad (i = 1, 2, 3). \quad (5.2)$$

We assume no stress perpendicular to the sample plane, as the crystal is free to move in this direction. Hence  $\sigma_3 = \partial F_{\text{el}}/\partial \varepsilon_3 = c_{11}\varepsilon_3 + c_{12}(\varepsilon_1 + \varepsilon_2) = 0$  which yields

$$\varepsilon_3 = -\frac{c_{12}}{c_{11}}(\varepsilon_1 + \varepsilon_2). \quad (5.3)$$

Therefore the out-of-plane strain  $\varepsilon_3$  is a function of the in-plane strains  $\varepsilon_1$  and  $\varepsilon_2$ . The in-plane strains are related by the Poisson ratio  $\nu$ :

$$\varepsilon_1 = -\nu\varepsilon_2, \quad (5.4)$$

with  $\nu = \nu^{\text{Piezo}} = 0.45$  for the used actuator, which is calculated from the piezoelectric constants of the actuator  $d_{31,\text{Piezo}} = -290$  pm/V and  $d_{33,\text{Piezo}} = +640$  pm/V [76]. As can be seen from Eqs. (5.3) and (5.4), a single experimentally determined strain  $\varepsilon_i$  is sufficient to calculate the strains in the two orthogonal directions. For instance, if  $\varepsilon_3$  is determined by measuring the strained out-of-plane lattice constant  $c$  with respect to the unstrained value  $c_0$ , the three orthogonal strains are given by:

$$\begin{aligned} \varepsilon_3 &= \frac{c - c_0}{c_0} = \frac{\Delta c}{c_0} \\ \varepsilon_1 &= -\frac{c_{11}}{c_{12}} \frac{\nu}{\nu - 1} \varepsilon_3 \\ \varepsilon_2 &= -\frac{c_{11}}{c_{12}} \frac{1}{1 - \nu} \varepsilon_3. \end{aligned} \quad (5.5)$$

## 5.3 Measurement results

The out-of-plane lattice constant  $c^{\text{MgO}}$  was determined as a function of actuator voltage by means of  $2\theta$ - $\theta$ -scans of the MgO (002) and (004) reflections. To determine the change in in-plane lattice constants  $a^{\text{MgO}}$  and  $b^{\text{MgO}}$ , reciprocal space maps of the MgO (204), (024) and (224) reflections were recorded at  $V_{\text{Piezo}} = -30 \text{ V}$  and  $V_{\text{Piezo}} = +90 \text{ V}$ . The reflection intensities of the  $\text{Fe}_3\text{O}_4$  thin film were unfortunately too small to allow for a quantitative analysis of strain in the ferromagnetic thin film itself within reasonable integration time. Hence, we will show only results obtained from the MgO reflections, as already mentioned above.

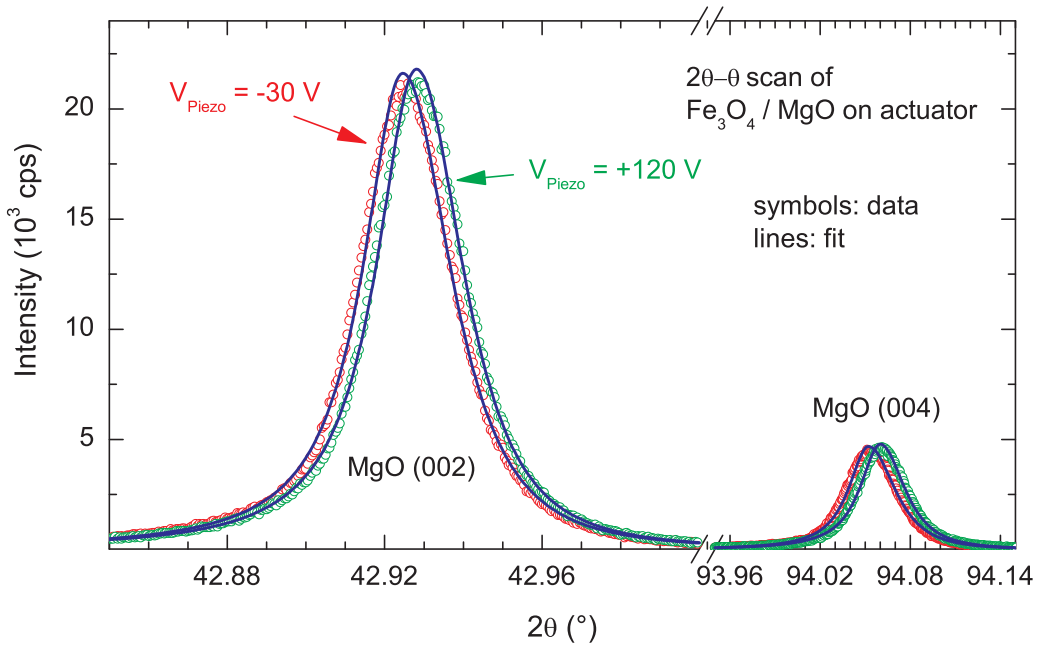
### 5.3.1 Strain effect on the out-of-plane lattice constant

Fig. 5.2 shows the raw data obtained from a  $2\theta$ - $\theta$ -scan of the MgO (002) and (004) reflections for  $V_{\text{Piezo}} = -30 \text{ V}$  and  $V_{\text{Piezo}} = +120 \text{ V}$ . To determine the peak position, a split Pearson VII fit [85] is applied, which gives a very good fit of the experimental data (cf. Fig. 5.2). The Nelson-Riley formalism (cf. Chapter 4) is used to calculate the corrected out-of-plane lattice constant  $c^{\text{MgO}}$ , which is shown in Fig. 5.3(a) as a function of actuator voltage  $V_{\text{Piezo}}$ . The lattice constant evolves nearly linearly in the entire measurement range of  $-30 \text{ V} \leq V_{\text{Piezo}} \leq +120 \text{ V}$ .

Fig. 5.3(b) shows the strains along the MgO cubic axes (cf. Eq. (5.5)). Whereas  $\varepsilon_3$  is directly obtained from the determination of lattice constants as a function of actuator voltage (cf. Fig. 5.3(a)),  $\varepsilon_1$  and  $\varepsilon_2$  are calculated with elastic theory by using Eq. (5.5). All strains are displayed relative to the strains at  $V_{\text{Piezo}} = 0 \text{ V}$ , thus for  $V_{\text{Piezo}} = 0 \text{ V}$  all strains vanish in Fig. 5.3(b). For  $-30 \text{ V} \leq V_{\text{Piezo}} \leq +90 \text{ V}$  we observe the following strains<sup>2</sup>:

$$\begin{aligned} \Delta\varepsilon_1^{-30\text{V},+90\text{V}} &= -13 \times 10^{-5} \\ \Delta\varepsilon_2^{-30\text{V},+90\text{V}} &= 28 \times 10^{-5} \\ \Delta\varepsilon_3^{-30\text{V},+90\text{V}} &= -5 \times 10^{-5} . \end{aligned} \tag{5.6}$$

<sup>2</sup>We calculate strains only for  $-30 \text{ V} \leq V_{\text{Piezo}} \leq +90 \text{ V}$  for good comparison to the later discussed reciprocal space map measurements



**Figure 5.2:** Data (points) and fit (lines) for the MgO (002) and (004) symmetric reflections at actuator voltages  $V_{\text{Piezo}} = -30 \text{ V}$  and  $V_{\text{Piezo}} = +120 \text{ V}$ .

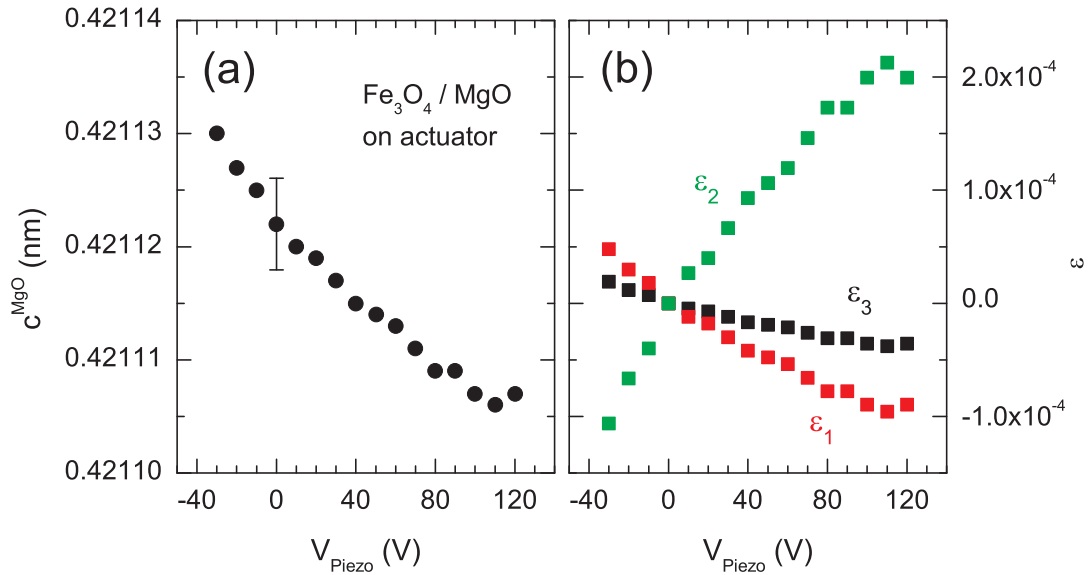


**Figure 5.3:** (a) MgO out-of-plane lattice constant as a function of actuator voltage. The error bar represents the maximum fitting error as discussed in Section 5.3.2. (b) Strains  $\varepsilon_i$  calculated from Eq. (5.5).

### 5.3.2 Estimation of the measurement uncertainty

An estimate of the error in  $c^{\text{MgO}}$  is given by the fitting error of the raw data shown in Fig. 5.2. This error was determined to be smaller than  $\delta(2\theta) = 0.001^\circ$ . According to Eq. (4.22), this yields errors in  $c$  of  $\delta c = 9.0 \times 10^{-6}$  nm for the MgO (002) reflection and  $\delta c = 3.4 \times 10^{-6}$  nm for the MgO (004) reflection. These errors are now incorporated into the Nelson-Riley correction and yield the error bars in Fig. 5.4. The dashed lines in Fig. 5.4 correspond to the resulting two extreme possible linear fits of the lattice constants determined from the MgO (002) and (004) reflection at each voltage  $V_{\text{Piezo}}$ . Thus, the error in  $c^{\text{MgO}}$  is enclosed by the dashed lines at  $f(\theta) = 0$  for each  $V_{\text{Piezo}}$ . For  $-30 \text{ V} \leq V_{\text{Piezo}} \leq +120 \text{ V}$  the error in  $c^{\text{MgO}}$  is determined in this fashion and the error bar in Fig. 5.3(a) corresponds to the maximum error.

Finally, we argue that the constant slope of the linear fits for  $-30 \text{ V} \leq V_{\text{Piezo}} \leq +90 \text{ V}$  (cf. Fig. 5.4) is a good indication that the determination of  $c^{\text{MgO}}$  using the Nelson-Riley correction is accurate in our case. As described in Chapter 4, the Nelson-Riley function accounts for systematic errors, with the slope of the linear fit representing the magnitude of these errors. One can see from Fig. 5.4 that the slope – and hence the systematic error – remains nearly constant for  $-30 \text{ V} \leq V_{\text{Piezo}} \leq +90 \text{ V}$ . The systematic error is caused by diffractor misalignment, beam divergence, specimen shape, absorption and displacement from the diffractometer axis. All these errors are present for our samples, but are not expected to change with  $V_{\text{Piezo}}$ . Therefore a constant linear fit slope is a good indication for an accurate determination of  $c^{\text{MgO}}$  for each reflection at all actuator voltages. Due to the linear and reversible evolution of  $c^{\text{MgO}}$  with  $V_{\text{Piezo}}$ , spurious effects such as temperature drift can be ruled out as the cause of lattice constant change.

Taken together, even with a rather conservative error calculation, the HRXRD data unambiguously shows that the influence of the actuator-induced strain on the MgO lattice can be accurately determined with HRXRD.

### 5.3.3 Strain effect on the in-plane lattice constants

To determine the effect of strain on the in-plane lattice constants, reciprocal space maps of the MgO (204), (024) and (224) reflections were recorded. A conventional reciprocal space map (RSM) is shown exemplarily in Chapter 4. As the shift of reflections caused by changes in lattice constants as a function of actuator voltage are

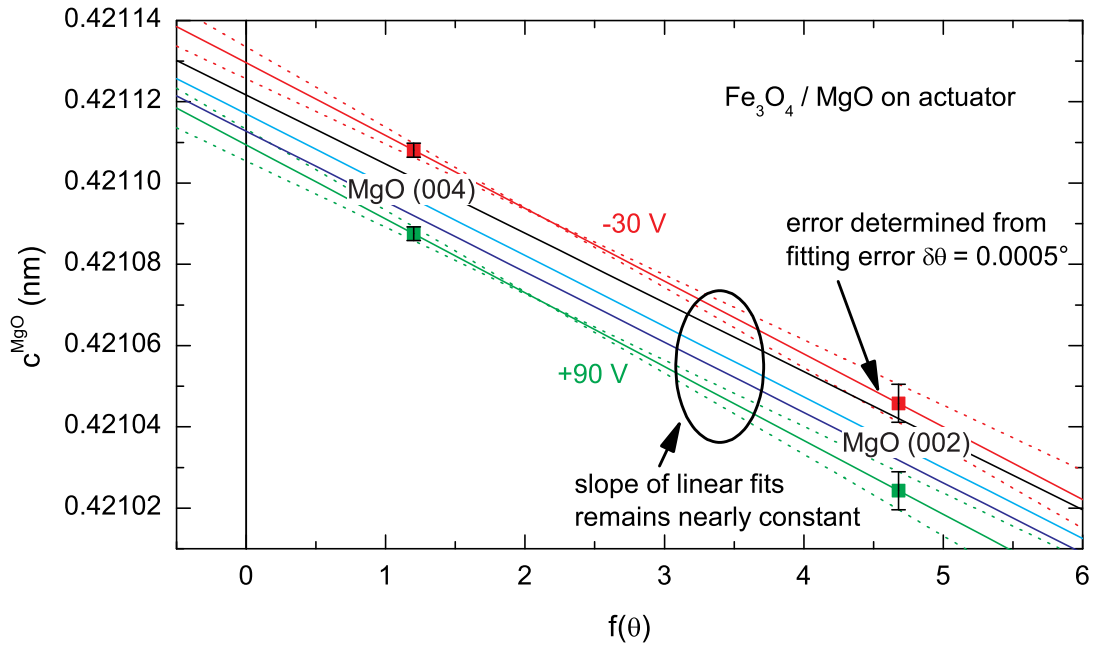


**Figure 5.4:** Nelson Riley correction of  $c^{\text{MgO}}$ . Linear fits (solid lines) are displayed in steps of 30 V. Data points and error bars are only displayed for  $V_{\text{Piezo}} = -30$  V and  $V_{\text{Piezo}} = +90$  V. The corrected lattice constants are obtained at  $f(\theta) = 0$  and the maximum error  $\delta c$  is enclosed by the dotted lines at  $f(\theta) = 0$ .

much smaller than the reflection width (cf. Fig. 5.2) two non-standard approaches to the visualization of RSMs are used here, both focusing on showing the difference between two reciprocal space maps rather than absolute values.

For each available reflection, we recorded one RSM at  $V_{\text{Piezo}} = -30$  V and one at  $V_{\text{Piezo}} = +90$  V. We now normalize each measurement point in a given RSM with respect to the maximum intensity ( $I_{\text{max}}^{\text{norm}} = 1$ ). Figs. 5.5(a), 5.6(a) and 5.7(a) show the contour lines at the half maximal normalized intensity  $I^{\text{norm}} = 0.5$  for the MgO (204), (024) and (224) reflections at both actuator voltages, while Figs. 5.5(b), 5.6(b) and 5.7(b) show the difference of normalized intensity  $I_{\text{diff}}^{\text{norm}} = I_{-30\text{V}}^{\text{norm}} - I_{+90\text{V}}^{\text{norm}}$  for the respective reflections.

One sees, that a precise quantitative determination of the peak positions is difficult in these RSMs, as the reflection peak widths are big if compared to the shifts of the reflections as a function of actuator voltage. Hence we will only qualitatively compare

the measurements to theoretical expectations. The calculations performed in the following thus are mainly intended to reveal the difficulty of precise lattice parameter determination from reciprocal space maps.

The shift of the reflections in Figs. 5.5, 5.6 and 5.7 can be described by different scattering vectors (cf. Chapter 4) for  $V_{\text{Piezo}} = -30 \text{ V}$  and  $V_{\text{Piezo}} = +90 \text{ V}$ . The observed shift in the RSMs is caused by a movement of the reflections in reciprocal space as a function of actuator voltage. Hence the shift can be estimated by calculating  $\Delta q_{\perp} = q_{\perp-30\text{V}} - q_{\perp-90\text{V}}$  and  $\Delta q_{\parallel} = q_{\parallel-30\text{V}} - q_{\parallel-90\text{V}}$ . This will be done in the following.

The basic relation between the in-plane lattice constants<sup>3</sup>  $a^{\text{MgO}}$  and  $b^{\text{MgO}}$  and the scattering vectors  $q_{\parallel\text{a}}$  and  $q_{\parallel\text{b}}$  is given by equations (4.19) and (4.20). The out-of-plane lattice constant  $c^{\text{MgO}}$  that is related to  $q_{\perp}$  by (4.21) was already measured by  $2\theta$ - $\theta$ -scans as a function of actuator voltage and is thus assumed to be known. Thus we will calculate all shifts as a function of the known strain  $\Delta\varepsilon_3 = \varepsilon_3(-30 \text{ V}) - \varepsilon_3(+90 \text{ V})$  from Eq. (5.6).

For all reflections, the change in the out-of-plane lattice constant  $\Delta c = c_{+90\text{V}} - c_{-30\text{V}} = \Delta\varepsilon_3 c_{-30\text{V}}$  (with  $\Delta\varepsilon_3$  taken from Eq. (5.5)) is expected to result in a shift in  $q_{\perp}$ , which can be derived by:

$$\begin{aligned} \Delta c &= c_{+90\text{V}} - c_{-30\text{V}} \stackrel{(4.21)}{=} \left[ \frac{1}{q_{\perp+90\text{V}}} - \frac{1}{q_{\perp-30\text{V}}} \right] \frac{\lambda}{2} l = \Delta\varepsilon_3 c_{-30\text{V}} \quad (5.7) \\ \Leftrightarrow \Delta q_{\perp} &= q_{\perp-30\text{V}} - q_{\perp+90\text{V}} = q_{\perp-30\text{V}} q_{\perp+90\text{V}} \Delta\varepsilon_3 c_{-30\text{V}} \frac{2}{\lambda l}. \end{aligned}$$

We now neglect the difference between  $q_{\perp-30\text{V}}$  and  $q_{\perp+90\text{V}}$  in the product  $q_{\perp-30\text{V}} q_{\perp+90\text{V}}$ . This can be done here as the change  $q_{\perp-30\text{V}} - q_{\perp+90\text{V}}$  is expected to be in the order of  $1 \times 10^{-4}$  rlu as can be seen from Figs. 5.5(a) to 5.7(a). This approximation yields:

$$\Delta q_{\perp} = q_{\perp}^2 \Delta\varepsilon_3 c_{-30\text{V}} \frac{2}{\lambda l} \approx -4 \times 10^{-5} \text{ rlu}, \quad (5.8)$$

with  $q_{\perp} = 0.731$  rlu estimated from Fig. 5.5(a). Thus we expect the reflection measured with  $V_{\text{Piezo}} = -30 \text{ V}$  to be shifted to smaller values of  $q_{\perp}$  with respect to the reflection measured with  $V_{\text{Piezo}} = +90 \text{ V}$ .

In the following, we will calculate the expected difference  $\Delta q_{\parallel}$  of the in plane component of the scattering vector for  $-30 \text{ V} \leq V_{\text{Piezo}} \leq +90 \text{ V}$  for all three investigated reflections.

<sup>3</sup>For better readability, the superscript "MgO" will be omitted in the following discussion.

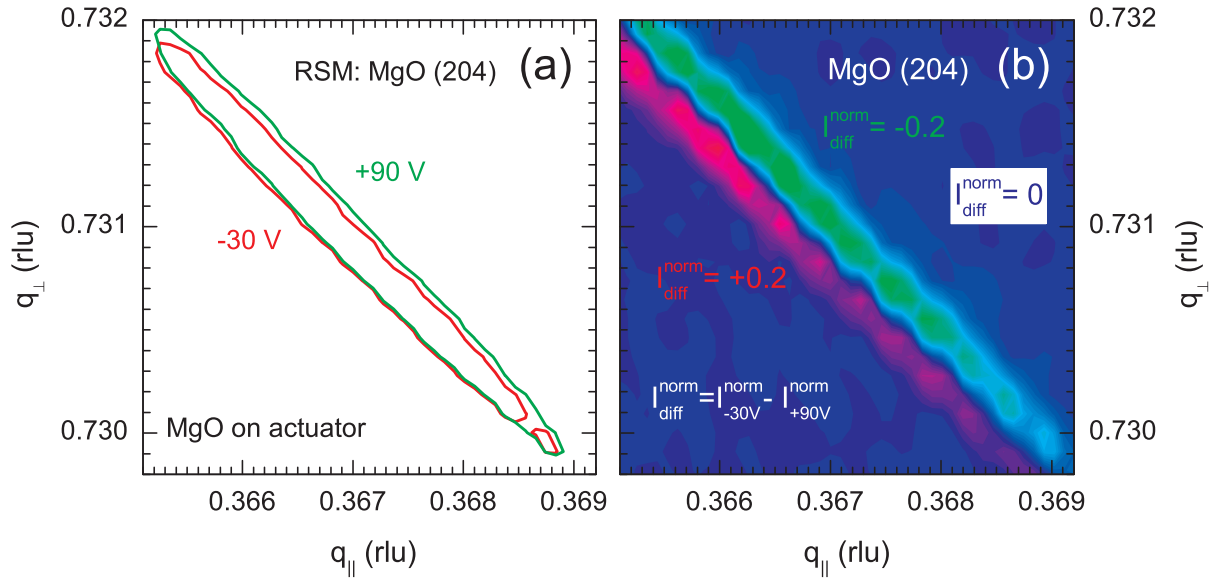


**Figure 5.5:** Reflection peak shift for the MgO (204) reflection: (a) Contours at half maximal normalized intensity for  $V_{\text{Piezo}} = -30 \text{ V}$  and  $V_{\text{Piezo}} = +90 \text{ V}$ . (b) Difference in normalized intensity  $I_{\text{diff}}^{\text{norm}}$  (red:  $I_{\text{diff}}^{\text{norm}} = 0.2$ , green:  $I_{\text{diff}}^{\text{norm}} = -0.2$ , dark blue:  $I_{\text{diff}}^{\text{norm}} = 0$ ).

### MgO (204)

We start from the basic relation of the lattice constant  $a$  and its representation by  $q_{\parallel a}$  in reciprocal space given in Eq. (4.19). We obtain the representation of the difference of the lattice constant  $a$  for  $V_{\text{Piezo}} = -30 \text{ V}$  and  $V_{\text{Piezo}} = +90 \text{ V}$  in reciprocal space:

$$a_{+90\text{V}} - a_{-30\text{V}} = \Delta a = \left[ \frac{1}{q_{\parallel a+90\text{V}}} - \frac{1}{q_{\parallel a-30\text{V}}} \right] \frac{\lambda}{2} h \Leftrightarrow \Delta \left[ \frac{1}{q_{\parallel a}} \right] = \Delta a \frac{2}{\lambda h}. \quad (5.9)$$

Approximating that the crystal is cubic at  $V_{\text{Piezo}} = -30 \text{ V}$  and the application of other voltages to the actuator results in an orthorhombic distortion yields:

$$\frac{a_{+90\text{V}} - a_{-30\text{V}}}{a_{-30\text{V}}} = \frac{\Delta a}{a_{-30\text{V}}} = \frac{\Delta a}{c_{-30\text{V}}} \Leftrightarrow \Delta a = \Delta \varepsilon_1 a_{-30\text{V}} \approx \Delta \varepsilon_1 c_{-30\text{V}}. \quad (5.10)$$

Combining Eq. (5.10) and (5.9), we can evaluate

$$\Delta \left[ \frac{1}{q_{\parallel a}} \right] = \frac{2\Delta \varepsilon_1}{\lambda h} c_{-30\text{V}}. \quad (5.11)$$

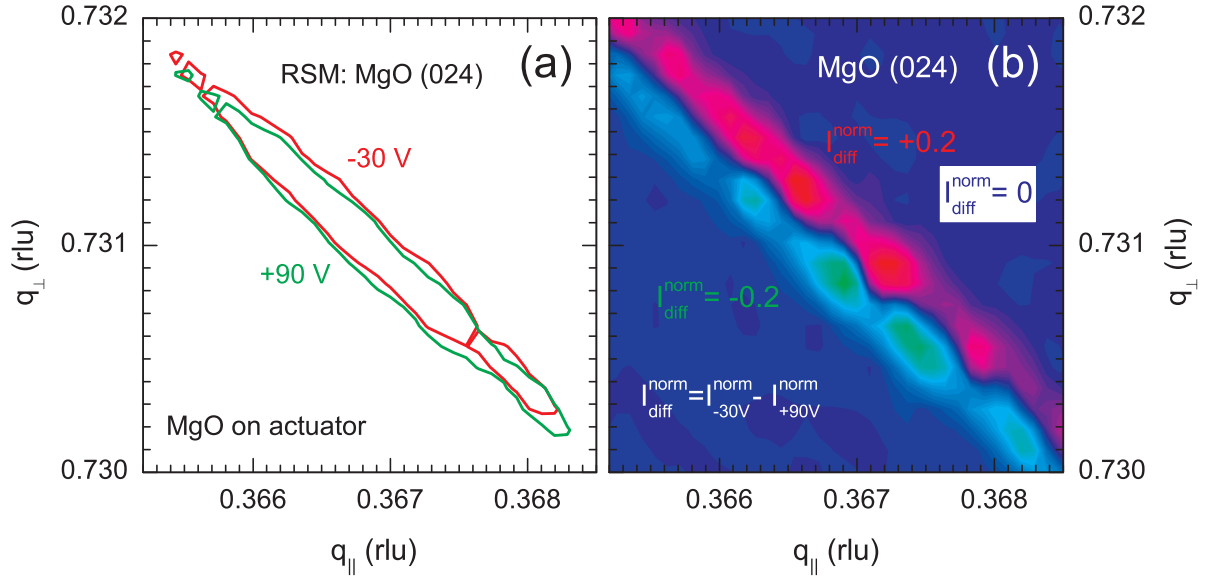


**Figure 5.6:** Reflection peak shift for the MgO (024) reflection: (a) Contours at half maximal normalized intensity. (b) Difference in normalized intensity  $I^{\text{norm}}$ .

In order to be able to compare the measured shift  $\Delta q_{\parallel a}$  to the theoretical expectations we solve Eq. (5.11) for  $\Delta q_{\parallel a}$ :

$$\begin{aligned} \Delta q_{\parallel a} = q_{\parallel a-30V} - q_{\parallel a+90V} &= q_{\parallel a-30V} q_{\parallel a+90V} \frac{2\Delta\varepsilon_1}{\lambda h} c_{-30V} \\ &\approx q_{\parallel a}^2 \frac{2\Delta\varepsilon_1}{\lambda h} c_{-30V} = -5 \times 10^{-5} \text{ rlu} , \end{aligned} \quad (5.12)$$

with  $q_{\parallel a} = 0.367 \text{ rlu}$  (cf. Fig. 5.5(a)). This shift corresponds well to the shift  $\Delta q_{\parallel}$  seen in Fig. 5.5(a). The calculated out-of-plane shift derived in Eq. (5.8) matches the experiment as well.

### MgO (024)

The shift expected for this reflection can be calculated in the same way as shown for the MgO (204) reflection, starting from Eq. (4.20). The result is:

$$q_{\parallel b-30V} - q_{\parallel b+90V} \approx q_{\parallel b}^2 \frac{2\varepsilon_2}{\lambda k} c_{-30V} = 1 \times 10^{-4} \text{ rlu} , \quad (5.13)$$

with  $q_{\parallel a} = 0.367 \text{ rlu}$  (cf. Fig. 5.6(a)). This is in good accordance with the shift observed in Fig. 5.6(a). However, the shift  $\Delta q_{\perp}$  calculated from Eq. (5.8) is not present in

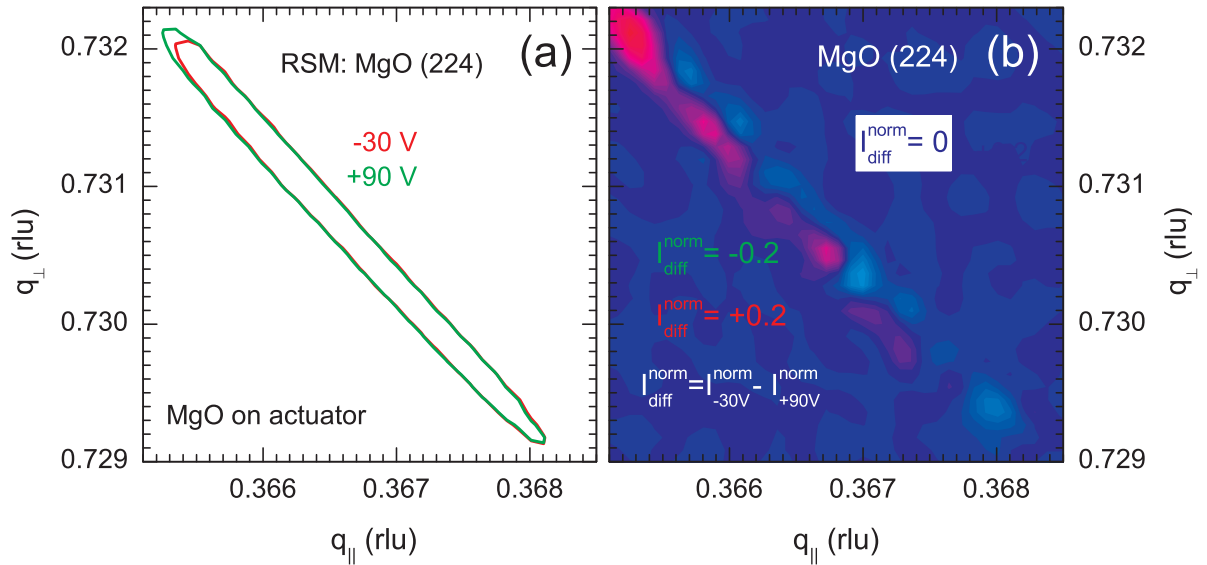


**Figure 5.7:** Reflection peak shift for the MgO (224) reflection: (a) Contours at half maximal normalized intensity. (b) Difference in normalized intensity  $I^{\text{norm}}$ .

Fig. 5.6(a). This may be due to the reflection line shape changing for  $V_{\text{Piezo}} = -30$  V compared to  $V_{\text{Piezo}} = +90$  V.

### MgO (224)

In order to calculate the expected shift for this reflection, we have to take into consideration that the  $a$  and  $b$  lattice constants are both involved in this reflection. Hence we no longer observe a lattice constant change  $\Delta a$  or  $\Delta b$  but a change in the diagonal of the rectangle spanned by  $a$  and  $b$ , which will be referred to as the diagonal lattice constant  $\sqrt{a_{+90\text{V}}^2 + b_{+90\text{V}}^2} - \sqrt{a_{-30\text{V}}^2 + b_{-30\text{V}}^2} = \Delta\sqrt{a^2 + b^2}$ .

Using  $h = k = 2$  as well as Eqs. (4.19) and (4.20), we can express the diagonal lattice constant change in reciprocal space as follows:

$$\Delta\sqrt{a^2 + b^2} = \lambda\Delta\sqrt{\frac{1}{q_{\parallel a}^2} + \frac{1}{q_{\parallel b}^2}}. \quad (5.14)$$

We now express the change in the lattice constants  $a$  and  $b$  as a function of the applied strains:  $a_{+90\text{V}} = a_{-30\text{V}}(1 + \Delta\varepsilon_1)$  and  $b_{+90\text{V}} = b_{-30\text{V}}(1 + \Delta\varepsilon_2)$ . Furthermore, we once

again assume that  $a_{-30V} = b_{-30V}$ . We can now evaluate the left side of Eq. (5.14) to

$$\begin{aligned} \Delta\sqrt{a^2 + b^2} &= \sqrt{a_{-30V}^2(1 + \Delta\varepsilon_1)^2 + b_{-30V}^2(1 + \Delta\varepsilon_2)^2} - \sqrt{a_{-30V}^2 + b_{-30V}^2} \\ &\approx a_{-30V}\sqrt{(1 + \Delta\varepsilon_1)^2 + (1 + \Delta\varepsilon_2)^2} - a_{-30V}\sqrt{2} \approx 0. \end{aligned} \quad (5.15)$$

We hence expect no change in the diagonal lattice constant  $\sqrt{a^2 + b^2}$ , as the strains  $\varepsilon_2 \approx -\varepsilon_1 \ll 1$  are small and of opposite signs. In reciprocal space, the diagonal lattice constant is represented by  $\frac{1}{q_{\parallel}} = \sqrt{\frac{1}{q_{\parallel a}^2} + \frac{1}{q_{\parallel b}^2}}$ . According to Eq. (5.14) this leads to the final conclusion:

$$\Delta\sqrt{\frac{1}{q_{\parallel a}^2} + \frac{1}{q_{\parallel b}^2}} = \Delta\frac{1}{q_{\parallel}} \approx 0 \Leftrightarrow \Delta q_{\parallel} = q_{\parallel -30V} - q_{\parallel +90V} \approx 0. \quad (5.16)$$

No shift is expected for the MgO (224) reflection, which is in good accordance with Fig. 5.7(a). The small difference of reflections only visible in Fig. 5.7(b) may be accounted to a pure shift in  $q_{\perp}$  as calculated in Eq. (5.8).

## 5.4 Discussion

Comparing the results obtained from  $2\theta$ - $\theta$ -scans (cf. Sec. 5.3.1) and reciprocal space maps (cf. Sec. 5.3.3), it is evident that  $2\theta$ - $\theta$ -scans are more suitable to quantify strains that cause very small lattice distortions of the order of  $10^{-4}$ . Whereas we observed a systematic evolution of the out-of-plane lattice constant  $c^{\text{MgO}}$  in  $2\theta$ - $\theta$ -scans, no definite quantitative conclusion on the in-plane lattice constants  $a^{\text{MgO}}$  and  $b^{\text{MgO}}$  was obtained from the RSMs. As the exact peak position in RSMs can not easily and reproducibly be obtained by a numerical fit, RSMs only allow for a qualitative investigation of strains of this order of magnitude. Thus, while RSMs usually allow to directly determine in-plane crystal properties, without suffering from the potential deviations of the elastic moduli and Poisson ratio, they are not suitable for the quantitative measurements of very small in plane strains.

However, elastic theory enables us to calculate all pure strains  $\varepsilon_i$  induced in the sample along the three cubic axes, even if only one lattice constant can be experimentally determined. We quantify the out-of-plane lattice constant by  $2\theta$ - $\theta$ -scans and find that we are able to reversibly and linearly tune the in-plane strain in the MgO single crystal by up to  $\varepsilon_2 = 2.8 \times 10^{-4}$  along the actuator's dominant elongation axis

for  $-30 \text{ V} \leq V_{\text{Piezo}} \leq +90 \text{ V}$ . This amounts to approximately 30% of the nominal expansion of the actuator  $\delta L/L = 8.7 \times 10^{-4}$  in the same voltage range. We attribute this deviation from the nominal actuator stroke to imperfect strain transmission due to the epoxy and strain relaxation in the MgO crystal itself. Thus, thinner samples that are deposited directly onto the actuator are expected to reduce this loss of strain significantly.



# Chapter 6

## Strain-induced magnetization switching in ferromagnetic thin films

In the previous Chapter, we found that the strain transmitted from a piezoelectric actuator into a 50  $\mu\text{m}$  thick MgO crystal amounts to only  $\approx 30\%$  of the nominal full stroke of the actuator. This was attributed to imperfect strain transmission caused by the glue, and strain relaxation in the crystal. To achieve a better strain transmission, it is hence desirable to omit the use of a substrate and glue. We therefore evaporated nickel and cobalt thin films directly onto the actuator. As these thin films are polycrystalline, no net crystalline anisotropy is expected, and the magnetic free energy density can ideally be reduced to the terms describing the uniaxial shape anisotropy and the uniaxial anisotropies arising from the strain induced by the actuator's elongation as a function of applied voltage.

The aim of this Chapter is to prove that the voltage dependent expansion of the actuator induces anisotropies into the ferromagnetic thin film that enable us to completely control the equilibrium orientation of the magnetization in a range of up to  $90^\circ$ . Furthermore, an application for this voltage-strain-control of magnetic anisotropy, that allows for a very precise determination of magnetoelastic effects, will be presented.

### 6.1 Motivation

The effect of strain in a MgO/Fe<sub>3</sub>O<sub>4</sub>/piezoactor heterostructure on the magnetic anisotropy of the Fe<sub>3</sub>O<sub>4</sub> thin film was investigated in a previous thesis by Andreas Brandlmaier [56] by FMR measurements. The main result is shown in Fig. 6.1. One

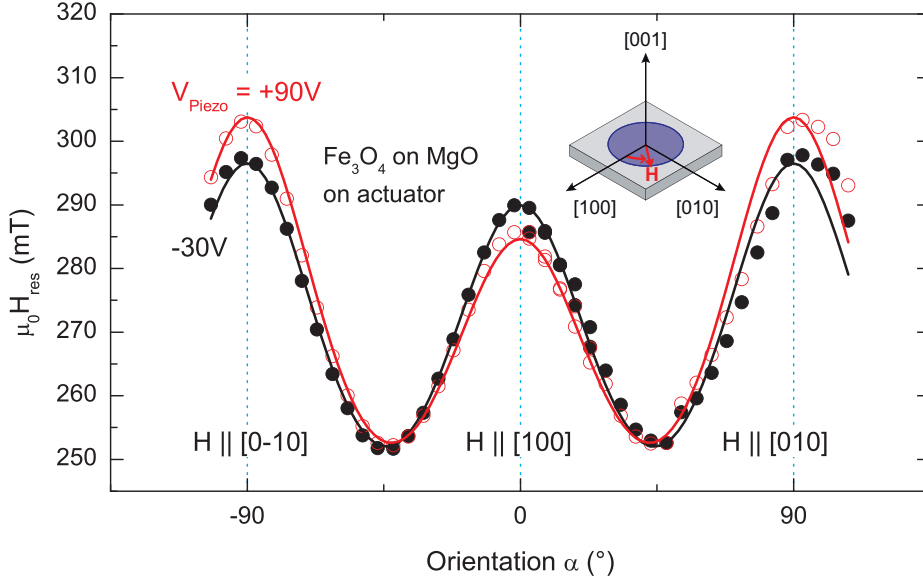


**Figure 6.1:** The sample used for XRD measurements shows a change in magnetic anisotropy for actuator voltages  $-30 \text{ V} \leq V_{\text{Piezo}} \leq +90 \text{ V}$ .

can clearly see that the ferromagnetic resonance field shifts if the actuator voltage and therefore the strain is varied, but no qualitative change of anisotropy is achieved. From these experiments, a magnetization rotation of  $\Delta\Theta = 6^\circ$  is obtained for  $-30 \text{ V} \leq V_{\text{Piezo}} \leq +90 \text{ V}$  [86]. A qualitative change of the magnetic anisotropy is prevented by the cubic anisotropy present in the ferromagnetic  $\text{Fe}_3\text{O}_4$  thin film. Its magnitude  $K_{c1}/M_s = -14.9 \text{ mT}$  is much larger than the strain induced change in uniaxial anisotropy. If a perfect strain transmission is assumed, a magnetization reorientation of  $\Delta\Theta = 17^\circ$  is predicted [86]. To achieve any larger effect on magnetization orientation, the cubic anisotropy needs to be reduced – which can most easily be achieved by the use of polycrystalline materials. As these materials can be deposited directly onto the actuator without the need for a substrate, the strain transmission is perfect and much larger effects on the magnetic anisotropy are expected. This is the main idea behind the experiments presented in the following.

## 6.2 Sample preparation

Andreas Brandlmaier evaporated 100 nm thick cobalt or nickel films onto piezoelectric actuators. A brief review of the properties of cobalt and nickel is given in Chapter 3. To prevent an oxidation of our  $2 \times 2 \text{ mm}^2$  polycrystalline films, a protective layer of

10 nm gold is deposited on top of the films. We once again use Piezomechanik PSt 150/2x3/5 actuators [76] that are built in an on stack isolating design illustrated in Fig. 6.2(b). The actuator's face is covered by a less than 50  $\mu\text{m}$  thick polymer coating. As the inner diameter of the cryostat shown in Fig. 4.2(b) measures only 4 mm, the actuators were polished down from their original dimensions  $a \times b \times L = 2 \times 3 \times 5 \text{ mm}^3$  to  $a \times b \times L = 2 \times 3 \times 2.5 \text{ mm}^3$  as shown in Fig. 6.2(b). As the piezo-stacks are arranged perpendicular to the dominant elongation axis, this results in the removal of stacks. Assuming an evenly distributed expansion over the entire actuator length  $L$ , the polishing is expected to remain without consequences for the nominal expansion of  $\frac{\delta L}{L} = 0.13\%$  in the specified voltage range of  $-30 \text{ V} \leq V_{\text{Piezo}} \leq +150 \text{ V}$ . In total, two actuators with cobalt thin films named CP1 and CP2 and two samples with nickel thin films named<sup>1</sup> NP2 and NP3 were prepared in this way and investigated. A schematic view of the samples is displayed in Fig. 6.2(a). The actuator's main axis of elongation points along the  $[010]$  direction of the sample coordinate system.

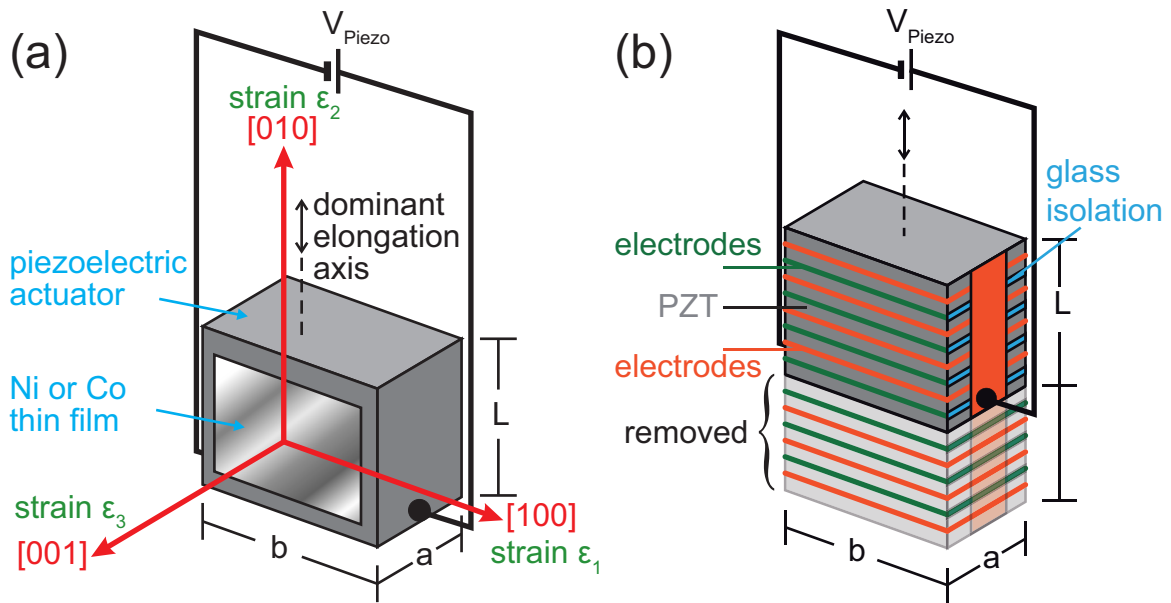


**Figure 6.2:** (a) Schematic view of the ferromagnetic thin film on actuator. (b) Schematic view of the actuator, showing the stack structure and the removed part.

For our measurements we use a Keithley 237 sourcemeter and apply voltages  $-30 \text{ V} \leq V_{\text{Piezo}} \leq +100 \text{ V}$  to the actuator. We record the ferromagnetic resonance spectra of

<sup>1</sup>The first sample, NP1, was not polished and thus did not fit into the cryostat.

our samples at room temperature using a Bruker ESP 300 X-band (9.3 GHz) spin resonance spectrometer. An introduction to ferromagnetic resonance and the used measurement setup is given in Chapter 4. The orientation of the samples in the external magnetic field is varied with the magnetic field rotated either in the (001) or in the (010) plane. These two measurement configurations shown in Fig. 6.3 are referred to as "in-plane" (ip) and "out-of-plane" (oop), respectively. The angle for the in-plane rotation is defined as  $\alpha$  and the angle for the out-of-plane rotation is defined as  $\chi$ . Experimentally, an orientation of  $\alpha = 0^\circ$  as well as  $\chi = 0^\circ$  denote  $\mathbf{H}_0 \parallel [100]$  for both in-plane and out-of-plane rotations. This is not consistent with the definition of angles in Fig. 2.3 that is used in all theoretical descriptions, but offers the advantage that the results of out-of-plane and in-plane measurements can be more easily compared, as  $0^\circ$  refers to the same direction of  $\mathbf{H}_0$  in both cases. In the theoretical calculations, we use the definition of angles customary in the literature. The transformation from the theoretical definition of angles  $(\theta, \phi)$  to the experimentally used angles  $(\alpha, \chi)$  is given by

$$\begin{aligned}\alpha &= 90^\circ - \theta & \phi &= 90^\circ \\ \chi &= 90^\circ - \phi & \theta &= 90^\circ.\end{aligned}\tag{6.1}$$

The rotation of the external magnetic field in relation to the sample is technically always restricted to the rotation in one plane, making one angle sufficient to describe the orientation as can be seen from Eq. (6.1). Unless stated otherwise, all rotations are carried out using a goniometer with an angular precision better than  $0.001^\circ$ . All samples were mounted on specimen holders as shown in Fig. 6.3. To determine all the samples' magnetic anisotropy contributions for a given  $V_{\text{Piezo}}$ , the samples are rotated in both in-plane and out-of-plane configuration. For each orientation  $\alpha$  or  $\chi$  and voltage  $V_{\text{Piezo}}$  a FMR spectrum is recorded. The resonance field  $\mu_0 H_{\text{res}}$  and linewidth  $\mu_0 \Delta H_{\text{pp}}$  are extracted as described in Chapter 4. As the spectra show only one single strong FMR resonance for these samples, this is a rather straightforward process.

### 6.3 Cobalt thin films

The samples CP1 and CP2 (cobalt on actuator) were prepared under identical conditions and showed nearly identical results. Therefore only the measurements for sample

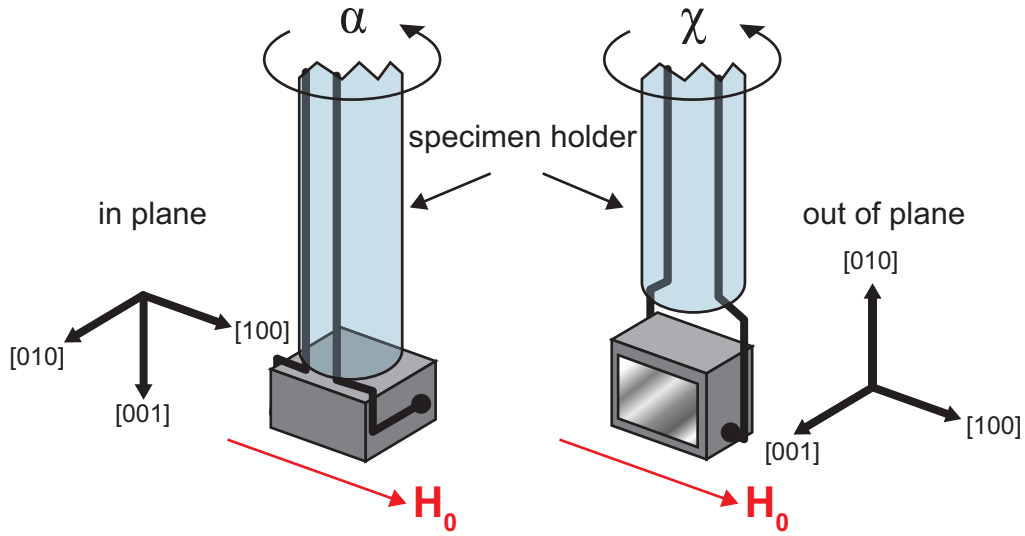


**Figure 6.3:** Schematic view of samples mounted for in-plane and out-of-plane measurements. Both configurations are shown at  $0^\circ$  orientation of the sample in the external magnetic field, showing the equivalency of both configurations for  $\alpha = \chi = 0^\circ$ .

CP1 will be discussed here.

### 6.3.1 In-plane FMR measurements

The angular dependence of the FMR resonance field is displayed in Fig. 6.4(a) for the in-plane rotation. CP1 shows a resonance field minimum at  $\mathbf{H}_0 \parallel [100]$  and a resonance field maximum at  $\mathbf{H}_0 \parallel [010]$  for all investigated actuator voltages. The observed shift of resonance field for  $V_{\text{Piezo}} = -30 \text{ V}$  to  $V_{\text{Piezo}} = +100 \text{ V}$  is  $\mu_0 H_{\text{res},[100],+100\text{V}} - \mu_0 H_{\text{res},[100],-30\text{V}} = \mu_0 \Delta H_{\text{res},[100]} = -4 \text{ mT}$  for  $\mathbf{H}_0 \parallel [100]$  and  $\mu_0 \Delta H_{\text{res},[010]} = 4 \text{ mT}$  for  $\mathbf{H}_0 \parallel [010]$ . The linewidth  $\mu_0 \Delta H_{\text{pp}}$  is shown in Fig. 6.4(b).  $\mu_0 \Delta H_{\text{pp}}$  changes less than 2 mT for different voltages and orientations.

### 6.3.2 Discussion

For each voltage  $V_{\text{Piezo}}$ , we estimate the error of the experimentally determined resonance field positions  $\mu_0 H_{\text{res}} = \mu_0 \frac{1}{2} (H_{\text{max}} - H_{\text{mix}})$  (cf. Fig. 4.3) caused by a variation of line shape. We assume that the damping is not influenced by the sample orientation in the magnetic field and thus the linewidth should remain constant for all orienta-

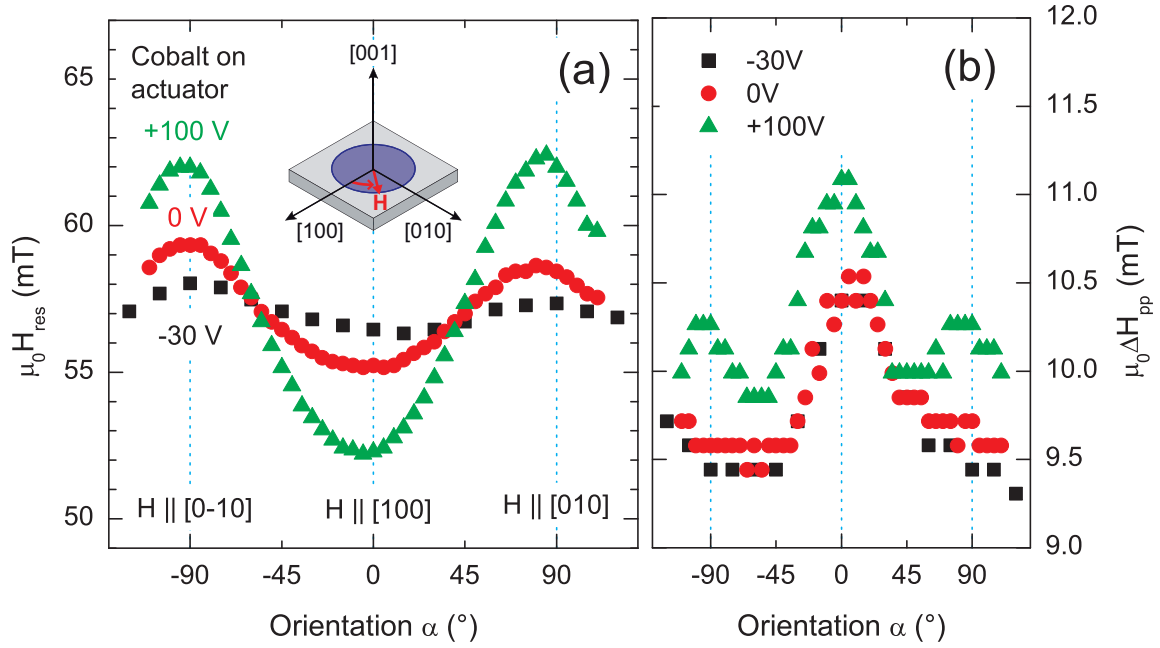


**Figure 6.4:** CP1 (cobalt on actuator) resonance fields as a function of in-plane rotation angle and actuator voltage at  $T = 300$  K (a) and corresponding linewidth (b).

tions. At any voltage  $V_{\text{Piezo}}$ , we now determine the standard deviation of the mean linewidth  $\sigma \langle \mu_0 \Delta H_{\text{pp}} \rangle$  for the complete in-plane rotation. As the linewidth change influences the resonance position for each single spectrum no more than  $\pm \frac{1}{2} \mu_0 \Delta H_{\text{pp}}$  the standard deviation of  $\mu_0 H_{\text{res}}$  due to a change in linewidth is given by

$$\sigma \mu_0 H_{\text{res}} = \pm \frac{1}{2} \sigma \langle \mu_0 \Delta H_{\text{pp}} \rangle . \quad (6.2)$$

Evaluation of (6.2) for the linewidths shown in Fig. 6.4(b) yields values below 0.2 mT for all voltages. This error is smaller than the symbol size in Fig. 6.4(a). A change in linewidth with actuator voltage can therefore clearly be ruled out as the origin of resonance field shifts. Further experimental errors that may influence resonance field positions, such as those caused by temperature or microwave frequency deviations between single measurements and the error caused by an imperfect sample mounting are not taken into account in Eq. (6.2). However, given the systematic evolution of resonance fields at all investigated voltages, they are ruled out as the cause of the resonance field shifts, but may explain the small mismatch of resonance fields at  $\mathbf{H}_0 \parallel [010]$  and  $\mathbf{H}_0 \parallel [0\bar{1}0]$  at all voltages.

An inversion of the angular anisotropy is clearly not observed for this sample. This is due to the in-plane uniaxial anisotropy already present at  $V_{\text{Piezo}} = 0 \text{ V}$  that is reduced, but can not be inverted by applying  $-30 \text{ V} \leq V_{\text{Piezo}} \leq 0 \text{ V}$  to the actuator. For  $V_{\text{Piezo}} > 0 \text{ V}$  the uniaxial anisotropy already present at  $V_{\text{Piezo}} = 0 \text{ V}$  becomes even more distinct (cf. Fig. 6.4(a)). As the voltage range of the actuator is  $-30 \text{ V} \leq V_{\text{Piezo}} \leq +150 \text{ V}$ , it is hence not possible to invert the magnetic anisotropy of our cobalt samples. Therefore the desired  $90^\circ$  switching of magnetization can not be achieved in these samples. No further investigation of the origin of the uniaxial anisotropy already present at  $V_{\text{Piezo}} = 0 \text{ V}$  was done. As this anisotropy was observed for both cobalt samples prepared under identical conditions, it may be caused by an anisotropic thermal expansion of the actuator during the evaporation process. Other possible explanations are the ordering of cobalt microcrystals or the exchange bias caused by antiferromagnetic cobalt oxide [87].

As a voltage dependent inversion of the in-plane magnetic anisotropy – mandatory for a switching of the equilibrium orientation of the magnetization by  $90^\circ$  – was clearly not observed for the cobalt samples, the voltage dependence of the angular anisotropy of the out-of-plane resonance fields was not investigated.

## 6.4 Nickel thin films

The samples NP2 and NP3 were prepared in the same fashion as the cobalt thin films on actuators. For both samples, the in-plane and the out-of-plane anisotropy of the ferromagnetic resonance field was determined.

### 6.4.1 In-plane FMR measurements

The in-plane FMR measurements of NP2 and NP3 show similar characteristics and are displayed in Figs. 6.5(a) and 6.6(a). Both show a clear inversion of anisotropy for  $V_{\text{Piezo}} = -30 \text{ V}$  with respect to  $V_{\text{Piezo}} = +20 \text{ V}$ . Compared to sample NP2, the in-plane resonance fields of sample NP3 are generally shifted to lower fields by approximately  $10 \text{ mT}$ . Furthermore, opposed to NP2, NP3 shows no uniaxial anisotropy for  $V_{\text{Piezo}} = 0 \text{ V}$ . The angular dependent change of linewidth is small for NP3 (cf. Fig. 6.6(b)), therefore the experimental error calculated from (6.2) is smaller than the symbol size and no error bars are displayed in Fig. 6.6(a). For NP2 the linewidth shows a distinct  $180^\circ$  periodic anisotropy shown in Fig. 6.5(b) but is not influenced by  $V_{\text{Piezo}}$ .

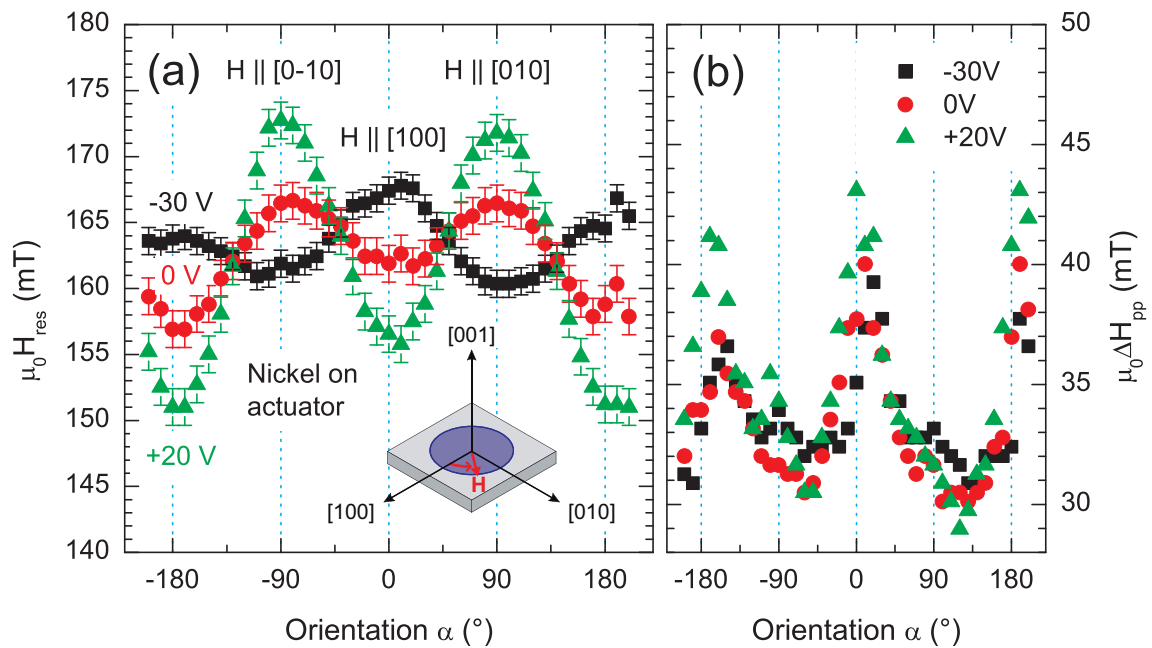


**Figure 6.5:** Resonance fields (a) and linewidth (b) for sample NP2 (nickel on actuator) with the magnetic field rotated in the (001) plane. The error bars in (a) are calculated according to Eq. (6.2).

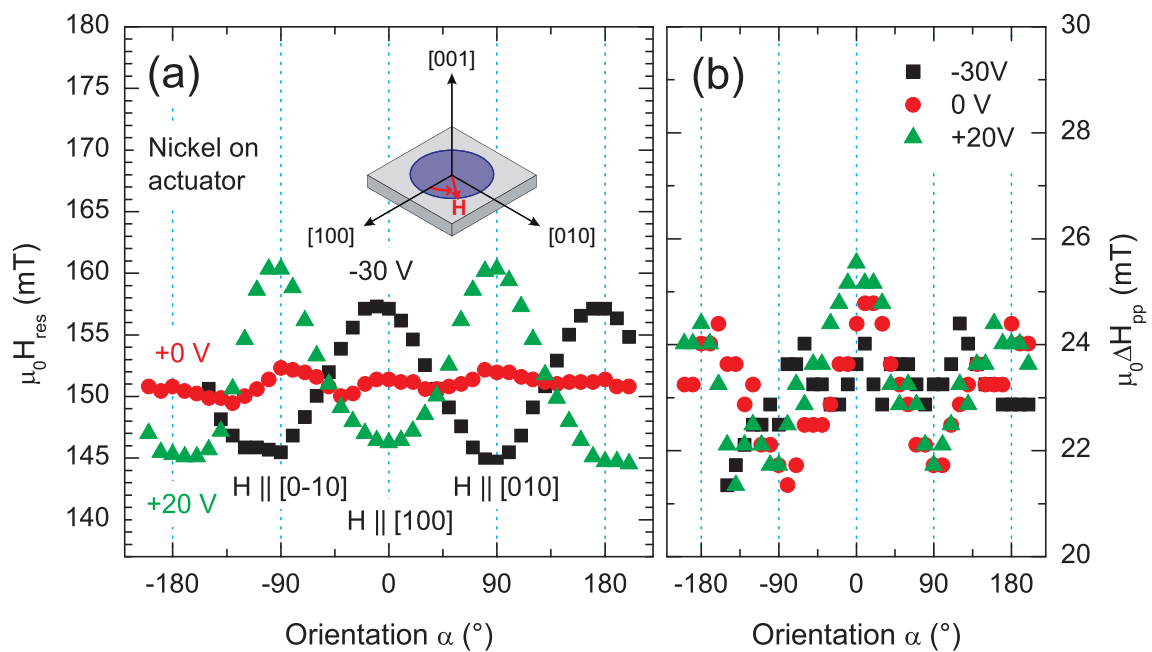


**Figure 6.6:** Resonance fields (a) and linewidth (b) for sample NP3 (nickel on actuator) with the magnetic field rotated in the (001) plane.

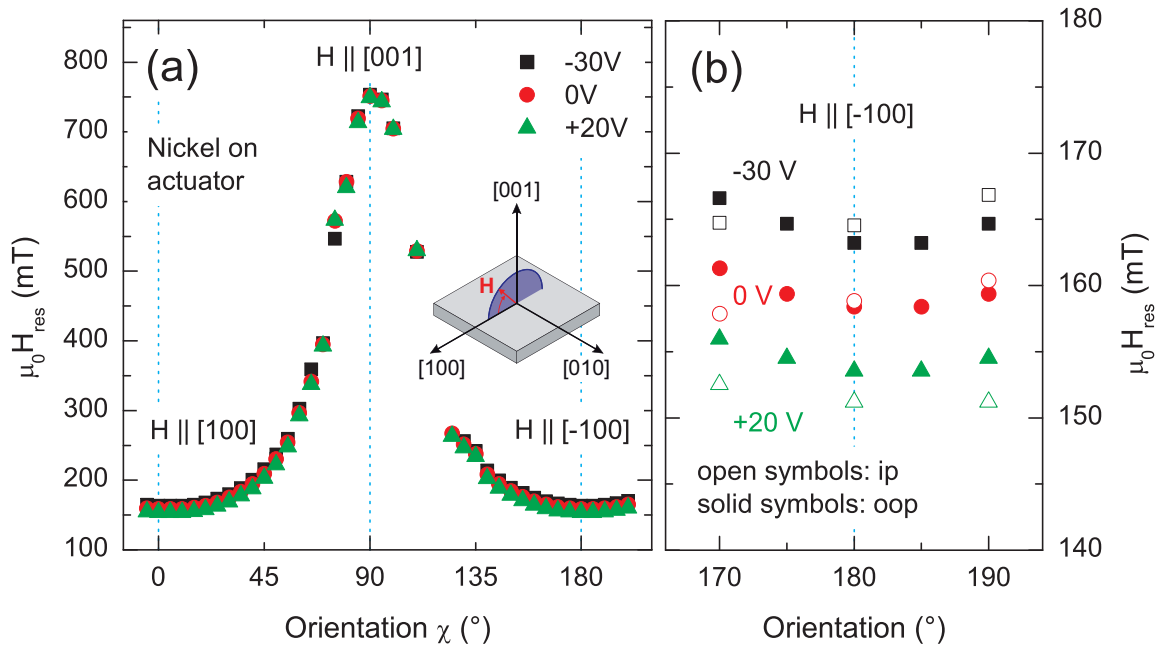


**Figure 6.7:** NP2 (nickel on actuator) resonance fields for the out-of-plane rotation (a) and comparison of in-plane and out-of-plane resonance fields (b).

### 6.4.2 Out-of-plane FMR measurements

The resonance fields obtained for the magnetic field rotation in the (010) plane are shown in Fig. 6.7(a) for sample NP2 and in Fig. 6.8(a) for sample NP3. The resonance fields for  $\mathbf{H}_0 \parallel [001]$  are  $\mu_0 H_{\text{res}} \approx 750$  mT for NP2 and  $\mu_0 H_{\text{res}} \approx 790$  mT for NP3 at all actuator voltages. Figs. 6.7(b) and 6.8(b) show a comparison of in-plane and out-of-plane measurements for  $\mathbf{H}_0 \parallel [\bar{1}00]$ . A good match of in-plane and out-of-plane resonance fields is observed for these nominally identical orientations of  $\mathbf{H}_0$ .

For sample NP3, the unsystematic shift of the resonance field for  $\mathbf{H}_0 \parallel [001]$  (cf. Fig. 6.8(a)) is caused by a change of sample mounting between measurements.

### 6.4.3 Linearity and reversibility of voltage dependence

To check for the linearity and reversibility of the  $V_{\text{Piezo}}$ -dependence of resonance fields, measurements at  $-30 \text{ V} \leq V_{\text{Piezo}} \leq +90 \text{ V}$  were carried out for  $\mathbf{H}_0 \parallel [100]$ ,  $\mathbf{H}_0 \parallel [010]$  (Fig. 6.9(a)) and  $\mathbf{H}_0 \parallel [001]$  (Fig. 6.9(b)). Fig. 6.9 shows a nearly linear shift of resonance fields for  $-30 \text{ V} \leq V_{\text{Piezo}} \leq +90 \text{ V}$  at all three investigated orientations of the external magnetic field. In Fig. 6.9(a), we show a comparison to the values

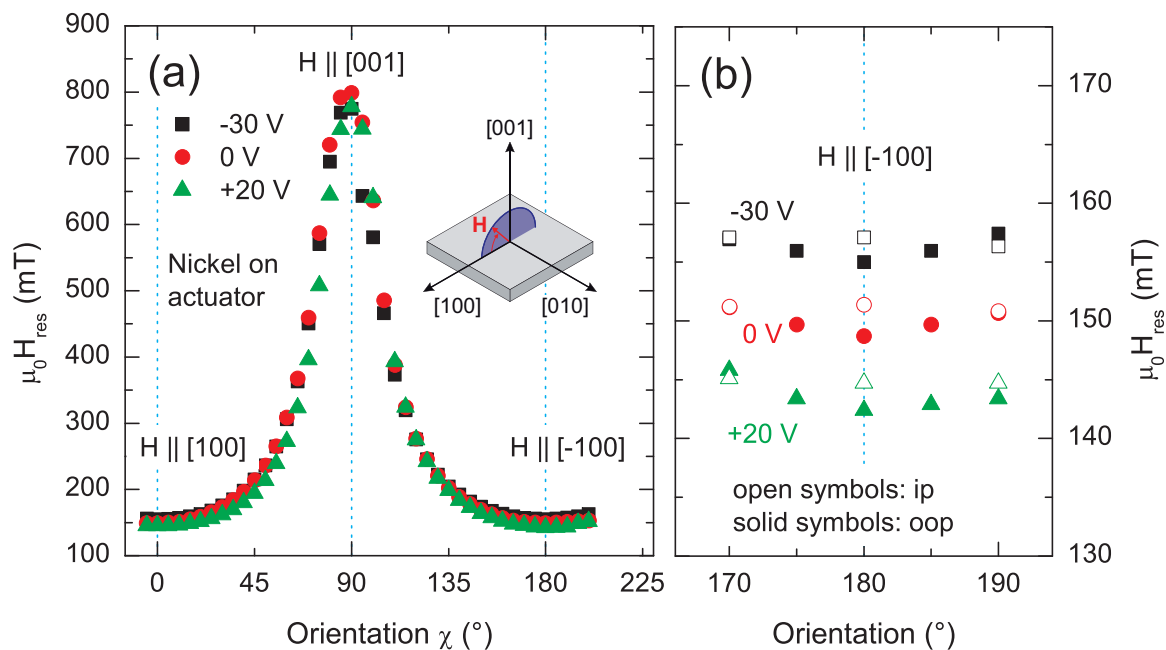


**Figure 6.8:** NP3 (nickel on actuator) resonance fields for the out-of-plane rotation (a) and comparison of in-plane and out-of-plane resonance fields (b).

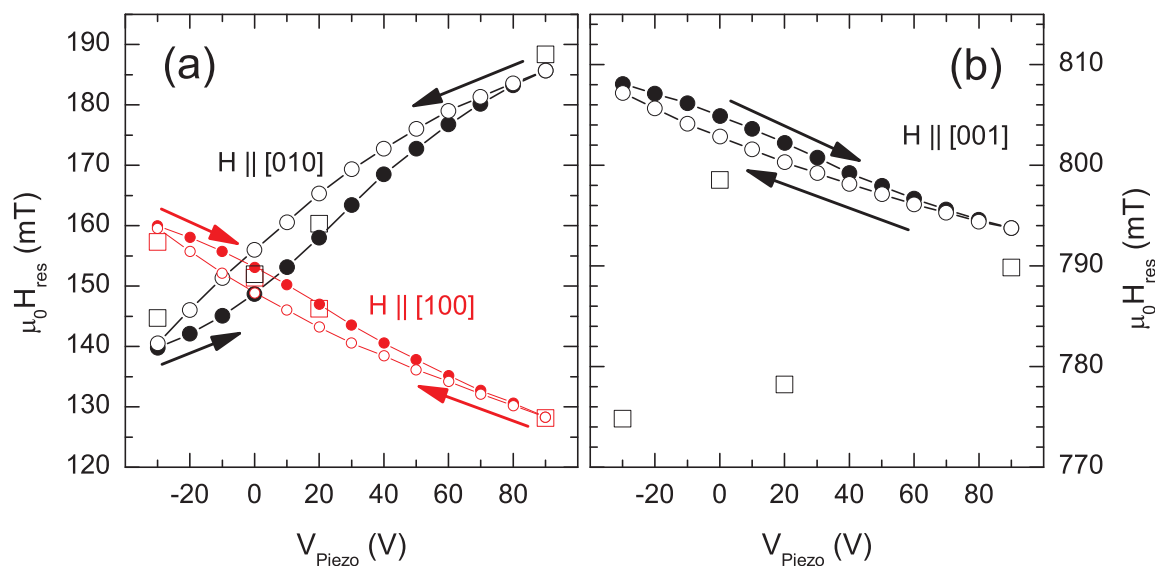


**Figure 6.9:** NP3 (nickel on actuator) resonance fields for selected orientations of  $H_0$ . The open squares correspond to the results presented in Fig. 6.6(a) and 6.8(a) (the lines are intended as guides to the eyes).

taken from the in-plane rotation (cf. Fig. 6.6(a)) that demonstrates the excellent reproducibility of our results. For  $\mathbf{H}_0 \parallel [001]$  (Fig. 6.9(b)), the resonance fields display a systematic linear dependence on actuator voltage as well, but they differ from the resonance fields obtained from the out-of-plane rotations (cf. Fig. 6.8(a)) at this orientation. This is very probably due to the already mentioned sample tilting during the rotation measurements. A small hysteresis of  $\mu_0 H_{\text{res}}(V_{\text{Piezo}})$  is observed, as the actuator elongation also exhibits hysteresis according to the actuator's data sheet [76].

#### 6.4.4 Discussion

The good match of in-plane and out-of-plane measurements at  $\mathbf{H}_0 \parallel [\bar{1}00]$  shows the equivalence of both in-plane and out-of-plane sample mountings at this orientation. We observe a clear inversion of resonance field anisotropy for both nickel samples upon the application of voltages in the range of  $-30 \text{ V} \leq V_{\text{Piezo}} \leq +20 \text{ V}$  to the actuator. This shows that we are able to invert the magnetic free energy density, which corresponds to a  $90^\circ$  switching of the magnetization. The measurement shown in Fig. 6.9 proves that the switching is fully reversible and the hysteresis of the actuator has no influence on the inversion of the magnetic free energy density for  $|V_{\text{Piezo}}| \geq 20 \text{ V}$ .

#### 6.4.5 Numerical simulations

In this Section, we phenomenologically evaluate the dependence of the magnetic anisotropy on the actuator voltage. Given the similar results for both nickel samples, only results for NP3 will be discussed in this Section. A free energy  $F_{\text{tot}}$  with a cubic and two uniaxial anisotropy terms is expected to be sufficient to describe the magnetic anisotropy:

$$\begin{aligned}
 F_{\text{tot}} = & -\mu_0 M H_0 (\sin \Theta \sin \Phi \sin \theta \sin \phi + \cos \Theta \cos \theta + \sin \Theta \cos \Phi \sin \theta \cos \phi) + \\
 & K_{\text{u,eff},[001]} \sin^2 \Theta \cos^2 \Phi + \\
 & K_{\text{u},[010]} \cos^2 \Theta + \\
 & \frac{1}{4} K_{\text{c1}} (\sin^2 (2\Theta) + \sin^4 \Theta \sin^2 (2\Phi)) .
 \end{aligned} \tag{6.3}$$

We iteratively adjust the anisotropy constants of  $F_{\text{tot}}$  until solving the ferromagnetic equation of motion yields resonance fields coinciding with the afore experimentally determined resonance fields. The anisotropy constants determined in this Section will

be compared to those expected from magnetoelastic theory in the next Section.

Numerically solving the ferromagnetic equation of motion given in (4.5) with  $F_{\text{tot}}$  from (6.3) yields four independent fitting parameters:  $K_{\text{c1}}/M_{\text{s}}$ ,  $K_{\text{u},[010]}/M_{\text{s}}$ ,  $K_{\text{u,eff},[001]}/M_{\text{s}}$  and the  $g$  factor. All FMR resonance fields obtained for sample NP3 can be fitted assuming only a change in  $K_{\text{u},[010]}$  and  $K_{\text{u,eff},[001]}$  while  $K_{\text{c1}}/M_{\text{s}} = 0.5 \text{ mT} = \text{const}$  and  $g = 2.15 = \text{const}$ . This  $g$  value is in good agreement with the value  $g = 2.185$  for bulk nickel (cf. Tab. 3.1). The saturation magnetization  $M_{\text{s}}$  is assumed to remain constant, and its absolute value does not effect the calculated anisotropy fields. Table 6.1 shows the anisotropy fields that were numerically determined. Fig. 6.10

$V_{\text{Piezo}}$ (V)	$\frac{K_{\text{u},[010]}}{M_{\text{s}}} \text{ (mT)}$	$\frac{K_{\text{u,eff},[001]}}{M_{\text{s}}} \text{ (mT)}$	$K_{\text{c1}} \text{ (mT)}$
-30	-3.4	238.6	-0.5
0	0.2	239.2	-0.5
+20	4.2	237.9	-0.5
+90	17.4	233.0	-0.5

**Table 6.1:** Anisotropy constants of NP3 (nickel on actuator) determined from numerical simulations.

shows a comparison of simulation and experimental data for the in-plane measurements and Fig. 6.11(a) shows the comparison of simulation and experimental data for the out-of-plane measurements. The anisotropy fields  $K_{\text{u},[010]}/M_{\text{s}}$  and  $K_{\text{u,eff},[001]}/M_{\text{s}}$  are plotted as a function of  $V_{\text{Piezo}}$  in Fig. 6.11(b).

The simulated resonance fields are in very good agreement with the measurements. This proves that the anisotropy terms in Eq. (6.3) are sufficient to describe the magnetic anisotropy of NP3 at all investigated actuator voltages. Fig. 6.11(b) shows the nearly linear change of  $K_{\text{u},[010]}$  with  $V_{\text{Piezo}}$  while the relative change of  $K_{\text{u,eff},[001]}$  remains small.

As the actuator-induced stress can be fully described by its influence on the uniaxial anisotropy constants  $K_{\text{u},[010]}$  and  $K_{\text{u,eff},[001]}$ , magnetoelastic theory can be applied to calculate the expected change in magnetic anisotropy as a function of actuator voltage. This is the goal of the following Section.

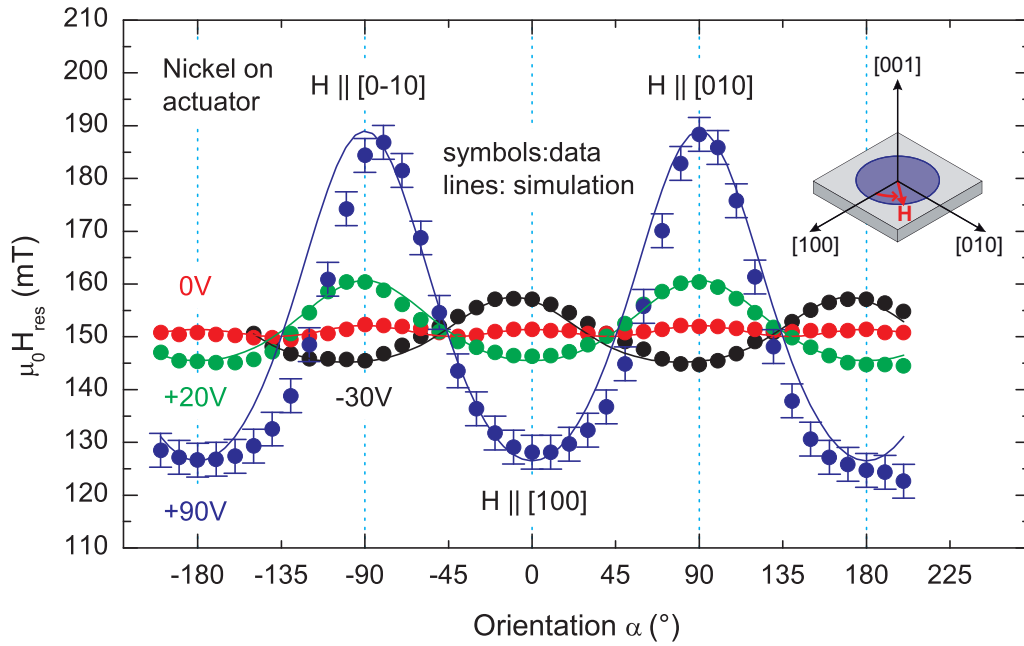


**Figure 6.10:** Numerical simulations of the FMR resonance fields (lines) with anisotropy constants taken from Tab. 6.1 and experimental data (symbols) for NP3 (nickel on actuator) with  $\mathbf{H}_0$  rotated in-plane.

## 6.5 Theoretical description

The actuator-induced stress affects the magnetization due to the magnetoelastic effect as described in Chapter 2. The lattice strain in the Ni thin film results in uniaxial contributions to its magnetic free energy density that can be calculated by magnetoelastic theory.

We assume that the strains in the Ni film vanish at an actuator voltage of  $V_{\text{Piezo}} = 0 \text{ V}$ . Hence, in this case, the magnetic free energy density given in Eq. (6.3) is appropriate to describe the system with the anisotropy constants at  $V_{\text{Piezo}} = 0 \text{ V}$  (cf. Tab. 6.1).

Upon the application of a voltage  $V_{\text{Piezo}} \neq 0 \text{ V}$ , the actuator induces two orthogonal in-plane strains  $\varepsilon_1$  and  $\varepsilon_2$  into the Ni film. The resulting magnetoelastic effect can be described by uniaxial contributions to the magnetic free energy density at  $V_{\text{Piezo}} = 0 \text{ V}$ . These uniaxial contributions are given by the magnetoelastic free energy density  $F_{\text{magel}}$ . We will now derive an expression for  $F_{\text{magel}}$  suitable to describe our system.

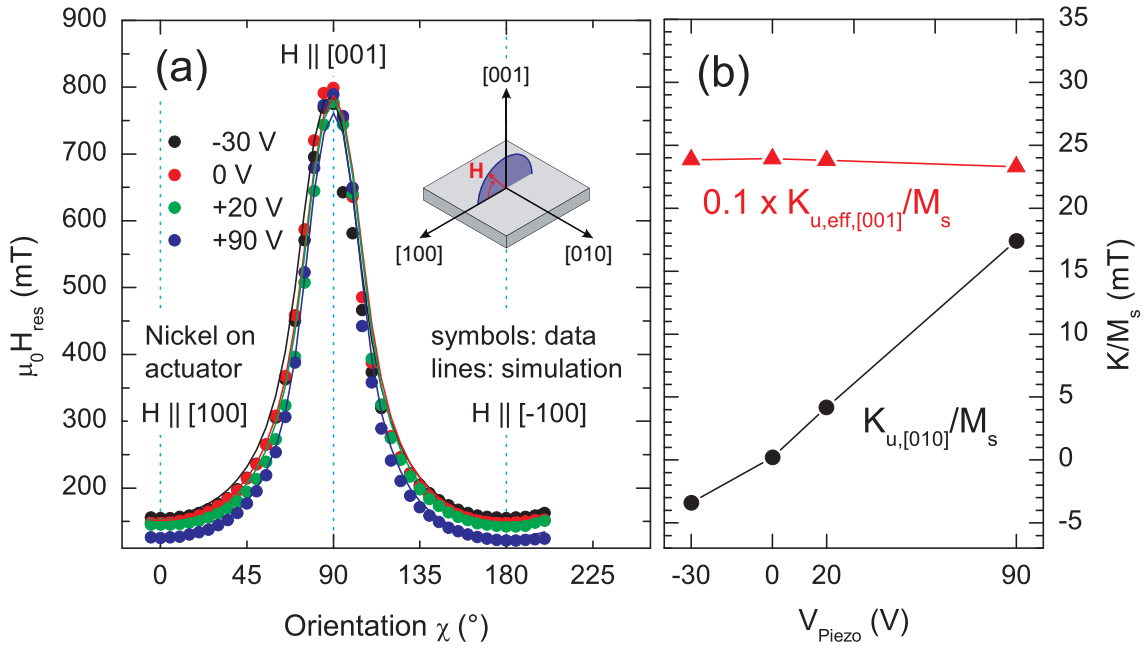


**Figure 6.11:** (a) NP3 (nickel on actuator) FMR resonance fields (symbols) and numerical simulations (lines) for the out-of-plane rotation. (b) NP3 anisotropy constants as a function of actuator voltage (the lines are guides to the eyes only).

To this end, we start from the general expression for  $F_{\text{magnet}}$  given in [29]:

$$F_{\text{magnet}} = \frac{3}{2} \bar{\lambda} (c_{12}^{\text{Ni}} - c_{11}^{\text{Ni}}) (\varepsilon_1 (\alpha_1^2 - 1/3) + \varepsilon_2 (\alpha_2^2 - 1/3) + \varepsilon_3 (\alpha_3^2 - 1/3)) . \quad (6.4)$$

This expression contains the averaged magnetostrictive constant  $\bar{\lambda}$  that will be defined later, as well as the elastic moduli  $c_{11}^{\text{Ni}}$  and  $c_{12}^{\text{Ni}}$  of Ni (cf. Tab. 3.1). Here,  $\alpha_i$  ( $i = 1, 2, 3$ ) denote the directional cosines of the magnetization. With respect to the coordinate system shown in Fig. 6.2(a) the directional cosines can be expressed by:

$$\begin{aligned} \alpha_1 &= \sin \Theta \sin \Phi \\ \alpha_2 &= \cos \Theta \\ \alpha_3 &= \sin \Theta \cos \Phi . \end{aligned} \quad (6.5)$$

In (6.4),  $\varepsilon_i$  ( $i = 1, 2, 3$ ) denote the strains along  $[100]$ ,  $[010]$  and  $[001]$ . Hence shear strains are neglected. This simplification is justified as the change in the magnetic

anisotropy of the Ni thin film as a function of actuator voltage was described by a change only in uniaxial anisotropies in the previous Section. The fact that our films are polycrystalline is accounted for by the introduction of the longitudinal averaged magnetostrictive constant [29]

$$\bar{\lambda} = \frac{2}{5}\lambda_{100} + \frac{3}{5}\lambda_{111} . \quad (6.6)$$

$\bar{\lambda}$  is calculated from the single cubic crystal magnetostrictive constants  $\lambda_{100}$  and  $\lambda_{111}$  by averaging the elongation  $\delta l/l$  in the direction  $(\beta_1, \beta_2, \beta_3)$

$$\begin{aligned} \frac{\delta l}{l} = & \frac{3}{2}\lambda_{100} \left( \alpha_1^2\beta_1^2 + \alpha_2^2\beta_2^2 + \alpha_3^2\beta_3^2 - \frac{1}{3} \right) \times \\ & 3\lambda_{111}(\alpha_1\alpha_2\beta_1\beta_2 + \alpha_2\alpha_3\beta_2\beta_3 + \alpha_3\alpha_1\beta_3\beta_1) , \end{aligned} \quad (6.7)$$

for different orientations  $\alpha_i$ , assuming  $\alpha_i = \beta_i$ . The values for  $\lambda_{100}$  and  $\lambda_{111}$  are taken from Tab. 3.1.

Using elastic theory, the strains  $\varepsilon_i$  can be described as a function of  $\varepsilon_2$  which is the strain component pointing along the actuator's main axis of elongation (see Fig. 6.2(a)). In Chapter 5, we showed a method of determining  $\varepsilon_3$  with HRXRD. This method is not applicable here, as our samples are not suited for lattice constant determinations by HRXRD because of the small film thickness and its polycrystalline structure. However, HRXRD is not necessary in the case of ferromagnetic thin films evaporated directly onto actuators, as these thin films do not influence the expansion of the actuator. Hence we can estimate  $\varepsilon_2$  by assuming a linear expansion of the actuator in the entire voltage range  $-30 \text{ V} \leq V_{\text{Piezo}} \leq +150 \text{ V}$  to

$$\varepsilon_2 = \frac{\delta L}{L} \frac{V_{\text{Piezo}}}{180 \text{ V}} , \quad (6.8)$$

with the nominal full stroke of the actuator  $\frac{\delta L}{L} = 0.13\%$  [76]. To determine  $\varepsilon_1$  and  $\varepsilon_3$ , we rely on continuum elastic theory [36], which was briefly introduced in Chapter 5 and which yields

$$\varepsilon_1 = -\nu^{\text{Piezo}}\varepsilon_2, \quad \varepsilon_3 = -\frac{C_{12}^{\text{Ni}}}{C_{11}^{\text{Ni}}}(\varepsilon_1 + \varepsilon_2) . \quad (6.9)$$

From the point of view of magnetic anisotropy, Equation (6.4) describes a superposition of three uniaxial anisotropies. The magnitude of these anisotropies is given by

the three uniaxial magnetoelastic anisotropy constants:

$$\begin{aligned} K_{\text{u,magel},[100]}^* &= \frac{3}{2}\bar{\lambda}(c_{12}^{\text{Ni}} - c_{11}^{\text{Ni}})\varepsilon_1 \\ K_{\text{u,magel},[010]}^* &= \frac{3}{2}\bar{\lambda}(c_{12}^{\text{Ni}} - c_{11}^{\text{Ni}})\varepsilon_2 \\ K_{\text{u,magel},[001]}^* &= \frac{3}{2}\bar{\lambda}(c_{12}^{\text{Ni}} - c_{11}^{\text{Ni}})\varepsilon_3 . \end{aligned} \quad (6.10)$$

As three orthogonal uniaxial anisotropies can always be expressed in terms of two orthogonal uniaxial anisotropies as shown in [56], we use:

$$\begin{aligned} K_{\text{u,magel},[100]} &= K_{\text{u,magel},[100]}^* - K_{\text{u,magel},[100]}^* = 0 \\ K_{\text{u,magel},[010]} &= K_{\text{u,magel},[010]}^* - K_{\text{u,magel},[100]}^* = \frac{3}{2}\bar{\lambda}(c_{12}^{\text{Ni}} - c_{11}^{\text{Ni}})(\varepsilon_2 - \varepsilon_1) \\ K_{\text{u,magel},[001]} &= K_{\text{u,magel},[001]}^* - K_{\text{u,magel},[100]}^* = \frac{3}{2}\bar{\lambda}(c_{12}^{\text{Ni}} - c_{11}^{\text{Ni}})(\varepsilon_3 - \varepsilon_1) \end{aligned} \quad (6.11)$$

in the following.

We thus finally obtain the magnetoelastic term:

$$\begin{aligned} F_{\text{magel}} &= K_{\text{u,magel},[001]} \sin^2 \Theta \cos^2 \Phi + K_{\text{u,magel},[010]} \cos^2 \Phi \\ &\quad - \frac{1}{2}\bar{\lambda}(c_{12}^{\text{Ni}} - c_{11}^{\text{Ni}})(\varepsilon_1 + \varepsilon_2 + \varepsilon_3) . \end{aligned} \quad (6.12)$$

Adding this term to the total free energy density (6.3), one finds

$$\begin{aligned} F_{\text{tot,magel}} &= F_{\text{stat}} + F_{\text{magel}} + F_{\text{u,eff},[001],0V} + F_{\text{u},[010],0V} + F_c \\ &= -\mu_0 M H_0 (\sin \Theta \sin \Phi \sin \theta \sin \phi + \cos \Theta \cos \theta + \sin \Theta \cos \Phi \sin \theta \cos \phi) + \\ &\quad (K_{\text{u,eff},[001],0V} + K_{\text{u,magel},[001]}) \sin^2 \Theta \cos^2 \Phi + \\ &\quad (K_{\text{u},[010],0V} + K_{\text{u,magel},[010]}) \cos^2 \Theta + \\ &\quad \frac{1}{4} K_{\text{cl}} (\sin^2 (2\Theta) + \sin^4 \Theta \sin^2 (2\Phi)) - \\ &\quad \frac{1}{2}\bar{\lambda}(c_{12}^{\text{Ni}} - c_{11}^{\text{Ni}})(\varepsilon_1 + \varepsilon_2 + \varepsilon_3) . \end{aligned} \quad (6.13)$$

We can now analytically calculate the resonance fields expected for  $\mathbf{H}_0 \parallel [100]$ ,  $\mathbf{H}_0 \parallel [010]$  and  $\mathbf{H}_0 \parallel [001]$ . Analytical expressions for  $\mu_0 H_{\text{res}}$  at these orientations are given in Chapter 4 for  $F_{\text{tot}}$  without the magnetoelastic contribution  $F_{\text{magel}}$ . For  $F_{\text{tot,magel}}$  we obtain:

- $\mathbf{H}_0 \parallel [100]$  ( $\phi = 90^\circ$ ,  $\theta = 90^\circ$ ):

$$\begin{aligned} \mu_0 H_{\text{res}} &= -\frac{K_{\text{u,eff},[001],0\text{V}} + K_{\text{u,magel},[001]}}{M} - \frac{K_{\text{u},[010],0\text{V}} + K_{\text{u,magel},[010]}}{M} - 2\frac{K_{\text{c1}}}{M} \\ &+ \sqrt{\left(\frac{K_{\text{u,eff},[001],0\text{V}} + K_{\text{u,magel},[001]}}{M} - \frac{K_{\text{u},[010],0\text{V}} + K_{\text{u,magel},[010]}}{M}\right)^2 + \left(\frac{\omega}{\gamma}\right)^2} \end{aligned} \quad (6.14)$$

- $\mathbf{H}_0 \parallel [010]$  ( $\phi = 90^\circ$ ,  $\theta = 0^\circ$ ):

$$\begin{aligned} \mu_0 H_{\text{res}} &= -\frac{K_{\text{u,eff},[001],0\text{V}} + K_{\text{u,magel},[001]}}{M} + 2\frac{K_{\text{u},[010],0\text{V}} + K_{\text{u,magel},[010]}}{M} - 2\frac{K_{\text{c1}}}{M} \\ &+ \sqrt{\left(\frac{K_{\text{u,eff},[001],0\text{V}} + K_{\text{u,magel},[001]}}{M}\right)^2 + \left(\frac{\omega}{\gamma}\right)^2} \end{aligned} \quad (6.15)$$

- $\mathbf{H}_0 \parallel [001]$  ( $\phi = 0^\circ$ ):

$$\begin{aligned} \mu_0 H_{\text{res}} &= 2\frac{K_{\text{u,eff},[001],0\text{V}} + K_{\text{u,magel},[001]}}{M} - \frac{K_{\text{u},[010],0\text{V}} + K_{\text{u,magel},[010]}}{M} - 2\frac{K_{\text{c1}}}{M} \\ &+ \sqrt{\left(\frac{K_{\text{u},[010],0\text{V}} + K_{\text{u,magel},[010]}}{M}\right)^2 + \left(\frac{\omega}{\gamma}\right)^2} \end{aligned} \quad (6.16)$$

Using this set of expressions we can now calculate the ferromagnetic resonance fields expected from magnetoelastic theory and compare them to our measurements. This will be done for  $\mathbf{H}_0 \parallel [100]$  and  $\mathbf{H}_0 \parallel [010]$ .

The unstrained anisotropy constants  $K_{\text{u,eff},[001],0\text{V}}$ ,  $K_{\text{u},[010],0\text{V}}$  and  $K_{\text{u,magel},[010]}$  are given by those displayed in Tab. 6.1 at  $V_{\text{Piezo}}=0\text{ V}$ . The magnetoelastic anisotropy contributions are calculated using Eq. (6.11) and the resonance fields are now calculated with Eqs. (6.14) and (6.15). A comparison of the resonance fields thus obtained from magnetoelastic theory (incorporating the bulk saturation magnetization  $M_s$  taken from Tab. 3.1) to the measured ones is displayed in Fig. 6.12. For  $\mathbf{H}_0 \parallel [100]$  the calculated resonance fields show a very good agreement to the measured ones. The same applies to  $\mathbf{H}_0 \parallel [010]$  within  $|V_{\text{Piezo}}| \leq 30\text{ V}$ . We observe a small deviation of the measured resonance fields from those expected from magnetoelastic theory for  $|V_{\text{Piezo}}| > 30\text{ V}$  that will be discussed later.

Finally, we address the free energy surfaces to show that magnetoelastic theory is

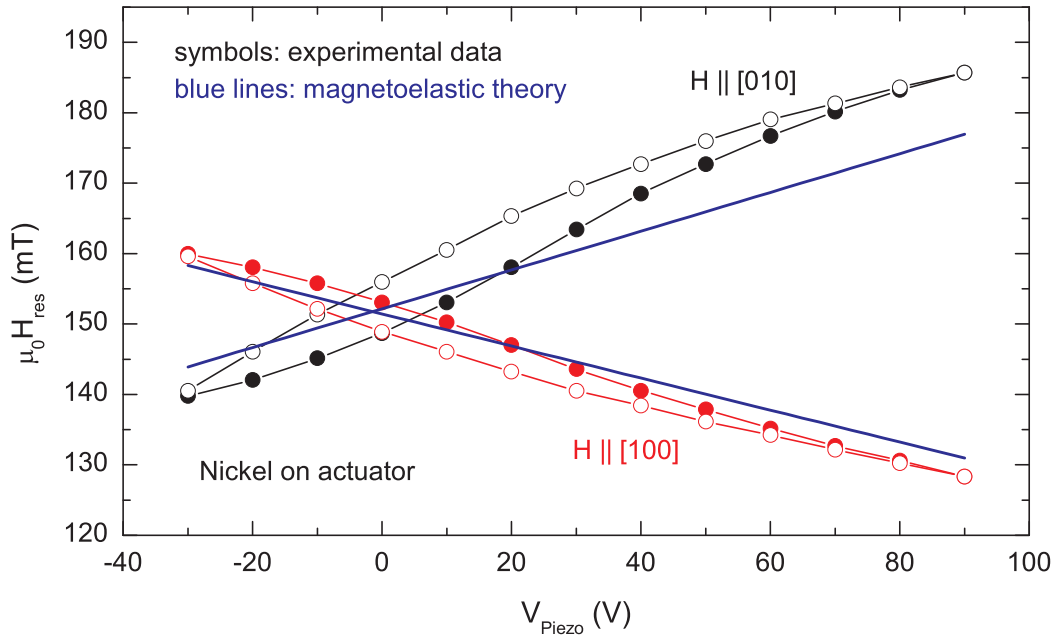


**Figure 6.12:** Experimentally determined FMR resonance fields of sample NP3 (symbols) in comparison to the resonance fields calculated from magnetoelastic theory (blue lines) as a function of the actuator voltage. Full symbols correspond to increasing voltage, open symbols to decreasing voltage (the thin lines connecting the symbols are guides to the eyes only).

appropriate to describe the observed magnetic anisotropy as a function of actuator voltage.

The free energy  $F_{\text{tot}}$  (cf. Eq. (6.3)) is calculated with the phenomenologically determined anisotropy constants listed in Tab. 6.1 and is compared to the free energy  $F_{\text{tot,magel}}$  (cf. Eq. (6.13)) obtained from magnetoelastic theory as described above. The free energy contours in the (001) plane thus obtained for different actuator voltages at zero external magnetic field are displayed in Fig. 6.13.

As one can see from Figs. 6.12 and 6.13, magnetoelastic theory yields results for both resonance fields and free energy that qualitatively closely represent the measured resonance fields and phenomenologically obtained free energy surfaces.

The reasons for the small deviation of magnetoelastic theory and measurement were not investigated in detail. We can only speculate that the quantitative deviations of magnetoelastic theory from the measurement results may be due to a deviation of the Poisson ratio  $\nu^{\text{Piezo}}$  from the specified value  $\nu^{\text{Piezo}} = 0.45$ . This deviation can be caused by a non-uniform strain transmission through the polymer layer. Perfect

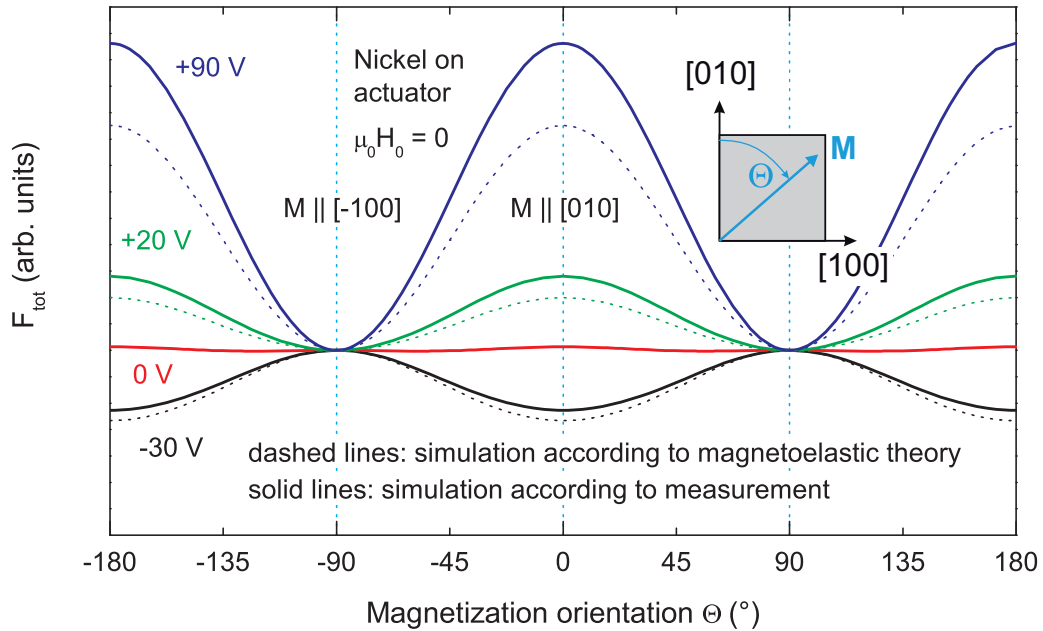


**Figure 6.13:** Section of the NP3 (nickel on actuator) free Energy surfaces in the (001) plane. Solid lines show the free energies (cf. Eq. (6.3)) calculated with the phenomenological anisotropy constants from Tab. 6.1 and dashed lines show the free energies calculated from magnetoelastic theory (cf. Eq. (6.13)).

agreement of magnetoelastic theory and experiment is achieved, if  $\nu^{\text{Piezo}}$  is varied from  $\nu^{\text{Piezo}} = 0.45$  to  $\nu^{\text{Piezo}} = 1$  as a function of actuator voltage.

## 6.6 Manipulating the magnetization switching behavior with external magnetic fields

In the previous Sections, we showed that we are able to reversibly invert the in-plane magnetic anisotropy of our samples. In this Section, the switching of the magnetization will be visualized by free energy calculations for various external magnetic field strengths and orientations.

The simple case of vanishing magnetic field is displayed in Fig. 6.13. The comparison of positive and negative actuator voltages shows the shift of the free energy minimum from  $[100]$  to  $[010]$  if the actuator voltage is changed from positive to negative values. Assuming that  $\mathbf{M}$  stays in a minimum of the free energy in equilibrium, this suggests that a  $90^\circ$  switching of magnetization orientation should be possible by changing  $V_{\text{Piezo}}$

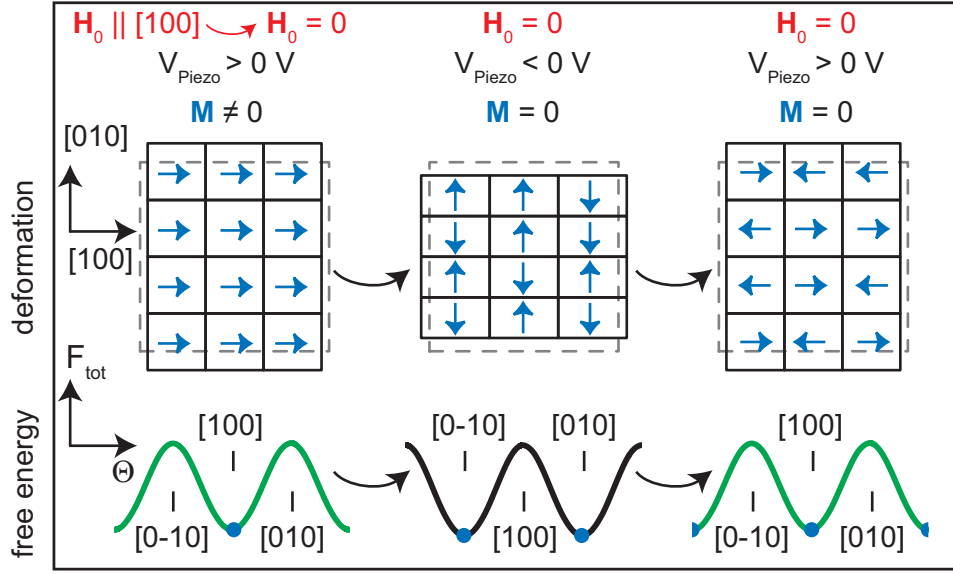


**Figure 6.14:** For vanishing magnetic field, actuator voltage polarity change causes an irreversible demagnetization process in a sample fully magnetized along  $[100]$ . The dashed contours show a top view of the unstrained sample at  $V_{\text{Piezo}} = 0 \text{ V}$ . Magnetization orientation in a given sample area is depicted by blue arrows, and possible equilibrium orientations of  $\mathbf{M}$  are shown as blue dots in the free energy.

alone. However, without the application of an external magnetic field, all minima of the free energy are degenerate. This means that the magnetization orientations  $\Theta$  and  $\Theta + 180^\circ$  are equivalent. This is an obvious result of the fact that for  $\mu_0 H_0 = 0$ ,  $F_{\text{tot,magel}}$  contains only cubic and uniaxial contributions that are both  $180^\circ$  periodic.

As we now argue, in vanishing external magnetic field, this results in the demagnetization of a ferromagnetic thin film upon changing the polarity of  $V_{\text{Piezo}}$ . As illustrated in Fig. 6.14, we start with a fully ordered state, chosen to be  $\mathbf{M} \parallel [100]$  due to an external magnetic field  $\mu_0 \mathbf{H}_0 \parallel [100]$  without loss of generality. The magnetic field is now turned off, resulting in degenerate minima in the free energy. However, due to the ferromagnetic hysteresis, the macroscopic magnetization remains oriented along  $[100]$ . If we now change the actuator voltage polarity and the anisotropy of the free energy is hence reversed, demagnetization will occur as the magnetization of each domain switches to any one of the degenerate free energy minima with the same probability (in this simple model, interactions between domains are neglected).

This decay of magnetization into domains can easily be avoided by the application of a small, but finite, static external magnetic field  $\mu_0 \mathbf{H}_0$ . In respect to the contributions

to the free energy  $F_{\text{tot}}$ , the external magnetic field influences only the Zeemann term  $F_{\text{stat}}$ . As shown in Section 2.3.1 of Chapter 2, an external magnetic field causes a unidirectional contribution to the free energy with the minimum in the direction of  $\mu_0 \mathbf{H}_0$ . The degeneracy of free energy minima can hence be removed if the magnitude and direction of  $\mu_0 \mathbf{H}_0$  are chosen appropriately.

This is illustrated in a three dimensional plot of the switching angle

$$\Delta\Theta = \Delta\Theta(\theta, H, \Phi = \pi/2, \phi = \pi/2) \quad (6.17)$$

of magnetization as a function of the external magnetic field's orientation  $\theta$  and magnitude  $\mu_0 H_0$  in Figs. 6.15(a) and 6.15(b). In the numerical calculations of  $\Delta\Theta$  we assumed that the external magnetic field and thus the magnetization remain in the sample plane ( $\phi = \Phi = \pi/2$ ). We simulate the switching of the magnetization by numerically<sup>2</sup> minimizing  $F_{\text{tot}}(\theta, H)$  for two different actuator voltages  $V_{\text{Piezo}} \in \{V_1, V_2\}$ . This is done by using the anisotropy constants listed in Tab. 6.1 and the free energy defined in Eq. 6.3. This yields the equilibrium orientation  $\Theta_0$  of  $\mathbf{M}$  for both  $V_{\text{Piezo}} = V_1$  and  $V_{\text{Piezo}} = V_2$  so that  $\Delta\Theta = |\Theta_{0,V_1} - \Theta_{0,V_2}|$  can be calculated. Figures 6.15(a) and 6.15(b) show the achievable switching angle  $\Delta\Theta$  as a function of magnitude and orientation of the external magnetic field  $\mu_0 \mathbf{H}_0$  for  $V_{\text{Piezo}} \in \{+20 \text{ V}, -30 \text{ V}\}$  and  $V_{\text{Piezo}} \in \{+90 \text{ V}, -30 \text{ V}\}$ , respectively. One can clearly see the dependence of  $\Delta\Theta$  on the voltages chosen. As the anisotropy constants evolve nearly linearly with actuator voltage as shown in Fig. 6.11(b), it is generally desirable to apply as high voltages as possible to achieve large  $\Delta\Theta$  in a given external magnetic field. The optimal orientation of the sample in the magnetic field is dependent on  $V_1$  and  $V_2$  as well. For  $\mu_0 H_0 = 50 \text{ mT}$  the optimal magnetic field orientation  $\theta$  is approximately  $\theta = 30^\circ$  if  $V_{\text{Piezo}}$  is alternated from  $V_{\text{Piezo}} = +90 \text{ V}$  to  $V_{\text{Piezo}} = -30 \text{ V}$  (cf. Fig. 6.15(b)) and approximately  $\theta = 45^\circ$  if  $V_{\text{Piezo}}$  is alternated from  $V_{\text{Piezo}} = +20 \text{ V}$  to  $V_{\text{Piezo}} = -30 \text{ V}$  (cf. Fig. 6.15(a)).

For the simplest and most application relevant case of applying an oscillating voltage  $\pm V_{\text{Piezo}}$  to the actuator, we finally show some exemplary free energy surfaces calculated from magnetoelastic theory for different, fixed magnetic field orientations and magnitudes (cf. Fig. 6.16). The orientation  $\theta$  of the magnetic field with respect to the sample is numerically optimized to obtain the largest possible magnetization switching angle  $\Delta\Theta$  in each case. Magnetoelastic theory thus allows to calculate the

---

<sup>2</sup>All numerical calculations performed in Maplesoft Maple 9.

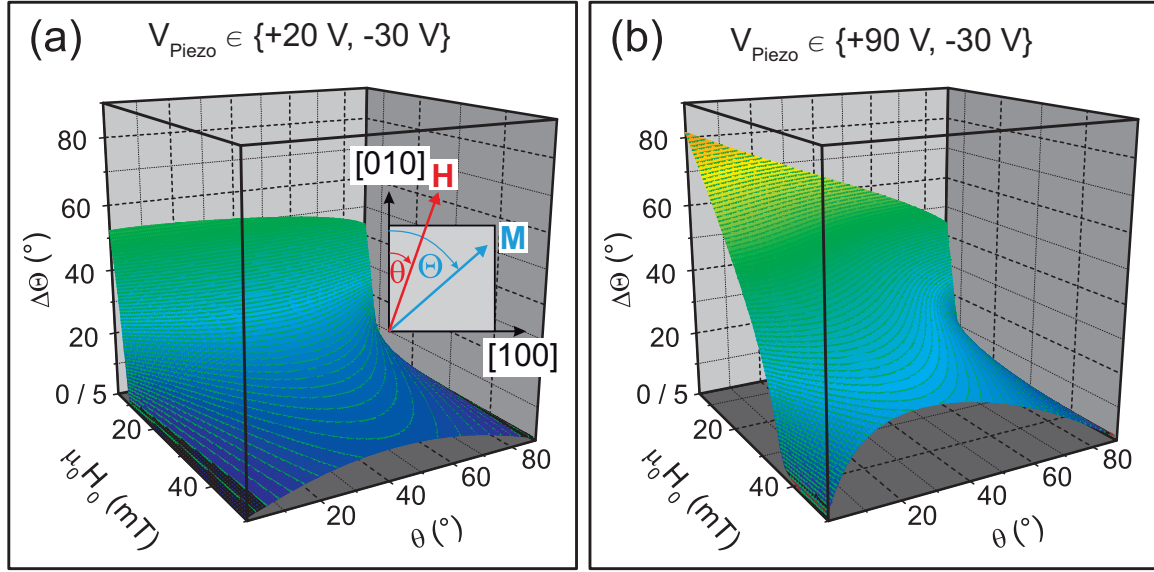


**Figure 6.15:** Magnetization switching angle  $\Delta\Theta$  as a function of the magnitude  $\mu_0H_0$  and the orientation  $\theta$  of the external magnetic field. (a)  $\Delta\Theta$  for  $V_{\text{Piezo}} \in \{+20 \text{ V}, -30 \text{ V}\}$ . (b)  $\Delta\Theta$  for  $V_{\text{Piezo}} \in \{+90 \text{ V}, -30 \text{ V}\}$ .

optimal external magnetic field magnitude and orientation for a desired switching angle  $\Delta\Theta$  and actuator voltages.

For an external magnetic field with magnitude  $\mu_0H = 1 \text{ mT}$  thus a magnetization switching of  $\Delta\Theta \approx 80^\circ$  is expected if an AC voltage  $V_{\text{Piezo}} = \pm 30 \text{ V}$  is applied to the actuator (cf. Fig. 6.16). We now estimate whether a magnetic field of this magnitude is sufficient to remove the degeneracy of the free energy density of the Ni film at  $V_{\text{Piezo}} = 30 \text{ V}$  at room temperature. If  $\mu_0H = 1 \text{ mT}$  is applied at the optimal orientation ( $\theta = 9^\circ, \phi = 90^\circ$ ) we can calculate

$$\begin{aligned} F_{\text{tot, magel, diff}} &= |F_{\text{tot, magel}}(M, H, \Theta_1, 90^\circ, 9^\circ, 90^\circ) - F_{\text{tot, magel}}(M, H, \Theta_2, 90^\circ, 9^\circ, 90^\circ)| \\ &\approx 130 \text{ N/m}^2, \end{aligned} \quad (6.18)$$

where  $\Theta_1$  and  $\Theta_2$  are the two minima of  $F_{\text{tot, magel}}$  at  $V_{\text{Piezo}} = 30 \text{ V}$ .  $F_{\text{tot, magel, diff}}$  needs to be larger than the thermal energy density  $E_T = k_B T / V_{\text{film}}$  within the volume  $V_{\text{film}} = 4 \times 10^{-13} \text{ m}^3$  of the Ni thin film. At  $T = 300 \text{ K}$ , the thermal energy density is  $E_T = 1 \times 10^{-8} \text{ N/m}^2$ . Thus, in this simple estimation, the degeneracy is easily removed by a magnetic field  $\mu_0H = 1 \text{ mT}$ .

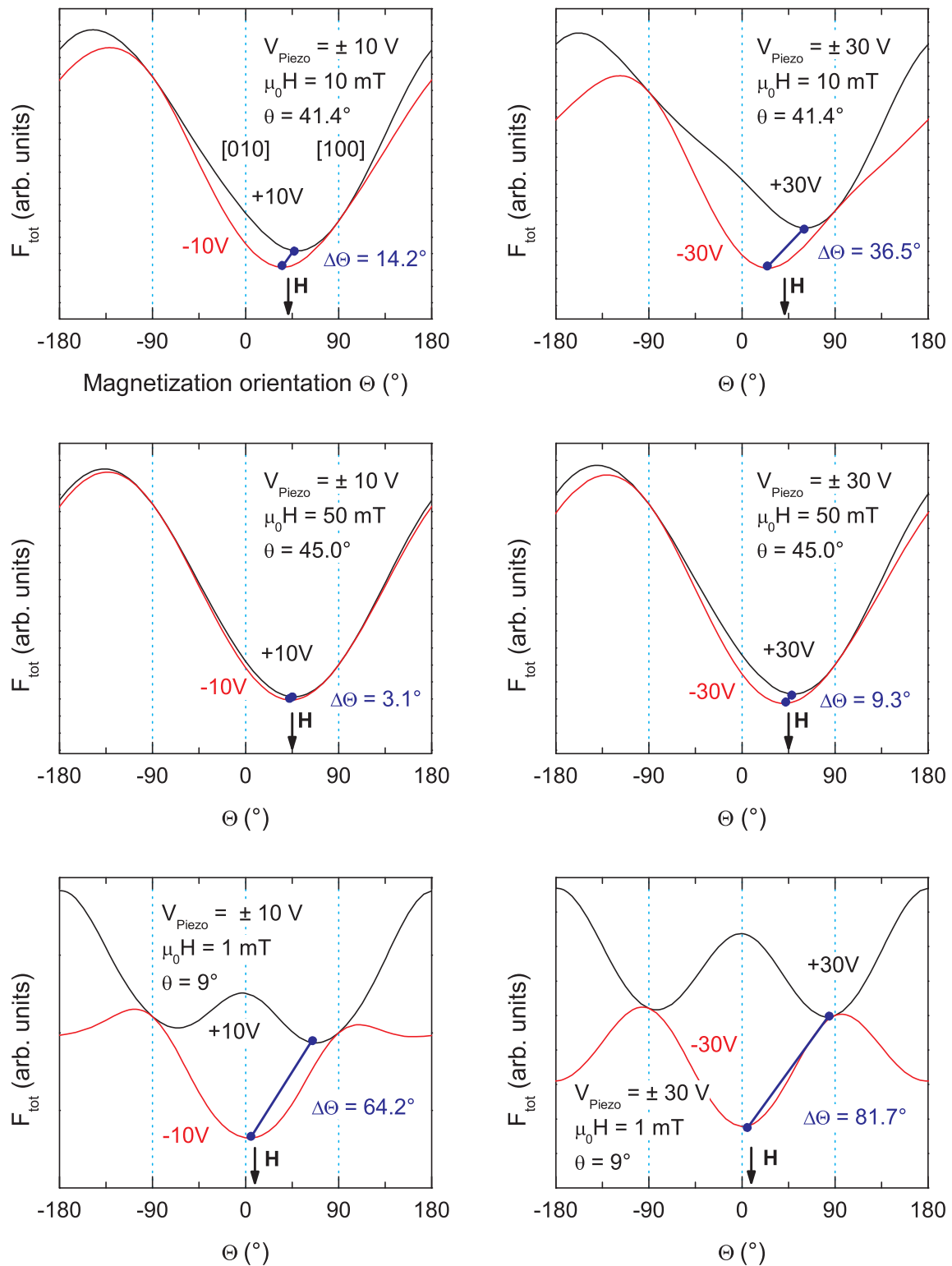


**Figure 6.16:** Free energy contours in the (001) plane for sample NP3 (nickel on actuator). Magnetoelastic theory yields the maximum achievable switching angle  $\Delta\Theta$  of the magnetization for selected actuator voltages and external magnetic field magnitudes.

## 6.7 Application: Piezomodulated ferromagnetic resonance

To achieve optimal sensitivity, conventional electron paramagnetic and ferromagnetic resonance setups usually take advantage of lock-in techniques (cf. Chapter 4). Usually magnetic field modulation is used, as it is technologically easy to realize, but other modulation parameters such as microwave frequency modulation are possible as well. In this Section, we will use voltage-strain controlled magnetic anisotropy as the modulation parameter.

A technique that replaces the magnetic field modulation by strain modulation was originally developed by Collins et al. [88] in 1972 for ESR spectroscopy. A setup for strain-modulated ESR measurements (SMESR) is described in [89]. The technique was adapted by Henning and den Boef [90] in 1978 for FMR. The latter work introduced the term strain-modulated ferromagnetic resonance (SMFMR) for the technique. SMFMR is used to determine magnetostrictive constants at high precision [91, 92] and is hence mentioned in review articles on the topic of magnetostriction [93, 94].

However, SMFMR requires a specifically designed microwave cavity as the stress is exerted by a complex sample holder. A further drawback so far was the inability to measure magnetic anisotropy with SMFMR, as the sample holders could not be rotated in the magnetic field. These disadvantages are resolved by piezomodulated ferromagnetic resonance (PMFMR), in which the stress is exerted by an actuator attached to the sample that can easily be installed and rotated in a standard microwave cavity.

### 6.7.1 Modulation parameters

The key to the lock-in measurement technique is the periodic modulation of one measurement parameter. In conventional FMR,  $\mu_0 \mathbf{H}_0$  is modulated by a parallel AC magnetic field  $\mu_0 \mathbf{H}_{\text{mod}}$  of much smaller magnitude (all conventional FMR measurements shown here use  $\mu_0 H_{\text{mod}} = 3.2 \text{ mT}$ ). This modulation results in the output signal  $V_{\text{sig,mod}}(\mu_0 H_0)$  defined in Eq. (4.14).

In PMFMR, we no longer use magnetic field modulation, but rather apply an AC voltage to the actuator. The AC voltage is characterized by the modulation frequency  $\nu_{\text{pmod}}$  and peak-to-peak amplitude  $V_{\text{Piezo}}^{\text{PP}}$  that will be referred to as modulation ampli-

tude, though strictly speaking the modulation amplitude is the shift of resonance field observed for the two extreme values of the sinusoidal actuator voltage  $V_{\text{Piezo}}$ . As this shift can only be approximately calculated with magnetoelastic theory (or measured by conventional FMR, which is not feasible for very small modulation amplitudes) we stick to the exactly known peak-to-peak voltage  $V_{\text{Piezo}}^{\text{PP}}$  to quantify the modulation amplitude.

Due to the magnetoelastic effect, the application of an AC voltage to the actuator results in a periodic shift of the FMR resonance field  $\mu_0 H_{\text{res}}$ . This is different from conventional magnetic field modulation, where  $\mu_0 H_{\text{res}}$  is constant and the magnetic field is varied sinusoidally. This difference in modulation leads to two important differences between PMFMR and conventional FMR. Firstly, the PMFMR modulation does not affect every spin resonance signal present in the cavity as only signals magnetoelastically coupled to the actuator are modulated. This results in the elimination of any spin resonance signal detectable in conventional FMR, the resonance position of which is independent of the actuator's elongation. Secondly, due to the magnetic anisotropy, the FMR resonance field shift due to the AC modulation is dependent on the orientation of the sample in the external magnetic field. This is schematically shown in Fig. 6.17 and will be referred to as anisotropic signal modulation.

## 6.7.2 PMFMR experiments

We chose to exemplarily investigate the sample CP1 (cobalt on actuator) with PMFMR because it showed the best signal-to-noise ratio and smallest linewidth of all samples in the FMR measurements. Moreover, as evident from Fig. 6.17, a voltage-induced inversion of the magnetic anisotropy is *not* required for PMFMR. The sample is installed in the in-plane configuration as discussed above. The AC modulation voltage with peak-to-peak amplitude  $V_{\text{Piezo}}^{\text{PP}}$  at a frequency of  $\nu_{\text{pmod}}$  is provided by a Hewlett Packard HP3245A universal source which also provides the reference frequency signal for the lock-in amplifier. Due to a large pickup signal proportional to  $V_{\text{Piezo}}$  superimposed on the detector diode signal  $V_{\text{FMR}}$ , the difference signal  $V_{\text{FMR}} - \lambda V_{\text{Piezo}}$  ( $0 < \lambda < 1$ ) is investigated. This is experimentally realized by scaling the modulation voltage  $V_{\text{Piezo}}$  with a phase retaining adjustable voltage divider before connecting  $\lambda V_{\text{Piezo}}$  to the  $B$  input of the lock-in amplifier, with the resonance signal  $V_{\text{FMR}}$  connected to the  $A$  input. Now the lock-in's  $A - B$  input mode is used which results in the subtraction of a signal proportional to  $V_{\text{Piezo}}$  from the resonance signal to compensate for the pick

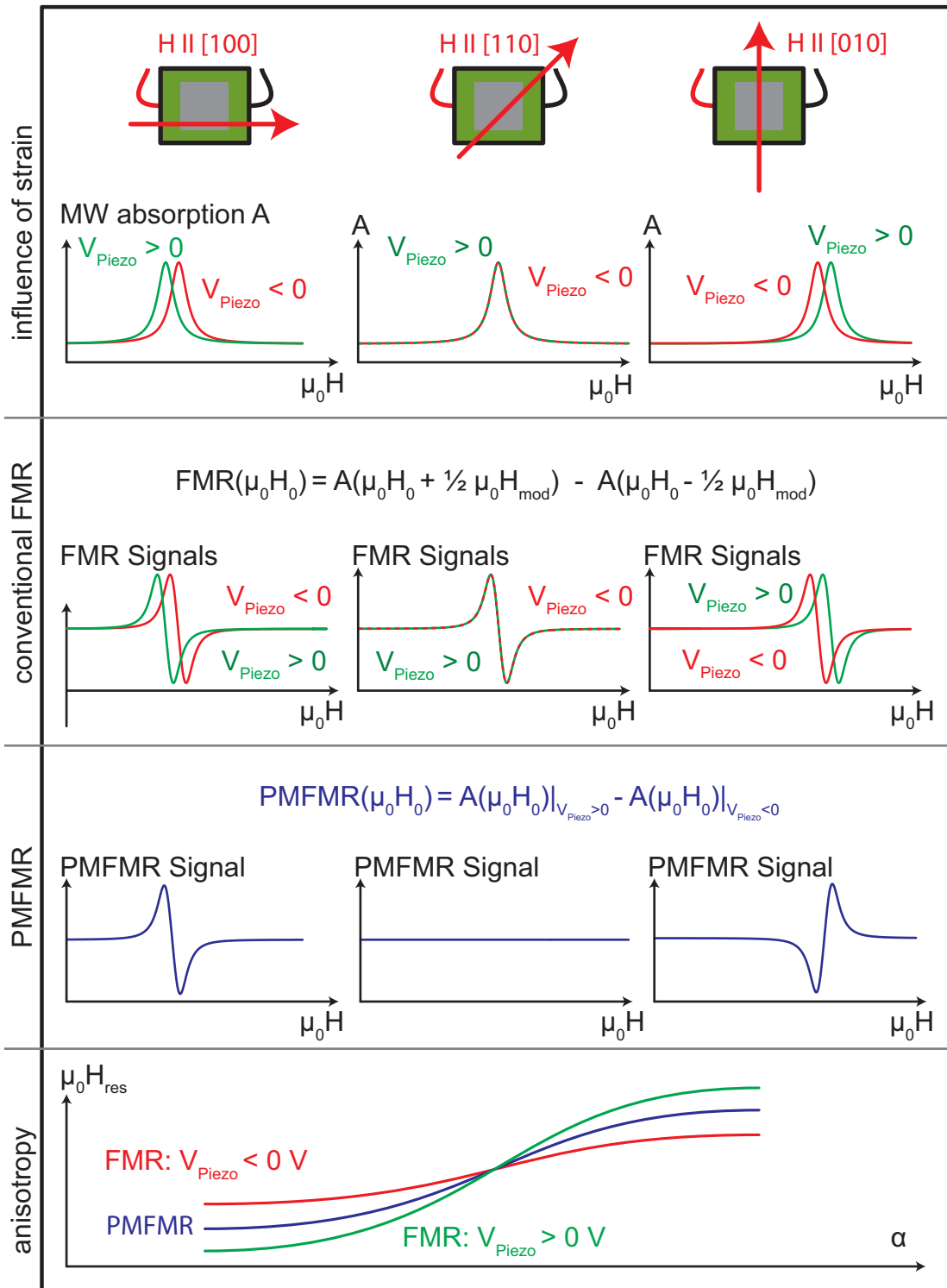
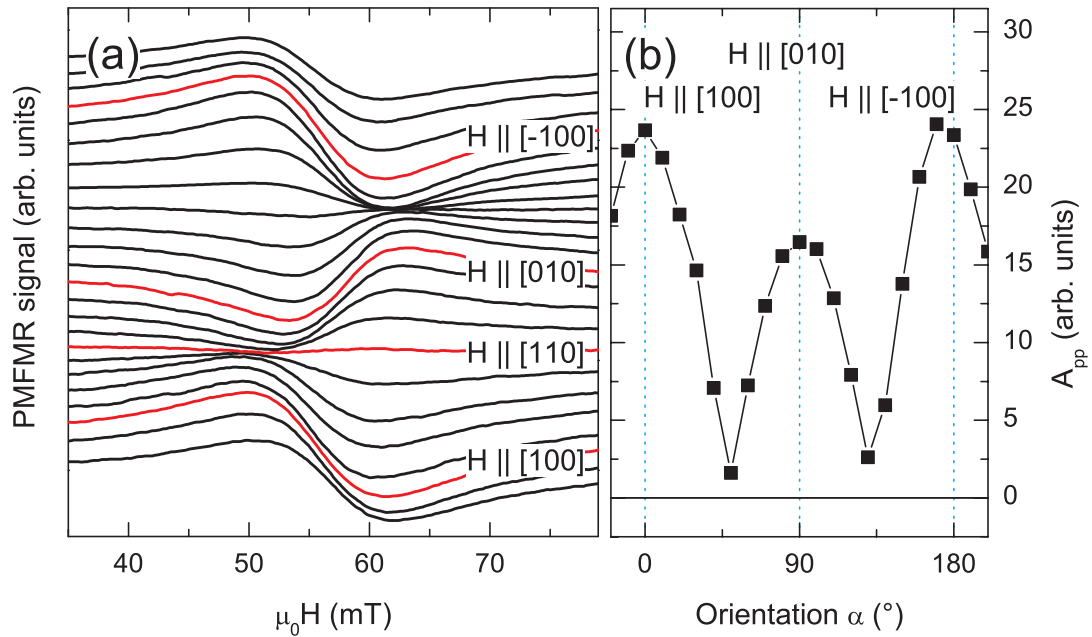


Figure 6.17: Schematic principle of anisotropic signal modulation.



**Figure 6.18:** (a) PMFMR spectra of sample CP1 (cobalt on actuator) as a function of in-plane orientation of  $\mathbf{H}_0$ . The spectra are offset by a constant value. (b) PMFMR signal amplitude as a function of in-plane orientation  $\alpha$  (the lines are guides to the eyes only).

up signal.

### 6.7.3 In-plane anisotropy

For sample CP1 (cobalt on actuator), the in-plane anisotropy at room temperature was determined for angles  $-20^\circ \leq \alpha \leq 210^\circ$  in steps of  $10^\circ$  using anisotropic signal modulation as shown in Fig. 6.17. These measurements were carried out with a modulation amplitude of  $V_{\text{Piezo}}^{\text{pp}} = 20 \text{ V}$  with zero DC bias voltage at a modulation frequency  $\nu_{\text{pmod}} = 2013 \text{ Hz}$ . Fig. 6.18(a) shows the raw data. The predicted inversion of the PMFMR resonance signal sign every  $90^\circ$  can clearly be seen. Fig. 6.18(b) shows the peak-to-peak PMFMR signal amplitude  $A_{pp}$  as a function of the in-plane orientation  $\alpha$ , from which the extinction of the PMFMR signal at  $\mathbf{H}_0 \parallel [110]$  and  $\mathbf{H}_0 \parallel [\bar{1}\bar{1}0]$  is again obvious.

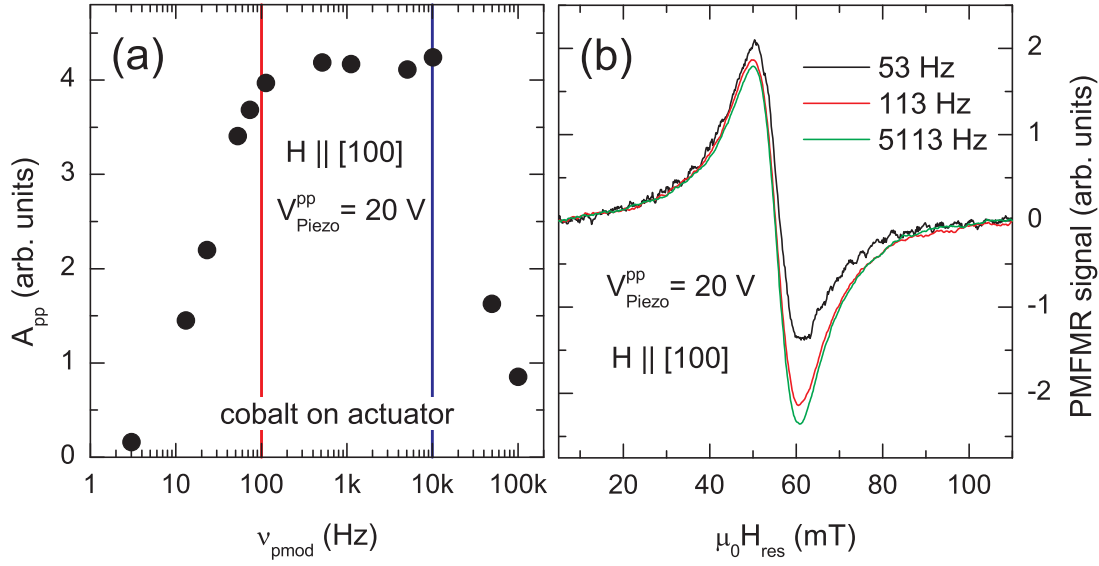


**Figure 6.19:** (a) Influence of modulation frequency on PMFMR signal amplitude. For  $\nu_{\text{pmod}} \leq 100$  Hz, AC coupling attenuates the signal (see text). For  $\nu_{\text{pmod}} > 10$  kHz the voltage source power limit was exceeded. (b) Piezomodulated resonance spectra obtained at modulation frequencies of  $\nu_{\text{pmod}} = 53$ , 113 and 5113 Hz with  $\mathbf{H}_0 \parallel [100]$ .

#### 6.7.4 Influence of modulation amplitude and frequency

With the proof-of-principle experiment summarized in Fig. 6.17, we now determine the dependence of the PMFMR signal amplitude on the modulation amplitude and frequency for  $\mathbf{H}_0 \parallel [100]$ . In Fig. 6.19(a) the PMFMR signal amplitude is displayed for modulation frequencies  $3 \text{ Hz} \leq \nu_{\text{pmod}} \leq 100 \text{ kHz}$  at a constant modulation amplitude  $V_{\text{Piezo}}^{\text{pp}} = 20 \text{ V}$ . We obtain a constant signal amplitude in the range of  $100 \text{ Hz} \leq \nu_{\text{pmod}} \leq 10 \text{ kHz}$ . For  $\nu_{\text{pmod}} < 100$  Hz, the signal is attenuated by the capacitive coupling of the ESR signal cable to the voltage amplifier of the microwave detector diode signal. The reduction of the signal amplitude at frequencies above 10 kHz is probably caused by the power limit of the voltage source. From Fig. 6.19(b) one can see that for frequencies above 100 Hz noise is no longer significantly reduced at a modulation amplitude of  $V_{\text{Piezo}}^{\text{pp}} = 20 \text{ V}$ . In PMFMR, the modulation frequency represents the number of actual magnetoelastic measurements performed per second. Hence, for high modulation frequencies, we can gather very good statistical information on strain-induced resonance field shifts.

Next we address the dependence of the PMFMR signal amplitude on the modu-

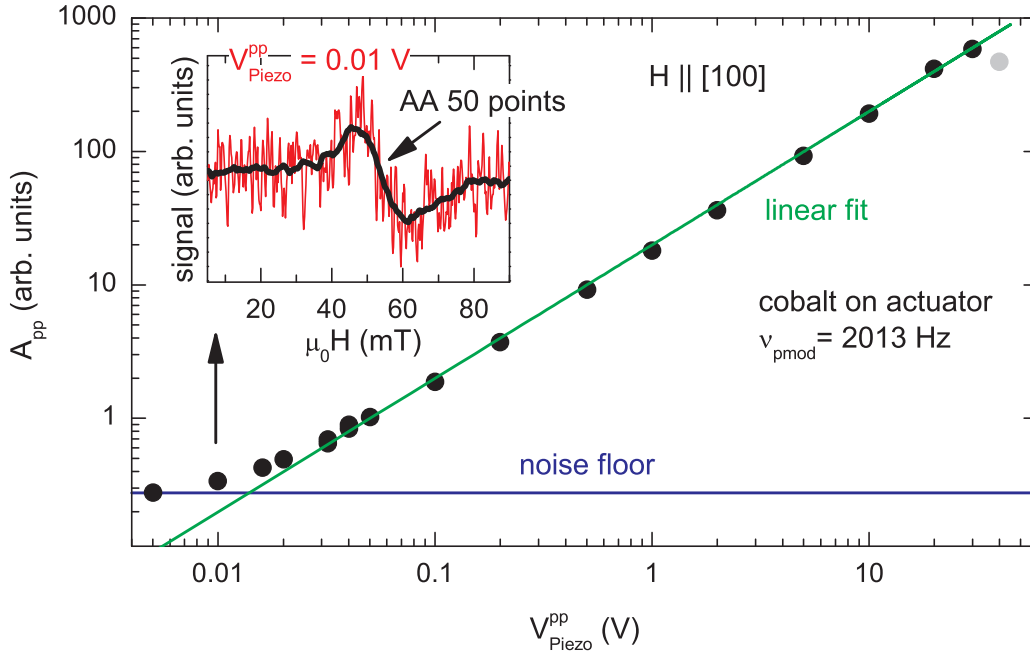


**Figure 6.20:** Influence of the modulation amplitude on the PMFMR signal amplitude for  $\mathbf{H}_0 \parallel [100]$ . For the grey symbol, the source power limit was exceeded. The inset shows the piezomodulated resonance spectrum obtained at a modulation amplitude of  $V_{\text{Piezo}}^{\text{pp}} = 0.01 \text{ V}$  (red), as well as a 50 points averaging over the total 1024 points of this data set (black).

lation amplitude  $V_{\text{Piezo}}^{\text{pp}}$ . As displayed in Fig. 6.20, the PMFMR signal amplitude is linearly dependent on the modulation amplitude at a constant modulation frequency  $\nu_{\text{pmod}} = 2013 \text{ Hz}$ . At small modulation amplitudes the noise floor becomes visible and at  $V_{\text{Piezo}}^{\text{pp}} = 40 \text{ V}$  the voltage source reaches its power limit. Due to the high number of magnetostrictive measurement cycles compared during a single magnetic field sweep, we are able to detect a signal at modulation amplitudes as small as  $V_{\text{Piezo}}^{\text{pp}} = 0.01 \text{ V}$ , as can be seen in the inset showing the raw signal and a 50 point adjacent averaging at  $V_{\text{Piezo}}^{\text{pp}} = 0.01 \text{ V}$ . According to Eq. (6.8), a peak to peak voltage of  $V_{\text{Piezo}}^{\text{pp}} = 0.01 \text{ V}$  corresponds to an in-plane strain along the dominant axis of elongation in  $[010]$  direction of  $\varepsilon_2 = 7 \times 10^{-8}$ . For an actuator length  $L = 2.5 \text{ mm}$  we hence are able to observe a variation  $\Delta L = 0.2 \text{ nm}$  utilizing the magnetoelastic effect. Thus, with PMFMR, we are able to detect strains two orders of magnitude smaller than those detectable in HRXRD (cf. Chapter 5).

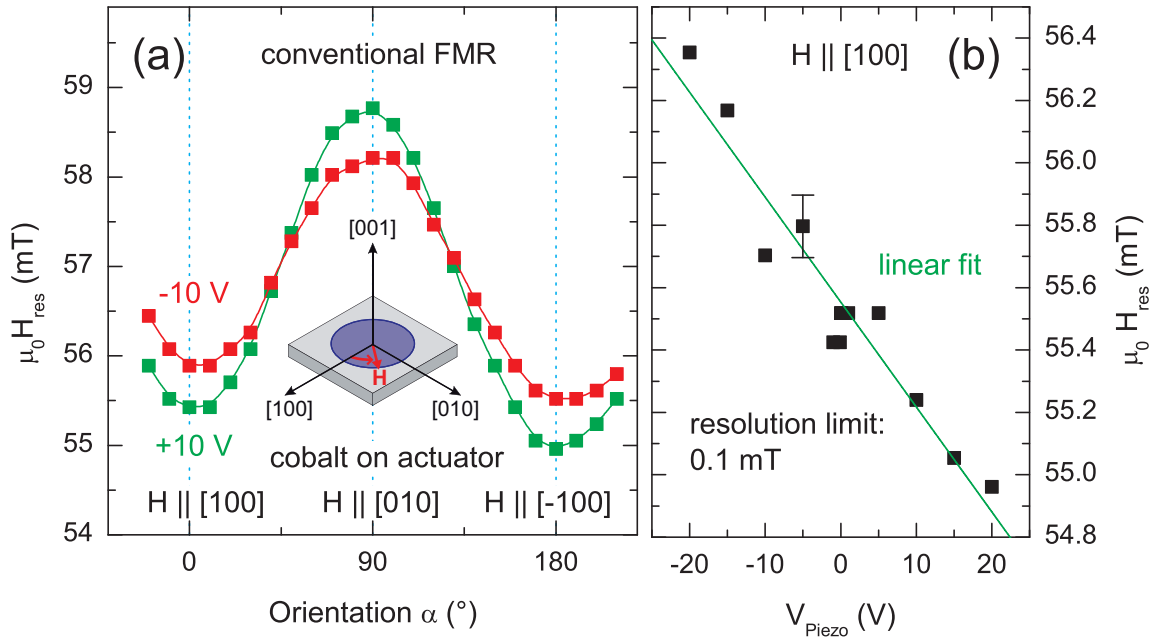


**Figure 6.21:** (a) Angular dependence of resonance fields obtained from conventional FMR measurement. (b) FMR resonance fields as a function of actuator voltage for  $\mathbf{H}_0 \parallel [100]$ .

### 6.7.5 Comparison to conventional FMR measurements

We now compare our measurements results obtained by PMFMR to those obtained by conventional magnetic field modulation in the identical setup. In conventional FMR, we record the resonance field as a function of applied strain to determine magnetoelastic effects.

In Fig. 6.21(a) the in-plane angular anisotropy of the resonance field for actuator voltages  $V_{\text{Piezo}} = +10 \text{ V}$  and  $V_{\text{Piezo}} = -10 \text{ V}$  is displayed. For the strain caused by the application of these voltages to the actuator, a magnetoelastic effect is clearly visible and results in an angle dependent shift of the FMR resonance field. We now recorded FMR spectra for  $\mathbf{H}_0 \parallel [100]$ , systematically varying  $V_{\text{Piezo}}$  in the range  $-20 \text{ V} \leq V_{\text{Piezo}} \leq +20 \text{ V}$ . The results are shown in Fig. 6.21(b). While we observe the expected linear dependence of resonance field for  $|V_{\text{Piezo}}| > 5 \text{ V}$ , for  $|V_{\text{Piezo}}| \leq 5 \text{ V}$  the resolution limit is met.

We will now briefly discuss the cause of this resolution limit. The experimentally achievable resolution is limited by the magnetic field step size during the magnetic

field sweep. Generally, the resolution is given by:

$$\Delta\mu_0 H_0 = \frac{\text{sweepwidth}}{\text{magnetic field steps}}. \quad (6.19)$$

The setup at the Walter Schottky Institute currently is set to 1024 magnetic field steps independent of the sweepwidth. The sweepwidth needs to be larger than the FMR signal linewidth. This explains why we can not resolve the small shift of resonance field for  $|V_{\text{Piezo}}| \leq 5 \text{ V}$ . However, in PMFMR, we can exploit the maximum resolution of the setup of  $\Delta\mu_0 H_0 \approx 2 \mu\text{T}$  which is the smallest magnetic field step size with which  $\mu_0 H_0$  can technically be varied.

Thus, if we want to determine a small shift in FMR resonance field due to magnetoelastic coupling, PMFMR is a convenient way to do so. While in conventional FMR the number of measurements needs to be increased to gather statistical information on the magnetoelastic effect, in PMFMR we only have to increase the modulation frequency. This makes conventional FMR more susceptible to time effects such as temperature or microwave frequency drift.



# Chapter 7

## Converse magnetoelectric effect in $\text{Fe}_3\text{O}_4/\text{BaTiO}_3$ heterostructures

In the previous Chapter, we investigated heterostructures of ferromagnetic thin films and PZT-based actuators. In these samples, the two ferroic phases are separated by a non-ferroic polymer layer. While these heterostructures showed interesting multiferroic properties, heterostructures featuring a direct ferroic phase boundary are of greater fundamental interest. Furthermore, from a technological point of view, it is desirable to produce multiferroic heterostructures in as few steps as possible. Following Andreas Brandlmaier's proposal [56], Stephan Geprägs fabricated such heterostructures by depositing ferromagnetic magnetite ( $\text{Fe}_3\text{O}_4$ ) thin films directly onto ferroelectric barium titanate ( $\text{BaTiO}_3$ ) substrates by pulsed laser deposition.

In this Chapter, we investigate the converse magnetoelectric effect – the effect of an electric field on the magnetization – in these heterostructures. To this end, an electric field is applied perpendicular to the sample plane. The structural properties of the ferroelectric  $\text{BaTiO}_3$  substrate are established as a function of the electric field by high resolution X-ray diffraction (HRXRD). The effect of the electric field on the static magnetic properties is evaluated using superconducting quantum interference device (SQUID) magnetometry. Finally, to determine the dynamic converse magnetoelectric effect, we rely on ferromagnetic resonance (FMR) measurements.

### 7.1 Introduction

The effect of an electric field on the magnetization is referred to as the converse magnetoelectric effect (cf. Chapter 2). From a technological point of view, it is the most

important multiferroic property, as it allows to control the magnetization by an electric field which is considered a milestone on the way to functional multiferroic devices. The physical origin of the (converse) magnetoelectric effect in single-phase multiferroics is vastly different from that in heterostructures [32]. The discussion in this thesis is limited to the converse magnetoelectric effect in multiferroic heterostructures. Only such heterostructures show robust multiferroic properties at room temperature and thus are relevant technologically [5].

### 7.1.1 The converse magnetoelectric effect in multiferroic heterostructures

To understand the converse magnetoelectric effect in heterostructures consisting of a ferromagnetic thin film deposited onto a ferroelectric substrate, we have to consider the coupling of the ferroelectric and the ferromagnetic phase.

In multiferroic heterostructures, mechanical coupling is the dominant effect [95, 26, 96, 97]. The mechanical coupling results in a strain transmission from the ferroelectric phase to the ferromagnetic phase. Thus, it involves the piezoelectric effect in the ferroelectric phase and the magnetoelastic effect in the ferromagnetic phase (cf. Chapter 2). Apart from the piezoelectric effect, which describes the macroscopic deformation of the ferroelectric phase as a function of electric field, the clamping of the ferromagnetic film to the ferroelectric substrate may yield considerable locale strains if the ferroelectric domain structure is changed [20].

Non-strain-mediated converse magnetoelectric effects in multiferroic heterostructures have been predicted [98], however to our knowledge no sizable non-mechanical effect in heterostructures so far has been reported.

### 7.1.2 Sample

Stephan Geprägs fabricated a multiferroic heterostructure consisting of an approximately 100 nm thick film of  $Fe_3O_4$  grown on an approximately 400  $\mu\text{m}$  thick  $BaTiO_3$  substrate by pulsed laser deposition at a growth temperature  $T = 593$  K. As the lattice mismatch of  $BaTiO_3$  and  $Fe_3O_4$  amounts to approximately 5% (cf. Chapter 3) at the growth temperature, the magnetite film relaxes after a few monolayers. Due to interface roughness [99], the exact thickness of the  $Fe_3O_4$  film could not be determined. The lateral dimensions of the samples are  $A = 5 \times 5 \text{ mm}^2$ . We use one of these

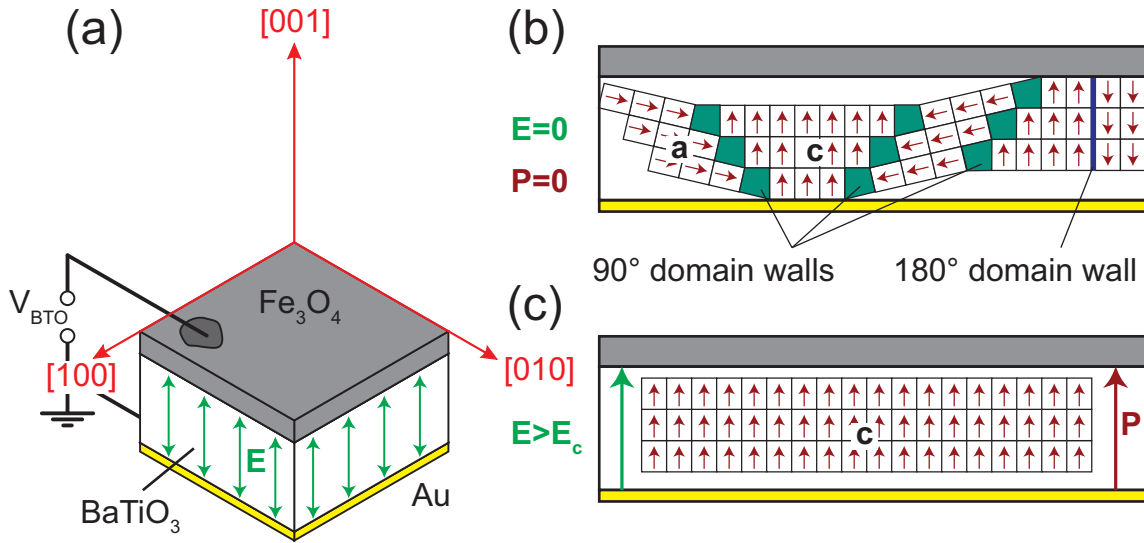


**Figure 7.1:** (a) Coordinate system and schematic view of the sample used for all measurements in this Chapter. (b) Schematic random unit cell distribution into  $a$ - and  $c$ -domains in the  $\text{BaTiO}_3$  substrate if no electric field is applied. (c) Expected single domain state for an electric field  $E > E_c$ .

samples, which is schematically shown in Fig. 7.1(a). On the substrate side of the sample, an approximately 200 nm thick Au electrode is sputter-deposited. To control the polarization of the substrate, an electric field  $\mathbf{E}$  is applied in the  $[001]$  direction by applying a voltage  $V_{\text{BTO}}$  to the sample. This is done using the  $\text{Fe}_3\text{O}_4$  film and the Au film as electrodes with the gold electrode connected to ground and the  $\text{Fe}_3\text{O}_4$  electrode connected to potential (cf. Fig. 7.1(a)). The basic properties of  $\text{Fe}_3\text{O}_4$  and  $\text{BaTiO}_3$  are discussed in Chapter 3.

Prior to the experiments, the sample was cut in two pieces that were afterwards polished to lateral dimensions of  $A_a = 2 \times 5 \text{ mm}^2$  (referred to as MB1a) and  $A_b = 1.5 \times 1.5 \text{ mm}^2$  (referred to as MB1b), respectively.

## 7.2 Polarization in the ferroelectric $\text{BaTiO}_3$ phase

At room temperature,  $\text{BaTiO}_3$  is in its tetragonal phase with lattice constants  $a = 0.3993 \text{ nm}$  and  $b = 0.4034 \text{ nm}$  (cf. Fig. 3.1).  $\text{BaTiO}_3$  can thus form either  $a_1$ -,  $a_2$ - or  $c$ -domains as shown in Fig. 3.3.

The application of an electric field  $E_3$  to the ferroelectric  $\text{BaTiO}_3$  substrate in-

duces a polarization  $P_3$ . The resulting hysteretic  $P(E)$ -loop is schematically shown in Fig. 2.1(b). In Chapter 2, the  $P(E)$ -loop was found to be a result of ferroelectric domain (re)formation to minimize the total free energy of the crystal as a function of electric field. Thus, we expect that the  $BaTiO_3$  substrate can be tuned from a multi-domain state to a single-domain state by applying electric fields  $|E| > |E_c|$  with the coercive field  $E_c$ . If no external electric field is applied and the crystal is thus in a multi-domain state with  $a$ - and  $c$ -domains, Jona and Shirane [19] showed that close to the  $90^\circ$  domain walls between  $a$ - and  $c$ -domains, the unit cells in the  $a$ -domain are tilted, which is schematically depicted in Fig. 7.1(b). Upon the application of an external electric field  $E > E_c$  we expect the  $BaTiO_3$  crystal to enter a single  $c$ -domain state as depicted in Fig. 7.1(c).

### 7.3 HRXRD measurements

To prove that the  $BaTiO_3$  crystal can reversibly be tuned from a multi-domain to a single-domain state by the application of an electric field, we used high resolution X-ray diffraction (HRXRD) to establish the lattice parameters as a function of electric field at room temperature. To this end, the symmetric  $BaTiO_3$  (002) reflection was mapped in reciprocal space (as explained in Chapter 4) for  $-120 \text{ V} \leq V_{BTO} \leq +120 \text{ V}$ . This enables us to determine the  $BaTiO_3$  out-of-plane lattice constant(s). The measurements were carried out using a Bruker AXS-D8 Discover four circle diffractometer that was already introduced in Chapter 4.

Sample MB1a ( $A_a = 2 \times 5 \text{ mm}^2$ ) was used in HRXRD measurements. The poling voltage  $V_{BTO}$  was provided by a Keithley 2410 high voltage sourcemeter. Reciprocal space maps (RSMs) were recorded for  $-120 \text{ V} \leq V_{BTO} \leq +120 \text{ V}$  which corresponds to an electric field of approximately  $-300 \text{ V/mm} \leq E \leq 300 \text{ V/mm}$ . This voltage range comprises the coercive fields of  $BaTiO_3$  single crystals which are expected to be  $|E_c| \approx 100 \text{ V/mm}$  [100].

As the  $BaTiO_3$  thickness is only known to a precision of  $\pm 50 \mu\text{m}$  all measurement results will display the precisely known applied voltage  $V_{BTO}$  instead of the electric field.

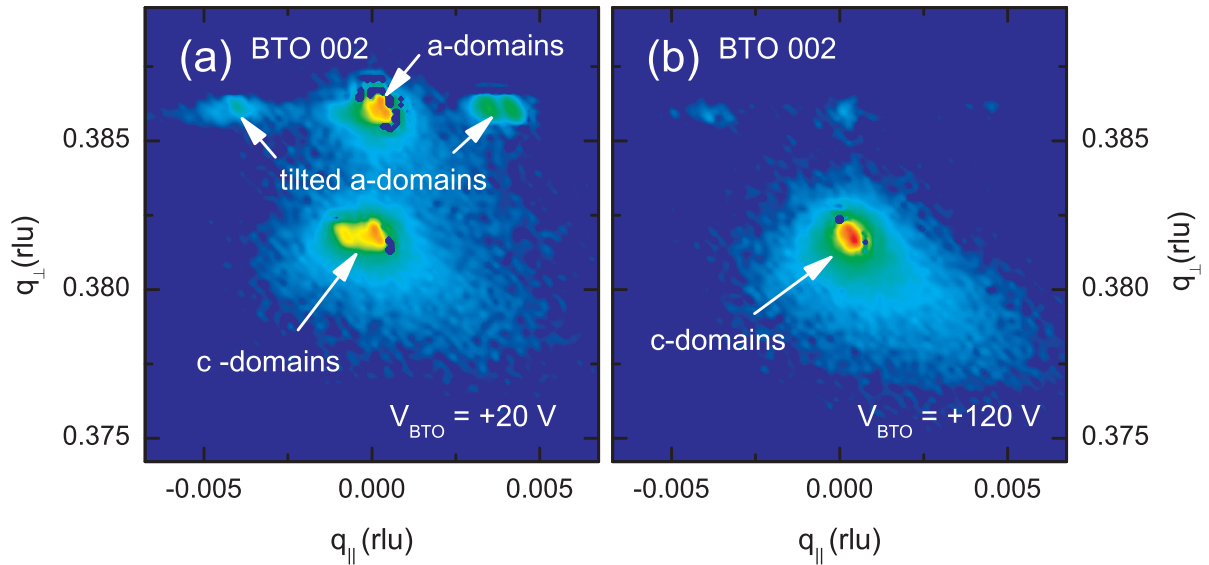


**Figure 7.2:** Reciprocal space mapping of the BTO (002) reflection for voltages of (a)  $V_{\text{BTO}} = +20 \text{ V}$  and (b)  $V_{\text{BTO}} = +120 \text{ V}$ . The color scale is logarithmic and ranges from 0 cps (blue) to 144000 cps (red).

### 7.3.1 Measurement results

Prior to the actual measurements, the diffractometer alignment was carried out using the  $\text{BaTiO}_3$  (002) reflection at  $V_{\text{BTO}} = 0 \text{ V}$ . The first measurement was recorded at the highest investigated electric field  $V_{\text{BTO}} = +120 \text{ V}$ . Subsequently, the voltage was successively reduced to  $V_{\text{BTO}} = -120 \text{ V}$  and raised back to  $V_{\text{BTO}} = +120 \text{ V}$ .

We show two exemplary reciprocal space maps of this measurement series, both recorded at increasing voltage. In Fig. 7.2(a), the raw data obtained for  $V_{\text{BTO}} = +20 \text{ V}$  is displayed and in Fig. 7.2(b) the raw data obtained for  $V_{\text{BTO}} = +120 \text{ V}$  is displayed.

In Fig. 7.2(a) we can easily identify four reflections. We observe one reflection at  $q_{\perp} = 0.382 \text{ rlu}$  and three reflections at  $q_{\perp} = 0.386 \text{ rlu}$ . In Fig. 7.2(b) only a single reflection of sizable intensity at  $q_{\perp} = 0.382 \text{ rlu}$  is visible.

### 7.3.2 Discussion

As we investigate the symmetric  $\text{BaTiO}_3$  (002) reflection, the out-of-plane lattice constant can be calculated with Eq. (4.21) for each reflection. We obtain  $a = 0.399 \text{ nm}$  for the reflections at  $q_{\perp} = 0.386 \text{ rlu}$  and  $c = 0.404 \text{ nm}$  for the reflection at  $q_{\perp} =$

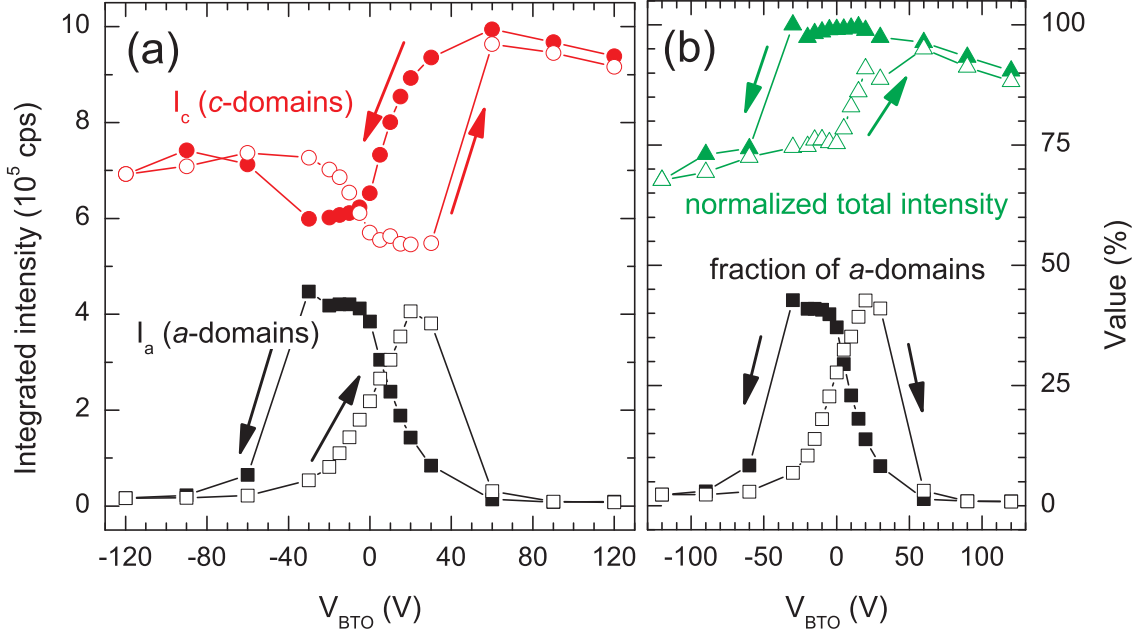


**Figure 7.3:** (a) Total intensity accounted to  $c$  and  $a$  domains, respectively. (b) Fraction of  $a$  domains and total intensity as a function of  $V_{BTO}$ . The lines are guides to the eye.

0.382 rlu. These lattice parameters are in good agreement with the expected lattice constants for  $a$ - and  $c$ -domains respectively (cf. Fig. 3.1). Thus a multi-domain state is observed in Fig. 7.2(a). In Fig. 7.2(b) one sees only a single reflection of sizable intensity, thus we observe a single  $c$ -domain state.

The splitting of the  $a$ -domain reflections in Fig. 7.2(a) is attributed to the aforementioned unit cell tilting (cf. 7.1(b)). A slight splitting of the  $c$ -domain reflections is observed as well for small fields, but vanishes as the field is increased. This indicates a slight tilting of some  $c$ -domains at small electric fields.

To visualize the evolution of domain fractions with electric field, the integrated intensity  $I(q_{\perp} > 0.384 \text{ rlu}) = I_a$  for all points with coordinates  $(q_{\perp} > 0.384 \text{ rlu} | q_{\parallel})$  in each RSM is attributed to  $a$ -domains whereas  $I(q_{\perp} < 0.384 \text{ rlu}) = I_c$  is attributed to  $c$ -domains. This results in the integrated intensities shown in Fig. 7.3(a) as a function of  $V_{BTO}$ . In Fig. 7.3(b) the normalized total intensity  $I_{\text{tot}} = (I_a + I_c) / (I_a^{0V} + I_c^{0V})$  and the fraction  $I_a^{\text{frac}} = I_a / (I_a + I_c)$  of  $a$ -domains are depicted as a function of  $V_{BTO}$ .

The loss of total intensity for negative voltages  $V_{BTO}$  (cf. Fig. 7.3(b)) was not expected. It may however be explained by the change of the structure factor with the

displacement of the  $\text{Ti}^{4+}$  ion that amounts for a change of approx. 3% in intensity in thin films [101], and more importantly a diffractometer misalignment due to the structural change in the substrate as soon as the voltage is changed from the alignment voltage  $V_{\text{BTO}} = 0 \text{ V}$ .

In Fig. 7.3(b) it is further evident that we are able to almost completely and reversibly pole the ferroelectric  $\text{BaTiO}_3$  substrate with a calculated  $a$ -domain fraction of less than 3% at high electric fields and a distribution of about 45%  $a$ -domains to 55%  $c$ -domains in the multi-domain state. These absolute values are to be taken as a coarse approximation as the alignment was not carried out for single  $a$ - and  $c$ -domain states as no pure  $a$ -domain state can be achieved with the current sample setup. Thus the absolute values of the reflection intensities for  $a$ - and  $c$ -domains are afflicted with alignment errors that may reach several percent. Nevertheless, the obtained results are clear evidence for the reversible poling of the ferroelectric  $\text{BaTiO}_3$  substrate as a function of electric field.

## 7.4 Magnetization in the ferromagnetic $\text{Fe}_3\text{O}_4$ phase

The magnetization is related non-linearly to an external magnetic field as schematically shown in Fig. 2.1(b). Due to the magnetic anisotropy, the shape of this hysteretic  $M(H)$ -loop is a function of the orientation of the sample in the external magnetic field [30]. Hence, if the magnetic anisotropy is changed, the shape of the  $M(H)$ -loop changes as well. We will now investigate whether the application of an electric field to our sample results in a change of the magnetic anisotropy of the  $\text{Fe}_3\text{O}_4$  film.

To this end, we carried out SQUID measurements to establish the static magnetic response as a function of external magnetic and electric fields which will be presented and evaluated in the following.

## 7.5 SQUID measurements

All measurements were carried out by Stephan Geprägs using a Quantum Design MPMS XL-7 SQUID magnetometer and a sample holder he specifically designed to provide electrical contacts in the sample space. The poling voltage  $V_{\text{BTO}}$  was provided by a Keithley 2410 high voltage sourcemeter, which was additionally used to record the current flowing between the electrodes in-situ. The same sample that was used

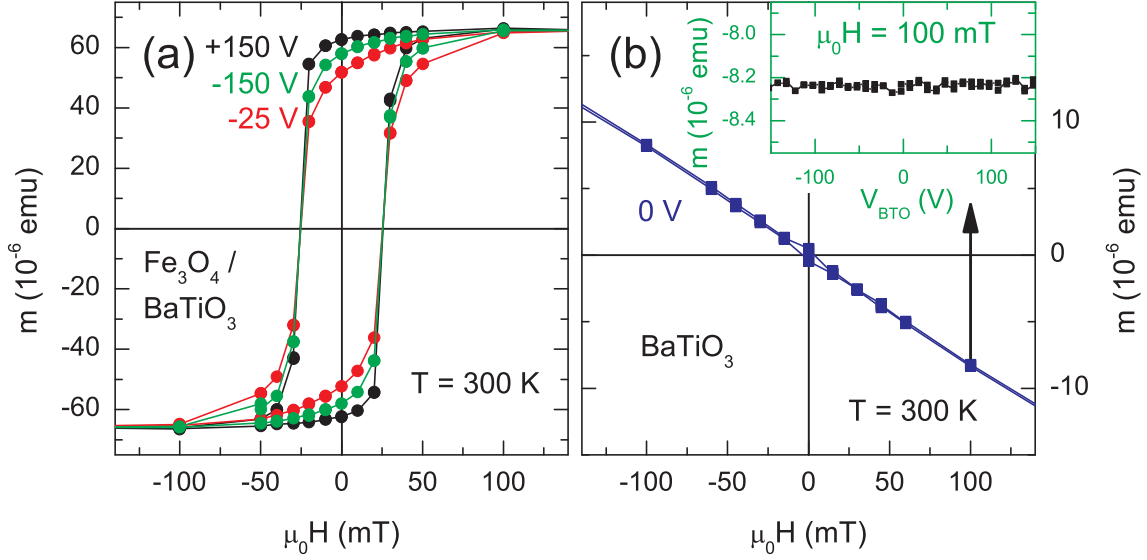


**Figure 7.4:** (a)  $M(H)$ -loop of the  $\text{Fe}_3\text{O}_4/\text{BaTiO}_3$  heterostructure at saturation and coercive electric fields (see text) with the magnetic field along [100]. (b) Diamagnetic response of a pure  $\text{BaTiO}_3$  substrate without ferromagnetic film, the inset shows that the diamagnetism is not electric field dependent. The lines are guides to the eye.

for the HRXRD measurements (MB1a) was investigated. To fit it into the SQUID sample holder its lateral dimensions were reduced to  $2 \times 1.5 \text{ mm}^2$ .

The projection  $m$  of the total magnetic moment  $\mathbf{m} = \int_V \boldsymbol{\mu} dV$  onto the direction of the external magnetic field  $\mu_0 \mathbf{H}$  was recorded as a function of the poling voltage  $V_{\text{BTO}}$  and external magnetic field  $\mu_0 \mathbf{H}$ . As the exact film thickness and thus its volume  $V$  is unknown, no absolute values of the magnetization  $\mathbf{M} = \mathbf{m}/V$  can be given.

$M(H)$ -loops were recorded for  $-7 \text{ T} \leq \mu_0 H \leq 7 \text{ T}$  with  $\mathbf{H} \parallel [100]$  and  $\mathbf{H} \parallel [001]$  at constant poling voltages  $-150 \text{ V} \leq V_{\text{BTO}} \leq +150 \text{ V}$ . Furthermore, the magnetic moment was recorded as a function of the poling voltage  $V_{\text{BTO}}$  at constant external magnetic field  $-1 \text{ T} \leq \mu_0 H \leq 1 \text{ T}$ . These  $M(E)$ -loops were carried out for  $\mathbf{H} \parallel [100]$  and  $\mathbf{H} \parallel [001]$ , respectively. Additionally,  $M(H)$ - and  $M(E)$ -loops of a  $\text{BaTiO}_3$  single crystal with two gold electrodes were recorded. All measurements were carried out at room temperature.

### 7.5.1 Measurement results

Firstly, we will present some of the measurements that were performed with  $\mathbf{H} \parallel [100]$ .

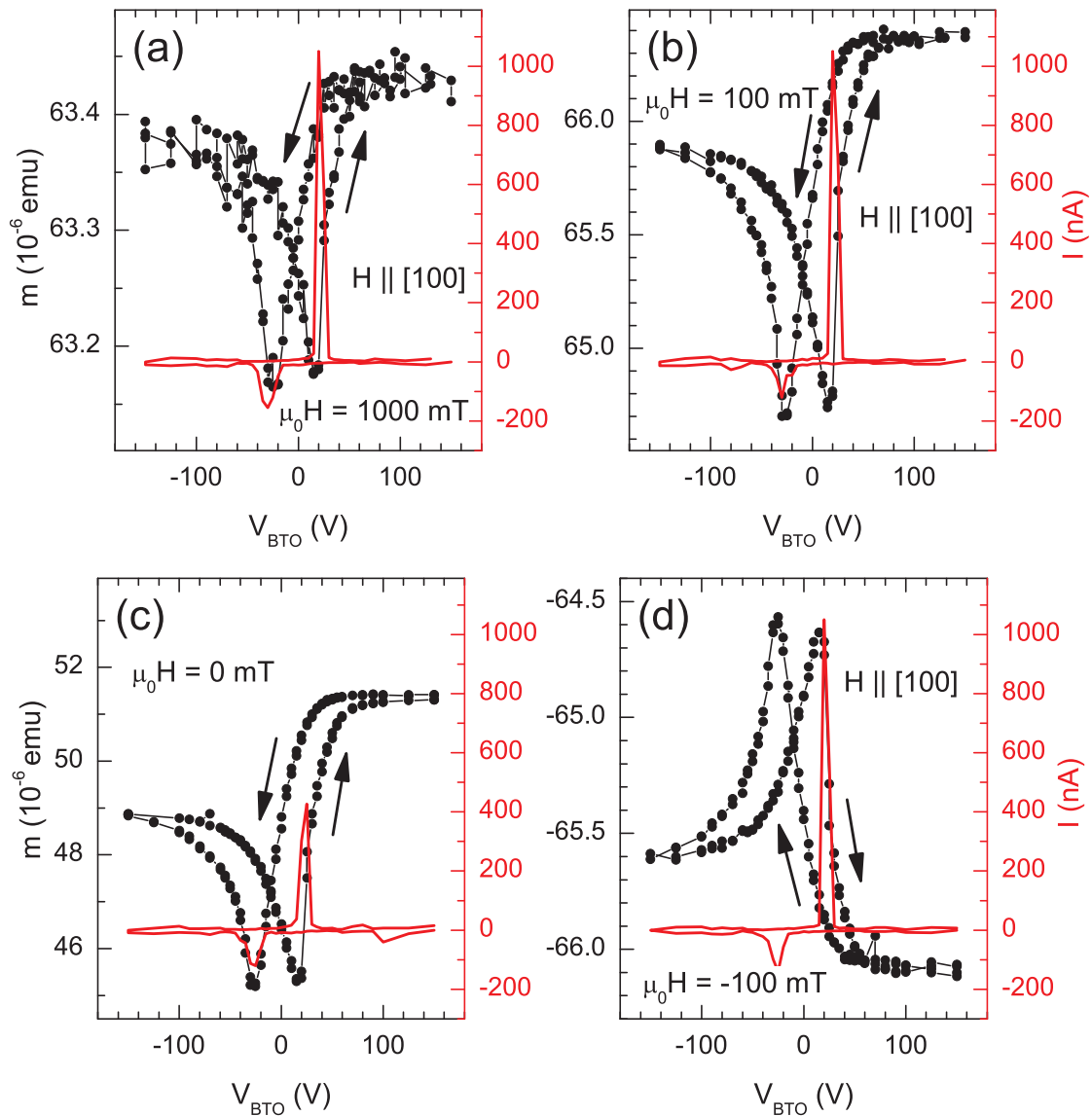


**Figure 7.5:** (a)-(c) show the projection of the magnetization vector onto the  $[100]$  axis for external magnetic fields from 1 T to 0 T along the  $[100]$  axis. (d) shows that the loop is inverted if the external magnetic field is applied along  $[\bar{1}00]$ . The lines are guides to the eye. Also shown is the current flowing between the electrodes (red, right scale).

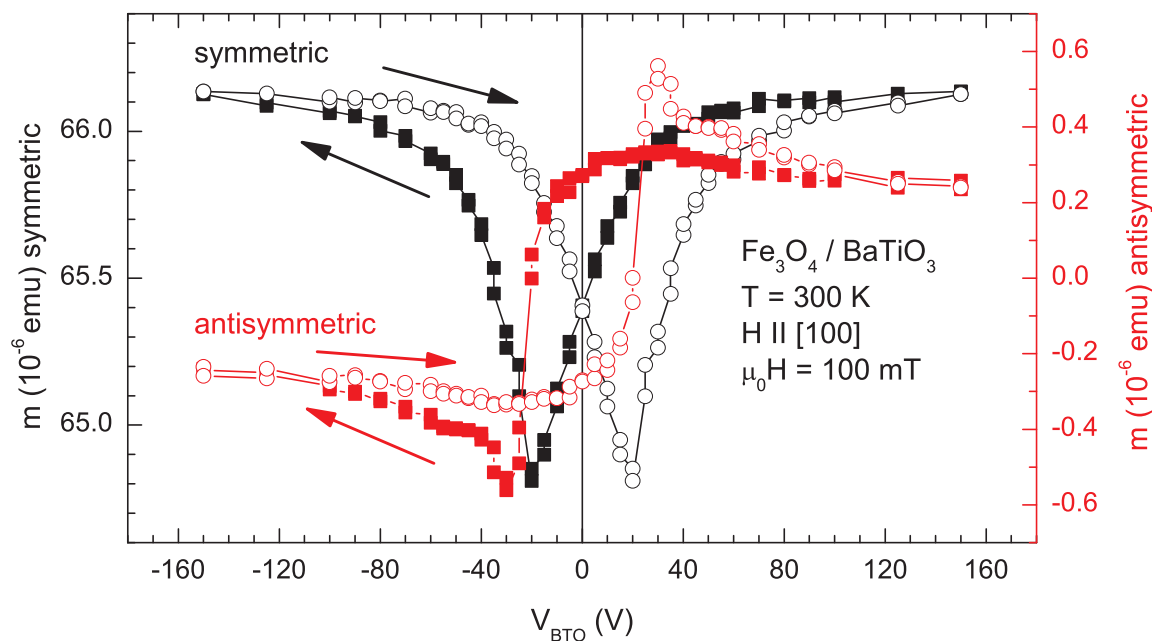


**Figure 7.6:** Symmetric and antisymmetric contribution to the measured magnetization for  $\mathbf{H} \parallel [100]$  ( $\mu_0 H = 100$  mT) as a function of  $V_{BTO}$ . The lines are guides to the eye.

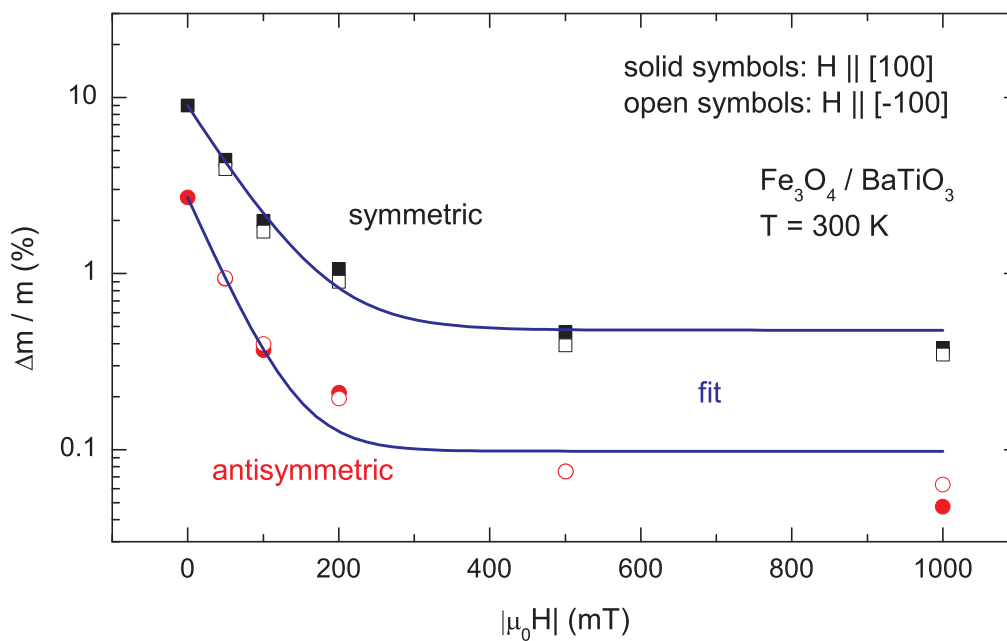


**Figure 7.7:** Relative change  $\Delta m / m$  (see text) in the symmetric and antisymmetric contribution to  $m$  as a function of external magnetic field  $\mu_0 \mathbf{H}$ . Fit calculated according to Eq. (7.1).

### In-plane measurement results

The  $M(H)$ -loops that are shown in Fig. 7.4(a) were recorded (in this order) at  $V_{\text{BTO}} = +150 \text{ V}$ ,  $V_{\text{BTO}} = -25 \text{ V}$  and  $V_{\text{BTO}} = -150 \text{ V}$ . A clear influence of the electric field on the shape of the  $M(H)$ -loops is observed, whereas the coercive field  $\mu_0 H_c = 25.5 \text{ mT}$  remains identical within the resolution of the experiment. At  $V_{\text{BTO}} = -25 \text{ V}$  we observe a remanent magnetic moment  $m_{\text{R}}^{-25\text{V}} = 52 \times 10^{-6} \text{ emu}$ , at  $V_{\text{BTO}} = -150 \text{ V}$  we observe  $m_{\text{R}}^{-150\text{V}} = 58 \times 10^{-6} \text{ emu}$  and at  $V_{\text{BTO}} = +150 \text{ V}$  we observe  $m_{\text{R}}^{+150\text{V}} = 63 \times 10^{-6} \text{ emu}$ .

A  $M(H)$ -loop of the diamagnetic  $\text{BaTiO}_3$  substrate at  $V_{\text{BTO}} = 0 \text{ V}$  is displayed in Fig. 7.4(b). As the inset shows, the diamagnetic response is independent of  $V_{\text{BTO}}$ .

Exemplary  $M(E)$ -loops are presented in Fig. 7.5 for constant external magnetic field  $-100 \text{ mT} \leq \mu_0 \mathbf{H} \leq 1 \text{ T}$ . Prior to the recording of each  $M(E)$ -loop, the external magnetic field was set to  $\mu_0 H = 7 \text{ T}$ . All  $M(E)$ -loops show a qualitatively identical hysteretic behavior and the peaks in the current coincide with the extrema of the hysteresis loops. The influence of the electric field on  $m$  is reduced as the magnetic field is increased.

Fig. 7.6 shows the symmetric ( $M(E) = M(-E)$ ) and antisymmetric ( $M(E) = -M(-E)$ ) contribution to the  $M(E)$ -loop at  $\mu_0 H = 100 \text{ mT}$  (cf. Fig. 7.5(b)).

Finally, in Fig. 7.7 the symmetric and antisymmetric contribution to the maximum relative change<sup>1</sup>  $\frac{\Delta m}{m}$  in  $m$  in the voltage range  $-150 \text{ V} \leq V_{\text{BTO}} \leq +150 \text{ V}$  is displayed as a function of external magnetic field  $\mu_0 \mathbf{H}$ . We observe an exponential decay of both the symmetric and the antisymmetric contribution to  $\frac{\Delta m}{m}$  as a function of  $\mu_0 \mathbf{H}$ . For  $\mu_0 H \geq 500 \text{ mT}$  the relative change in  $m$  saturates. Furthermore, regardless of the magnitude of the external magnetic field, the symmetric contribution is always stronger than the antisymmetric contribution by a factor of approximately 3. The exponential decay in Fig. 7.7 is fitted by:

$$\frac{\Delta m}{m} = \frac{\Delta m}{m} \Big|_{\mu_0 H=0} \exp(-\beta \mu_0 H) + \frac{\Delta m_s}{m_s}, \quad (7.1)$$

which yields  $\frac{\Delta m_s}{m_s} = 0.5\%$  for the symmetric and  $\frac{\Delta m}{m} = 0.1\%$  for the antisymmetric contribution.

<sup>1</sup>For the symmetric contribution we use  $\Delta m = |m(20 \text{ V}) - m(150 \text{ V})|$  and for the antisymmetric contribution we use  $\Delta m = |m(-150 \text{ V}) - m(+150 \text{ V})|$ .

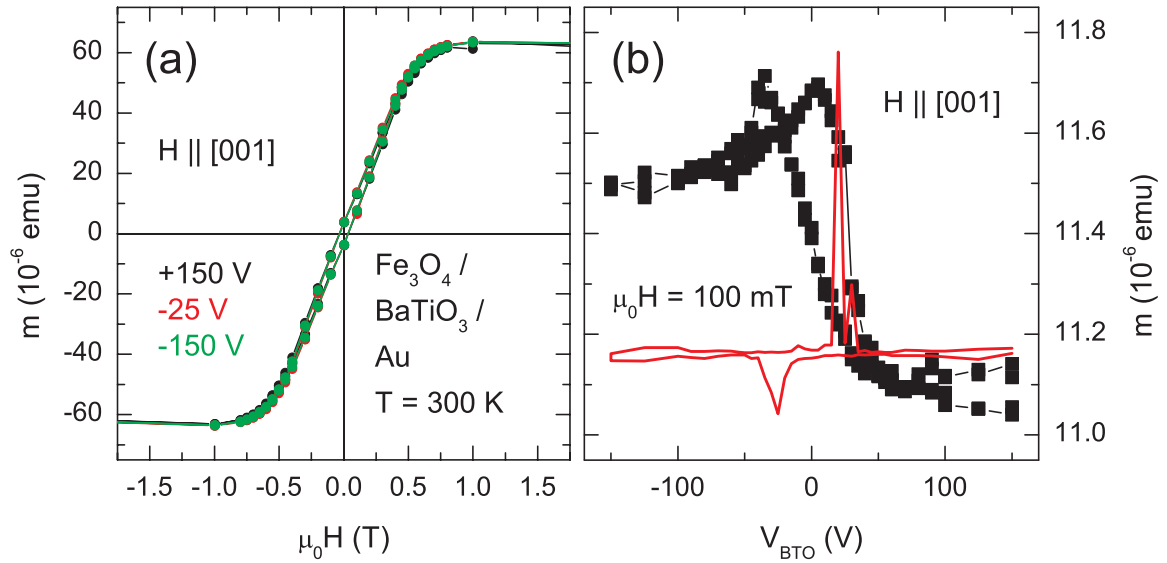


**Figure 7.8:** (a)  $M(H)$ -loop of the  $Fe_3O_4/BaTiO_3$  heterostructure at saturation and coercive electric fields (see text) with  $\mathbf{H} \parallel [100]$ . (b)  $m$  as a function of  $V_{BTO}$  for  $\mathbf{H} \parallel [001]$  with  $\mu_0 H = 100$  mT. The lines are guides to the eye.

### Out-of-plane measurement results

$M(H)$ -loops for  $\mathbf{H} \parallel [001]$  that were recorded (in this order) at  $V_{BTO} = +150$  V,  $V_{BTO} = -25$  V and  $V_{BTO} = -150$  V are shown in Fig. 7.8(a). The influence of the electric field on  $m$  is only apparent if  $M(E)$ -loops are considered. Such an  $M(E)$ -loop at  $\mu_0 H = 100$  mT is displayed in Fig. 7.8(b). It shows an inverted effect of the electric field on  $m$  if compared to the in-plane measurements (cf. Fig. 7.5).

### 7.5.2 Discussion

We clearly observe a converse magnetoelectric effect as  $m$  is a function of the electric field. As can already be seen in the  $M(H)$ -loop in Fig. 7.4(a), this effect is most distinct at small external magnetic fields. This is interpreted as a result of the fact that an external magnetic field aligns the magnetic moments to its direction. Thus, the larger the magnetic field, the smaller the influence of the electric field.

We now consider two possible causes of the electric field dependence of  $m$ : As  $m$  is the projection of the vector  $\mathbf{m}$  to the direction of the external magnetic field  $\mu_0 \mathbf{H}$ , we may observe a change of  $\mathbf{m}$  in either magnitude or orientation (or both). The magnitude of  $\mathbf{m}$  is given by the saturation magnetic moment  $m_s$  and the orientation

of  $\mathbf{m}$  is defined by the magnetic anisotropy.

We will now first assume that either  $m_s$  or the orientation of  $\mathbf{m}$  changes, but not both. Now, if  $m_s$  was a function of the electric field, we would expect the same symmetry of the  $M(E)$ -loops regardless of the orientation of  $\mathbf{H}$  as the saturation magnetization is a scalar property. In particular, we would expect the same symmetry for  $\mathbf{H} \parallel [100]$  and  $\mathbf{H} \parallel [001]$ . Comparing the in-plane (cf. Fig. 7.5) and out-of-plane (cf. Fig. 7.8(b)) measurements we however find that the symmetry of both the antisymmetric and symmetric contribution to the  $M(E)$  loop is inverted: Whereas the peaks in the hysteresis loops are directed downwards for  $\mathbf{H} \parallel [100]$ , they are directed upwards for  $\mathbf{H} \parallel [001]$  and whereas we observe a large absolute value of  $m$  at  $V_{\text{BTO}} = +150\text{V}$  for  $\mathbf{H} \parallel [100]$ , we observe a small absolute value of  $m$  at  $V_{\text{BTO}} = +150\text{V}$  for  $\mathbf{H} \parallel [001]$ . Thus, we can rule out changes of  $m_s$  as the dominant effect.

Furthermore, if the saturation magnetization was dominantly affected by the electric field, the change in  $m$  would be expected to saturate at a magnetic field of approximately  $\mu_0 H = \mu_0 H_c = 25.5\text{ mT}$  for  $\mathbf{H} \parallel [100]$  (which will later be shown to be an easy axis). However, we observe such a saturation only at much larger magnetic fields  $\mu_0 H \geq 500\text{ mT}$  (cf. Fig. 7.7). Again, an effect of  $V_{\text{BTO}}$  purely on  $m_s$  thus is not appropriate to describe the data. Only a small effect of  $\frac{\Delta m_s}{m_s} \approx 0.6\%$  (cf. Eq. (7.1)) is in accordance with the experiment. Hence we conclude that the electric field dominantly affects the magnetic anisotropy of the  $\text{Fe}_3\text{O}_4$  thin film rather than its saturation magnetization.

As ferromagnetic resonance (FMR) is a very precise means to determine the magnetic anisotropy, we will evaluate whether FMR yields results that underline this assumption before giving a theoretical description of its physical origin.

## 7.6 FMR measurements

The ferromagnetic resonance measurements were carried out at room temperature using the already introduced Bruker ESP 300 spin resonance spectrometer at a microwave power of  $0.8\text{ mW}$  and a microwave frequency of  $\nu_{\text{MW}} = 9.3\text{ GHz}$  in a  $\text{TE}_{102}$  cavity. A description of the setup can be found in Chapter 4.

Prior to the FMR measurements presented in the following, the leakage current was recorded in-situ (at a magnetic field of  $100\text{ mT}$  and a microwave power of  $0.8\text{ mW}$ ) as a function of  $V_{\text{BTO}}$  with a Keithley 2400 sourcemeter.

For the ferromagnetic resonance measurements, we used sample MB1b with lateral dimensions  $A_b = 1.5 \times 1.5 \text{ mm}^2$  (cf. Fig. 7.1(a)). A sample this small was used as the high dielectric constant of  $BaTiO_3$  (cf. Chapter 3) affects the microwave  $E_1$  field in the cavity, and thus for larger samples no stable microwave tuning could be achieved.

Furthermore, no stable microwave tuning could be achieved if an electric field was applied to the sample MB1b in the in-plane configuration ( $\mathbf{H}_0$  in the (001) plane). Due to the limited time allocated to this thesis, the measurements could not be repeated with a smaller sample, which is expected to rule out the microwave tuning problems. Therefore, no complete set of anisotropy constants as a function of electric field could be obtained and all measurements recorded at  $V_{BTO} \neq 0 \text{ V}$  were performed in the out-of-plane configuration, thus with  $\mathbf{H}_0$  in the (010) plane.

The FMR measurements were carried out starting at a poling voltage  $V_{BTO} = +120 \text{ V}$  which was subsequently reduced stepwise to  $V_{BTO} = -120 \text{ V}$  and raised back again to  $V_{BTO} = +120 \text{ V}$  to record the complete hysteresis. The poling voltage  $V_{BTO}$  was provided by a Keithley 237 sourcemeter.

### 7.6.1 Measurement results

Firstly, we present the results obtained for  $\mathbf{H}_0 \parallel [100]$ .

#### Poling results for $\mathbf{H}_0 \parallel [100]$

The raw spectra for the extreme bias voltages  $V_{BTO} = \pm 120 \text{ V}$  as well as for  $V_{BTO} = 0 \text{ V}$  are displayed in Fig. 7.9. The spectra each show one broad FMR line with the resonance field in the vicinity of  $\mu_0 H = 100 \text{ mT}$  as well as ESR lines, that originate from impurities in the  $BaTiO_3$  substrate (see next Chapter for details on paramagnetic impurities in  $BaTiO_3$ ). Within the resolution of the experiment, the ESR lines show no voltage-dependent shift. The FMR line, however, shows a shift of  $\Delta\mu_0 H_{\text{res}} \approx 10 \text{ mT}$  for  $-120 \text{ V} \leq V_{BTO} \leq +120 \text{ V}$ .

The ferromagnetic resonance fields as well as the corresponding leakage current are shown in Fig. 7.10(a) for  $\mathbf{H}_0 \parallel [100]$  as a function of  $V_{BTO}$ . We observe a hysteretic behavior of  $\mu_0 H_{\text{res}}$ . The linewidth  $\mu_0 \Delta H_{\text{pp}}$  of the FMR line as well as the magnetic field corresponding to the maximum and minimum of the FMR line as a function of  $V_{BTO}$  are provided in Fig. 7.10(b). The symmetric and antisymmetric contributions to  $\mu_0 H_{\text{res}}(V_{BTO})$  are displayed in Fig. 7.11.

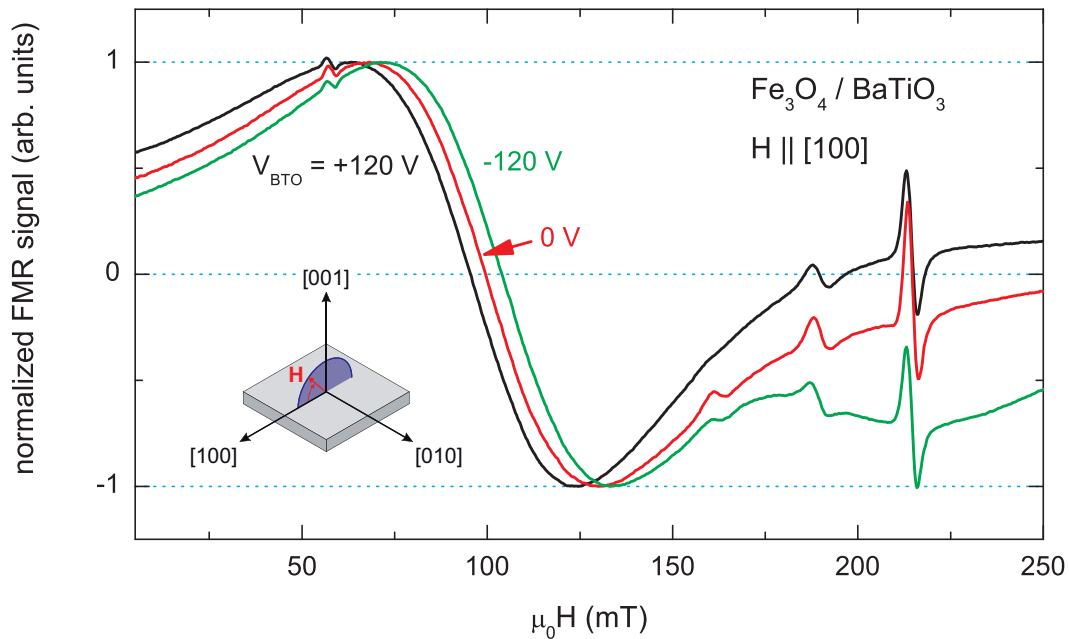


**Figure 7.9:** FMR spectra recorded with  $\mathbf{H}_0 \parallel [100]$  at maximum poling voltages  $V_{\text{BTO}} = \pm 120$  V and  $V_{\text{BTO}} = 0$  V.

### Poling results for $\mathbf{H}_0 \parallel [001]$

Raw spectra for  $V_{\text{BTO}} \in \{-120 \text{ V}, 0 \text{ V}, +120 \text{ V}\}$  for the measurement with  $\mathbf{H}_0 \parallel [001]$  are presented in Fig. 7.12. The raw spectra show the emergence of a second FMR line at negative poling voltages. As the two FMR lines can not unambiguously be distinguished, it is not possible to calculate reliable FMR resonance fields at this orientation of  $\mathbf{H}_0$ .

Finally, we present the results obtained for the rotations of the sample in the external magnetic field at  $V_{\text{BTO}} = 0$  V.

### In-plane and out-of-plane rotations

From the in-plane rotation displayed in Fig. 7.13(a) we observe a purely cubic anisotropy at  $V_{\text{BTO}} = 0$  V with the easy axes in the  $[100]$  and  $[010]$  directions. The out-of-plane-rotation (cf. Fig. 7.13(b)) shows a FMR resonance field of approximately  $\mu_0 H_{\text{res}} = 970$  mT for  $\mathbf{H}_0 \parallel [001]$ .

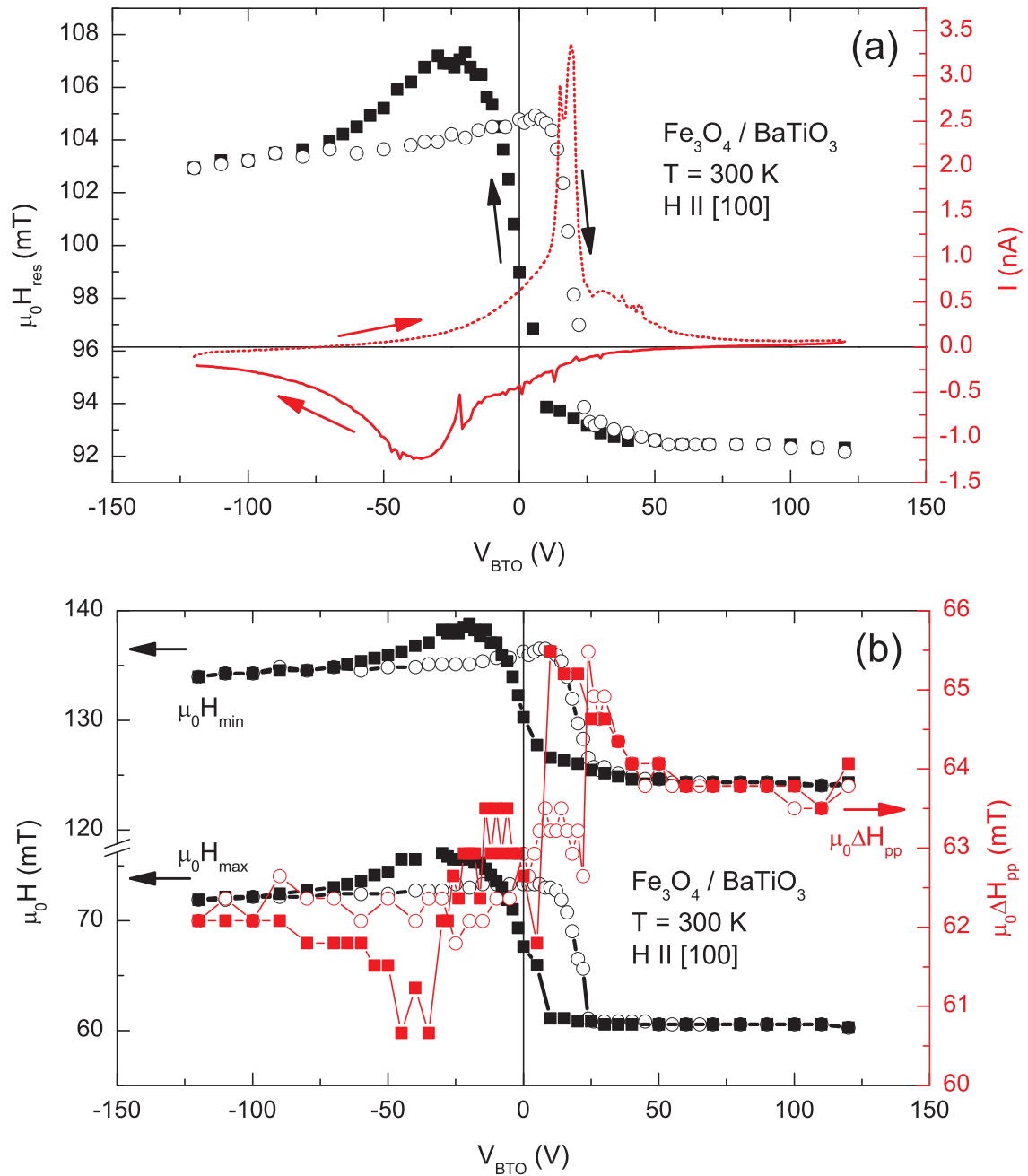


**Figure 7.10:** (a) Ferromagnetic resonance fields  $\mu_0 H_{\text{res}}$  and leakage current  $I$  as a function of the applied poling voltage  $V_{\text{BTO}}$  with  $\mathbf{H}_0 \parallel [100]$  (open symbols: increasing voltage, solid symbols: decreasing voltage). (b) Corresponding ferromagnetic resonance linewidth  $\mu_0 \Delta H_{\text{pp}}$  and magnetic field value of minima ( $\mu_0 H_{\text{min}}$ ) and maxima ( $\mu_0 H_{\text{max}}$ ) of the spectra. The lines are guides to the eye.

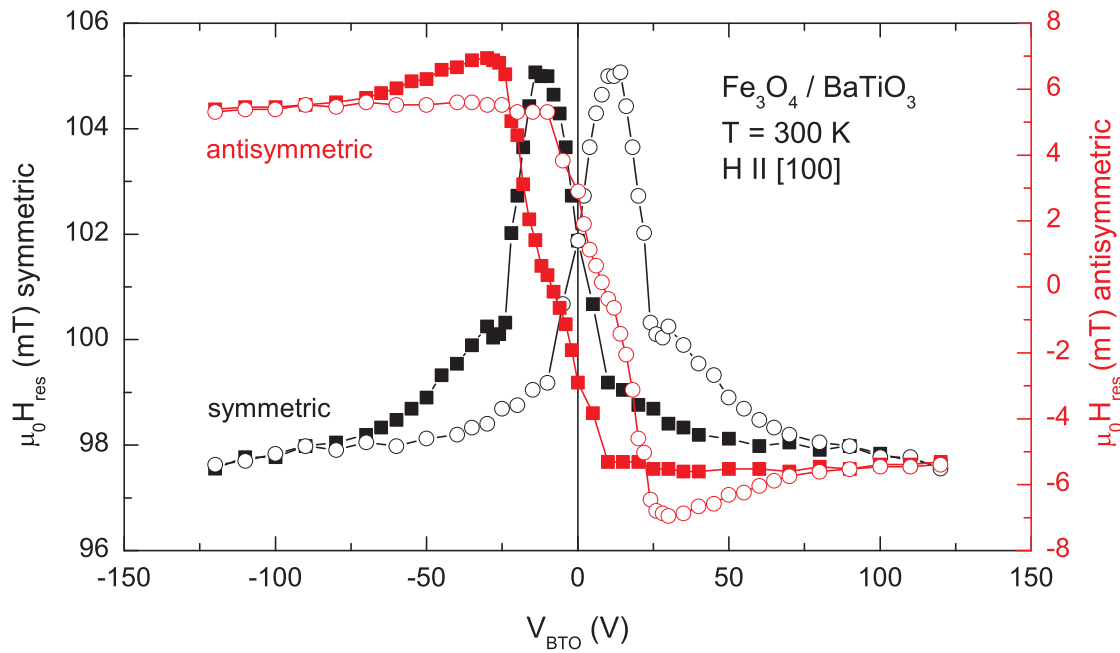


**Figure 7.11:** Symmetric and antisymmetric contributions to the electric field dependent shift of the ferromagnetic resonance fields for  $\mathbf{H}_0 \parallel [100]$  (the lines are guides to the eye).

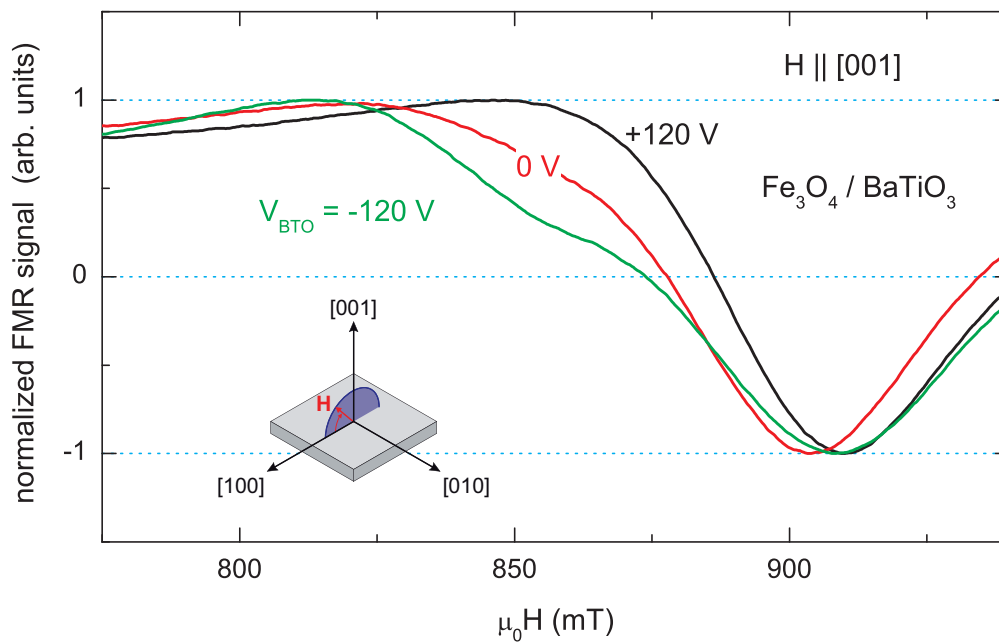


**Figure 7.12:** Spectra recorded with  $\mathbf{H}_0 \parallel [001]$  at maximum poling voltages  $V_{\text{BTO}} = \pm 120 \text{ V}$  and  $V_{\text{BTO}} = 0 \text{ V}$ . The emergence of a second FMR line at  $V_{\text{Piezo}} = -120 \text{ V}$  is clearly visible.

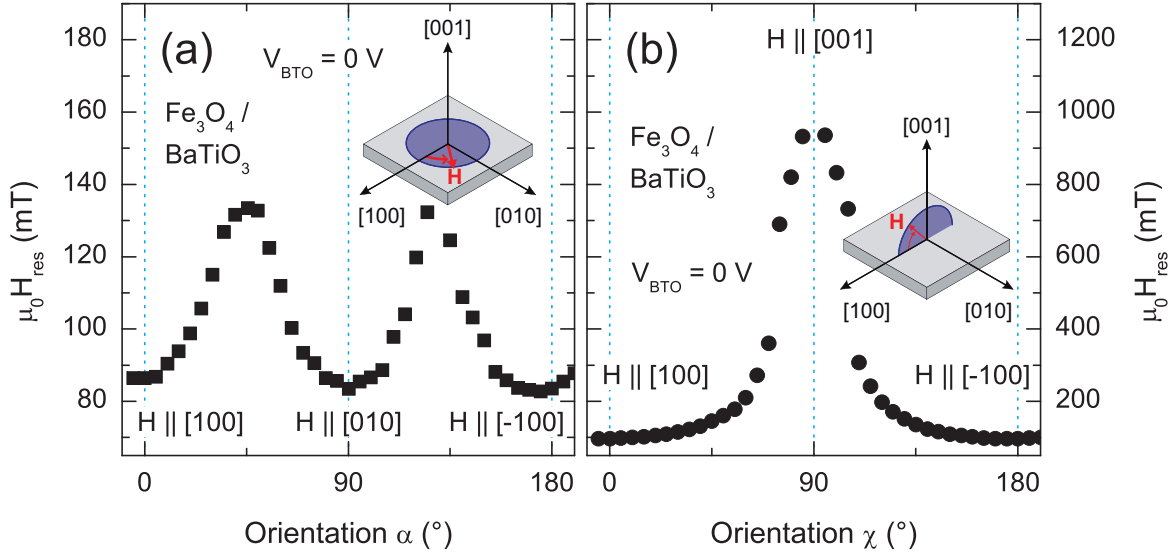


**Figure 7.13:** (a) FMR resonance fields  $\mu_0 H_{\text{res}}$  obtained for the rotation of  $\mathbf{H}_0$  in the (001) plane. (b)  $\mu_0 H_{\text{res}}$  obtained for the rotation of  $\mathbf{H}_0$  in the (010) plane.

$g$ -factor	$\frac{K_{c1}}{M_s}$ (mT)	$\frac{K_{u,[010]}}{M_s}$ (mT)	$\frac{K_{u,\text{eff},[001]}}{M_s}$ (mT)
2.12	13	0	390

**Table 7.1:** Anisotropy constants of  $\text{Fe}_3\text{O}_4/\text{BaTiO}_3$  at  $V_{\text{BTO}} = 0$  V determined from numerical simulations.

## 7.6.2 Discussion

We use the free energy  $F_{\text{tot}}$  from Eq. (6.3) and perform numerical simulations to determine the anisotropy constants of the  $\text{Fe}_3\text{O}_4$  film at  $V_{\text{BTO}} = 0$  V. The procedure is identical to that described in Chapter 6, and thus only the calculated anisotropy fields are presented here in Tab. 7.1. The  $g$ -factor in Tab. 7.1 is identical to the bulk value found in Tab. 3.4 and similar cubic anisotropy fields were reported for  $\text{Fe}_3\text{O}_4$  on MgO in [56].

From the measurements performed with  $\mathbf{H}_0 \parallel [100]$  (cf. Fig. 7.10(a)) we see that we are able to reversibly tune the FMR resonance field by up to 15 mT by the application of an electric field. As the voltage dependent change in linewidth is no more than 5 mT, a change of lineshape can be ruled out as the origin of the voltage dependent shift of the FMR resonance field. Furthermore, given the systematic evolution of the

resonance field as a function of  $V_{\text{BTO}}$ , spurious effects such as temperature drift can be excluded. The microwave frequency was stable to  $1 \times 10^{-4}$ , thus frequency drift also cannot be the cause for the FMR resonance field shift. Moreover, possible effects of the voltage dependent dielectric constant of  $\text{BaTiO}_3$  [102] on the microwave field in the cavity [103] can be excluded as the cause for resonance field shift as well due to the independence of the ESR resonance fields from  $V_{\text{BTO}}$ .

Fig. 7.11 shows that the antisymmetric contribution dominates by a factor of approximately 2 over the symmetric contribution for the in-plane FMR measurements.

The shoulders in the recorded current (cf. Fig. 7.10(a)) correspond to the displacement currents accompanying any polarization change in the  $\text{BaTiO}_3$  substrate. The asymmetry of the current is not observed if two electrodes of identical material are used to pole a  $\text{BaTiO}_3$  crystal. Thus the asymmetry is attributed to an electrode effect, probably caused by a space charge region.

Assuming that we observe a change in magnetic anisotropy as a function of  $V_{\text{BTO}}$ , we conclude that the [100] axis is magnetically harder for  $V_{\text{BTO}} < 0\text{V}$  than it is for  $V_{\text{BTO}} > 0\text{V}$ . Regarding only the symmetric contribution (cf. Fig. 7.11) the [100] direction is harder in the  $\text{BaTiO}_3$  multi-domain state than in the single-domain state.

In conclusion, the FMR measurements corroborate the conclusion drawn from the SQUID data: We observe a converse magnetoelectric effect which dominantly affects the magnetic anisotropy of the  $\text{Fe}_3\text{O}_4$  film.

## 7.7 Theoretical description

In the introductory remarks to this Chapter we mentioned that the converse magnetoelectric effect in multiferroic heterostructures is dominantly strain-mediated. Two different effects for a strain-mediated influence of the electric field on the magnetization were proposed: The piezoelectric effect, describing the *macroscopic* deformation of the ferroelectric phase (and thus the compound) as a function of electric field, and ferroelectric domain (re)formation that leads to *local* strains.

As both effects are expected to be purely symmetric with respect to the external electric field, both models presented in the following can only explain influences on the magnetization that are symmetric as well.

The observed contribution antisymmetric to the influence of the electric field on magnetization can thus not be explained in the context of the following theories.

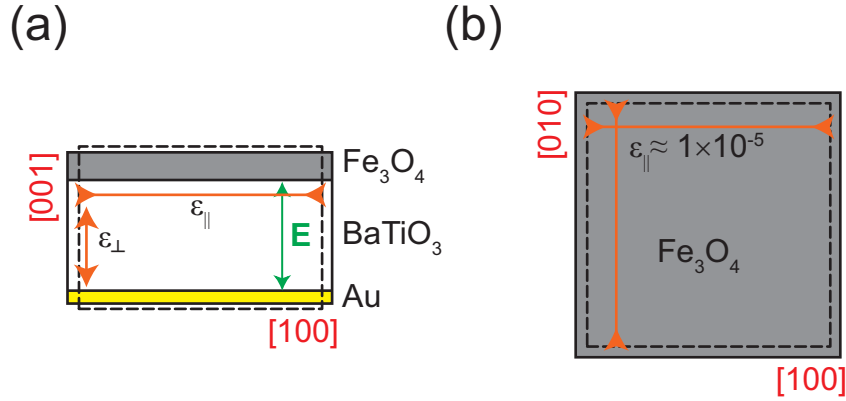


**Figure 7.14:** (a) Side view and (b) top view of our heterostructure. The dotted lines show the macroscopic deformation of the heterostructure in an external electric field. This deformation is isotropic in the film plane.

In the last section of this Chapter, possible causes for the antisymmetric effect are summarized.

### 7.7.1 Linear piezoelectric effect

The piezoelectric effect describes the expansion (or contraction) of a single domain ferroelectric crystal as a function of electric field (cf. Chapter 2). As the electric field in our case is applied perpendicular to the sample plane, a piezoelectric  $d_{31}$ -effect is expected. This is schematically shown in Fig. 7.14. Hence, we expect the piezoelectric  $d_{31}$ -effect to result in a uniform, voltage dependent in-plane strain  $\varepsilon_1 = \varepsilon_2 = \varepsilon_{\parallel}$  that is expected to be losslessly transferred into the  $Fe_3O_4$  film.

The magnitude of this strain can be described by the magnitude of the linear piezoelectric  $d_{31}$ -effect of  $BaTiO_3$  for  $E > -E_c$  (or  $E < E_c$ , with the symmetry  $\varepsilon_{\parallel}(E) = \varepsilon_{\parallel}(-E)$ ):

$$\varepsilon_{\parallel} = d_{31}E_3 = d_{31} \frac{V_{BTO}}{x_{BTO}}, \quad (7.2)$$

with  $d_{31}$  from Tab. 3.5 and the substrate thickness  $x_{BTO} \approx 400 \mu\text{m}$ . The thus calculated in-plane strain  $\varepsilon_{\parallel}$  is shown in Fig. 7.15 as a function of  $V_{BTO}$ . According to elastic theory, the in-plane strain  $\varepsilon_{\parallel}$  results in an out-of-plane strain  $\varepsilon_{\perp}$  in the magnetite film that can be calculated according to Chapter 5. We once again assume that the film can freely expand in the out-of-plane direction, thus no out-of-plane stress is

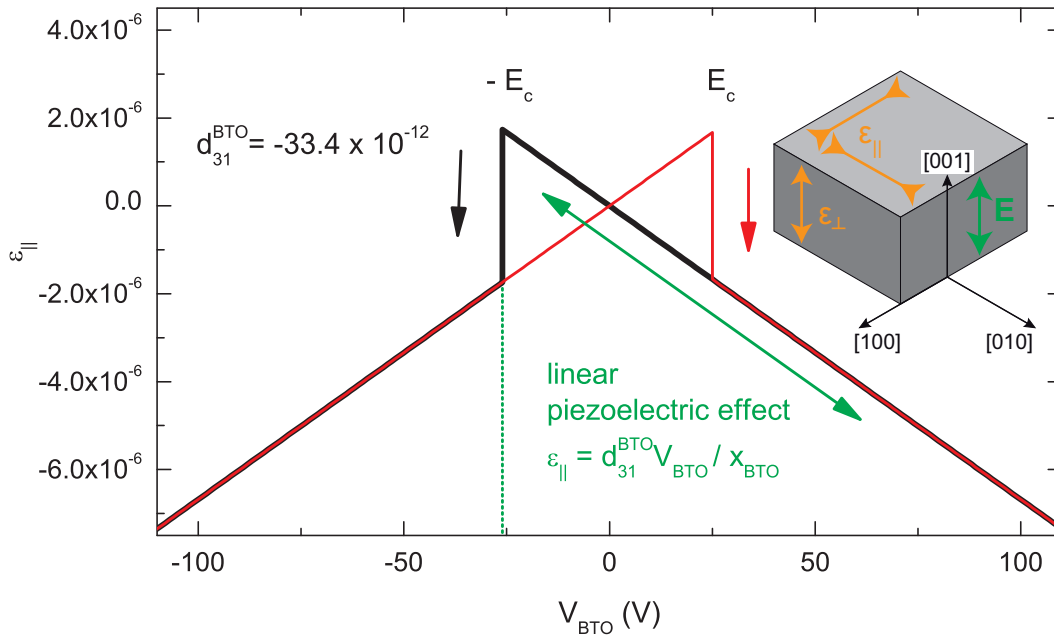


**Figure 7.15:** The electric field  $\mathbf{E}$  is applied perpendicular to the sample plane. We thus observe a  $d_{31}$ -effect at the  $\text{Fe}_3\text{O}_4/\text{BaTiO}_3$  interface.

present:  $\sigma_{\perp} = 0$ . This yields the out-of-plane strain

$$\begin{aligned} \varepsilon_{\perp}(V_{\text{BTO}}) &= -\frac{c_{12}^{\text{Fe}_3\text{O}_4}}{c_{11}^{\text{Fe}_3\text{O}_4}}(\varepsilon_1 + \varepsilon_2) \\ &= -2\frac{c_{12}^{\text{Fe}_3\text{O}_4}}{c_{11}^{\text{Fe}_3\text{O}_4}}\varepsilon_{\parallel}. \end{aligned} \quad (7.3)$$

With the  $\text{Fe}_3\text{O}_4$  elastic moduli taken from Tab. 3.4 we can calculate the strain  $\Delta\varepsilon$  in the film if  $V_{\text{BTO}}$  is lowered from its extreme value  $V_{\text{BTO}} = +120 \text{ V}$  to  $V_{\text{BTO}} = -25 \text{ V}$ :

$$\begin{aligned} \Delta\varepsilon_{\parallel} &= \varepsilon_{\parallel}(-25 \text{ V}) - \varepsilon_{\parallel}(+120 \text{ V}) = 1.2 \times 10^{-5} \\ \Delta\varepsilon_{\perp} &= -9.3 \times 10^{-6}. \end{aligned} \quad (7.4)$$

This strain corresponds to the largest piezoelectric stroke in the voltage range  $-120 \text{ V} \leq V_{\text{BTO}} \leq +120 \text{ V}$  (cf. Fig. 7.15). Thus it gives an approximation of the largest expected effect due to the piezoelectric-magnetoelastic coupling.

We can now apply magnetoelastic theory and calculate the magnetoelastic anisotropy constants. In the previous Chapter, the expressions for the magnetoelastic anisotropy constants were derived in Eq. (6.11). Considering the appropriate material constants

and the isotropic in-plane strain  $\varepsilon_1 = \varepsilon_2 = \varepsilon_{\parallel}$ , the following expressions can easily be derived with the strains from Eq. (7.4):

$$\begin{aligned}
K_{u,\text{magel},[010]} &= \frac{3}{2}\lambda_{100}^{\text{Fe}_3\text{O}_4}(c_{12}^{\text{Fe}_3\text{O}_4} - c_{11}^{\text{Fe}_3\text{O}_4})(\varepsilon_2 - \varepsilon_1) \\
&= \frac{3}{2}\lambda_{100}^{\text{Fe}_3\text{O}_4}(c_{12}^{\text{Fe}_3\text{O}_4} - c_{11}^{\text{Fe}_3\text{O}_4})(\Delta\varepsilon_{\parallel} - \Delta\varepsilon_{\parallel}) = 0 \\
K_{u,\text{magel},[001]} &= \frac{3}{2}\lambda_{100}^{\text{Fe}_3\text{O}_4}(c_{12}^{\text{Fe}_3\text{O}_4} - c_{11}^{\text{Fe}_3\text{O}_4})(\varepsilon_3 - \varepsilon_1) \\
&= \frac{3}{2}\lambda_{100}^{\text{Fe}_3\text{O}_4}(c_{12}^{\text{Fe}_3\text{O}_4} - c_{11}^{\text{Fe}_3\text{O}_4})(\Delta\varepsilon_{\perp} - \Delta\varepsilon_{\parallel}) = -106.7 \text{ N/m}^2.
\end{aligned} \tag{7.5}$$

The anisotropy constant  $K_{u,\text{magel},[001]}$  in this equation corresponds to the anisotropy field  $K_{u,\text{magel},[001]}/M_s = -0.35 \text{ mT}$  calculated with a saturation magnetization  $M_s = 305 \text{ kA/m}$  reported for similar films [56] (as the film thickness is unknown,  $M_s$  could not be calculated from SQUID measurements). Comparison of this value to the net unstrained anisotropy yields a negligible contribution to the out-of-plane anisotropy field which was determined from measurements at  $V_{\text{BTO}} = 0 \text{ V}$  to  $K_{u,[001]}/M_s = 390 \text{ mT}$ .

Furthermore, the piezoelectric effect predicts no magnetoelastic contribution to the in-plane anisotropy:  $K_{u,\text{magel},[010]} = 0$  (cf. Eq. (7.5)). Thus the in-plane anisotropy is independent of  $V_{\text{BTO}}$  in this model.

We however clearly observe an effect of  $V_{\text{BTO}}$  on the in-plane magnetization in SQUID measurements, that was accounted to a change in magnetic anisotropy as a function of  $V_{\text{BTO}}$ . This effect can not be explained by the piezoelectric effect. Instead of considering macroscopic deformations due to the piezoelectric effect, we thus now will investigate the domain-related strains in the heterostructure.

## 7.7.2 Domain effects

The magnetite unit cell ( $a^{\text{Fe}_3\text{O}_4} = 0.8396 \text{ nm}$ ) comprises slightly more than four barium titanate unit cells ( $a^{\text{BTO}} = 0.399 \text{ nm}$  and  $c^{\text{BTO}} = 0.404 \text{ nm}$ ) at the  $Fe_3O_4/BaTiO_3$  interface. For the sake of simplicity, in the following, we will neglect the lattice mismatch and assume the  $Fe_3O_4$  unit cell to span exactly four  $BaTiO_3$  unit cells. We furthermore assume that the strain transmission is lossless, so that the results obtained in the following are an approximation of the maximum expected effect.

At room temperature, each  $BaTiO_3$  tetragonal unit cell may show a rectangular ( $a$ -domain) or square ( $c$ -domain) surface to the magnetite film (cf. Fig. 7.16(a)). We

BaTiO <sub>3</sub> domain	$\varepsilon_1$	$\varepsilon_2$	$\varepsilon_3$	$\frac{K_{u,\text{magel},[010]}}{M_s}$ (mT)	$\frac{K_{u,\text{magel},[001]}}{M_s}$ (mT)
$c$	0	0	0	0	0
$a_1$	0	0.0125	-0.0048	211	-82
$a_2$	0.0125	0	-0.0048	-211	-293

**Table 7.2:** Local strains and magnetoelastic anisotropy constants.

will now consider the strains in the  $a_1$ -,  $a_2$  and  $c$ -domains.

In  $c$ -domains – that show a square surface to the magnetite film – only isotropic strains are present in our simplified model. These isotropic strains do not alter the in-plane magnetic anisotropy. Due to the net cubic crystalline anisotropy of Fe<sub>3</sub>O<sub>4</sub> (cf. Fig. 7.13(a)) the easy axes are along the [100] and [010] directions. Hence in those regions where the Fe<sub>3</sub>O<sub>4</sub> film is clamped to BaTiO<sub>3</sub>  $c$ -domains, the easy axes will be unaffected. This is schematically shown in Fig. 7.16(a).

In contrast,  $a$ -domains induce anisotropic strains into the respective regions of the Fe<sub>3</sub>O<sub>4</sub> film. Because of the negative magnetostrictive constant  $\lambda = -20 \times 10^{-6}$  of Fe<sub>3</sub>O<sub>4</sub>, the BaTiO<sub>3</sub>  $a_1$ -domains induce an easy axis along the [100] direction into the magnetite film (cf. Fig. 7.16(a)). In BaTiO<sub>3</sub>  $a_2$ -domains an easy axis along the [010] direction is induced into the magnetite film.

In the following, we calculate the magnitude of this strain-induced, domain-wise anisotropy. The local strains  $\varepsilon_1 \parallel [100]$  and  $\varepsilon_2 \parallel [010]$  are  $\{\varepsilon_1 = 0, \varepsilon_2 = (c^{\text{BTO}} - a^{\text{BTO}})/a^{\text{BTO}}\}$  in  $a_1$  domains and  $\{\varepsilon_1 = (c^{\text{BTO}} - a^{\text{BTO}})/a^{\text{BTO}}, \varepsilon_2 = 0\}$  in  $a_2$ -domains (cf. Fig. 7.16(a)). The out-of-plane strain  $\varepsilon_{\perp} = \varepsilon_3$  is calculated according to Eq. (7.3). To estimate the strain-induced anisotropy fields  $K_{u,\text{magel},[010]}/M_s$  and  $K_{u,\text{magel},[001]}/M_s$  we use Eq. (7.5). Tab. 7.2 shows the strains in the three possible BaTiO<sub>3</sub> domains and the thus calculated magnetoelastic anisotropy constants of the regions of the Fe<sub>3</sub>O<sub>4</sub> film clamped to each respective BaTiO<sub>3</sub> domain.

We will now evaluate whether this domain-wise magnetoelastic model is capable of explaining the SQUID-measurements with  $\mathbf{H} \parallel [100]$ . Due to the anisotropy field  $K_{u,\text{magel},[010]}/M_s = -211$  mT (cf. Tab. 7.2), there is a finite angle between the [100] direction and  $\mathbf{m}$  even at fields larger than  $\mu_0 H = 100$  mT in  $a_2$ -domains. As the SQUID-magnetometer is only sensitive to the projection  $m$  of  $\mathbf{m}$  to [100], any  $a_2$ -domain will reduce the observed magnetization as depicted in Fig. 7.16(b). Due to the  $P(E)$ -hysteresis, this model thus predicts an  $M(E)$ -loop as shown in the right of



Fig. 7.16(b). This  $M(E)$ -loop is in good qualitative agreement with the symmetric contribution to the SQUID measurements (cf. Fig. 7.6).

A rough approximation for the predicted magnitude of the symmetric contribution to the  $M(E)$ -loop will now be given at zero external magnetic field. HRXRD measurements showed that there are approximately 40%  $a$ -domains in the multi-domain state (cf. Fig. 7.3(b)). Assuming an equal amount of  $a_1$ - and  $a_2$ -domains, this yields 20% of the  $\text{Fe}_3\text{O}_4$  film clamped to  $a_2$ -domains, thus with the magnetization at an equilibrium orientation along  $[010]$  (cf. Fig. 7.16(a)). Hence the maximum observable effect on the magnetization projected to  $[100]$  is a reduction of 20%. In Fig. 7.7, an effect of approximately 10% can be seen, corroborating our model, considering its simple approach and the unknown distribution of  $a$ -domains into the  $a_1$  and  $a_2$  type. We note that the 10% effect observed in Fig. 7.7 can be explained in the context of this model, if 10%  $a_2$ -domains and 30%  $a_1$ -domains are assumed in the multi-domain  $\text{BaTiO}_3$  state.

If we regard the magnetization projection to the  $[001]$  direction, we expect all  $a$ -domains to result in an easier axis out of plane due to the negative anisotropy fields  $K_{\text{u,magel},[001]}/M_s < 0$  (cf. Tab. 7.2). This is in qualitative accordance with the SQUID-measurements performed with  $\mathbf{H} \parallel [001]$  (cf. Fig. 7.8(b)) that showed that  $\mathbf{m}$  rotates towards  $[001]$  in the multi-domain state.

However, there are clear indications that the model fails to quantitatively account for all experimental observations. According to Morrish [30], for  $\mathbf{H} \parallel [100]$ , the magnetization is expected to saturate at a magnetic field of  $\mu_0 H = 2K/M_s \approx 2K_{\text{u,magel},[010]}/M_s = -422 \text{ mT}$ . Thus for  $\mu_0 H \gtrsim 422 \text{ mT}$  the magnetization is predicted to be aligned along  $[100]$  even in  $a_2$ -domains. However, at  $\mu_0 H = 1 \text{ T}$  we still observe a 0.5% effect (cf. Fig. 7.7). This effect is very probably caused by the influence of  $V_{\text{BTO}}$  on  $m_s$  discussed above that is not included in this model.

Taken together, for the SQUID measurements, we find that this domain-wise strain model is capable of explaining the observed symmetric contribution to the  $M(E)$ -loops in good qualitative and quantitative agreement.

We will now investigate whether this model also accounts for the symmetric effect observed in FMR measurements for  $\mathbf{H}_0 \parallel [100]$  (cf. Fig. 7.11). FMR is sensitive to the magnetic hardness in the direction of the applied external magnetic field  $\mu_0 \mathbf{H}_0$ . Assuming an equal amount of  $a_1$ - and  $a_2$ -domains, the in-plane anisotropy of the entire film thus is independent of the fraction of  $a$ -domains and thus of the electric

field. Hence in this model we can explain the symmetric contribution to the FMR measurement (cf. Fig. 7.11) only for an unequal distribution of  $a$ -domains in the  $a_1$ - and  $a_2$ -type.

Note that the shoulders in the antisymmetric contribution to both SQUID and FMR measurements (cf. Figs. 7.6 and 7.11) can be explained as well if the fraction of  $a_1$ - to  $a_2$ -domains is different for increasing and decreasing  $V_{BTO}$ .

In conclusion, our simple, domain-wise model yields qualitative agreement to the symmetric contribution in all SQUID  $M(E)$ -loops for  $\mathbf{H} \parallel [100]$  and  $\mathbf{H} \parallel [001]$  as well as the FMR measurements for  $\mathbf{H}_0 \parallel [100]$ . If the distribution of  $a$ -domains into  $a_1$ - and  $a_2$ -domains is considered as a free parameter, even an exact quantitative match of theory and the experimentally derived symmetric contribution can be achieved.

### 7.7.3 Possible antisymmetric effects

The origin of the antisymmetric contribution to the  $M(E)$ -loops (cf. Fig. 7.6) and FMR measurements (cf. Fig. 7.11) can neither be explained by the domain-wise strain model (except for the shoulders) nor by the piezoelectric effect, as they both predict a symmetric dependence of magnetization on electric field.

We will now consider possible causes for the antisymmetric contribution to the SQUID  $M(E)$ -loops and the FMR measurements.

A tilting of the sample in the SQUID magnetometer's sample space in such a way that the external magnetic field  $\mathbf{H}$  and the sample's  $[100]$  (or  $[001]$ ) direction enclose a finite angle can not explain the antisymmetric contribution: Large electric fields of either sign both induce a single  $c$ -domain in the  $BaTiO_3$  substrate. Thus the magnetic anisotropy is expected to be identical for both large positive and large negative electric fields and any projection of the magnetization vector will yield the same result for both single  $c$ -domain states.

If we stick to the model of solely strain-induced effects, the observed antisymmetric behavior implies different saturated domain configurations at high negative and high positive electric fields. This was proven to be false in the bulk of the substrate by the purely symmetric HRXRD measurements. This leaves only local differences at the interface of substrate and film as a possible explanation.

A non strain-mediated magnetoelectric effect in heterostructures was predicted in  $Fe/BaTiO_3$  heterostructures by Duan et al. [98], which they account to the polarization dependent interface bonding that alters the saturation magnetization of the

ferromagnetic film. In conclusion, they predict an effect in the same order of magnitude as the strain dependent coupling at room temperature, but with the symmetry of polarization. As it is an interface effect due to the overlap of atomic orbitals and was predicted for a ferromagnetic Fe-film with a thickness of 1 nm, it is however unlikely that it still has an observable effect on the magnetization of our approximately 100 nm thick Fe<sub>3</sub>O<sub>4</sub> film. Furthermore, in Section 7.5.2, we already pointed out that we dominantly observe a change of magnetic anisotropy and not of the Fe<sub>3</sub>O<sub>4</sub> saturation magnetization.

In conclusion, the physical origin of the antisymmetric contribution is beyond the explanations so far discussed in this thesis. We however already showed that it is dominantly an effect of the magnetic anisotropy and not of saturation magnetization. We will now point out that the antisymmetric effect may be caused by an influence of the carrier density  $n$  in the Fe<sub>3</sub>O<sub>4</sub> film on its magnetic anisotropy  $K$ . The argument goes as follows: We observe an effect antisymmetric to the electric field  $E$ . The ferromagnetic phase (Fe<sub>3</sub>O<sub>4</sub>) is described by the order parameter  $\mathbf{M}$  and the external field  $\mathbf{H}$ , both of which are independent of  $\mathbf{E}$  apart from the *symmetric* strain-mediated converse magnetoelectric effect. However, the polarization  $\mathbf{P}$  in the ferroelectric phase (BaTiO<sub>3</sub>) shows the correct *antisymmetric* dependence on the electric field  $\mathbf{E}$  (cf. Fig. 2.1(b)). Now  $\mathbf{P}$  induces surface charges  $\sigma_{\text{BTO}}$  at the interface of Fe<sub>3</sub>O<sub>4</sub> and BaTiO<sub>3</sub>:

$$\sigma_{\text{BTO}} = P_3 . \quad (7.6)$$

Within the Thomas-Fermi screening length, these polarization charges are compensated by free charge carriers in the Fe<sub>3</sub>O<sub>4</sub> film. Thus the Fe<sub>3</sub>O<sub>4</sub> charge carrier density  $n$  is a function of  $P$ . Note that  $n(P)$  is antisymmetric to the electric field ( $n(E_3) = -n(-E_3)$ ) due to the antisymmetry of  $\mathbf{P}$  to  $\mathbf{E}$ . Hence we propose that the magnetic anisotropy  $K$  of Fe<sub>3</sub>O<sub>4</sub> is not only dependent on the strain  $\varepsilon$ , but on the free charge carrier density  $n$  in Fe<sub>3</sub>O<sub>4</sub> as well. Thus the Taylor expansion of  $K(n, \varepsilon)$  to the first order is:

$$K(n, \varepsilon) = K_0 + \frac{\partial K(n, \varepsilon)}{\partial n} n + \frac{\partial K(n, \varepsilon)}{\partial \varepsilon} \varepsilon . \quad (7.7)$$

Effects of the charge carrier density on magnetic anisotropy have been predicted [104], but so far no experimental evidence of an effect in the order of magnitude that we observe is known to us. As the Thomas-Fermi screening length is expected to be in

the nm scale due to the high charge carrier density of  $Fe_3O_4$ , the term proportional to  $n$  in Eq. (7.7) is a function of the  $Fe_3O_4$  film thickness. To validate the proposed effect of the charge carrier density on the magnetic anisotropy of  $Fe_3O_4$ , first of all further similar samples need to be investigated to confirm that we observe a generic effect. Samples with varying film thickness could provide information on the screening length, as the antisymmetric contribution is expected to decrease with increasing film thickness. Secondly, samples with smaller lateral dimensions that allow for a full determination of in-plane magnetic anisotropy by FMR are of great importance. Thus this heterostructure offers great potential for further experimental and theoretical investigations of its intriguing converse magnetoelectric effect.

# Chapter 8

## Temperature dependent magnetic resonance in $\text{Fe}_3\text{O}_4/\text{BaTiO}_3$ heterostructures

In the previous Chapter, the converse magnetoelectric effect in the magnetite ( $\text{Fe}_3\text{O}_4$ ) / barium titanate ( $\text{BaTiO}_3$ ) heterostructure was investigated at room temperature, that is in the tetragonal ferroelectric  $\text{BaTiO}_3$  phase. If the temperature is lowered, barium titanate exhibits two more ferroelectric phases. The lattice parameters of  $\text{BaTiO}_3$  thus show a distinct temperature dependence and it is hence expected that a significant stress can be exerted on the  $\text{Fe}_3\text{O}_4$  film as a function of temperature.

The temperature dependence of ferromagnetic and paramagnetic resonances of the heterostructure is presented and it is shown that the structural phase transitions of  $\text{BaTiO}_3$  have a distinct influence on the electron spin resonance (ESR) and ferromagnetic resonance (FMR) of the compound. The magnetic anisotropy of the  $\text{Fe}_3\text{O}_4$  film is derived in each investigated  $\text{BaTiO}_3$  phase and it is verified whether its temperature dependence can be explained by magnetoelastic theory.

### 8.1 Introduction

We investigate a sample consisting of an approximately 100 nm thick  $\text{Fe}_3\text{O}_4$  film deposited by Stephan Geprägs on an approximately 400  $\mu\text{m}$  thick  $\text{BaTiO}_3$  substrate with lateral dimensions of  $2 \times 2 \text{ mm}^2$  by pulsed laser deposition. The sample is schematically shown in Fig. 8.1(a). It is similar to the samples investigated in the previous Chapter, but no gold electrode is present here and all measurements were carried out

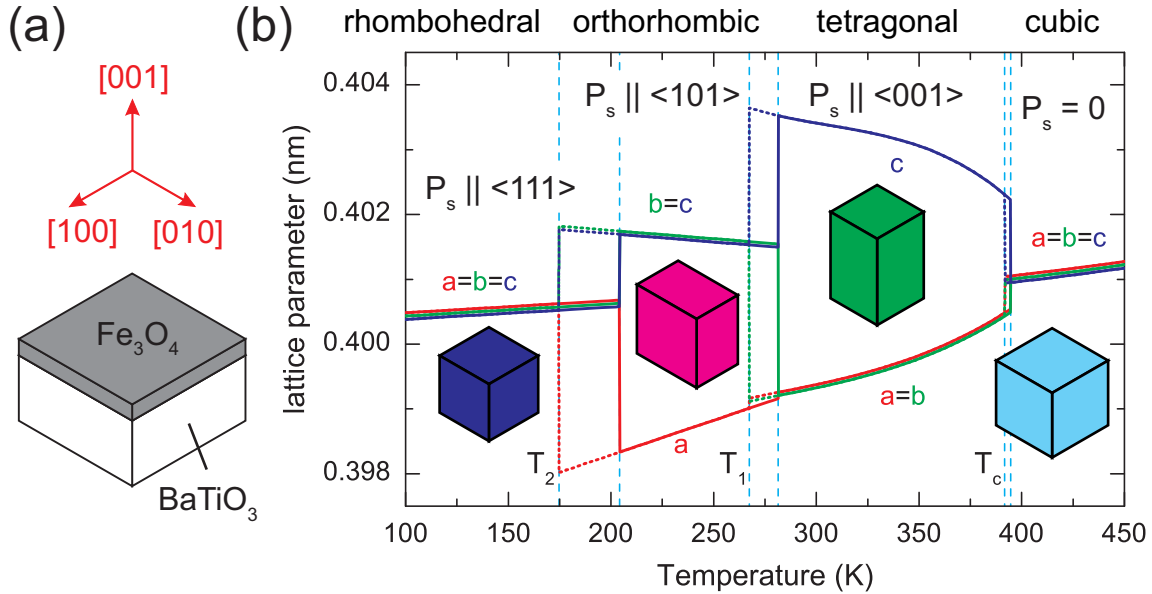


**Figure 8.1:** (a) Schematic view of the  $Fe_3O_4/BaTiO_3$  heterostructure. (b)  $BaTiO_3$  lattice parameters as a function of temperature [71] (solid lines: increasing temperature, dotted lines: decreasing temperature). The three marked transition temperatures are the Curie temperature  $T_c$ , the transition between the tetragonal and the orthorhombic ferroelectric phase at  $T_1$  and between the orthorhombic and rhombohedral phase at  $T_2$ . Transition temperatures are hysteretic (vertical dotted blue lines). The color code for the four  $BaTiO_3$  phases is used throughout this Chapter.

at zero electric field. The  $BaTiO_3$  substrate thus was always in the unpoled state (cf. Chapter 7).

In Chapter 3, the structural phase transitions of barium titanate were already introduced. Whereas at the Curie temperature  $T_c = 390$  K, a transition from the paraelectric cubic phase to the ferroelectric tetragonal phase occurs, barium titanate exhibits two more ferroelectric phases at lower temperatures. At a temperature of approximately  $T_1 = 280$  K a phase transition from the tetragonal to the orthorhombic state occurs, and at a temperature of approximately  $T_2 = 185$  K a phase transition from the orthorhombic to the rhombohedral state occurs ( $T_c$ ,  $T_1$  and  $T_2$  are hysteretic, cf. Fig. 8.1(b)). These phase transitions are accompanied by an abrupt change in the lattice parameters as can be seen in Fig. 8.1(b). The  $BaTiO_3$  lattice strain accompanying the phase transitions is expected to be transferred into the ferromagnetic thin

film and alter its magnetic anisotropy via magnetoelastic interactions.

The aim of this Chapter hence is to determine the magnetic anisotropy of the affixed  $\text{Fe}_3\text{O}_4$  thin film as a function of the stress exerted by the  $\text{BaTiO}_3$  substrate. To this end, we rely on ferromagnetic resonance measurements which will be discussed in the following.

## 8.2 Measurement results

All ESR and FMR measurements shown in this Chapter were carried out at a microwave frequency of 9.3 GHz using a Bruker ESP 300 spin resonance spectrometer that is described in Chapter 4. To allow for a precise temperature control in the range of  $100 \text{ K} \leq T \leq 400 \text{ K}$  a nitrogen cryostat was used. A liquid nitrogen reservoir was connected to the cryostat and the temperature was regulated using two heaters, one to control the  $\text{N}_2$  gas flow and the second one to heat the gas. The temperature was stable in all measurements within  $\pm 2 \text{ K}$  as checked with a temperature sensor in the sample space.

### 8.2.1 ESR spectra of barium titanate

Prior to the determination of the ferromagnetic resonance of the heterostructure, we investigated the electron spin resonance (ESR) of a pure  $\text{BaTiO}_3$  crystal to verify whether the structural phase transitions of  $\text{BaTiO}_3$  as a function of temperature affect its dynamic paramagnetic response. In Fig. 8.2, ESR spectra of the nominally undoped  $\text{BaTiO}_3$  crystal at two temperatures, in the tetragonal (300 K) and orthorhombic (235 K)  $\text{BaTiO}_3$  phase, are displayed for magnetic field orientations along the cartesian axes of the sample coordinate system (cf. Fig. 8.1(a)). At identical magnetic field orientations, a clear difference in the ESR spectra of the tetragonal and orthorhombic phase can be seen.

The first observation of paramagnetic resonances in  $\text{BaTiO}_3$  was reported by Hornig et al. [105, 106], who accounted the resonances to  $\text{Fe}^{3+}$  impurities located at the titanium position in the  $\text{BaTiO}_3$  unit cell. Also at the beginning of the investigation of paramagnetic resonances in  $\text{BaTiO}_3$ , Low and Shaltiel stated in their investigation of single crystal samples [107] that the high intensity of the ESR lines, as well as their dependence on the crystalline phase and polarization of  $\text{BaTiO}_3$ , is a strong indication that the ESR originates from  $\text{BaTiO}_3$  itself and not from impurities.

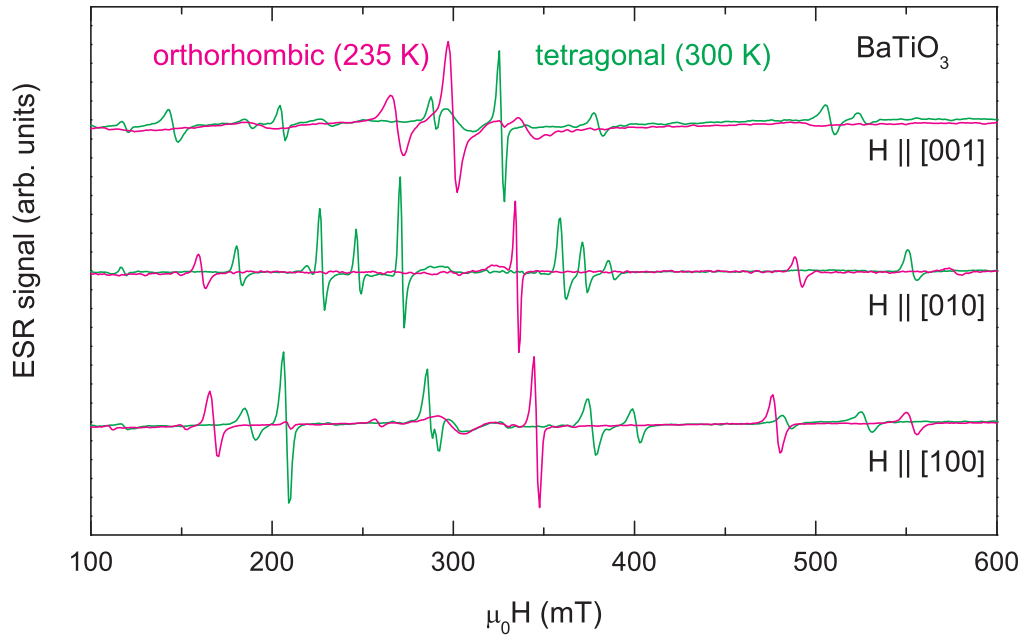


**Figure 8.2:** ESR spectra of BaTiO<sub>3</sub> in the tetragonal (300 K) and orthorhombic (235 K) phase with  $\mathbf{H}_0 \parallel [100]$  (in-plane),  $\mathbf{H}_0 \parallel [010]$  (in-plane) and  $\mathbf{H}_0 \parallel [001]$  (out-of-plane).

As we have (as will be discussed later) clear evidence of an irreversible change in the domain structure of BaTiO<sub>3</sub> upon a phase transition, but nevertheless observe very similar ESR spectra for each crystalline phase (cf. Fig. 8.5) – even if the sample underwent several phase transitions in between two measurements – we account the ESR lines to impurities. This is strongly underlined by the facts that calculations of the expected resonance fields for Fe<sup>3+</sup> impurities in the rhombohedral phase match the experimental data for similar BaTiO<sub>3</sub> crystals [108] and that the paramagnetic resonances originating from the Ti<sup>4+</sup> ion are only visible at temperatures below 35 K [109]. As the paramagnetic defects’ nature and concentration may vary for different crystals, no exact match of the here observed paramagnetic resonances to those of the sample used for further measurements is observed.

### 8.2.2 Temperature dependence of FMR

We now investigate the ferromagnetic resonance (FMR) of the Fe<sub>3</sub>O<sub>4</sub>/BaTiO<sub>3</sub> heterostructure as a function of temperature at zero applied electric field. The sample shown in Fig. 8.1(a) was mounted in the in-plane configuration to allow for a rotation

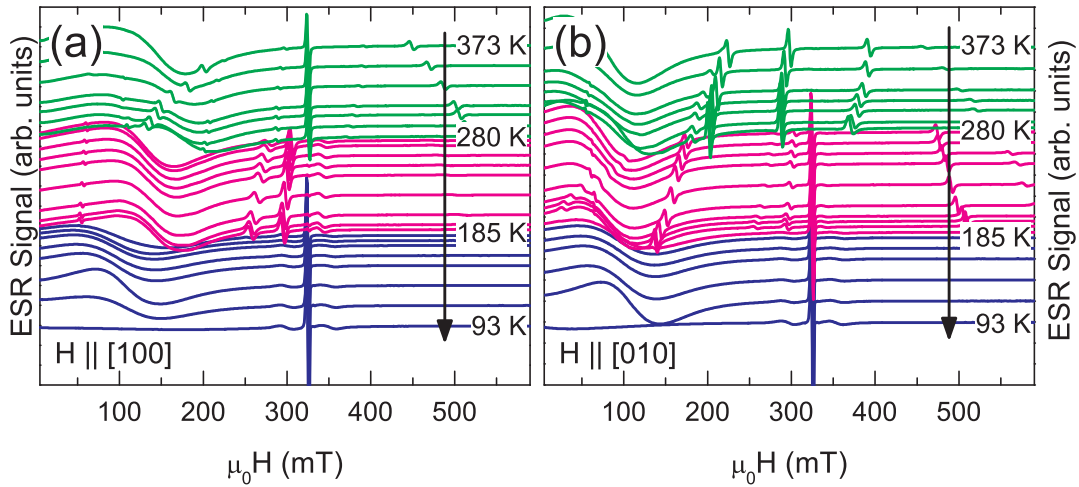


**Figure 8.3:** ESR spectra as a function of temperature for (a)  $\mathbf{H}_0 \parallel [100]$  and (b)  $\mathbf{H}_0 \parallel [010]$ . Color coding denominates the tetragonal, orthorhombic and rhombohedral phase according to Fig. 8.1(b).

of the magnetic field  $\mathbf{H}_0$  in the (001) plane. At any selected temperature in the range  $93 \text{ K} \leq T \leq 373 \text{ K}$  two ESR spectra were recorded with the magnetic field along the [100] and [010] direction, respectively. This temperature range encloses all three ferroelectric BaTiO<sub>3</sub> phases (cf. Fig. 8.1(b)). Unfortunately, no measurements in the cubic paraelectric phase could be carried out, as no stable microwave tuning could be achieved for  $T > 390 \text{ K}$ . This is likely due to the order-disorder phase transition at  $T = T_c$  that causes a discontinuity of the dielectric constant [11] in the BaTiO<sub>3</sub> substrate. It is hence proposed that a smaller sample would yield a stable microwave tuning even for  $T \geq T_c$ . However, due to time constraints, the measurements presented in this Chapter could not be repeated with a smaller sample.

In the ferroelectric phases, one measurement series was performed at increasing and one at decreasing temperature. The raw data for the measurement series recorded at decreasing temperature is shown in Fig. 8.3(a) for  $\mathbf{H}_0 \parallel [100]$  and in Fig. 8.3(b) for  $\mathbf{H}_0 \parallel [010]$ . Each single spectrum shows one broad line that is clearly identified as a ferromagnetic resonance and is missing in the spectra obtained from the pure BaTiO<sub>3</sub> crystal (cf. Fig. 8.2). We observe that the ESR lines do not match those acquired for the pure BaTiO<sub>3</sub> sample, indicating differences in the impurities of the two crystals. One can clearly see the qualitative change in the spectra at temperatures  $T_1 = 280 \text{ K}$  and  $T_2 = 185 \text{ K}$ . The transition temperatures  $T_1$  and  $T_2$  are in reasonable agreement

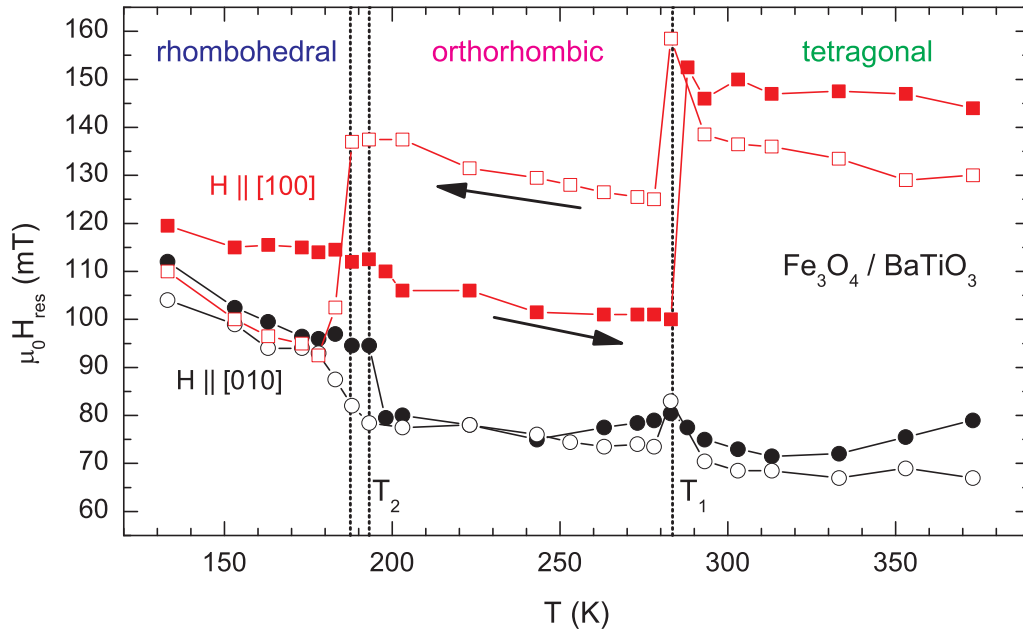


**Figure 8.4:** Ferromagnetic resonance fields as a function of temperature (the lines are guides to the eye only).

with the expected transition temperatures displayed in Fig. 8.1(b) and hence the qualitative change in the spectra can clearly be attributed to the structural phase transitions of  $\text{BaTiO}_3$ . The shift of the  $\text{BaTiO}_3$  transition temperatures in crystals of high crystalline quality with respect to the values commonly referred to in literature was reported in [110] as well. Similar transition temperatures can be found in the thesis of Matthias Althammer [111].

We now extract the FMR resonance field  $\mu_0 H_{\text{res}}$  from the ESR spectra obtained for increasing (not shown) and decreasing (cf. Fig. 8.3) temperature. The result is shown in Fig. 8.4. One can clearly observe the discontinuous shift of the FMR resonance field at the  $\text{BaTiO}_3$  transition temperatures, whereas the resonance field varies only slowly within one  $\text{BaTiO}_3$  phase. This is a clear proof of the influence of the structural phase transitions on the magnetization of the ferromagnetic film. We observe a small temperature hysteresis at the lower transition temperature  $T_2$  but none at  $T_1$ .

Furthermore, we observe that the resonance fields for increasing and decreasing temperature do not coincide for  $\mathbf{H}_0 \parallel [100]$  (cf. Fig. 8.4). Thus we assume that the magnetization is irreversibly changed upon a  $\text{BaTiO}_3$  phase transition. Similar results (including the irreversible magnetization change) were recently obtained for films of ferromagnetic  $\text{CoFe}_2\text{O}_4$  on  $\text{BaTiO}_3$  [112] and Fe films on  $\text{BaTiO}_3$  [113]. Both

publications attribute the change of magnetization at the structural phase transitions of BaTiO<sub>3</sub> to interface strain coupling. The irreversible change of magnetization is hence a clear indication of an irreversible change in the BaTiO<sub>3</sub> domain structure upon a phase transition.

Further evidence for a new domain formation upon every phase transition was found by a second run (not shown) of the measurement series shown in Fig. 8.4 that yielded non-comparable FMR resonance fields, while still showing discontinuous resonance field jumps at the BaTiO<sub>3</sub> transition temperatures.

### 8.2.3 Magnetic anisotropy of the Fe<sub>3</sub>O<sub>4</sub> film as a function of the BaTiO<sub>3</sub> crystalline phase

After finding strong evidence for strain coupled effects of the BaTiO<sub>3</sub> structural phase transitions on the magnetization of the Fe<sub>3</sub>O<sub>4</sub> thin film, we now quantitatively determine the magnetic anisotropy in each BaTiO<sub>3</sub> structural phase. As each crystalline phase transition evokes a distinct change in lattice constants (cf. Fig. 8.1(b)), a significant amount of strain is expected to be transmitted into the magnetite thin film upon a barium titanate phase transition. For a single domain substrate, the lattice constant change would according to Fig. 8.1(b) induce uniaxial strains in the film plane in the order of one percent. Strains within one phase are one order of magnitude smaller but thus still in the order of strains exerted by piezoelectric actuators (cf. Chapter 6). However, as no electric field is applied to the ferroelectric BaTiO<sub>3</sub> substrate, it remains in an unpoled multidomain state in all ferroelectric phases.

We recorded the full magnetic anisotropy for temperatures in all three BaTiO<sub>3</sub> ferroelectric phases. Raw data of the measurements performed in the in-plane configuration ( $\mathbf{H}_0$  rotated in the (001) plane) at temperatures ranging from the tetragonal to the rhombohedral substrate phase are shown in Fig. 8.5. It is noteworthy that only the measurements at  $T = 258$  K and  $T = 288$  K were performed in direct succession while the sample was exposed to room temperature in between all other measurements. One can clearly see that the spectra change qualitatively upon a phase transition but remain qualitatively the same at two different temperatures within one BaTiO<sub>3</sub> phase.

To determine the FMR resonance field, two attempts were made. Besides the so far applied procedure of determining the minimum and maximum magnetic field of the FMR resonance and calculating the resonance field to the mean value of the extrema, we assumed an angular independent linewidth and only determined the minimum

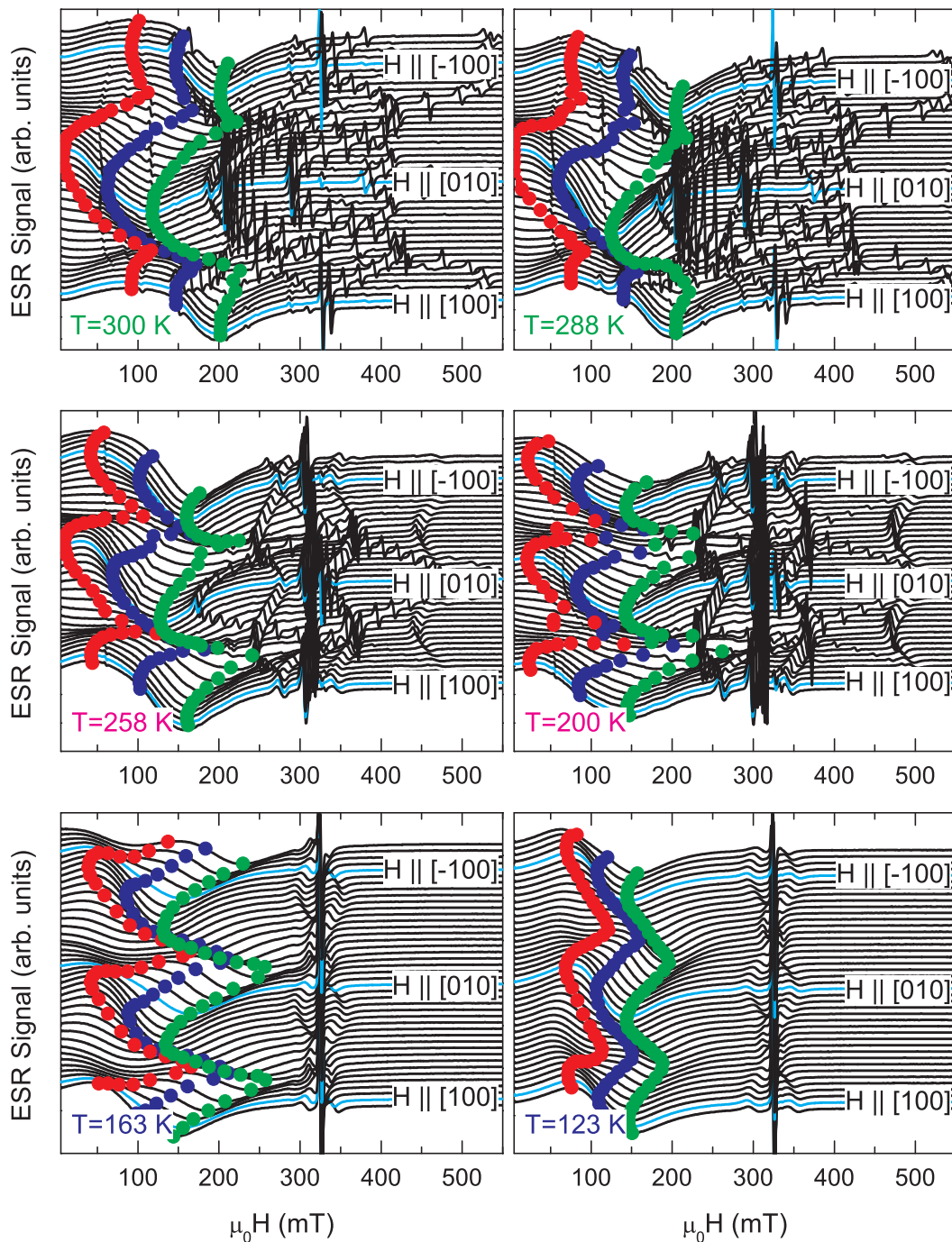


**Figure 8.5:** Angular dependence of ESR spectra in the different  $BaTiO_3$  crystalline phases. First row: tetragonal phase, middle row: orthorhombic phase, bottom row: rhombohedral phase. The blue symbols depict the ferromagnetic resonance field obtained from the minimum of the ferromagnetic resonance line (green symbols) by the assuming an angular independent linewidth.

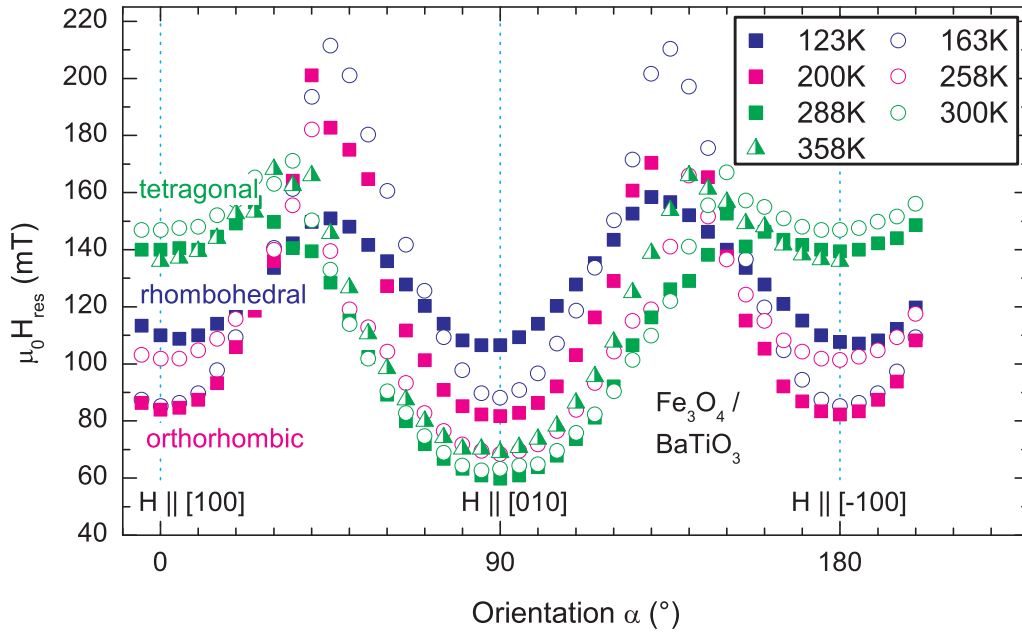


**Figure 8.6:** In-plane angular anisotropy of the ferromagnetic resonance fields of  $\text{Fe}_3\text{O}_4/\text{BaTiO}_3$  in the different  $\text{BaTiO}_3$  crystalline phases.

(green symbols in Fig. 8.5) of the FMR line and calculated the maximum (red symbols) and the resonance field (blue symbols). This approach was used as the maximum of the FMR line could not unambiguously be determined at certain temperatures and magnetic field orientations. The thus calculated maxima (red symbols in Fig. 8.5) are in good agreement with the experimental data.

The FMR resonance fields obtained with the latter approach are displayed in Fig. 8.6. We observe a dominant cubic anisotropy in the rhombohedral  $\text{BaTiO}_3$  phase (blue symbols in Fig. 8.6). In the tetragonal phase (green symbols) we observe very similar results for  $288 \text{ K} \leq T \leq 358 \text{ K}$  (spectra at  $T = 358 \text{ K}$  not shown in Fig. 8.5). All measurements in the tetragonal phase show a global minimum of the FMR resonance field at  $\mathbf{H}_0 \parallel [010]$ , thus a uniaxial in-plane anisotropy is present. In the orthorhombic phase, the anisotropy shows a qualitative change as a function of temperature that will be investigated in more detail in the next Section.

We will now quantify the magnetic anisotropy as a function of temperature by performing numerical simulations of the resonance fields.

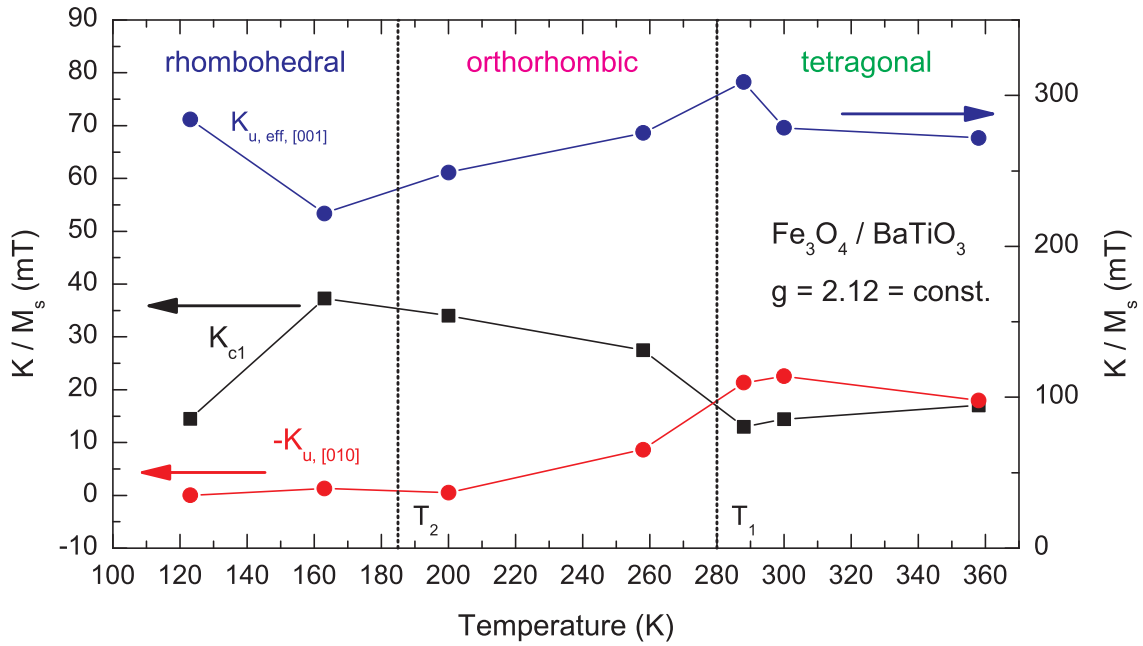


**Figure 8.7:** Anisotropy fields of  $\text{Fe}_3\text{O}_4/\text{BaTiO}_3$  as a function of temperature (the lines are guides to the eyes).

### 8.3 Numerical simulations

We perform numerical simulations of the resonance fields shown in Fig. 8.6 to obtain the anisotropy fields. To this end, we use the magnetic free energy density  $F_{\text{tot}}$  from Eq. (6.3). The procedure is identical to that described in Chapter 6, thus we will only present the results. Eq. (6.3) yields four fitting parameters  $K_{c1}/M_s$ ,  $K_{u,[010]}/M_s$  and  $K_{u,\text{eff},[001]}/M_s$  and the  $g$ -factor. The resulting anisotropy fields, that gave a good agreement of simulated and experimentally derived resonance fields, are displayed in Fig. 8.7. One clearly sees a qualitative change in magnetic anisotropy at the transition from the tetragonal to the orthorhombic state at  $T = T_1$ . Whereas in the tetragonal phase the magnetic anisotropy shows similar cubic and uniaxial contributions, it is dominantly cubic in the orthorhombic phase. No qualitative change of magnetic anisotropy upon the second phase transition at  $T = T_2$  is observed. The  $g$ -factor was assumed to be  $g = 2.12 = \text{const.}$  and corresponds to the bulk value for  $\text{Fe}_3\text{O}_4$  (cf. Tab. 3.4).

## 8.4 Theoretical description

In the following, we attempt to describe the change in magnetic anisotropy as a function of temperature using magnetoelastic theory. We neglect the temperature dependence of the magnetite cubic anisotropy constant  $K_{c1}$  in the temperature range  $123 \text{ K} \leq T \leq 358 \text{ K}$ . While a cubic anisotropy constant that is independent of temperature was reported for magnetite thin films on MgO substrates for  $5 \text{ K} \leq T \leq 300 \text{ K}$  [56], it is only a coarse approximation in our case, as the cubic anisotropy is clearly temperature dependent (cf. Fig. 8.7).

As all in-plane uniaxial anisotropies in cubic thin films are considered as a result of strain in the scope of this thesis, we model the entire change of anisotropy as a result of the strain transferred from the barium titanate to the film. In this simple model, the in-plane strains  $\varepsilon_1 \parallel [100]$  and  $\varepsilon_2 \parallel [010]$  are calculated as the average strain in the ferromagnetic thin film in the respective direction. No stress perpendicular to the sample is assumed and thus the out-of-plane strain  $\varepsilon_3$  in the  $\text{Fe}_3\text{O}_4$  film can be calculated according to Eq. (5.3).

Utilizing the additivity of the free energy density  $F_{\text{tot,magel}}(T) = F_{\text{tot}}(T^*) + F_{\text{magel}}(T)$ , we can start from the total free energy density  $F_{\text{tot}}(T^*)$  from Eq. (6.3) at any given temperature  $T^*$  and add the magnetoelastic free energy density  $F_{\text{magel}}(T)$ :

$$F_{\text{magel}}(T) = K_{\text{u,magel},[001]}(T) \sin^2 \Theta \cos^2 \Phi + K_{\text{u,magel},[010]}(T) \cos^2 \Phi \quad (8.1)$$

$$- \frac{1}{2} \lambda^{\text{Fe}_3\text{O}_4} (c_{12}^{\text{Fe}_3\text{O}_4} - c_{11}^{\text{Fe}_3\text{O}_4}) (\varepsilon_1(T) + \varepsilon_2(T) + \varepsilon_3(T)),$$

with  $F_{\text{magel}}(T^*) = 0$ . The temperature dependence of the anisotropic terms in Eq. (8.1) is given by the two magnetoelastic anisotropy constants:

$$K_{\text{u,magel},[010]}(T) = \frac{3}{2} \lambda_{100}^{\text{Fe}_3\text{O}_4} (c_{12}^{\text{Fe}_3\text{O}_4} - c_{11}^{\text{Fe}_3\text{O}_4}) (\varepsilon_2(T) - \varepsilon_1(T)) \quad (8.2)$$

$$K_{\text{u,magel},[001]}(T) = \frac{3}{2} \lambda_{100}^{\text{Fe}_3\text{O}_4} (c_{12}^{\text{Fe}_3\text{O}_4} - c_{11}^{\text{Fe}_3\text{O}_4}) (\varepsilon_3(T) - \varepsilon_1(T))$$

$$= \frac{3}{2} \lambda_{100}^{\text{Fe}_3\text{O}_4} (c_{12}^{\text{Fe}_3\text{O}_4} - c_{11}^{\text{Fe}_3\text{O}_4}) \left( -\frac{c_{12}^{\text{Fe}_3\text{O}_4}}{c_{11}^{\text{Fe}_3\text{O}_4}} (\varepsilon_1(T) + \varepsilon_2(T)) - \varepsilon_1(T) \right).$$

Adding  $F_{\text{magnet}}(T)$  to  $F_{\text{tot}}(T^*)$  results in the total free energy density:

$$\begin{aligned}
F_{\text{tot,magnet}}(T) = & -\mu_0 M H_0 (\sin \Theta \sin \Phi \sin \theta \sin \phi + \cos \Theta \cos \theta + \sin \Theta \cos \Phi \sin \theta \cos \phi) + \\
& (K_{\text{u,eff,[001]}}(T^*) + K_{\text{u,magnet,[001]}}(T)) \sin^2 \Theta \cos^2 \Phi + \\
& (K_{\text{u,[010]}}(T^*) + K_{\text{u,magnet,[010]}}(T)) \cos^2 \Theta + \\
& \frac{1}{4} K_{\text{c1}}(T^*) (\sin^2 (2\Theta) + \sin^4 \Theta \sin^2 (2\Phi)) , \tag{8.3}
\end{aligned}$$

with the side condition  $K_{\text{u,magnet,[001]}}(T^*) = K_{\text{u,magnet,[010]}}(T^*) = 0$ . In Eq. (8.3), isotropic terms are neglected as they do not influence the FMR resonance field (cf. Eqs. (4.5) and (4.6)).

In the following, we present a comparison of the measurements and magnetoelastic theory. In the theoretical description, the strains  $\varepsilon$  are free parameters, thus we will first present the free energy surfaces phenomenologically calculated from the experimentally determined resonance fields and then iteratively adjust the strains to give the best possible fit of magnetoelastic theory and experiment.

We calculate the free energy surfaces for  $123 \text{ K} \leq T \leq 358 \text{ K}$  from  $F_{\text{tot}}$  (cf. Eq. (6.3)) using the phenomenologically obtained anisotropy fields displayed in Fig. 8.7. This yields the simulation of the free energy depicted in Fig. 8.8 by solid lines.

In the next step, we attempt to find the best possible fit to these free energy surfaces in the context of the so far derived magnetoelastic theory. To this end we use  $F_{\text{tot,magnet}}(T)$  and arbitrarily choose  $T^* = 300 \text{ K}$  as the reference temperature. Thus we obtain  $K_{\text{u,eff,[001]}}(T^*)/M_s = 278.5 \text{ mT}$ ,  $K_{\text{u,[010]}}(T^*)/M_s = -22.5 \text{ mT}$  and  $K_{\text{c1}}/M_s = 14.4 \text{ mT}$  (cf. Fig. 8.7).

These values are inserted into Eq. (8.3) and  $K_{\text{u,magnet,[001]}}(T)/M_s$  and  $K_{\text{u,magnet,[010]}}(T)/M_s$  are iteratively adjusted to give the best fit of  $F_{\text{tot,magnet}}(T)$  to the afore phenomenologically calculated  $F_{\text{tot}}(T)$  at any temperature  $T$  with the anisotropy constants displayed in Fig. 8.7.

The resulting free energy contours of  $F_{\text{tot,magnet}}(T)$  in the (001) plane are depicted by the dotted lines in Fig. 8.8. The respective magnetoelastic anisotropy fields  $K_{\text{u,magnet,[010]}}(T)/M_s$  and  $K_{\text{u,magnet,[001]}}(T)/M_s$  are displayed in Fig. 8.9(a) as a function of temperature. One sees that magnetoelastic theory in general is capable of describing the change in the magnetic anisotropy of the Fe<sub>3</sub>O<sub>4</sub> film in good approximation for most temperatures. However, as the change in the cubic anisotropy is neglected, no perfect match is obtained in the orthorhombic phase ( $T = 200 \text{ K}$  and  $T = 258 \text{ K}$ )

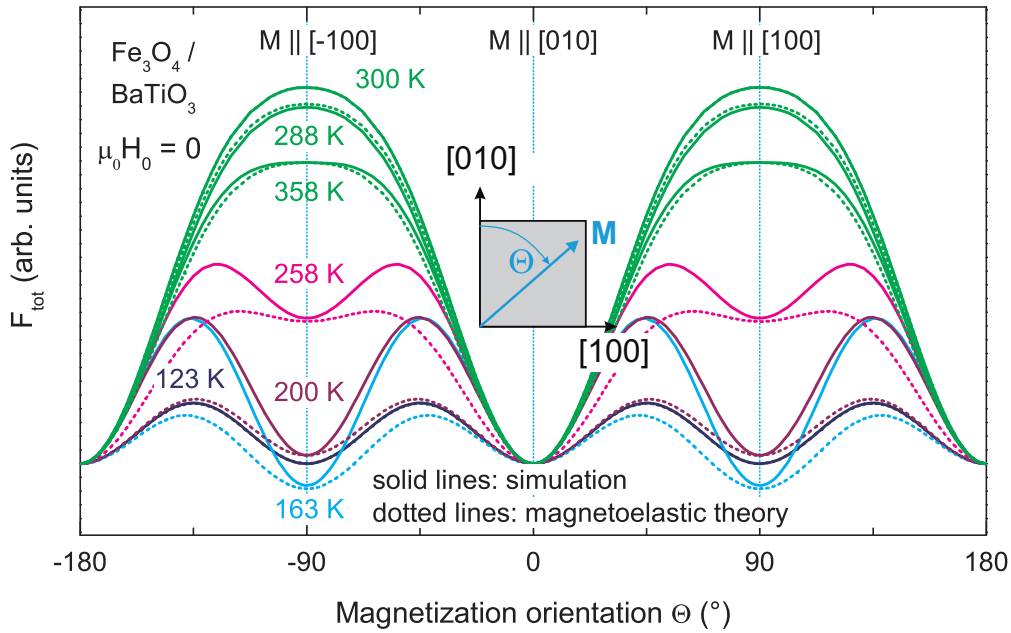


**Figure 8.8:** Free energy contours in the (001) plane obtained from simulation with the phenomenologically determined anisotropy constants displayed in Fig. 8.7 (solid lines) and free energy obtained from magnetoelastic theory (dotted lines).

and at  $T = 163$  K. For these temperatures, the cubic anisotropy differs significantly from the cubic anisotropy at  $T^* = 300$  K (cf. Fig. 8.7).

As the only free variables contributing to the magnetic anisotropy in Eq. (8.3) are the in-plane strains  $\varepsilon_1$  and  $\varepsilon_2$ , they can easily be derived from the system of equations (8.2). The material constants taken from Tab. 3.4 are inserted and a saturation magnetization of  $M_s = 305$  kA/m (reported for similar  $\text{Fe}_3\text{O}_4$  films on MgO substrates [56]) is assumed. The thus calculated strains are displayed in Fig. 8.9(b) as a function of temperature. To explain the change in the uniaxial anisotropy as a function of temperature by magnetoelastic theory, hence net strains of up to 0.35% are necessary.

The delicate question arising at this point is whether these strains are feasible in our heterostructure. This can only be checked if a possible domain configuration that may lead to these strains is derived for each measurement. It is important to note here that not all measurements were performed in succession. We already know that the  $\text{BaTiO}_3$  substrate undergoes irreversible domain configuration changes upon a phase transition. We thus can not rely on the domain configuration being identical

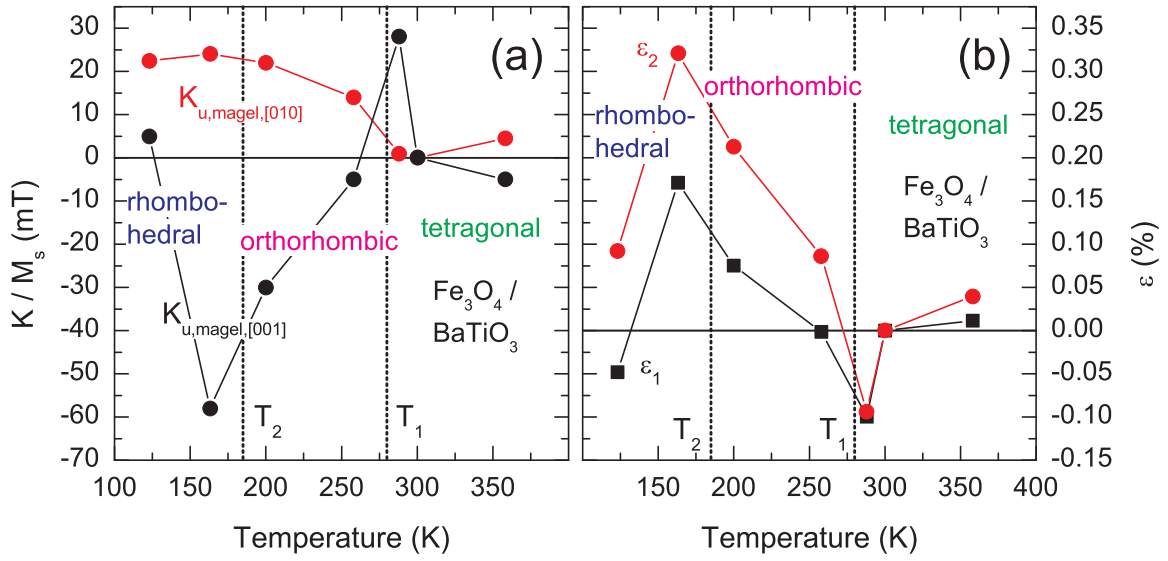


**Figure 8.9:** (a) Magnetoelastic anisotropy fields as a function of temperature. (b) In-plane strains as a function of temperature. The lines are guides to the eyes.

for all measurements performed in one  $BaTiO_3$  phase if a phase transition occurred in between measurements.

If the strains displayed in Fig. 8.9(b) are to be explained by a certain  $BaTiO_3$  domain configuration, we have to take into account the domain configuration at  $T = T^* = 300$  K, i.e. in the tetragonal phase, as well as the domain configuration in the phase corresponding to the measurement temperature. Furthermore, it has to be considered that not all domain transitions are allowed upon a phase transition (cf. Fig. 3.3).

For a single domain (sd) all possible strain pairs  $\{\epsilon_1^{sd}, \epsilon_2^{sd}\}$  are given by the difference in lattice constants between the reference temperature  $T^* = 300$  K and the measurement temperature  $T$ . Still assuming a single domain, this already yields several possibilities. For example, a tetragonal  $c$ -domain at  $T = T^*$  may transform into an orthorhombic  $c_1$ - or  $c_2$ -domain (but not into an  $a$ -domain) if  $T$  is in the orthorhombic phase. All possibilities are marked by arrows in Fig. 3.3. Hence, even in the simple case of a single domain  $BaTiO_3$  crystal, no unique set of expected strains can be calculated. We rather obtain two independent transition probabilities for possible domain formations upon the phase transition from the cubic to the tetragonal phase plus three independent transition probabilities from the tetragonal to the orthorhombic phase (cf. Fig. 3.3). Furthermore, domain walls may evolve, vanish

or move upon phase transitions, thus for example a single tetragonal  $c$ -domain may divide into orthorhombic  $c_1$ - and  $c_2$ -domains.

Hence, for completely unknown domain configurations, we have a huge set of free variables which can not be solved unambiguously to explain the strains in Fig. 8.9(b). As no in-situ study of the  $\text{BaTiO}_3$  domain distributions could be performed, no concluding remark whether the calculated strains are feasible can be made. In future experiments, it is desirable to prepare a  $\text{BaTiO}_3$  single-domain state at all temperatures by the application of an external electric field. In this case, magnetoelastic theory can directly be applied to calculate the expected strains and thus free energy surfaces that can be compared to those obtained from simulations of the measurements. However, the change of the cubic anisotropy with temperature – that is not expected in the magnetoelastic model – already clearly shows that an advanced model for this material system needs to be derived if the change of anisotropy as a function of the  $\text{BaTiO}_3$  lattice parameters is to be fully understood.



# Chapter 9

## Summary and Outlook

The ability to control the magnetization by means other than magnetic fields is of vast technological and fundamental interest. Intrinsic multiferroic materials, which unite ferromagnetic and ferroelectric properties in a single phase, show rather weak magnetoelectric interaction phenomena that can only be observed at low temperatures [114]. Thus they are of great fundamental interest, but difficult to use in everyday applications. Multiferroic heterostructures, however, exhibit room temperature magnetoelectric effects that are primarily due to interface strain at the ferroic phase boundary [95, 26, 96, 97].

In heterostructures of a ferromagnetic thin film deposited onto a ferroelectric substrate, the piezoelectric effect – which is inherent to all ferroelectric materials – can be utilized to apply an electric field-induced stress to the ferromagnetic thin film. The resulting strain influences the magnetic anisotropy of the magnetostrictive ferromagnetic phase and thus its magnetization. Hence, multiferroic heterostructures are very promising for realizing a voltage-strain-control of magnetization. With appropriately chosen ferroic constituents, giant and reversible converse magnetoelectric effects can be achieved at room temperature.

### 9.1 Summary

Magnetoelastic and magnetoelectric interactions in multiferroic heterostructures were investigated in this thesis. To this end, two classes of samples were prepared. Firstly, polycrystalline ferromagnetic thin films of cobalt or nickel were evaporated on piezoelectric PZT actuators by Andreas Brandlmaier. Secondly, ferromagnetic magnetite thin films were deposited on ferroelectric barium titanate substrates by pulsed laser

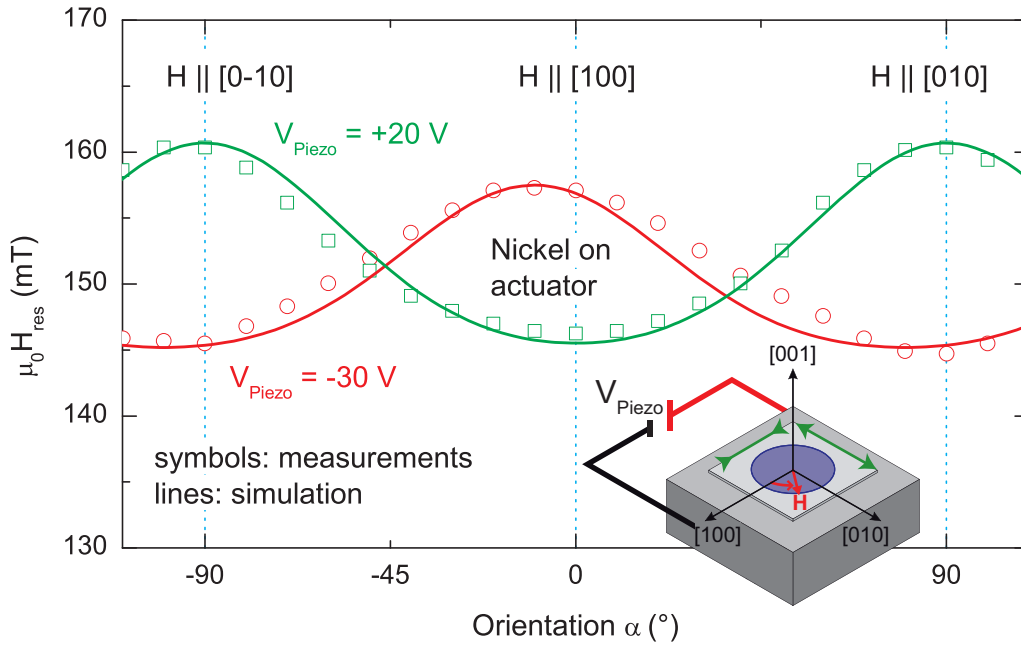


**Figure 9.1:** Inversion of the in-plane angular anisotropy of FMR resonance fields upon the application of positive and negative voltages to the actuator.

deposition by Stephan Geprags. Whereas in the first class of samples, the two ferroic phases are separated by a non-ferroic polymer layer, in the latter class a direct ferroic phase boundary exists. In the following, a summary of the most important findings in these heterostructures is given.

### 9.1.1 Strain-induced magnetization switching in ferromagnetic thin films

The actuator-based samples were investigated by ferromagnetic resonance (FMR) measurements using an X-band (9.3 GHz) spin resonance spectrometer. The samples' magnetic anisotropy was determined as a function of the voltage applied to the actuators and compared to the results expected from the application of magnetoelastic theory to a uniformly strained ferromagnetic thin film.

We observed linear and reversible shifts of the ferromagnetic resonance field in the order of several mT as a function of the voltage applied to the actuator. We found that the FMR resonance field shift as a function of actuator voltage is dependent on the orientation of the sample in the magnetic field. The two orthogonal in-plane directions

$\mathbf{H}_0 \parallel [100]$  and  $\mathbf{H}_0 \parallel [010]$  showed opposed shifts as a function of actuator voltage. The in-plane FMR resonance fields obtained for a Ni film evaporated on a piezoelectric actuator are shown in Fig. 9.1 for a negative and a positive voltage applied to the actuator. A clear in-plane uniaxial contribution to the magnetic anisotropy of the ferromagnetic thin film is induced by the stress exerted by the actuator. Upon the reversal of the polarity of the voltage applied to the actuator, the sign of this uniaxial contribution is inverted as well.

In the nickel film samples – which showed no net in-plane crystalline anisotropy after deposition– we are thus able to reversibly invert the magnetic free energy density and hence the equilibrium orientation of the magnetization by the application of voltages of different polarity to the actuator. In the cobalt film samples, we found a net uniaxial in-plane anisotropy after deposition. Still, the magnetic anisotropy of the cobalt samples could be tuned to a vast extent, but no inversion of anisotropy was observed.

The influence of external magnetic fields on the magnetization switching behavior of the nickel films was investigated theoretically. We found that small magnetic fields can be used to override the degeneracy of the free energy minima and to control the direction and magnitude of the magnetization switching. In the Ni films, magnetization switching by an angle of up to  $80^\circ$  in a magnetic field of 1 mT was predicted. Thus, these multiferroic heterostructures proved to be qualified for the application in voltage-controlled magnetization switching devices.

We finally also investigated an application of this voltage-strain-control of magnetic anisotropy: We replaced the conventional magnetic field modulation of the FMR setup by a strain modulation of the sample itself. This so called piezomodulated FMR (PMFMR) utilizes that the ferromagnetic resonance field is strain-dependent and anisotropic. The application of an AC voltage to the actuator hence results in an anisotropic signal modulation. PMFMR spectra at different modulation amplitudes and frequencies were recorded. We found that – due to the high number of magnetostrictive cycles carried out during one PMFMR measurement – PMFMR is a sensitive and fast way to measure very small strain-induced shifts of ferromagnetic resonance fields.

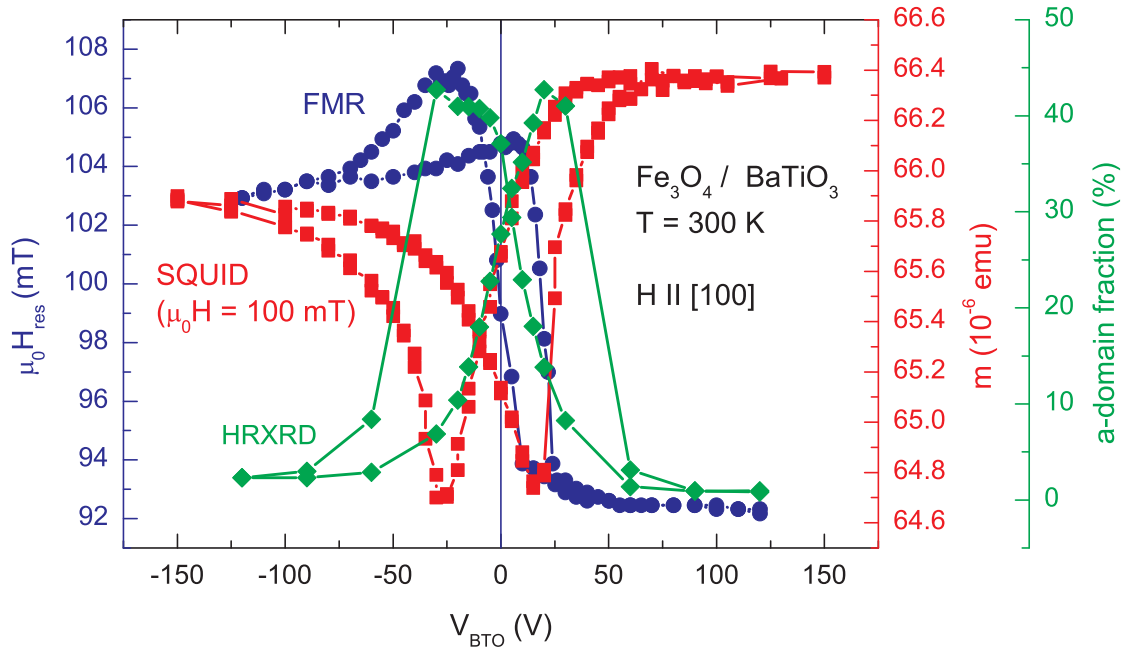


**Figure 9.2:** BaTiO<sub>3</sub> *a*-domain fraction determined by HRXRD (green), Fe<sub>3</sub>O<sub>4</sub> FMR resonance field (blue) and *M*(*E*)-loop (red) as a function of electric field (lines are guides to the eyes only).

### 9.1.2 Converse magnetoelectric effect in Fe<sub>3</sub>O<sub>4</sub>/BaTiO<sub>3</sub> heterostructures

In a complementary line of experiments, the effect of an electric field on the magnetization of multiferroic Fe<sub>3</sub>O<sub>4</sub>/BaTiO<sub>3</sub> heterostructure was investigated. To this end, thin films of Fe<sub>3</sub>O<sub>4</sub> were deposited on BaTiO<sub>3</sub> substrates by Stephan Geprägs. The domain formation in the BaTiO<sub>3</sub> substrate was investigated by HRXRD measurements as a function of applied electric field. The effect of the electric field on the magnetization of the magnetite thin film was quantified by SQUID magnetometry and FMR measurements.

By applying an electric field perpendicular to the ferroelectric BaTiO<sub>3</sub> substrate, we could show that we are able to completely and reversibly tune the BaTiO<sub>3</sub> substrate from a single *c*-domain state at high electric fields to a multi-domain state at no electric field. In these experiments, HRXRD measurements were utilized to establish the ferroelectric domain structure (cf. green symbols in Fig. 9.2).

SQUID magnetometry was used to record the magnetization as a function of exter-

nal magnetic and electric fields. Analyzing the experimental data provided by Stephan Geprägs, we found a distinct influence of the electric field on the  $M(H)$ -loops. The effect was investigated in more detail by recording the magnetization as a function of electric field at constant magnetic fields. These  $M(E)$ -loops showed contributions symmetric and antisymmetric to the electric field. An example loop for  $\mathbf{H} \parallel [100]$  is depicted by the red symbols in Fig. 9.2. The symmetric contribution qualitatively reminds of a ferroelectric strain-electric field butterfly loop, which is a strong indication for a strain-coupled converse magnetoelectric effect. However, the observed effect on magnetization is much larger than expected from the macroscopic deformation of the heterostructure upon the application of an electric field. Its magnitude can though be understood if the ferroelectric domains are regarded as elastic domains and magnetoelastic theory is applied domain-wise. The local, uniaxial strains in  $a$ -domains are in the order of 1% and can explain the observed symmetric effect.

FMR measurements were carried out to determine the ferromagnetic resonance field as a function of the electric field. The results for  $\mathbf{H}_0 \parallel [100]$  are depicted by blue symbols in Fig. 9.2. The results are comparable to those obtained by SQUID measurements, though the symmetric contribution is suppressed in FMR measurements as compared to the SQUID results. This is in accordance with the expectations from the multi-domain strain model discussed in Chapter 7.

Several possible causes of the considerable antisymmetric contribution to the  $M(E)$ -loops and the FMR resonance fields were considered. Sample misalignment was ruled out as its origin. As the antisymmetric contribution is visible in both SQUID and FMR measurements, artifacts associated with the respective measurement technique can be excluded as well. The HRXRD measurements clearly show that the domain formation is symmetric to the electric field, thus all strain effects are expected to be symmetric as well. A change of saturation magnetization was ruled out due to symmetry considerations. Hence, so far, the physical origin of the antisymmetric contribution is not understood, unless we observe  $a$ -domains directly at the ferroic interface even at high electric fields. We however proposed that the magnetic anisotropy in magnetite is a function of the free charge carrier density which in turn is influenced by the polarization of the ferroelectric BaTiO<sub>3</sub>.

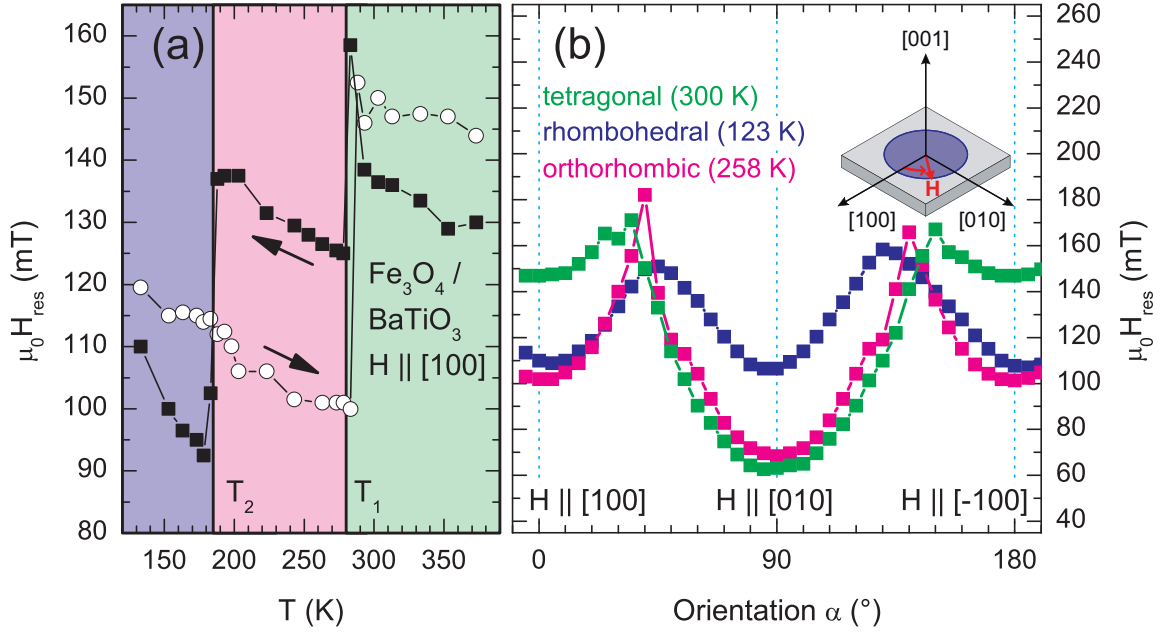


**Figure 9.3:** (a) Temperature dependence of FMR resonance field. The three ferroelectric BaTiO<sub>3</sub> phases are shaded in green (tetragonal), magenta (orthorhombic) and blue (rhombohedral). (b) In-plane anisotropy of resonance fields in the three ferroelectric BaTiO<sub>3</sub> phases. All lines are guides to the eyes only.

### 9.1.3 Temperature dependent magnetic resonance in Fe<sub>3</sub>O<sub>4</sub>/BaTiO<sub>3</sub> heterostructures

We finally investigated the effect of temperature on the magnetization of Fe<sub>3</sub>O<sub>4</sub>/BaTiO<sub>3</sub> heterostructures. Though, for application purposes, temperature is not a convenient control parameter for the magnetization, the temperature dependent magnetic behavior of this heterostructure is of fundamental interest due to the prominent temperature dependent properties of the BaTiO<sub>3</sub> substrate itself.

BaTiO<sub>3</sub> exhibits three ferroelectric phases below its Curie temperature  $T_c = 390$  K. For  $T_1 \approx 280 \text{ K} \leq T < T_c$  it is in its tetragonal phase, for  $T_2 \approx 185 \text{ K} \leq T < T_1$  in its orthorhombic phase and for  $T < T_2$  in its rhombohedral phase. The phase transitions are accompanied by discontinuities in the BaTiO<sub>3</sub> lattice constants and domain (re)formations as a function of temperature.

By FMR measurements, we observed discontinuous jumps of the Fe<sub>3</sub>O<sub>4</sub> FMR resonance fields at the BaTiO<sub>3</sub> transition temperatures  $T_1$  and  $T_2$ . This is shown in

Fig. 9.3(a). The influence of temperature on the FMR resonance fields was found to be irreversible if the BaTiO<sub>3</sub> substrate underwent a phase transition. Thus, we concluded that the BaTiO<sub>3</sub> substrate undergoes irreversible domain configuration changes upon a phase transition that transmit a strain into the ferromagnetic thin film and alter the magnetization through magnetoelastic interactions.

The magnetic anisotropy of the magnetite thin film was recorded in all three ferroelectric BaTiO<sub>3</sub> phases by FMR. Experimentally determined resonance fields are shown in Fig. 9.3(b) for one exemplary temperature per phase. Using magnetoelastic theory, the temperature dependence of magnetic anisotropy can be described approximately by considering the strain in the ferromagnetic thin film as a function of the BaTiO<sub>3</sub> lattice parameters and thus of temperature. However, in the unpoled state, no set of strains can theoretically be predicted, as the BaTiO<sub>3</sub> domain configuration is completely unknown and not reproducible upon phase transition. Due to the limited time allocated to this thesis, systematic temperature dependent experiments with simultaneous electrical poling of the ferroelectric substrate could not be carried out.

## 9.2 Outlook

The magnetization control in multiferroic heterostructures was described in two entirely different material systems in this thesis. We will now give an outlook on possible further applications and fundamental studies based on the results obtained.

For further applications, the possibility to switch the magnetization and the corresponding magnetic fields  $\mathbf{B} = \mu_0 \mathbf{M}$  in the actuator-based heterostructures is of great interest, as large, switchable magnetic fields have a great application potential. For instance, the generation of controllable magnetic fields is a fundamental problem in the realization of spintronic devices. An estimate of the magnitude of the switchable magnetic field for the Ni samples yields values of  $\mu_0 M_s \approx 0.5 \text{ T}$  in the film. This magnetic field decays as  $1/r^3$  into the space around the ferromagnet. This magnetic stray field could be measured, which would yield information about its magnitude and possible magnetization loss due to repeated switching processes.

Strain modulated FMR is a well-known technique to determine magnetostrictive constants. The approach to introduce the strain device (the piezoelectric actuator) *into* the FMR cavity itself, presented in this thesis, offers new perspectives: It is possible to rotate the sample in the magnetic field and thus anisotropic properties can

be investigated using strain-modulation. If precise means of determining strains are applied, PMFMR could be used for the determination of anisotropic magnetostrictive constants. The strains in the ferromagnetic film could be measured ex-situ by HRXRD, or more conveniently in-situ by laser interferometry.

Furthermore, it is desirable to evaporate ferromagnetic thin films on actuators that are switchable at frequencies in the MHz regime. At this frequencies it becomes possible to replace the microwave field used in FMR by the AC magnetic field of the actuator while still obtaining magnetic resonance fields in the order of several mT.

Regarding the  $\text{Fe}_3\text{O}_4/\text{BaTiO}_3$  heterostructure, smaller samples need to be fabricated to allow for the determination of in-plane anisotropy as a function of electric field. This will give valuable information on the electric field-control of the magnetic anisotropy in this heterostructure. As domain effects are a very important aspect to this heterostructure, means to spatially resolve magnetization orientation are needed. The magneto-optical Kerr effect (MOKE) [115] allows for such a spatially resolved determination of magnetization orientation. Furthermore, magnetic force microscopy (MFM) [116] could be used to gather qualitative information on the magnetization orientation at length scales below  $1\ \mu\text{m}$ .

Very promising is the combination of both FMR and MOKE in a single setup as described in [117], as this would allow to measure the macroscopic magnetic anisotropy while at the same time gathering information on ferromagnetic domains. A combined FMR/MOKE setup that allows for a temperature control, such as currently in development at the Walther-Meissner-Institut, is auspicious as well for further investigations of the temperature dependent properties of the  $\text{Fe}_3\text{O}_4/\text{BaTiO}_3$  heterostructure. Additionally, the temperature dependent properties of this heterostructure need to be investigated again in a single-domain substrate state, thus with an applied electric field. With this experiment, a reversible effect on the magnetization is expected.

Apart from these complementary investigations of the heterostructures described in this thesis, new multi-phase multiferroic material systems could be studied. Basically, two systems are of technological and fundamental interest: Bilayer structures with one ferromagnetic and one ferroelectric phase as well as multilayer structures.

For new bilayer structures, it is desirable to combine a ferroelectric substrate showing a distinct piezoelectric effect with a ferromagnetic thin film with huge magnetostriction and small net crystalline anisotropy. If the electric field is applied parallel

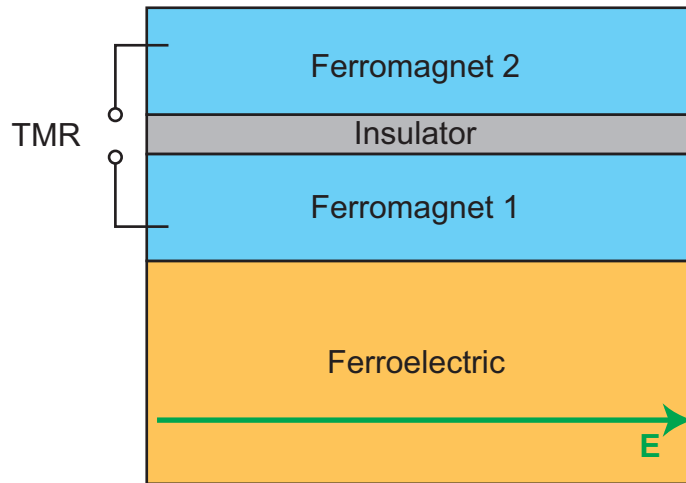


**Figure 9.4:** Possible multiferroic multilayer.

to the sample plane, the piezoelectric  $d_{33}$ -effect can be utilized to switch the magnetization of the ferromagnetic film.

Due to its large  $d_{33}$ -effect, PZT (cf. Chapter 3) is a very desirable ferroelectric substrate. In the paraelectric cubic phase, the lattice constant of pure  $\text{PbTiO}_3$  is 0.397 nm [118] and the lattice constant of pure  $\text{PbZrO}_3$  is 0.415 nm [119]. Reports of Ni/PZT heterostructures exist [120] and are expected to show magnetoelastic behavior similar to the Ni/piezoactuator heterostructures investigated in this thesis. Furthermore, with the successful deposition of  $\text{Fe}_3\text{O}_4$  on  $\text{BaTiO}_3$ , deposition of  $\text{Fe}_3\text{O}_4$  on PZT is expected to be possible as well due to the similarity of PZT and  $\text{BaTiO}_3$  lattice constants.

In Ferromagnet / Insulator / Ferromagnet tunnel junctions, tunnel magnetoresistance (TMR) was observed at room temperature [121]. Multiferroic multilayer structures could be designed as electric field-switchable magnetic tunnel junctions. These structures are theoretically predicted to be suitable as magnetoelectric magnetic recording heads [122] and thus are of utmost technological importance. A schematic view of such a possible multiferroic multilayer heterostructure is shown in Fig. 9.4. In such structures, experiments with different ferroic constituents could be made. For instance, it would be interesting to combine two ferromagnetic materials that show different magnetostriction. If an electric field is applied to such a heterostructure, the piezoelectric effect of the ferroelectric phase results in a strain in both ferromagnetic

phases.

The magnetization response to this strain is dependent on the magnetostrictive constants in the two ferromagnetic phases. Thus it may be possible to alter the magnetic anisotropy simultaneously in both phases in such a way that the magnetization orientations can be changed from parallel to antiparallel. Due to the tunnel magnetoresistance, an electric field could hence be used to switch this structure from a high resistive to a low resistive state.

For the ferroelectric phase, PZT can be used. For the ferromagnetic phases, nickel and permalloy ( $\text{Ni}_{1-x}\text{Fe}_x$ ) are a viable choice. While Ni shows negative magnetostriction, the magnetostriction of permalloy is dependent on the composition  $x$  and can thus be tuned from negative to positive values. At  $x = 0.2$ , permalloy shows no magnetostriction [123]. Thus it should be possible to influence only the Ni layer's magnetic anisotropy or even achieve inverted effects in both ferromagnetic layers which would allow to tune the magnetization from a parallel to an antiparallel state.

In conclusion, the investigation of multiferroic heterostructures is a very viable field of research that offers open questions in fundamental properties as well as a wide field of applications.

# Bibliography

- [1] M. N. Baibich, J. M. Broto, A. Fert, F. N. Van Dau, F. Petroff, P. Eitenne, G. Creuzet, A. Friederich, and J. Chazelas, *Physical Review Letters* **61**, 2472 (1988).
- [2] G. Binasch, P. Grünberg, F. Saurenbach, and W. Zinn, *Physical Review B* **39**, 4828 (1989).
- [3] J. F. Scott, *Nature Materials* **6**, 256 (2007).
- [4] M. Gajek, M. Bibes, S. Fusil, K. Bouzehouane, J. Fontcuberta, A. Barthelemy, and A. Fert, *Nature Materials* **6**, 296 (2007).
- [5] N. A. Spaldin and M. Fiebig, *Science* **309**, 391 (2005).
- [6] G. R. Fox, R. Bailey, W. B. Kraus, F. Chu, S. Sun, and T. Davenport, *Ferroelectric Random Access Memories Fundamentals And Applications* **93**, 139 (2004).
- [7] L. D. Landau and E. M. Lifshitz, *Statistical Physics*, Vol. 5 of *Course of theoretical physics*, 2nd ed. (Pergamon Press, London, 1959).
- [8] R. C. Smith, M. J. Dapino, and S. Seelecke, *Journal of Applied Physics* **93**, 458 (2003).
- [9] R. C. Smith, S. Seelecke, Z. Ounaies, and J. Smith, *Journal of Intelligent Material Systems and Structures* **14**, 719 (2003).
- [10] J. E. Massad, R. C. Smith, and G. P. Carman, in *Smart Structures and Materials: Modeling, Signal Processing and Control*, edited by R. C. Smith (SPIE, San Diego, 2003), No. 1, pp. 13–23.
- [11] A. F. Devonshire, *Philosophical Magazine* **40**, 1040 (1949).

- 
- [12] J. C. Slater, *Physical Review* **78**, 748 (1950).
- [13] P. Weiss, *Journal de Physique et le Radium* **4**, 661 (1907).
- [14] D. T. Haar and M. E. Lines, *Philosophical Transactions of the Royal Society of London. Series A* **254**, 521 (1962).
- [15] J. S. Smart, *Effective Field Theories of Magnetism* (Saunders, Philadelphia, 1966).
- [16] L. D. Landau and E. M. Lifshitz, *Theory of Elasticity*, 1st ed. (Pergamon Press, London, 1959).
- [17] J. C. Burfoot, *Ferroelectrics - An Introduction to the Physical Principles*, 1st ed. (D. Van Nostrand Company LTD., London, 1967).
- [18] E. Fatuzzo and W. J. Merz, in *Ferroelectricity*, edited by E. P. Wohlfarth (North-Holland Publishing Company, Amsterdam, 1967).
- [19] F. Jona and G. Shirane, in *Ferroelectric Crystals*, Vol. 1 of *Solid State Physics*, 1st ed., edited by R. Smoluchowski and N. Kurti (Pergamon Press, Frankfurt am Main, 1962).
- [20] L. Chen and A. L. Roytburd, *Applied Physics Letters* **90**, 102903 (2007).
- [21] N. A. Hill, *Journal of Physical Chemistry B* **104**, 6694 (2000).
- [22] N. A. Hill and A. Filippetti, *Journal of Magnetism and Magnetic Materials* **242-245**, 976 (2002).
- [23] T. Wu, M. A. Zurbuchen, S. Saha, R.-V. Wang, S. K. Streiffer, and J. F. Mitchell, *Physical Review B* **73**, 134416 (2006).
- [24] V. Laukhin, V. Skumryev, X. Marti, D. Hrabovsky, F. Sanchez, M. V. Garcia-Cuenca, C. Ferrater, M. Varela, U. Luders, J. F. Bobo, and J. Fontcuberta, *Physical Review Letters* **97**, 227201 (2006).
- [25] W. Eerenstein, N. D. Mathur, and J. F. Scott, *Nature* **442**, 759 (2006).
- [26] W. Eerenstein, M. Wiora, J. L. Prieto, J. F. Scott, and N. D. Mathur, *Nature Materials* **6**, 348 (2007).

- 
- [27] J.-G. Zhu, Y. Zheng, and G. A. Prinz, *Journal of Applied Physics* **87**, 6668 (2000).
- [28] S. T. B. Goennenwein, Ph.D. thesis, Technische Universität München, 2003.
- [29] S. Chikazumi, *Physics of Ferromagnetism, The international series of monographs on physics*, 2nd ed. (Oxford Science Publications, New York, 1997).
- [30] A. H. Morrish, *The Physical Principles of Magnetism*, 1st ed. (IEEE Press, New York, 2001).
- [31] A. K. Agyei and J. L. Birman, *Journal of Physics: Condensed Matter* **2**, 3007 (1990).
- [32] M. Fiebig, *Journal of Physics D* **38**, R123 (2005).
- [33] T. Lottermoser, T. Lonkai, U. Amann, D. Hohlwein, J. Ihringer, and M. Fiebig, *Nature* **430**, 541 (2004).
- [34] D. G. Sannikov and I. Zheludev, *Soviet Physics - Solid State* **27**, 826 (1985).
- [35] B. B. Van Aken, J.-P. Rivera, H. Schmid, and M. Fiebig, *Nature* **449**, 702 (2007).
- [36] D. Sander, *Reports on Progress in Physics* **62**, 809 (1999).
- [37] C. Kittel, *Introduction to Solid State Physics*, 7th ed. (Wiley, New York, 1995).
- [38] J. Donohue, *The Structure of the Elements*, 1st ed. (Wiley & Sons Ltd., New York, 1974).
- [39] H. Danan, A. Herr, and A. J. P. Meyer, *Journal of Applied Physics* **39**, 669 (1968).
- [40] A. J. P. Meyer and G. Asch, *Journal of Applied Physics* **32**, 330 (1961).
- [41] E. W. Lee, *Reports on Progress in Physics* **18**, 184 (1955).
- [42] M. Nishikawa, E. Kita, T. Erata, and A. Tasaki, *Journal of Magnetism and Magnetic Materials* **126**, 303 (1993).
- [43] J. Giber, R. Drube, and V. Dose, *Applied Physics A* **52**, 167 (1991).

- 
- [44] A. Y. Liu and D. J. Singh, 37th Annual Conference on Magnetism and Magnetic Materials **73**, 6189 (1993).
- [45] N. W. Ashcroft and N. D. Mermin, in *Solid State Physics*, 1st ed., edited by D. Crane (Saunders College, Philadelphia, 1976).
- [46] F. Schreiber, J. Pflaum, Z. Frait, T. Mühge, and J. Pelzl, Solid State Communications **93**, 965 (1995).
- [47] R. D. Dragsdorf, Journal of Applied Physics **31**, 434 (1960).
- [48] R. M. Bozorth, Physical Review **96**, 311 (1954).
- [49] M. Fonin, Y. S. Dedkov, R. Pentcheva, U. Rüdiger, and G. Güntherodt, Journal of Physics: Condensed Matter **19**, 315217 (2007).
- [50] B. A. Calhoun, Physical Review **94**, 1577 (1954).
- [51] P. Piekarczyk, K. Parlinski, and A. M. Oleś, Physical Review Letters **97**, 156402 (2006).
- [52] R. A. Lefever, *Part B, Landolt-Börnstein - Group III Condensed Matter* (Springer, Berlin, 1970).
- [53] S. Kale, S. M. Bhagat, S. E. Loffland, T. Scabarozzi, S. B. Ogale, A. Orozco, S. R. Shinde, T. Venkatesan, B. Hannoyer, B. Mercey, and W. Prellier, Physical Review B **64**, 205413 (2001).
- [54] D. T. Margulies, F. T. Parker, F. E. Spada, R. S. Goldman, J. Li, R. Sinclair, and A. E. Berkowitz, Physical Review B **53**, 9175 (1996).
- [55] P. A. A. van der Heijden, M. G. van Opstal, C. H. W. Swüste, P. H. J. Bloemen, J. M. Gaines, and W. J. M. de Jonge, Journal of Magnetism and Magnetic Materials **182**, 71 (1998).
- [56] A. Brandlmaier, Diploma thesis, Walther-Meissner-Institut, 2006.
- [57] E. J. W. Verwey and E. L. Heilmann, The Journal of Chemical Physics **15**, 174 (1947).
- [58] K. Kato and S. Iida, Journal of the Physical Society of Japan **51**, 1335 (1982).

- 
- [59] K. Kato, S. Iida, K. Yanai, and K. Mizushima, *Journal of Magnetism and Magnetic Materials* **31-34**, 783 (1983).
- [60] Y. Miyamoto and K. Ishiyama, *Solid State Communications* **87**, 581 (1993).
- [61] Y. Miyamoto, S. Ishihara, T. Hirano, M. Takada, and N. Suzuki, *Solid State Communications* **89**, 51 (1994).
- [62] H. B. Wang, Z. L. Liu, and O. H. Lu, *Chinese Journal of Inorganic Chemistry* **20**, 1280 (2004).
- [63] L. R. Bickford, *Physical Review* **78**, 449 (1950).
- [64] L. R. Bickford, J. Pappis, and J. L. Stull, *Physical Review* **99**, 1210 (1955).
- [65] R. F. S. Hearmon, *Advances in Physics* **5**, 323 (1956).
- [66] T. S. Benedict and J. L. Durand, *Physical Review* **109**, 1091 (1958).
- [67] A. von Hippel, *Reviews of Modern Physics* **22**, 221 (1950).
- [68] H. H. Wieder, *Journal of Applied Physics* **26**, 1479 (1955).
- [69] R. Landauer, D. R. Young, and M. E. Drougard, *Journal of Applied Physics* **27**, 752 (1956).
- [70] J. A. Hooton and W. J. Merz, *Physical Review* **98**, 409 (1955).
- [71] L. A. Shebanov, *Physica Status Solidi (a)* **65**, 321 (1981).
- [72] M. Zgonik, P. Bernasconi, M. Duelli, R. Schlessler, P. Günter, M. H. Garrett, D. Rytz, Y. Zhu, and X. Wu, *Physical Review B* **50**, 5941 (1994).
- [73] R. Bechmann and R. Hearmon, in *Landolt-Börnstein, New Series, Group III, Vol. 1: Elastic, Piezoelectric, Piezooptic and Electrooptic Constants of Crystals*, edited by K.-H. Hellwege and A. Hellwege (Springer, Berlin, 1966).
- [74] F. D. Morrison, D. J. Jung, and J. F. Scott, *Journal of Applied Physics* **101**, 094112 (2007).
- [75] E. Sawaguchi, *Journal of the Physical Society of Japan* **8**, 615 (1953).

- [76] *Low voltage co-fired multilayer stacks, rings and chips for actuation*, Piezomechanik GmbH, Munich, 2006, Model Pst 150/2x3/5.
- [77] Collaboration Authors and editors of the volumes III/17B-22A-41B, *II-VI and I-VII Compounds: Semimagnetic Compounds*, *Landolt-Börnstein - Group III Condensed Matter* (Springer, Berlin, 1999).
- [78] R. Gross and A. Marx, *Applied Superconductivity* (2006).
- [79] *Ferromagnetic Resonance*, Vol. 4 of *International Series of Monographs in Solid State Physics*, first english ed., edited by S. V. Vonsovskij (Pergamon Press, London, 1966).
- [80] C. P. Poole, *Electron Spin Resonance*, 2nd ed. (Dover Publications, New York, 1996).
- [81] R. Meckenstock, Ph.D. thesis, Ruhr-Universität Bochum, 1997.
- [82] C. Bihler, Diploma thesis, Technische Universität München, 2004.
- [83] B. D. Cullity and S. R. Stock, *Elements of X-Ray Diffraction*, 3rd ed. (Prentice Hall, New Jersey, 2001).
- [84] J. F. Nye, *Physical Properties of Crystals* (Oxford University Press, Oxford, 1985).
- [85] M. M. Hall, V. G. Veeraraghavan, H. Rubin, and P. G. Winchell, *Journal of Applied Crystallography* **10**, 66 (1977).
- [86] A. Brandlmaier, S. Gepreags, M. Weiler, A. Boger, M. Opel, H. Huebl, C. Bihler, M. S. Brandt, B. Botters, D. Grundler, R. Gross, and S. T. B. Goennenwein (unpublished).
- [87] R. Morel, A. Brenac, and C. Portemont, *Journal of Applied Physics* **95**, 3757 (2004).
- [88] M. A. Collins, S. D. Devine, R. A. Hoffman, and W. H. Robinson, *Journal of Magnetic Resonance* **6**, 376 (1972).
- [89] J. H. den Boef and J. C. M. Henning, *Review of Scientific Instruments* **45**, 1199 (1974).

- 
- [90] J. Henning and J. den Boef, *Applied Physics A* **16**, 353 (1978).
- [91] R. Zuberek, H. Szymczak, D. Zymińska, G. Suran, and M. Naili, *Journal of Magnetism and Magnetic Materials* **104-107**, 117 (1992).
- [92] R. Zuberek, K. Fronc, A. Szewczyk, and H. Szymczak, *Journal of Magnetism and Magnetic Materials* **260**, 386 (2003).
- [93] H. Szymczak, *Journal of Magnetism and Magnetic Materials* **200**, 425 (1999).
- [94] N. B. Ekreem, A. G. Olabi, T. Prescott, A. Rafferty, and M. S. J. Hashmi, *Journal of Materials Processing Technology* **191**, 96 (2007).
- [95] S. Shastry, G. Srinivasan, M. I. Bichurin, V. M. Petrov, and A. S. Tatarenko, *Physical Review B* **70**, 064416 (2004).
- [96] M. I. Bichurin, I. A. Kornev, V. M. Petrov, A. S. Tatarenko, Y. V. Kiliba, and G. Srinivasan, *Physical Review B* **64**, 094409 (2001).
- [97] C. Thiele, K. Dörr, O. Bilani, J. Rödel, and L. Schultz, *Physical Review B* **75**, 054408 (2007).
- [98] C.-G. Duan, S. S. Jaswal, and E. Y. Tsymlal, *Physical Review Letters* **97**, 047201 (2006).
- [99] F. Felten, G. A. Schneider, J. M. Saldana, and S. V. Kalinin, *Journal of Applied Physics* **96**, 563 (2004).
- [100] T. Ogawa, *Japanese Journal of Applied Physics* **40**, 5630 (2001).
- [101] S. J. van Reeuwijk, K. Karakaya, H. Graafsmab, and S. Harkema, *Journal of Applied Crystallography* **37**, 193 (2003).
- [102] D. A. Hall, M. M. Ben-Omran, and P. J. Stevenson, *Journal of Physics: Condensed Matter* **10**, 461 (1998).
- [103] M. Sueki, G. A. Rinard, S. S. Eaton, and G. R. Eaton, *Journal of Magnetic Resonance, Series A* **118**, 173 (1996).
- [104] M. Abolfath, T. Jungwirth, J. Brum, and A. H. MacDonald, *Physical Review B* **63**, 054418 (2001).

- 
- [105] A. W. Hornig, E. T. Jaynes, and H. E. Weaver, *Physical Review* **96**, 1703 (1954).
- [106] A. W. Hornig, R. C. Rempel, and H. E. Weaver, *Journal of Physics and Chemistry of Solids* **10**, 1 (1959).
- [107] W. Low and D. Shaltiel, *Physical Review Letters* **1**, 51 (1958).
- [108] E. Possenriede, P. Jacobs, and O. F. Schirmer, *Journal of Physics: Condensed Matter* **4**, 4719 (1992).
- [109] V. V. Laguta, A. M. Slipenyuk, I. P. Bykov, M. D. Glinchuk, M. Maglione, A. G. Bilous, O. I. V'yunov, J. Rosa, and L. Jastrabik, *Journal of Applied Physics* **97**, 073707 (2005).
- [110] R. Clarke, *Journal of Applied Crystallography* **9**, 335 (1976).
- [111] M. Althammer, Diploma thesis, Walther-Meissner-Institut, 2007.
- [112] R. V. Chopdekar and Y. Suzuki, *Applied Physics Letters* **89**, 182506 (2006).
- [113] S. Sahoo, S. Polisetty, C.-G. Duan, S. S. Jaswal, E. Y. Tsymlal, and C. Binek, *Physical Review B* **76**, 092108 (2007).
- [114] I. Kornev, M. Bichurin, J.-P. Rivera, S. Gentil, H. Schmid, A. G. M. Jansen, and P. Wyder, *Physical Review B* **62**, 12247 (2000).
- [115] H. Hornauer, T. M. Atmono, and K. Roll, *Journal of Magnetism and Magnetic Materials* **83**, 551 (1990).
- [116] L. Abelmann, S. Porthun, M. Haast, C. Lodder, A. Moser, M. E. Best, P. J. A. van Schendel, B. Stiefel, H. J. Hug, G. P. Heydon, A. Farley, S. R. Hoon, T. Pfaffelhuber, R. Proksch, and K. Babcock, *Journal of Magnetism and Magnetic Materials* **190**, 135 (1998).
- [117] M. Möller, D. Spoddig, and R. Meckenstock, *50th Annual Conference on Magnetism and Magnetic Materials* (AIP, San Jose, 2006), No. 8, p. 08J310.
- [118] G. Shirane, R. Pepinsky, and B. C. Frazer, *Acta Crystallographica* **9**, 131 (1956).
- [119] E. Sawaguchi, *Journal of the Physical Society of Japan* **7**, 110 (1952).

- 
- [120] H. Wan, C. Xu, and X. Z. Wu, *1st IEEE International Conference on Nano/Micro Engineered and Molecular Systems* (IEEE, Zhuhai, 2006), pp. 287–290.
- [121] J. S. Moodera, L. R. Kinder, T. M. Wong, and R. Meservey, *Physical Review Letters* **74**, 3273 (1995).
- [122] M. Vopsaroiu, J. Blackburn, and M. G. Cain, *Journal of Physics D: Applied Physics* **40**, 5027 (2007).
- [123] L. W. McKeehan and P. P. Cioffi, *Physical Review* **28**, 146 (1926).



# Acknowledgment

Finally, I would like to thank all those who contributed to this work with their invaluable professional and amicable support. In particular:

Prof. Dr. Rudolf Gross, for giving me the possibility to accomplish this work at the Walther-Meissner-Institut, the discussions of experimental results, all the anecdotes that contributed to the comfortable atmosphere and for generously allowing me to visit the IEFS in Berchtesgaden.

Dr. Sebastian T. B. Gönnerwein, for his overall support at all times. For his everlasting enthusiasm and his great capability of motivating his coworkers. For the numerous discussions in which he always had helpful ideas and a great sense of humor. For his overview of all the things I got lost into from time to time and the review of this thesis and all measurement results. And in general for his excellent guidance on my way of becoming a physicist.

Andreas Brandlmaier, for convincing me to accept this thesis in the first place and for accompanying me during its entire duration with the best imaginable support. For the contribution of numerous great ideas and the samples used for all piezo-related measurements – and all the other essential contributions to this thesis, including its detailed review.

Stephan Geprägs, for preparing the  $\text{Fe}_3\text{O}_4/\text{BaTiO}_3$  samples and for the SQUID measurements – and for being my definite resource for all questions regarding HRXRD and SQUID, which he answered in great detail. I am also thankful for the helpful discussions of all my measurements and the cheerful nature he always retained, despite all his numerous duties.

As this work would not have been possible without the overall assistance of the ESR group at the Walter Schottky Institute, I would like to express my gratefulness to everybody I frequently met in the "Café Resonance" and especially to:

Prof. Dr. Martin S. Brandt, who welcomed me like one of his own fellows from the very beginning and generously assigned measurement time in his ESR lab to me, despite my magical bad influence on the well-being of the setup. I would also like to thank him for the very useful discussions in the course of the Walt(h)er Seminar.

Christoph Bihler, who kindly assisted me with all questions and problems regarding the ESR setup and showed me the dirty tricks to overcome its sometimes stubborn nature. He sacrificed a tremendous amount of measurement and personal time to assist me with all FMR measurements and their discussion.

Dr. Hans Hübl, who always found time to answer my numerous questions and repaired the power source of the ESR magnet together with Christoph twice besides finishing his Ph.D. thesis.

Furthermore, all other members of the "Magnetiker" group at the Walther-Meissner-Institut contributed to this work in one way or the other. I would like to mention the support of:

Dr. Matthias Opel, for the discussions of the SQUID and FMR measurements and his motivating words if things did not work out as expected.

Matthias Althammer and Daniel Pantel, for the discussions on  $\text{BaTiO}_3$  and for exchanging our measurement results.

All other Diploma and Ph.D. students as well as the technical staff at the Walther-Meissner-Institut.

For their continuous amicable support I would like to thank:

My various colleagues in room 42, among others Johannes Büttner, Hans-Martin Eiter and Bernhard Muschler, for all the fun and sometimes fruitful discussions on physical and other topics.

My friends, for forgiving me that I only had so little time for them in the last months and for all the great moments we shared nevertheless. By name, I would like to mention Wilhelm Holderied, Ayla Yeginer, Thomas Flick and Marlin Schulze.

My family, for the best support in every possible aspect and their continuous encouragement on my way to the completion of my studies.